Multi Point Sensing and Defect Detection of Wind Turbine Blades

An Approach Using Fibre Bragg Gratings

Aananthalakshmy Sihivahana Sarma, BEng (Hons), MSc.

School of Engineering
University of Hull

A thesis submitted in partial fulfilment of the requirements for the degree of
Doctor of Philosophy (PhD.) in Electronic Engineering

April 2025

Abstract

Structural Health Monitoring (SHM) of Wind Turbine Blades (WTBs) plays a critical role in ensuring safe and cost-effective operations of these complex structures. However, detecting manufacturing-induced defects and operation-induced damages poses significant challenges. As stated by Güemes et al., 2018, defects are not direct physical parameters but rather local changes in material properties that degrade structural performance. Detecting these localised defects and subtle variations is particularly difficult with current SHM systems, which often lack sufficient spatial resolution and sensitivity.

This thesis investigates the application of Fibre Bragg Grating (FBG) sensors for multi-point sensing along the blade and explores advanced sensor data processing techniques to enhance early-stage defect detection. The main contributions of this work are: (1) a comprehensive review of common defects and damages in WTBs, as well as current condition monitoring, sensing, and non-destructive testing techniques; (2) the application of surface-bonded wavelength division multiplexed (WDM) FBG sensors for defect detection in laboratory-scale wind turbine blades and composite cantilever beams; and (3) the validation of FBG strain measurements against expected values derived from numerical simulations and analytical calculations.

The results of this work show that FBG sensors can successfully detect defects in wind turbine blades, with good agreement between measured and predicted strain values in both defect-free and defective composite cantilever beams. A novel investigation of the average measured strain over defects revealed that while smaller sensing lengths improve strain measurement accuracy, an optimal sensor length must be chosen to balance sensitivity with the number of sensors required for effective coverage of the blade. Additionally, the performance of FBG sensors in detecting defects was influenced by the complexity and nature of the defect, as well as sensor placement, but the FBG arrays effectively differentiated between healthy and defective blades.

To support these contributions, a LabVIEW-based data acquisition system was developed, along with an automated Gaussian FBG peak-fitting algorithm. Additionally, laboratory-

scale composite wind turbine blades (1.8 m) with and without an artificial defect were manufactured to validate the sensor system.

This work demonstrates that FBG sensors can reliably detect defects at an early stage in wind turbine blades. By leveraging these findings, the integration of FBG sensors into SHM systems could significantly enhance the operational efficiency and maintenance of wind turbine blades and related components.

Declaration

I hereby declare that except where specific reference is made to the work of others, the contents of this dissertation are original and have not been submitted in whole or in part for consideration for any other degree or qualification in this, or any other university. This dissertation is my own work and contains nothing which is the outcome of work done in collaboration with others, except as specified in the text and Acknowledgements. This dissertation contains fewer than 80,000 words including appendices, references, footnotes, tables and equations and has fewer than 330 figures.

Aananthalakshmy Sihivahana Sarma, BEng (Hons), MSc.
April 2025

Acknowledgements

I would like to acknowledge and thank the Doctoral College of the University of Hull for awarding me with the Research Studentship that covered the cost of my PhD and for the best student and researcher experience.

I am very grateful to a number of people, who have been instrumental in getting this thesis to completion and for supporting me with my research. Some, however, deserve special mention; first and foremost, my principal supervisor - Prof. James M Gilbert who has given me unfailing support, guidance, expertise, ideas, feedback, time and encouragement throughout this PhD journey. My secondary supervisor Prof. Ron Patton for his expertise, suggestions and valuable guidance.

My Amma and Appa whose love, understanding and unfailing support have kept me moving forwards and upwards and my brother Nivasan for always cheering me up and standing by me through the good times and bad. My partner Tharanitharan for his love, unconditional support and unwavering confidence in my skills and abilities and my cousins Vathsan and Ramya for their care and positive thinking encouragement.

I would like to express my gratitude to Dr. Kaushalkumar Bhavsar, Dr. Howard Snelling, Prof. Michael Fagan, Dr. Pete Watson and Stuart Butterick, Lee Wilson, Mike Jost and Simon Watson at the Electronics and Mechanical Engineering workshop and my colleague Oliver Morgan-Clague for helping whenever I needed and for their suggestions to run my experiments smoothly. In their own way, they were all instrumental in providing me the support to get the job done.

Finally, I would like to thank the wider EPSRC Prosperity Partnership community and SuperGen ORE Hub for their valuable discussions and contributions.

List of Publications

Materials from this thesis have been published at the following academic conferences; and a list of presentations and invited talks by the author occurring during the course of the PhD are given below:

1. “Multi-point sensing defect detection of wind turbine blades: An approach using Fibre Bragg Gratings”, Supergen Annual Assembly Early Career Forum 2023 | University of Southampton, UK - Won Poster Award.

2. “Wind turbine blades defect detection using FBG multi-point sensing”, European Academy of Wind Energy’s (EAWE) Wind Energy Science Conference (WESC) 2023 | Glasgow, UK.

3. “Wind turbine blades defect detection using fibre Bragg grating distributed sensing”, European Academy of Wind Energy’s (EAWE) PhD Seminar 2022 | Bruges, Belgium.

4. “Applications of fibre optic sensors for structural health monitoring of wind turbine blades”, presented 2 talks at regular session and at mini symposia at European Academy of Wind Energy’s (EAWE) PhD Seminar 2020 | Porto, Portugal - Online.

5. "Building your doctoral research from your master’s thesis" - Aura Centre For Doctoral Training (CDT) Seminar Series 2019 | University of Hull, UK.

Table of contents

List of figures

List of tables

Table of Symbols

Symbol	Description
ε	Strain
ε_{f}	Strain of fibre
ε_{m}	Strain of matrix
ε_{c}	Strain of resultant composite
$\mathrm{E_f}$	Young's Modulus of fibre
$\mathrm{E_m}$	Young's Modulus of matrix
$\mathrm{E_c}$	Young's Modulus of resultant composite
σ_{f}	Stress of fibre
σ_{m}	Stress of matrix
σ_{c}	Stress of resultant composite
f	Volume of fibre
$1\text{-}f$	Volume of matrix
w_c	Weight of composite
w_f	Weight of fibres
w_m	Weight of matrix
W_f	Weight fraction of fibre
W_m	Weight fraction of matrix
$\bar{z}$	Position of neutral axis
I_{xx}	Moment of inertia about the X-Axis
I_{yy}	Moment of inertia about the Y-Axis
n_L	Length scale factor
n_T	Time scale factor
$\theta(^\circ)$	Orientation angle
$\alpha(^\circ)$	Twist angle
ρ	Density
ω	Rotational Speed
Re	Reynold's Number
λ	Wavelength
T	Temperature

Table of Acronyms

Acronym	Meaning
ASHES	Aero Servo Hydro Elastic Simulations
CAD	Computer Aided Drawing
CM	Condition Monitoring
CNC	Computer numerical control
DAQ	Data Acquisition
DTG	Draw Tower Grating
FBG	Fibre Bragg Grating
FEA	Finite Element Analysis
FEM	Finite Element Method
FOS	Fibre Optic Sensors
FVF	Fibre Volume Fraction
FWHM	Full Width Half Maximum
GFRP	Glass Fibre Reinforced Plastic
GSV	Global Stiffness Variation
GW	Giga Watt
LE	Leading Edge
LPG	Long Period Grating
LSV	Local Stiffness Variation
MDF	Medium Density Fibreboard
MW	Mega Watt
NDI	Non-Destructive Imaging
NDT	Non-Destructive Testing
NI	National Instruments
NREL	National renewable Energy Laboratory
O&M	Operations and Maintenance
OSA	Optical Spectrum Analyser
PLA	Polylactic Acid
PS	Pressure Side
SGRE	Siemens Gamesa Renewable Energy
SHM	Structural Health Monitoring
SS	Suction Side
TE	Trailing Edge
USB	Universal Serial Bus
UV	Ultra-Violet
VARTM	Vacuum Assisted Resin Transfer Moulding
WDM	Wavelength Division Multiplexed
WT	Wind Turbine
WTB	Wind Turbine Blade

Chapter 1

Introduction

The wind energy industry has seen significant growth over the past 25 years, with continued expansion both onshore and offshore. According to the 2023 statistics and outlook report from WindEurope WindEurope, 2023, Europe installed a total of 18.3 GW of new wind power capacity in 2023, with 16.2 GW of this capacity coming from the 27 countries of the European Union (EU). This strong growth is pivotal in helping the EU meet its ambitious energy, climate, and net-zero targets by 2030. A key factor in achieving these goals has been the rapid development of offshore wind energy, which is expected to continue to play a major role in reinforcing energy security across the region, (See Figure 1.1).

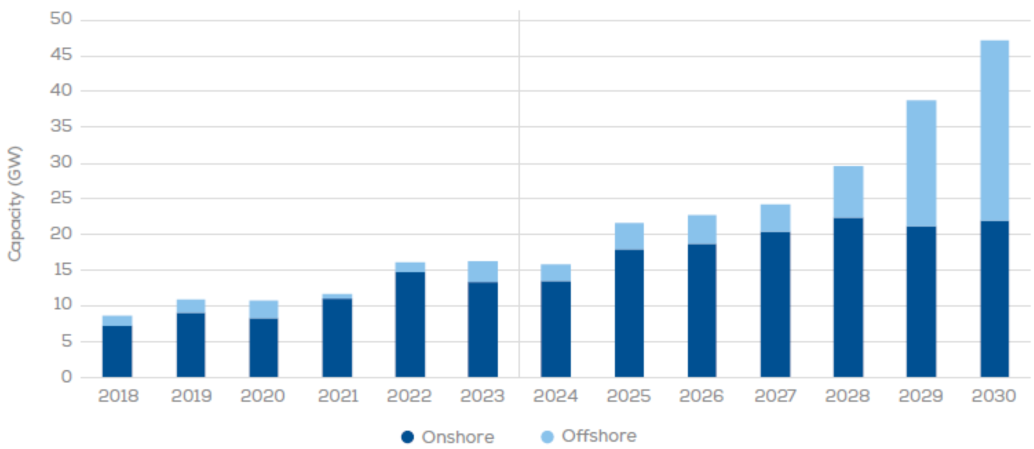

Figure. 1.1 Annual wind power installation outlook for 2024-2030 by WindEurope

The summary and outlook published in GlobalWindEnergyCouncil, 2023 states that along with the on-going supply chain delays and increasing logistical demands, all energy costs are on the rise. One of the main contributors to these price hikes is the rising costs associated with the operation and maintenance of wind turbine structures, as well as their components and sub-components. Both predictive and preventive maintenance heavily rely on sensors installed on the turbines however, in an offshore environment, wind and wave conditions are complex and come with extensive marine logistics and safety risks. Hence, access to these areas need to be planned ahead. Therefore, monitoring these structure's health and condition continuously from early-stage throughout its lifetime is necessary to help improve the reliability of diagnostic decisions and availability of wind energy for the long-term.

The following Section 1.1 describes the problem the work conducted for this thesis. Section 1.2 presents the aims and objectives of the tasks set out in this research and Section 1.3 states the original contributions of this thesis, particularly in the field of Structural Health Monitoring (SHM) of wind turbine blades using fibre optic sensing techniques. Finally Section 1.4 provides an overview of the thesis and outlines the structure of the thesis.

1.1 Addressing the Challenges in Wind Energy

Structural Health Monitoring (SHM) is becoming an integral part of the wind turbine operations and maintenance process. Generally, these SHM systems provide information necessary for action to improve performance, reliability and availability, particularly for offshore wind energy structures. According to Sheng et al., 2023, a 1% improvement in performance accounts for 2.7 billion US dollars additional revenue. Moreover, these monitoring systems are not only useful in predicting the remaining lifetime of wind turbine structures, rotor blades, tower etc. and to optimise the operations and maintenance (O & M), they can also be used for improving the design of components by identifying the failure modes. By continuously monitoring performance and detecting early signs of damage, engineers can adjust the design to enhance durability, load distribution, and efficiency. Furthermore, data collected through SHM can inform the development of more resilient materials and optimized geometries for future wind turbine designs, reducing maintenance costs and improving overall operational lifespan. However, this comes with a lot of challenges and opportunities for research and development.

Characterising failures involves quantifying factors that contribute to damage, such as loads, stress/strain, fatigue, corrosion, and temperature fluctuations. Damage, in this context, refers to any change in the material properties or structural integrity that occurs during the operational phase of a wind turbine, typically due to external forces or environmental factors that impact performance over time. It is important to distinguish between defects and damage: a defect typically refers to an inherent imperfection or flaw in the material or structure, often present from the manufacturing stage, whereas damage develops during operation as a result of wear, degradation, or external stresses. Damage can manifest as cracks, fatigue, or corrosion, and while it is a result of operational stresses, it often leads to a deterioration in the material properties of components. In this thesis, a 'healthy blade' refers to a structurally intact wind turbine blade without defects or damage, or alternatively defined as 'free from any artificially introduced defects.' A 'defective blade' contains a known structural defect that has been intentionally introduced to assess the performance of fibre optic sensors in detecting such artificially induced defects.

Simulations, numerical models, and digital twin models can provide valuable insights into potential damage and the effects of these factors, but evidence-based experimental data remains crucial for accurate and reliable assessments. Martinez-Luengo et al., 2016, Liu et al., 2023 Sheng et al., 2023 stated that this data plays a vital role in decision-making across sensing, operations, and maintenance (OM) processes, offering a more precise understanding of the wind turbine's structural health and its remaining operational life.

Several SHM and condition monitoring systems currently exist for wind energy applications such as supervisory control and data acquisition (SCADA) systems, acoustic measurements, vibration analysis systems, visual inspection etc. in Sørensen, Lading, et al., 2002, Krause et al., 2015, Carden and Fanning, 2004 Owen et al., 2010, Schubel, Crossley, et al., 2013 to name a few. Strain measurements are also utilised in the form of strain gauges however, early-stage defect detection using these conventional sensors are not practical in measuring small local changes in strain/ localised effects of defects. Optical sensing systems though utilised in wind energy such as in Kliewer, 2018, and Schroeder et al., 2006, use of these sensors is not common practise and require improvements to suit desired applications. For this particular reason, it is important to evaluate the performance of these optical sensors for defect detection using strain measurements. The results obtained from this thesis can be used for future applications as a stand-alone monitoring system or integration into existing broader SHM system to diagnose faults in blades.

1.2 Aims and Objectives

The main aim of the work, was to evaluate the viability of fibre optic sensors, particularly fibre Bragg gratings (FBG) for strain monitoring and defect detection that could potentially provide useful information on the structural health of wind turbine blades. The advantages provided by the FBG including their low cost, immunity to electro-magnetic interference, small size and weight, high sensitivity to strain and their ability to be multiplexed and used in numerous configurations were some of the main motivations for the research. An additional objective of the research was to assess the impact of sensor length on the average strain measured, along with evaluating the number of sensors needed to effectively detect a structural defect within a specified area.

The objectives of conducting the above explained research work in this thesis were as follows: (1) Identify and review the types of SHM systems, condition monitoring systems, non-destructive testing systems including fibre optic sensors, understand their working principle and evaluate the performance against different structural defect types. (2) design a data acquisition system which interfaces a sensors system based on multiple wavelength division multiplexed (WDM)-FBG arrays with required supplementary optical components. (3) identify and develop suitable data post-processing techniques to extract maximum information from the sensors. (4) identify the types of structural defect which can be reproduced in the laboratory (5) design and manufacture a test specimen i.e. blade of suitable size to conduct validation experiments. (6) determine the type of experiments to be conducted to investigate the performance (for example, static testing, component testing, fatigue testing etc.) (7) validate and demonstrate that in-situ FBGs can detect defects by measuring smaller variation in strain which can give information at early-stage defects of blades. (8) to provide suggestions for system design and suggestions for improvements for potential implementation and integration of the sensor devices to make up a SHM system for blades.

1.3 Contribution of this Thesis

This work has contributed to a better understanding of the performance of FBG sensors and the role of sensor placement in detecting structural defects in rotor blades, facilitated by the development of a systematic testing approach. The data acquisition system, alongside the modelling techniques and composite manufacturing methods used, has greatly simplified the process of conducting the necessary experiments. By streamlining the data collection and analysis, these approaches have enhanced the overall efficiency and feasibility of the experimental setup, making it easier to execute tests and obtain reliable results. To summarise, the original contributions to knowledge made by the author are as follows,

- A review of types of manufacture-induced defects and operation-induced damages occurring in a wind turbine blade during its lifetime and a review of existing SHM, condition monitoring and different types of non-destructive testing systems used in the wind energy industry.

- Application of a WDM-FBG sensor system for detecting structural defects in a damaged cantilever beam, combined with the development of a novel analytical method that links sensor length and the number of sensors to the minimum detectable strain under varying load conditions, enhancing sensor placement and configuration for improved defect detection sensitivity.
- A laboratory validation of measured strains from the WDM-FBG system and the expected strain for a scaled-down blade model designed and assembled to test the performance of these sensors. This also led to determining the performance of these FBGs for distinguishing defects going from a healthy blade.

1.4 Thesis Overview

This thesis is divided into chapter sections in the following order:

Chapter 2 provides an in-depth literature review on the different types of defects and damages occurring in wind turbine blades during each of its lifetime phases and presents a state-of-the-art overview of the solution techniques including structural health, condition monitoring, non-destructive testing techniques used currently. Furthermore, this chapter presents a novel contribution relevant to this research thesis by mapping the types of defects to the types of solutions available on the market and evaluates their suitability.

The following chapters detail the simulations and modelling work conducted. Before it is possible to perform experiments on a laboratory scaled blade, it is necessary to understand the application of the FBGs in a smaller, simplified manageable scale. Chapter 3 and 4 explain the approach taken for this thesis, provides necessary justification and draws conclusions about the effect of choosing the particular testing methods, testing specimen and the defect selected.

Chapter 3 Application of Fibre Optic Sensors: This chapter introduces the type of FBG used for this thesis. The preliminary sensor characterisation for axial strain and temperature are explored to determine the FBG's sensitivity to these parameters. A series of secondary FBG characterisation experiments on Aluminium and Composite cantilevered beam with and without a known defect were conducted and results are discussed in this chapter. A supplementary series of ANSYS Finite Element Analysis based simulations were also discussed.

The development and programming of the data acquisition system for the WDM-FBG arrays and the post processing technique used are also explained in detail. A novel contribution on the effect of sensor lengths vs average strain measured have also been presented.

Chapter 4 Aerodynamic, Structural Simulations and modelling of blades. The work presented in this chapter can be categorised into two; firstly a series of wind turbine simulations conducted and results have been reported. These aid in the evaluation of the type of defect that can be reproduced for the laboratory validation experiments and the discussion of the results provides a way of understanding the performance of a healthy blade compared to a blade with a structural defect present. The second part of the chapter describes the necessary scaling laws used and the theory applied for the design and modelling of the 1.8 m scaled blade model which were used for this thesis.

Chapter 5 Composite Scaled Blade Manufacture: This chapter elaborates on the common wind turbine blade manufacturing methods and the describes the methods explored for the composite manufacturing of the 1.8 m scaled down blade model for both the healthy case and the defective case. The assembly of the mould used for the blade, the materials used, the assumptions made as well as the assembly of the test platform with the adaptor plate and the test stand are detailed. The introduction of the defect and the steps taken for each task are given along with photographs taken during the actual manufacturing process.

Chapter 6 Implementation & Testing: Static Loading Setup: This chapter expands on the implementation of the experiments and the testing procedure conducted for both the healthy and the defective blades. The different blade mounting orientations, the different loading locations considered and the list of loads applied have been described in detail. The theoretical effect of defect have been presented along with the validation of the cross sectional properties of the blade's model with the manufactured blade's cross sectional properties. The collection of WDM-FBG arrays, their specification and their placement on the 1.8 m blade for both healthy and the defective case are tabulated.

Chapter 7 Results, Evaluation & Discussion: Here, the majority of the results taken from the WDM-FBG sensor array and data acquisition system have been plotted and are evaluated and validated against the expected results for the two blades considered. A number of different types of analyses have been provided based on the loading location, resultant spectra of the FBGs and the measured strain etc. The performance of the sensors are discussed in detail providing information on the viability of the FBGs bonded bended along the mid-line of the defect and at the periphery. Finally, the investigation on the minimum detectable strain and the comparison of healthy vs defective blade are presented.

Finally, **Chapter 8** concludes the research work in the thesis and highlights the key findings from each chapter and presents some suggestions for future study in the area of SHM of wind turbine blades using FBG sensors.

Chapter 2

Literature Review

2.1 Overview of Manufacturing-induced defects and Operation-induced damages in Wind Turbine Blades

2.1.1 Introduction

Chandrasekhar et al., 2017, Katnam et al., 2015 and Lorenzo et al., 2016 explain that with the current status of the offshore renewable energy industry, there is an increasing pressure for wind turbines to get bigger and the rotor blades to become larger in diameter. While this leads to an increase in energy production, rotor blades face higher operational monitoring demands to keep them running with minimal or amendable faults for 25-30 years. Employing non-destructive testing (NDT) techniques, both at the manufacturing stage and the operational stage can make condition/performance and SHM efficient, cost-effective and achievable. The specific feature of the NDT techniques which is appealing for wind energy structures is the ability to evaluate components without taking them apart and without disrupting the operation of the wind turbine. Over time, during the operational period, continuous condition monitoring can check for progressive damage which may have been initiated from manufacturing defects. Periodic non-destructive testing (NDT) or non-destructive imaging (NDI) techniques can provide critical/relevant information on the type of damage, size, depth, etc. By utilising these techniques, accurate and comprehensive information about the structural damage or failure can be obtained, enabling prognosis (e.g., residual strength or remaining life estimation) and the ability to assess and manage faults effectively.

This section provides an overview of the manufacturing defects potentially found in composite-based wind turbine blades and how these can develop over time and how they impact performance. A subsequent section will consider the Non-Destructive Testing (NDT) techniques which are most appropriate for detecting and monitoring these defects. An evaluation of the types of defects which can occur during each stage of the wind turbine blade lifetime is crucial in order to maintain the serviceability of the turbine. The significant failure modes of the wind turbine blades and root causes are discussed in this section.

Root Causes: to improve the understanding of blade failure and possible damage mitigation, defects are categorised based on the time at which they first occur as below,

- Design Flaws
- Manufacturing Defects
- Damage during transportation installation
- Damage occurring and/or progressing under wind turbine operation including extreme weather conditions
- Damage occurring or progressing due to poor service methods

Westergaard, 2013 theorises that almost always, failure is a sequence or combination of these root causes. For instance, design decisions may make it more difficult to achieve desired manufacturing quality, resulting in subsequent defects. Out of the above, most common defects occurring at the manufacturing stage and progressive or operation-induced damages are discussed in detail. A simple definition of design flaws is given below,

Design flaws are predominantly due to overlooking the combined load effects during the verification or testing. Not accommodating critical errors and excluding important failure mode combinations such as panel breathing which leads to accelerated peeling or stress in blades can also be categorized under this type of flaw.
These types of design flaws typically originate in the conceptual and engineering phases of blade development. While they can contribute to structural failure, their effects are more indirect and long-term, making them less suitable for direct detection using SHM techniques. On the other hand, manufacturing defects (e.g., delaminations, voids, misalignment) and operation-induced damages (e.g., fatigue cracks, debonding, deformation) manifest physically within the blade structure and evolve over time under real-world conditions. These issues are directly measurable using NDT methods and fibre optics sensing (FOS), allowing for early detection, monitoring, and mitigation. Therefore, this thesis prioritises these two aspects over design flaws, as they align more closely with the capabilities and objectives of fibre optic SHM systems. In this thesis, design flaws are not discussed in detail because the

primary focus is on manufacturing defects and operation-induced damages, which are more directly measurable and detectable using FOS and other NDT methods for SHM.

Different parts of a typical blade have different performance requirements and functions as mentioned in the Table 2.1 and is supported by Figure 2.1 below.

Table 2.1 Summary of Blade Requirements

Blade Element	**Function**	**Performance Requirements**	**Main Driver**
Root	Connect blade to hub and Transfer loads from blade to hub	Highly loaded and Provide space for bushings	Cost vs. Performance
Spar cap	Structural integrity of the blade	Provide stiffness and Carry loads	Performance
Shear web	Transfer shear forces between shells	Internal reinforcement	Cost
Shell	Aerodynamic Efficiency	Aerodynamic Surface	Cost

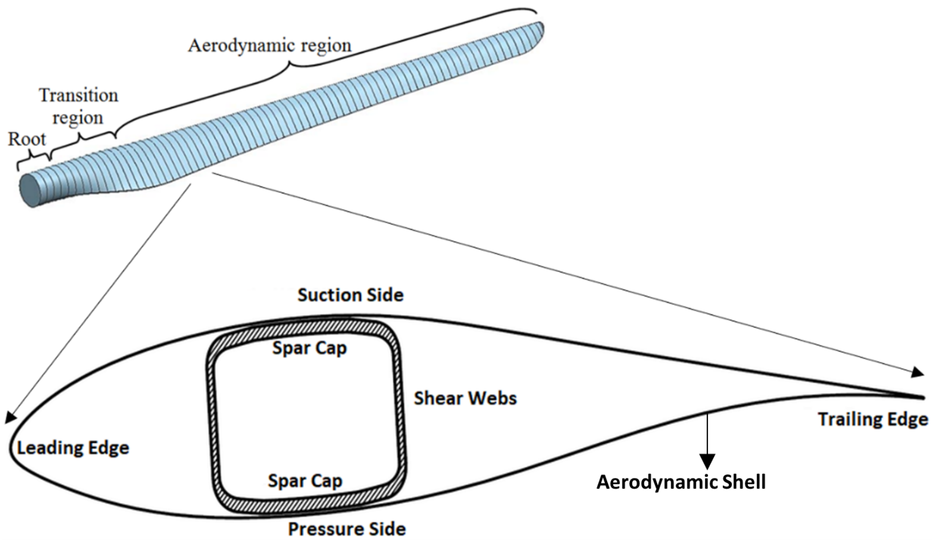

Figure. 2.1 Overall Blade Structure and Elements [edited, original source Esu, 2016]

Depending on the main drivers; either cost or performance, materials and manufacturing process are decided and generally, there could be trade-offs between them. This introduces the possibility of defects or imperfections at the next level even with the optimal design and manufacturing process.

For the purpose of this literature review and thesis, defects in composite materials are defined as inherent issues introduced during the manufacturing process, such as misalignments, voids, or improper curing. These flaws do not necessarily lead to immediate structural failure but can degrade the material's performance over time. In contrast, damage refers to the changes that occur during the service life of the structure, often as a result of operational stresses, impacts, or environmental conditions. Such damage can lead to more severe, irreversible effects, including fractures, deformations, or a significant reduction in strength. Recognising and distinguishing these is essential for effective monitoring and maintenance of composite structures such as wind turbine blades.

2.1.2 Manufacturing Defects

Manufacturing defects occur during the manufacturing process and can have a number of origins. Quality deviation in the materials used (fibre/ resin/ core/ metals such as steel/ aluminium etc) are one of the principal causes. Further, manufacturing defects could be due to random or systematic errors which includes incorrect application of fibres and/or adhesives, incomplete infusion of resin or dry spots due to poorly controlled curing or process parameters among others. Defects or imperfections may be initiated at the manufacturing phase and due to the cyclic, inertial and stochastic loads etc. which may lead to serious damages during the operational phase. However, some wind turbine manufacturers, such as Siemens Gamesa adopt a single shot casting method in their manufacturing process to eliminate the possibility of defects such as adhesive joint failure.

Delamination: Wind turbine blades are generally made of Fibre Reinforced Polymer (FRP) materials. The main components of laminates are matrix and reinforcements. The matrix (commonly, the resin) holds laminate components together, whereas the reinforcement provides transfer of loads. The reinforcement usually takes the form of very stiff and durable fibres. Different fibre layers can provide the same or different mechanical properties. By changing the configuration or orientation of reinforcing fibres, or laminated materials, the optimal material features can be obtained as mentioned in Doliński et al., 2018. Jüngert, 2008 defines delamination as the loss of cohesion between the laminate layers. The most probable causes can be air trapped within the laminates or some parts of the laminates not being fully immersed with resin.
Another reason is the wrinkling and misalignments of the dry fibre mats during handling. Delamination can occur at multiple locations on the blade but more commonly at the blade root

and the transition section (refer Figure 2.5). Because of delamination, Jüngert, 2008 stated that the rigidity of the turbine blade may be compromised. Shrinkage of the resin matrix during curing causes residual stress and can result in micro-buckling (of the reinforcement fibres). Eum et al, 2007 stated another consequence of resin shrinkage is the delamination in composite structures which reduces the dimensional stability of the final product. Impacts on the blade composite material normally lead to delamination between the fibre layers and the matrix material.
Delamination initiated at the manufacturing phase can progress into serious damage inducing element when blades undergo repeated loading. During long-term operations, the vortices formed by different wind speeds can cause surface delamination resulting from local resonance of the blade and crack damage resulting from material fatigue as explained by Chou et al., 2013. Another form of delamination is driven by the tensile, buckling or compressive load and it induces internal damage formation and growth in laminates in skin and/or main spar flanges as explored by Ciang et al., 2008.

Improper Curing: Curing can be described as a chemical and physical reaction procedure where the performing material ends up tougher/ harder and with more stable linkage. For example, combining resin and plies of fibre in a precise manner while varying environmental parameters such as temperature or pressure in order to obtain the wind turbine blade composite material or component. This process produces the toughening or hardening of a polymer material by cross-linking of polymer chains using heat, pressure, etc as mentioned in Schubel, Crossley, et al., 2013. Improper Curing may be due to non-uniform temperature resulting in poor quality of the composite. Low temperatures may result in slow curing while excessive temperature may cause the resin to adversely heat up. Since curing is an exothermic process, unfavourable limitations on time can also result in improper curing, not just the temperature applied. During the manufacturing process, technicians and experts can easily spot if the blade will be unsuitable by monitoring the temperature levels and other parameters. Since some composites are processed at high temperatures, when the mould is cooled, the differing thermal expansion of the matrix and reinforcement dictate that residual stresses will be present in the finished component. Resin shrinkage during the cross-linking polymerisation process contributes to the residual stresses. Later during wind turbine operation, these residual stresses can introduce damage in the form of matrix cracks and delamination, resulting in significant warping of the finished component.

Wrinkles: In-plane and out of plane waviness are significant flaws that can occur during the manufacturing process (See Figure 2.2). These types of geometrical distortions of the plies results in a considerable decrease of mechanical integrity of the localised region. The immediate consequence of wrinkles is delamination of the plies. Wrinkles can degrade blade strength and the fatigue life of the composite laminate and can make the blade's structure sensitive to low cycle fatigue. Further, wrinkles can lead to other faults such as fibre fracture, interface debonding, and matrix cracking, which are sources for micro buckling, translaminar crack growth, and delamination. Wrinkle caused damage can propagate to the point of failure after experiencing high loads for low number of cycles according to Douglas Cairns, 2016.

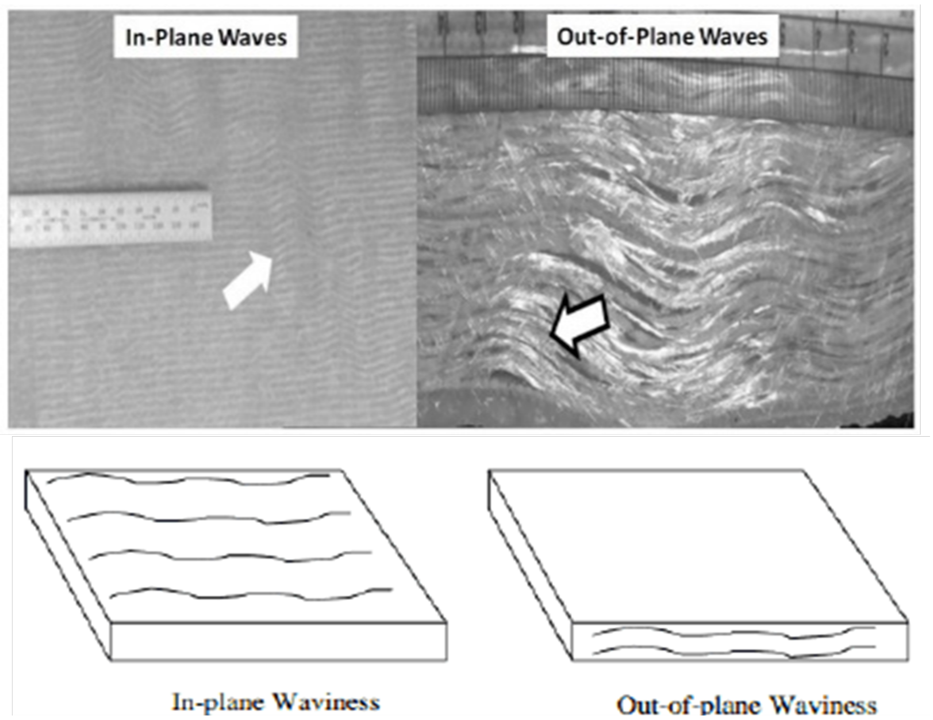

Figure. 2.2 Wrinkles - in-plane out-of-plane waviness adapted from Douglas Cairns, 2016 and Raghavan, 2015

Dry Spots: Martin et al., 2018 explained that dry spots are areas of poor or no bonding between adjacent plies caused by trapped air or a weak infusion of resin in the given area. The main causes for dry spots are improper vacuuming procedure which can trap air and/or insufficient wetting of the fibres in difficult/ tricky areas where the resin flow cannot easily reach. Formation of dry spots depends on the resin flow conditions, which are affected by the viscosity of the resin, the permeability of the preform, pressure, temperature, stacking pattern and infusion strategy as mentioned in Eum, Kageyama, Murayama, Uzawa, et al., 2007. This defect can degrade the mechanical properties of the blade significantly and dry spots can cause the debonding of the two interfaces that it affects, which are triggered by buckling-driven loads. Typically, the size of dry spots can range from a few centimetres to a few metres.

Voids: According to Mehdikhani et al., 2019 and Martin et al., 2018, voids are regions filled with trapped air and are caused by air bubbles trapped in the laminate during the curing cycle – specifically the infusion process or by nucleation from volatiles during processing. The air entrapment is mainly due to the inhomogeneous fibre architecture, resulting in non-uniform permeability of the fibre preform, which causes local variation in resin flow velocity. Voids can be stationary or could grow during the production or operational stage and can changes tensile, mechanical, flexural/elastic properties of the blade and cause intra and inter laminar fracture. Finally, voids may lead to transverse cracking and to compressive failure. Voids are normally smaller (typically, a few millimetres) compared to dry spots and are a problem only if there are too many of them which could potentially lead to growth, cracks and severe sub-surface defects.

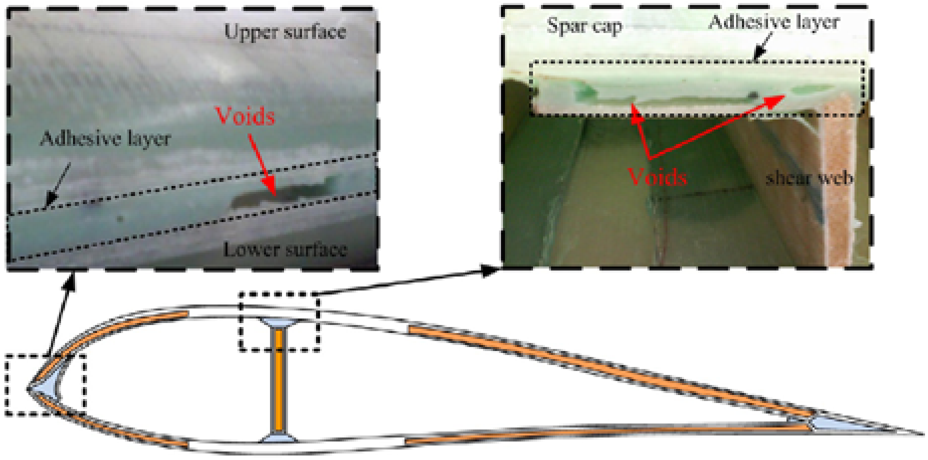

Figure. 2.3 Voids in the bonding lines of composite wind turbine blade, sourced from Mehdikhani et al., 2019

Misalignment: Mikkelsen and Mishnaevsky Jr, 2017 stated that misalignment is a type of defect which is essentially the mis-orientation of fibres. They can be either individual fibre misalignment or Lamina (fibre mats/ laminates) misalignment. This can be due to randomly placed fibres at different angles or randomly distributed fibres with non-uniformity or even due to kinking of fibres with one another (curve/twist when it is otherwise straight/flat). Misalignments can reduce static and fatigue properties significantly and leads to strong reduction of compressive and fatigue strength. Just like wrinkles, misalignments can further lead to failure mechanisms such as fibre fracture, interface debonding, and matrix cracking, which are sources for micro buckling, translaminar crack growth, and delamination which can be found in Douglas Cairns, 2016 and Cairns et al., 2011.

Debonding: Doliński et al., 2018 and Ciang et al., 2008 stated that debonding can be described as the loss of cohesion between individual fibres i.e. fibre splitting due to the loss of cohesion between fibres or between the fibres and the surrounding matrix (fibre-matrix interface) or it can be adhesive joint failure between skins i.e. failure between different material layers: adhesive bond and the skin of the composite structure, or between gel-coat and the underlying material. Based on Jüngert, 2008 and Myrent et al., 2015, generally, for shells at the leading or the trailing edge and internal spars, debonding can occur due to too little adhesive and leads to missing or partial bond between the two halves. Possible progression of the fault includes debonding of the gel-coat from the skin (gel-coat cracking and gel-coat/skin debonding) according to Ciang et al., 2008. Buckling of the skin due to damage formation and growth in the bond between skin and main spar under compressive load (skin/adhesive debonding induced by buckling). If a bond void is already present between the shear web and the blade shell before the turbine is even commissioned, the shear web debonding will likely increase in length due to shear stresses and fatigue. Debonding in the blade composite mainly occurs (in FRP structures) because of the delamination of the layers of laminates. As the reinforcements are only in-plane and no reinforcement are present in the out of plane direction, therefore such structures are prone to delamination. However, WT manufacturers such as Siemens Gamesa cast the entire blade in one piece hence, there is no debonding between the shells and adhesive joint failure in shear webs is also avoided by integrating the shear web with the structure while casting the entire blade.

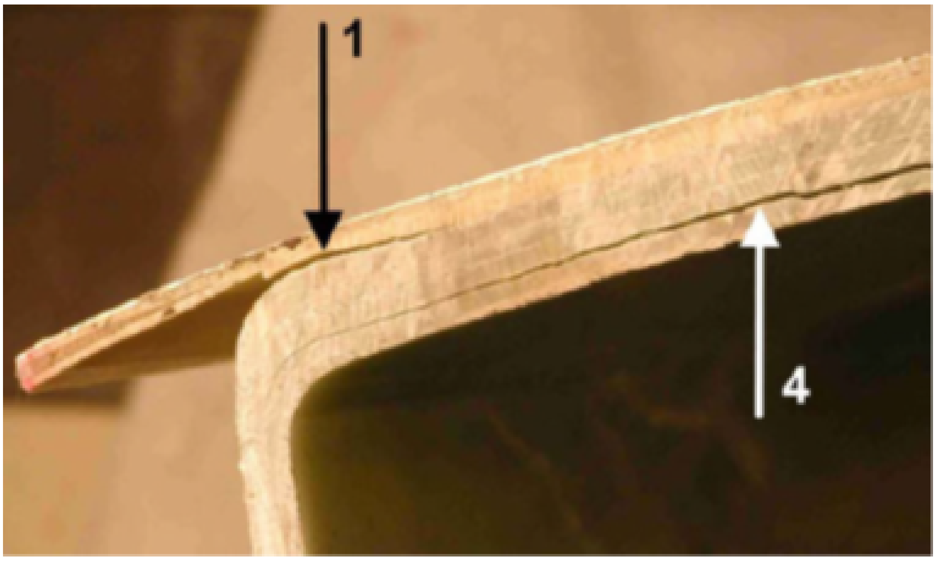

Figure. 2.4 Damage Type 5 (see Table B) Laminate Failure in Compression and Type 7: Gel coat cracking at the bottom of the leading edge, original source: Ciang et al., 2008

Other: Unfavourable occurrences during the blade manufacturing procedure also includes too much adhesive which brings in additionally weight and can cause unbalanced masses. It also affects the hardening process and can lead to fissures within the bond as explained by Jüngert, 2008.

2.1.3 Operation-induced Damages

Cairns et al., 2011 discussed that turbine components often enter the operational stage with allowable manufacturing defects or imperfections. Considering the reliability of wind turbines and operations maintenance costs, an understanding of faults and damage progression can lead to increased life cycle of the structures and effective exploitation of offshore wind.

Based on experiments mentioned in Price and Figueira, 2017 and Sanati et al., 2018, typical damages found in Carbon Fibre Reinforced Plastic (CFRP) and Glass Fibre Reinforced Plastic (GFRP) wind turbine blade can be classified into types and tabulated as below (Table 2.2) and illustrated in Figure 2.5, However, the table is not comprehensive and doesn't include all types of defects as elaborated in Sørensen, Joergensen, et al., 2004, Sørensen, Lading, et al., 2002 and Ciang et al., 2008.

Table 2.2 Typical damages in CFRP and GRP wind turbine blades, source: Ciang et al., 2008

Damage Types	Description
Type 1	Damage formation and growth in the adhesive layer joining skin and main spar flanges (skin/adhesive debonding and/or main spar/adhesive layer debonding).
Type 2	Damage formation and growth in the adhesive layer joining the upwind and downwind skins along leading and/or trailing edges (adhesive joint failure between skins).
Type 3	Damage formation and growth at the interface between face and core in sandwich panels in skins and main spar web (sandwich panel face/core debonding).
Type 4	Internal damage formation and growth in laminates in skin and/or main spar flanges, under a tensile or compression load (delamination driven by a tensional or a buckling load).
Type 5	Splitting and fracture of separate fibres in laminates of the skin and main spar (fibre failure in tension; laminate failure in compression).
Type 6	Buckling of the skin due to damage formation and growth in the bond between skin and main spar under compressive load (skin/adhesive debonding induced by buckling, a specific type 1 case).
Type 7	Formation and growth of cracks in the gelcoat; debonding of the gelcoat from the skin (gel-coat cracking and gelcoat/skin debonding).

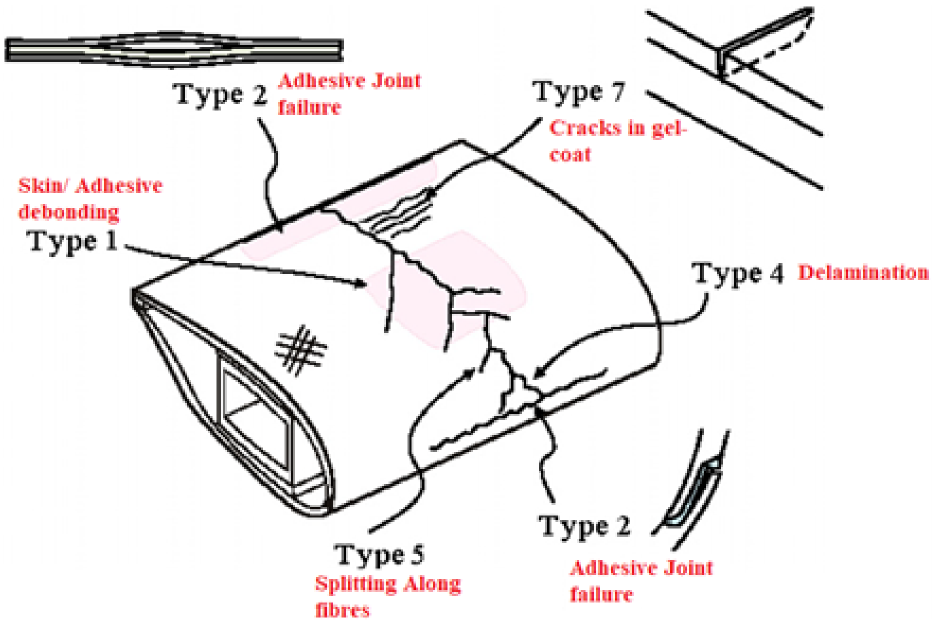

Figure. 2.5 Key types of damages defects, source: Ciang et al., 2008 (See Table 2.2)

Key damages and defects identified are described in detail below and additional defects are illustrated in Figure 2.6,

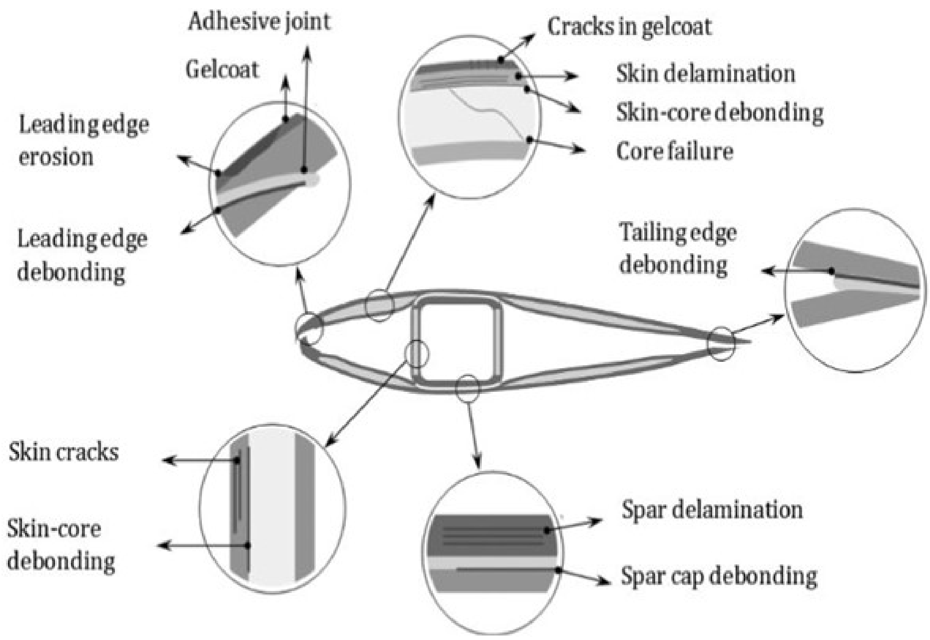

Figure. 2.6 Some common damage modes in composite wind turbine blades, sourced from Katnam et al., 2015

Buckling: This is one of the failure modes of a blade structure and may be caused by structural instability of the blade when it is loaded under compression. When the wind turbine blade is subjected to high compressive stress, buckling occurs due to the elastic instability of the blade. There can be two main types of buckling in blades, local buckling occurs primarily in the panels in the trailing edge and global buckling which occurs in trailing edge due to skin debonding. Both types of buckling depend on the thickness of the shell relative to the length of the blade and whether inner stiffeners exist or not. Buckling is considered to be a severe failure mode since it decreases the performance of the wind turbine and even cause failure of the blade.

Blade deformations: Although this is not a damage, this may occur during wind turbine operational phase and may drastically reduces the wind energy production and also can lead to catastrophic structural failures (failure-mode of the blades). Permanent and semi-permanent deformations change the aerodynamic performance of the blade and can have several causes such as twisting and erosion (leading edge). Twisting is a type of blade deformation where the blade tries to distort in the transverse direction (torsional movement) due to non-linearity of the wind loads blade structure, especially if blades have thin walls without any internal reinforcements. This distortion may become worse if the blade already has design (structural or manufacturing process) flaws and has non-symmetrical geometry from manufacturing.

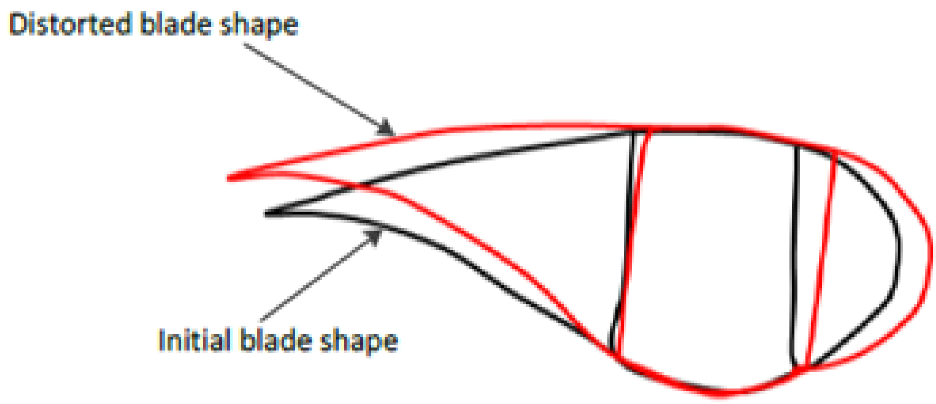

Figure. 2.7 Blade shape - before and after distortion, original from Esu, 2016

Deflections: Deflection of the blade is generally expected but adverse blade deflection (resulting in permanent/ semi-permanent deflection) has several causes: high out of plane loads or presence of delamination in the blade which results in no-resistance for the oncoming loads or complete lack of fibres in the transverse direction of the blade. For blade tip deflections, the lift force generated by the aerodynamic profile of the blade causes flap-wise bending (i.e., either static or dynamic). The natural variations in wind speed cause variations in flap-wise bending moments and thus cause blade fatigue as stated by Katnam et al., 2015. This changes the stiffness at the tip of the blade and causes the blade to bend and deflect and causes the clearing distance from tip to tower to decrease hence increasing the likelihood of the blade tip hitting the tower. Another phenomenon is extreme wind shear when the blade tip is at the top which causes the blade to bend and can lead to a semi-permanent or permanently bent tip.

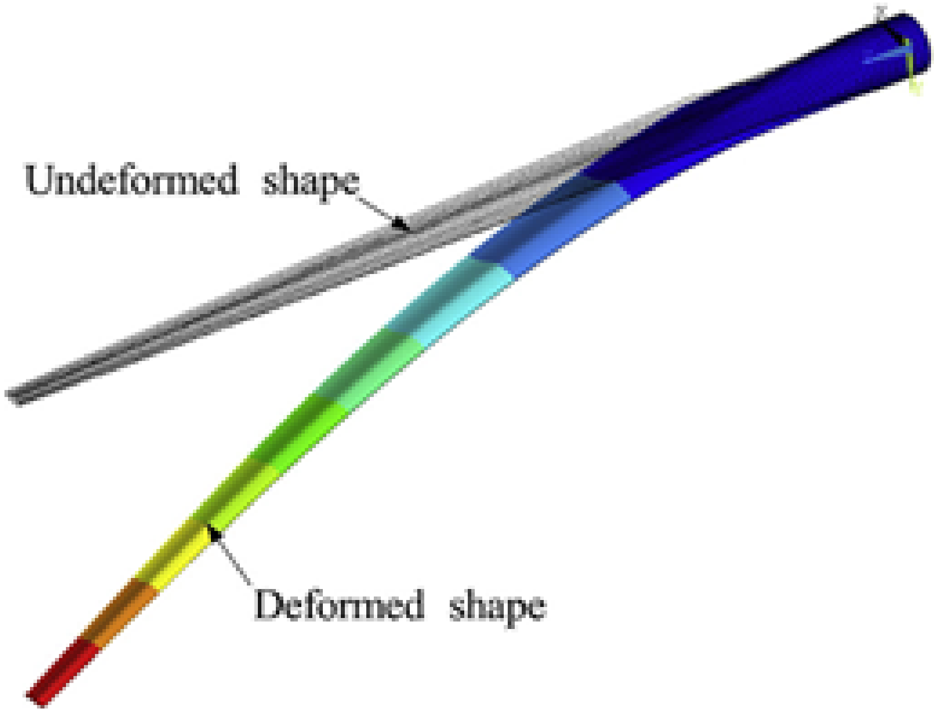

Figure. 2.8 Blade deformation due to adverse deflection (edited, original source: Esu, 2016)

Debonding at leading edge: Cross sectional shear adds loading to the leading-edge bonds which induces debonding. Initial causes include presence of dry spots or voids introduced during the manufacturing stage. Debonding at leading edge can progress into blade deformation or deterioration of the blade shape and a small percentage of this fault can contribute to leading edge erosion as well.

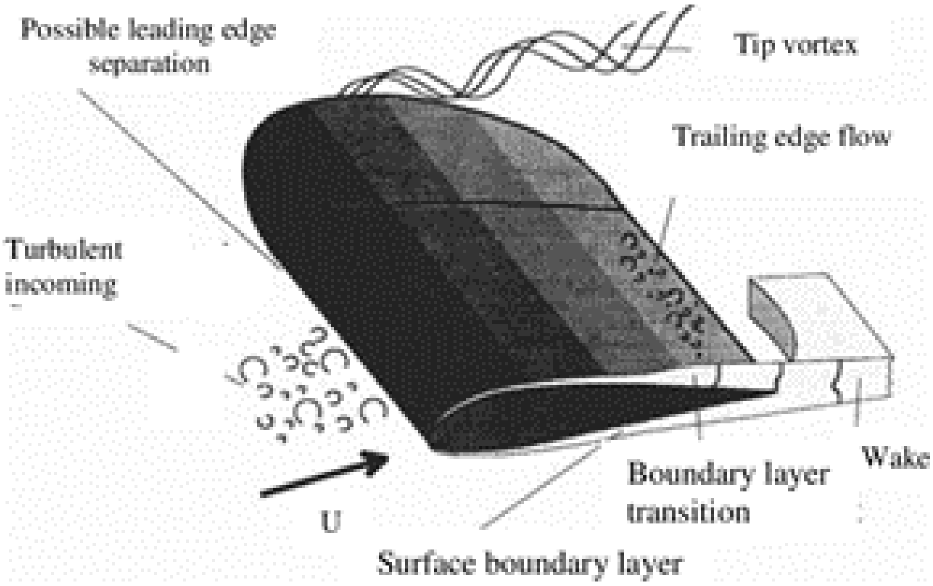

Figure. 2.9 Debonding in leading-edge of blade (edited, original source: Douglas Cairns, 2016)

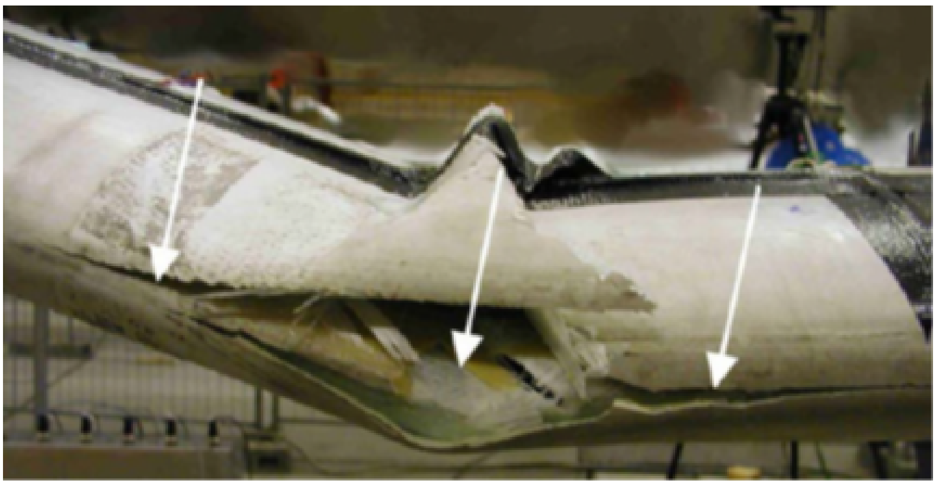

Figure. 2.10 Damage Type 2 - Adhesive Joint Failure between skins at the leading edge, original source: Ciang et al., 2008

Leading Edge Erosion: Another fault which can be found in the leading edge is erosion. Naturally, the leading edge is subjected to wind, water, ice and other natural agents (for example, Ultra Violet – UV rays) and airborne particles. Continuous impacts from these cause erosion and degradation during operation. Improper application of gelcoat or lack of protective film during the manufacturing stage can accelerate the initial causes. During turbine operation, blades that encounter the impact of sand particles and/or water droplets or mixtures will first show an increase in surface roughness that affects the aerodynamic performance negatively, for example by increased friction drag and by an earlier onset of stall as explained by Marulo et al., 2014. Katnam et al., 2015 stated that minor damage such as surface erosion can considerably reduce aerodynamic efficiency and thus power generation. Ciang et al., 2008 and Marulo et al., 2014 explain that eventually, it compromises the integrity of blade surfaces which in turn results in turbine downtime and high maintenance costs .

Figure. 2.11 Leading Edge Erosion, sourced from Marulo et al., 2014

Panel breathing peeling stress: Generally, this defect occurs in blades manufactured as two halves and then bonded together with an adhesive. The bond lines, especially at the trailing edge is the most common location for this fault. Due to stress concentration, the adhesive from the two shells peels away at the bond lines. The initiating cause from the manufacturing stage include dry spots and voids and leads to systematic debonding. Esu, 2016 discussed that during operation, blade panel deformations are induced by edgewise gravity induced loads and this makes the panels breath. Westergaard, 2013 added that the panel breathing accelerates the crack propagation through peeling and requires regular inspections and preventative repairs. Other minor effects include hairline fractures, which can progress into ultimate crack due to shear stress or debonding/rift or split of the two shells.

Cracks in trailing edge: Until peeling occurs, the stresses will create surface tension right at the trailing edge bond line eventually developing into (hairline) cracks. Initial causes include debonding caused by dry spots or voids in laminates and improper fibre-to-resin ratio and improper curing, leading to bond deviations as explained by Westergaard, 2013. Faults may progress into severe cracks during operation due to unforeseen blade loading events (systematic failure) and random failure in harsh, high wind conditions or extreme weather events. Trailing edge bonds are designed for shear stress, which occurs from blade bending during wind loading.

Cracks in laminates: The presence of voids in the adhesive or waviness/ wrinkles of the fibre matrix lead to reduced joint strength with earlier crack initiation and is mentioned in studies Hua et al., 2013 and Cairns et al., 2011. Adding o this, Jüngert, 2008 stated that during operation, impacts on fibre reinforced plastics may lead to delamination between the fibre layers and the matrix material. The main feature of this defect is that there is more than two-fold increase in the magnitude of interlaminar stresses in the adhesive layer with one through-thickness imperfection.

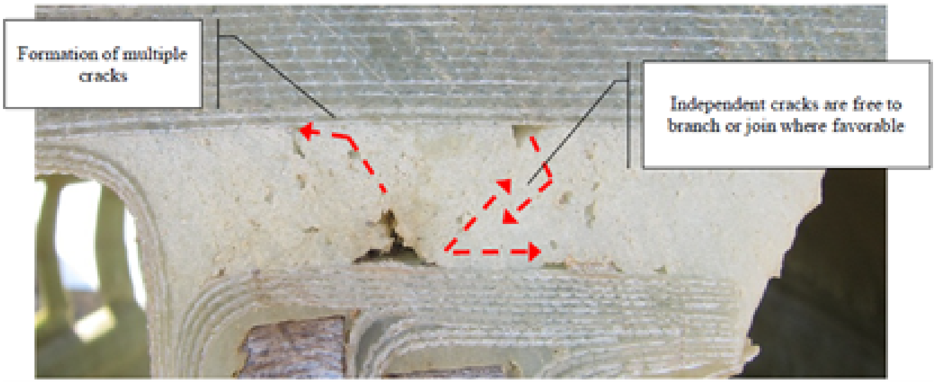

Figure. 2.12 Formation potential growth of cracks, sourced from Douglas Cairns, 2016

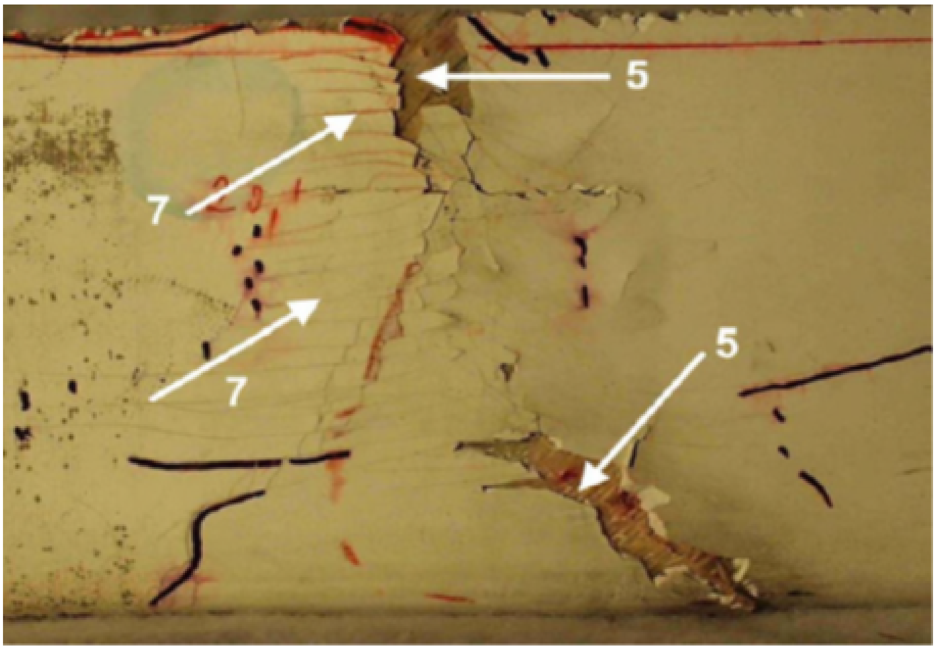

Figure. 2.13 Damage type 5 - laminate failure in compression and damage type 7 - gel coat cracking at the bottom of the leading edge, original from: Ciang et al., 2008

Brazier Effect: This is a non-linear geometric deformation 'ovalisation' caused by bending of a section of a wind turbine blade. When a wind turbine blade bends in the flap-wise (chord-wise) direction, the compressed panel produces a downward crushing load normal to the surfaces (for example, the upwind side) while the opposite occurs on the lower panel (for example, the downwind side). This flattening of the cross section is known as the Brazier effect and it mainly affects the shear web-spar cap region. Delamination, which occurs due to high out-of-plane loads where no fibres are present to resist the loading, is the major contributor to this structural failure. The lack of fibres in the transverse direction causes the cap to be relatively flexible in the lateral direction. According to Esu, 2016, the flattening effect is caused by transversal internal forces which are caused by inter-laminar shear force, which is the stress component in parallel with the cross-section of the main spar cap. The inter-laminar shear failure develops by crushing pressure causing biaxial stress distributions, inter-laminar and peeling stresses due to the curved structure being flattened out. This may ultimately lead to web failure which, in turn, results in catastrophic blade failure.

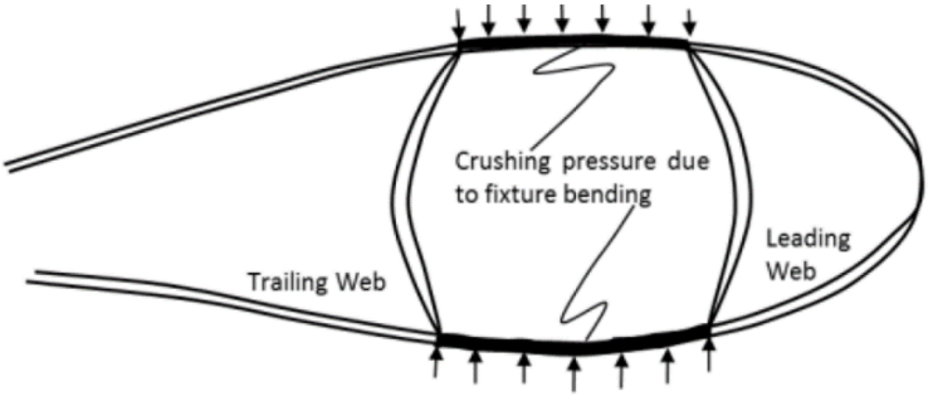

Figure. 2.14 Crushing pressure on a wind turbine blade section, from Esu, 2016

Delamination: Although this is a common defect identified under the manufacturing process, delamination, if neglected can progress into severe damage during turbine operation. Continuous condition monitoring techniques can easily pick up delamination at its prevalent locations such as shear web, spar cap, skin and even blade root.

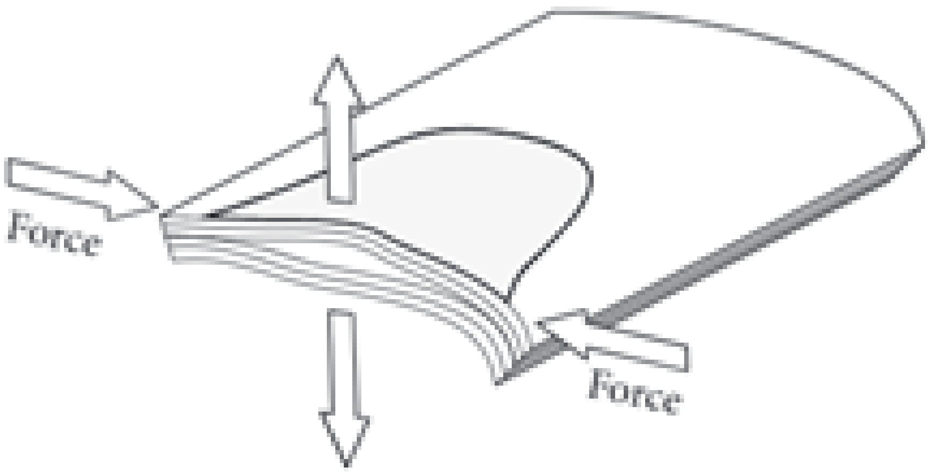

Figure. 2.15 A scheme of delamination initiation, as depicted by Doliński et al., 2018

Any sandwich panel area such as spar cap/ shear web or even skin on either side of the load carrying flange are under high stress and strain levels under loaded conditions. Therefore, delamination can easily occur or propagate into other damage inducing components under fatigue. Delamination at the blade root is mainly caused by debonding of the outer skin under the initial failure mechanism, followed by delamination buckling which leads to the blade's collapse. Jensen et al. and Lee, Kang, et al., 2015 believed the main root cause was the Brazier effect of the shell structure due to bending .

Defects which are not considered for this literature review chapter:

- Operational defects: dust, ice accumulation, insect contamination, blade over speed failure and damage due to bird and lightning strikes.
- Defects which may occur during transport and installation.

2.2 Non-Destructive Testing, Condition Monitoring & Sensors for Wind Turbine Blades

2.2.1 Introduction

There is a growing need for inspection techniques that can provide quantitative/qualitative information for assessing the structural health of the wind turbine blades. Güemes et al., 2018 states that damage is merely localised alteration in a material's properties or the structural boundaries, such as the formation of a crack, which acts as a new boundary. These changes reduce the structural efficiency and can adversely affect overall performance. In recent years, different Non-Destructive Techniques (NDT) capable of accurately delivering surface and sub-surface data have been developed. NDT systems should be able to quickly and efficiently scan large areas, to be economically beneficial to the wind turbine manufacturing industry. Martin et al., 2018 discussed that condition monitoring (CM) goes hand in hand with NDT for damage detection since it is another mechanism commonly employed for the early detection of faults and or continuous monitoring of critical parameters to minimise downtime and maximize productivity . This section provides a review of the state-of-the-art NDT/CM of wind turbine blades, describing the different techniques and methods, highlighting their capabilities.
The studies conducted by Martin et al., 2018, Cazzulani et al., 2018, Yang et al., 2016 group the techniques by categories based on their working principle or technology and they are:

- Oil analysis
- Vibration analysis
- Motor circuit analysis
- Thermography

- Radiography
- Ultrasonic/ Acoustic analysis
- Electromagnetic/ PZT/ MFC measurements
- Observation and surveillance (visual inspection)
- Fibre Optic Sensor

For SHM of wind turbine blades, oil analysis and motor circuit analysis become less significant compared to the rest of the types pointed out above.

With the emergence of a broad range of non-destructive testing, condition monitoring techniques and algorithms for damage data analysis, the various methods can be classified based on the level of identification as mentioned in Güemes et al., 2018 and Esu, 2016.

- Level 1: Identification of damage occurrence
- Level 2: Localisation
- Level 3: Identification of damage type
- Level 4: Quantification of damage
- Level 5: Prediction of residual strength

Together, these make up the integral elements of SHM of wind turbine blades. Here in this section, a brief summary of different NDT/CM techniques, followed by the suitability of those techniques for identifying different defects and processing techniques are reviewed. A short summary of the ancillary functions and a conclusion is also provided at the end of this section. Extensive evaluation of fibre optic sensors has been discussed considering the present (proposed) strategy of achieving condition and performance monitoring damage detection of rotor blades. Under section 2.4, in Table 2.4 to Table 2.11, the techniques have also been compared with each other for their capability of identifying different types of defects and faults. Relevant figures illustrating each technique have been provided for enhanced understanding.

2.2.2 Oil and Motor Circuit Analysis

Oil and motor circuit analysis play a crucial role in the condition monitoring of wind turbine drive train systems, ensuring optimal performance and preventing failures. Research has demonstrated the integration of non-destructive testing (NDT) methods and sensors for real-time monitoring of turbine oil systems and motor circuits. For example, a study by Gu et al., 2021 reviewed various techniques for detecting faults in wind turbine gearboxes, highlighting the importance of oil analysis and condition monitoring for diagnosing potential failures. Additionally, Salameh et al., 2018 explored how motor circuit analysis combined with advanced sensor technology can monitor the operational health of wind turbine motors, contributing to early detection of faults. Oil degradation, temperature fluctuations, and particle contamination are often monitored using sensors in oil-filled wind turbine gearboxes, as seen in studies like that of Dupuis, 2010, which evaluated the impact of oil analysis on detecting mechanical wear in wind turbines. These technologies enable predictive maintenance and timely intervention, reducing downtime and extending the service life of turbines.

While oil and motor circuit analysis are primarily used for drive train monitoring, they are often included in broader NDT and condition monitoring strategies for wind turbine blades because drive train failures can induce secondary effects on the blades. Imbalances, excessive vibrations, and sudden load variations due to gearbox or generator faults can contribute to structural fatigue and damage in blades over time. Thus, integrating oil and motor circuit analysis within the overall SHM framework helps provide a comprehensive assessment of wind turbine reliability and performance.

2.2.3 Observation and Surveillance

Observation and surveillance methods, more commonly known as visual inspection, is the most basic, commonly used technique for NDT/CM of wind turbine blades which categorically belongs to observation surveillance type of NDT. However, visual surveillance is only useful if the inspection results can be measured or critiqued against a documented set of guidelines as mentioned in the study conducted by Yang et al., 2016. Typically, visual inspection can be conducted with or without optical aids.

General optical aids include low-power magnifiers, microscopes, telescopes and specialised devices such as Borescopes, endoscopes etc. High-speed visual inspection with automated output is also possible and used for the inspection of the surface of sheet material and television techniques may be used for enhanced image and pattern recognition. Currently, a popular method of visual inspection utilises drones and naturally, they are mainly used for on-site analysis and assessment regarding the condition of the rotor blades. The principal benefit of using drones or other unmanned aerial vehicles (UAV) is the dramatic reduction of risk exposure of technicians working at height and at sea. UAV platforms provide access to areas that are too difficult to access. The drone system enables a more economic and efficient inspection than a traditional telephotography or other manual inspection methods. Damages such as surface erosion, delamination and cracks on the blade surface can be identified easily however, inspections can go beyond the visible spectrum in order to identify sub-surface defects as well.

2.2.4 Ultrasonic Testing and Acoustic Methods

Ultrasonic Testing and Acoustic Methods are widely recognised for their effectiveness in the non-destructive evaluation (NDE) of materials, especially for detecting internal flaws or structural damage in wind turbine blades. These methods use sound waves to penetrate the material, with any inconsistencies or defects in the structure causing alterations in the wave propagation, thus providing valuable insights into the health of the blade.
Acoustic Emission (AE): This monitoring method utilises surface mounted piezoelectric sensors to detect the elastic stress waves within the structure. Rumsey et al., 2008 states that the propagation of these waves is often changed by structural damage (that is, fibre breakage, delamination, debonding) occurring in the blade. The system is very sensitive and can detect much weaker signals than normally audible. Detection of an acoustic emission is known as an event; events trigger electrical signals from the sensors. If the signal exceeds the user's predetermined threshold then the event is logged. A logged AE event is known as an 'AE hit'. Schubel, Crossley, et al., 2013 states that these hits are characterised by amplitude, energy, counts, duration, rise time, counts to peak and average signal level. This testing method is generally used to detect defects in the following cases,

- Trailing edge
  - Peeling stress
  - Defects due to buckling
  - Tensile crack in bond line
  - Crack propagation into laminates/panel/shell on bond line interface (detectable depending on the layup)

- Blade Shell
  - Matrix cracking
  - Cracks caused by porosity
- Adhesive Defects
  - During manufacture
  - Tensile crack initiation and propagation

Based on the summarised experimental results mentioned in Krause et al., 2015, the acoustic emission method can be employed as an NDT technique to identify defects at manufacturing levels where defects typically initiate but can also be used to monitor the propagation of those defects. Appropriate signal processing can be used to extract important information such as stress and strain on the blade and further analysis of the signal amplitude, time duration, signal power and the signal to noise ratio (SNR) can help in detecting and localising the defect in real-time. Localisation may require multiple sensor nodes and also requires time of flight information. However, damage identification (type size), prediction and structural integrity assessment needs to be done by further analysis of results and cannot be directly extrapolated by AE signals, since AE has complex sound propagation in composites and requires significant calibration of the sensors. Utilising AE method for dynamic testing is yet to be perfected since this NDT method is susceptible to loud environment/ noise during turbine operation; which makes extracting a useful signal difficult. Versatility of the AE method includes its possibility of using it in both static and fatigue tests. However, based on studies carried out in Schubel, Crossley, et al., 2013, the load conditions below the threshold of damage propagation remain unrecorded as AE emission monitoring registers only progressive defects (Figure 2.16). Therefore, its use in active control and continuous load monitoring is limited.

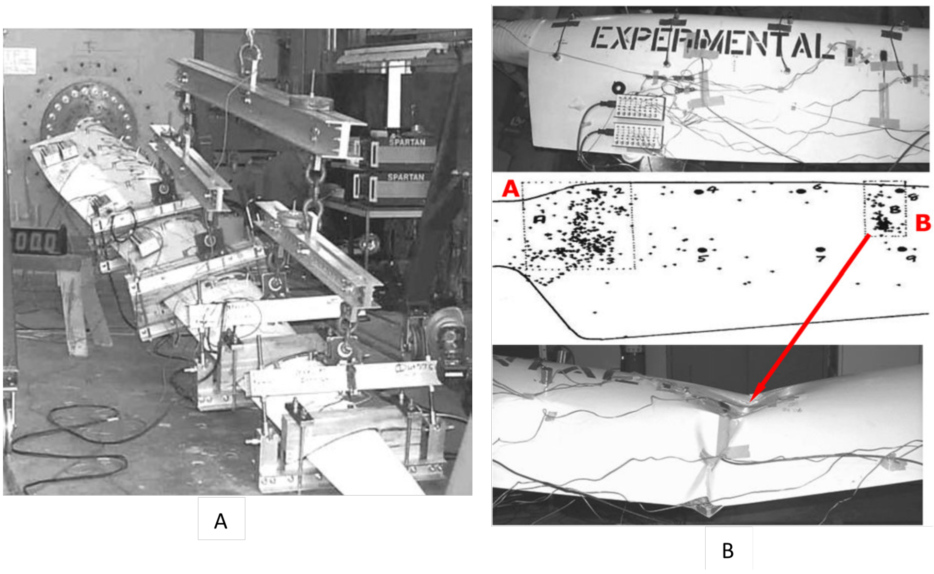

Figure. 2.16 (A) AE monitoring of a wind turbine blade during static testing, origin: Schubel, Crossley, et al., 2013 (B) The failure site registered by AE monitoring B with possible secondary failure site A identified

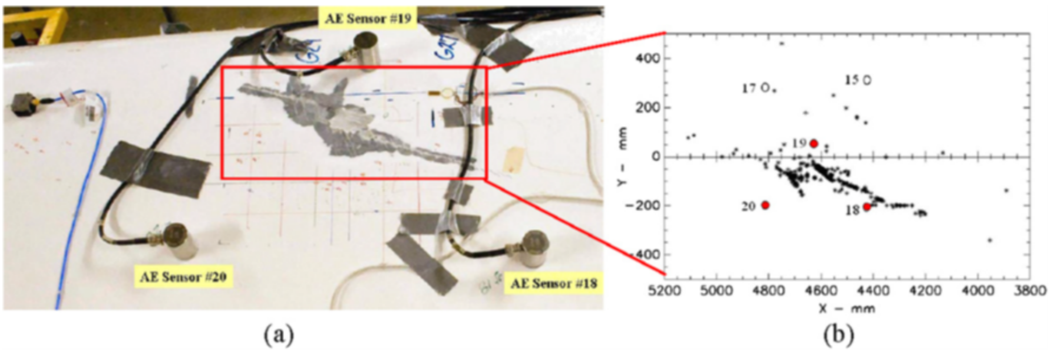

Figure. 2.17 Application of AE sensor on full scale blade test (a) Photo of AE sensors surrounding a damaged area; (b) characterization and localization of damage using AE sensor data sourced from Rumsey, 2011

Ultrasonic Testing: The basic principle of this testing technique is that an ultrasonic wave is passed through the material and is then reflected and/or mode converted by change in ultrasound properties at material interfaces and some defects. A transmitter transfers ultrasound waves into the material and the signal from this is picked up by a receiver once it has passed through the material. In the simplest arrangement, the transmitter and receiver are placed on opposite surfaces of the material and usually either water or oil is used as the coupling liquid between the surface of the sample and the transducers. Ultrasonic testing can detect surface and subsurface defects (internal flaws) or can characterize materials, measure thickness or monitor corrosion. Ultrasonic C-scan imaging has been used for area mapping of the composite delamination or interface debonding due to fatigue in normal field operation conditions of the turbine blade in the study conducted by Jasiūnienė et al., 2008. Furthermore, ultrasonic testing can also provide in-depth inspection of adhesively bonded multi-layered structures, laminated composite components, and inter-laminar weakness.

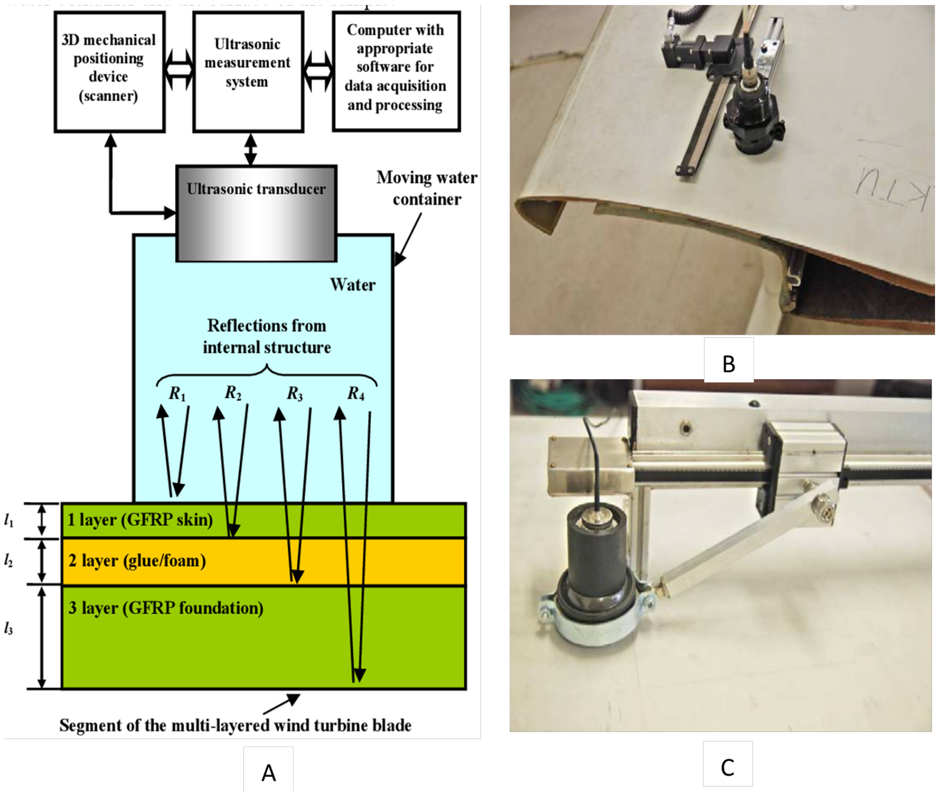

Figure. 2.18 A – The schematic diagram of the pulse echo immersion testing of the wind turbine blade, B - The experimental set-up for testing of the blade using 2.2 MHz focused transducer, C - The experimental set-up for testing of the blade using planar 400 kHz transducer, from Jasiūnienė et al., 2008

The technique may also be applied with a single transmitter/receiver transducer in a pulse-echo mode or with separate transmitter and receiver transducers placed on the same side of the material. It is also suitable for detecting cracks in adhesive that are oriented at right angles to an ultrasonic wave propagation, impact damage, voids and porosity. The experiment conducted in Jasiūnienė et al., 2008, uses two different transducers: focused 2.2 MHz and planar 400 kHz, to investigate artificial internal defects of the wind turbine blade (Figure 2.18) The performed measurements show that the contact pulse-echo immersion testing using the moving water container can help to identify the shape and the size of the internal defects better. The higher frequency focused transducer should be used in order to detect delamination type defects near the outer surface of the wind turbine blade. The low frequency planar transducer allows detecting delamination and thickness variations in deeper layers.

Since the ultrasonic wavefield imaging technology provides a scanned movie or snapshots, it can provide easy explanations on the wave propagation mechanism and the interaction of the wavefield with structural damage as stated in Ciang et al., 2008. Adding to this, Márquez et al., 2012 explored that signal-processing algorithms including time-frequency techniques and wavelet transforms can be used to extract more information.

In addition to C-scan imaging, ultrasonic testing employs A-scan and B-scan techniques for defect detection in wind turbine blades. A-scan provides a one-dimensional representation of the reflected ultrasonic signal, displaying amplitude versus time, which is useful for identifying the presence and location of defects such as delaminations or voids. B-scan offers a two-dimensional cross-sectional view, allowing for visualisation of defect depth and orientation within the blade structure. For instance, in a study by Raišutis et al., 2008, B-scan imaging was utilised to detect artificial defects in wind turbine blade samples, demonstrating its effectiveness in identifying internal flaws.

C-scan imaging, in contrast, provides a two-dimensional (2D) planar view of defects across the scanned area, similar to a top-down map of the internal structure. Unlike A-scan and B-scan, which focus on depth or cross-sections, C-scan represents variations in signal amplitude or time-of-flight over a defined scanning region, producing a detailed image of internal defects. This makes it particularly useful for area-based defect detection, enabling visualisation of delaminations, debonding, or impact damage across the blade surface.
These techniques complement each other by providing detailed information on defect characteristics, thereby enhancing the overall assessment of blade integrity.

Laser ultrasonic imaging: Another form of non-contact NDT monitoring method that has recently gained attention for applications in wind turbine blades is laser ultrasonic imaging and damage detection. Laser ultrasonics have been researched in the previous several decades for SHM like in Li, Ho, et al., 2015. In laser ultra-sonics, a high-powered pulse laser such as Nd:YAG (Neodymium-doped Yttrium Aluminium Garnet; $Nd : Y_3Al_5O_12$ is a crystal that is used as a lasing medium for solid-state lasers) or CO2 lasers are used to locally heat the surface of the monitored structure. The laser pulses cause thermoelastic expansion induced waves in the material at ultrasonic frequencies. These waves can be measured by other sensors such as PZTs and AE sensors, or by laser interferometry. Through an improved beam collimation (i.e. reducing the amount of beam dispersion per distance travelled) technique, the laser can be used for longer distances while maintaining enough focused power for generating ultrasonic waves. The waves generated by the laser are measured by an AE sensor and the data is processed through several wave subtraction algorithms to recreate an image of the plate surface in an effort to detect and localise damage.

2.2.5 Thermographic Methods

Thermographic Methods involve the use of infrared cameras to detect temperature variations across the surface of wind turbine blades. These temperature differences can indicate underlying issues such as cracks, delamination, or other structural defects, providing an effective means for non-destructive testing and condition monitoring of the blades.

Infrared Thermography Sanati et al., 2018 defines IRT as a non-contact, long distance NDT technique that can inspect extensive areas quickly by capturing thermal images of the object, i.e. the blade's surface. This technique relies on the thermal energy emitted by a body, which is a function of its external temperature and emissivity (i.e., its effectiveness in emitting power as thermal radiation). It allows plotting a thermal map of the object being tested based on the temperature measured by the camera's sensing elements associated with each pixel. In general, defective areas alter the temperature distributions on the surface that are measured by IR cameras. According to Sanati et al., 2018 Active and passive infrared thermography of various forms has been used to image, detect, and evaluate multiple fibreglass composite materials.

Similar methods have also been used to observe the time evolution of fatigue related defects as well as to inspect rotor blades with laboratory and field test evaluation. If employed during fatigue testing, IRT can detect defects in root and sub-surfaces such as inclusion of foreign matter air pockets. This can be done at various depths of the blade. Although the specific benefits of thermography vary by technique, IRT, in general, brings several advantages including higher inspection speed, higher resolution and sensitivity, improved detection of subsurface defects, and the methods, in general, do not require a couplant Sanati et al., 2018 and Martin et al., 2018 discussed in their studies. Thermographic inspection is typically divided into two categories: active and passive.

Active Thermography

The active approach uses an external stimulus source such as optical flash lamps, heat lamps, hot or cold air guns to induce relevant thermal contrasts on the test subject, i.e. the blade. Active thermography can be further divided into four groups based on the excitation techniques as follows,

1. **Pulsed (transient) thermography:** Pulsed thermography involves briefly heating the specimen and then recording its temperature decay curve. Because of its characteristics in highlighting differences in the material thermal properties, Martin et al., 2018 explained that this technique has been used for detecting adhesive defects of glass fibre-reinforced plastic (GFRP) composite plates .

2. **Lock-In (period heating) thermography (LT):** This is based on the application of a periodic thermal energy input to the surface of an object. When the resulting heat wave encounters a defect, some of it is reflected, causing a phase shift with respect to the input heatwave. The depth range for defect detection depends on the thermal diffusion length. The strength of LT is that the phase angle has the advantage of being less sensitive to local variations of illumination and/or of surface emissivity. However, because of its mono- frequency excitation, the depth resolution of a test is fixed by fixed thermal diffusion length. To detect defects located at various depths in the test sample, repetition of the test at various frequencies becomes a time-consuming process as mentioned in Yang et al., 2016.

3. **Long-Pulse (Step Heating) thermography:** In step heating thermography, a thermal pulse is applied to the material to be inspected. During the application of this thermal pulse, a measurement of the temporal evolution of the specimen surface temperature is made with an infrared camera allowing subsurface defects to be revealed. The temperature of the material changes rapidly after the initial thermal perturbation because the thermal front propagates by diffusion under the surface. The presence of a defect typically reduces the diffusion rate. The studies on this by Yang et al., 2016 discussed that when observing the surface temperature, defects appear as areas of different temperatures with respect to surrounding sound areas once the thermal front has reached them. Consequently, deeper defects will be observed later and with a reduced contrast.

4. **Vibro-thermography (mechanical vibration):** This type of thermographic inspection is based on the thermoelastic effect, which is the temperature change of elastic solid due to the change of stress. Based on this, higher stress concentration and different heat conduction near the defective region are expected, and hence the defective region will have a higher temperature. For this method, typically the blade is vibrated with a mechanical shaker to locate and evaluate the size of cracks and impact damage. This approach can also be used to evaluate voids and bonding quality during the manufacturing of composite materials. Two studies conducted by Hahn et al., 2002 and Dutton, 2004 as mentioned in Ciang et al., 2008 prove that this thermoelastic stress analysis is useful during fatigue test of the blade. The method allows the measurement of the surface stress distribution on a blade during cyclic loading and indicates stress concentrations and developing sub-surface damage long before any visible surface indications develop. This procedure not only identified the cracked areas in the foam filled sandwich area, but also successfully identified the root delamination and trailing-edge crack, and at the same time removed most of the signal noise. This technique can be applied to detect cracks in various types of materials, even on complex shaped components such as turbine blades.

Passive Thermography

This technique is used to investigate materials that are at a different temperature than the ambient (often higher). It often uses solar radiation as the heating source (heating at sunrise and cooling at sunset) for heating/cooling the blade. Passive thermography can be used for different materials (metals/ composites/ concrete) but requires detailed image processing (increases the quality of thermal images and visibility of internal defects) to analyse the thermal data as mentioned in Sanati et al., 2018. In-situ passive thermography is unsuitable if the blades are subjected to surface contamination due to dust accumulation etc. Hence, the passive approach is not common in wind turbine SHM and more modifications are required before it becomes a promising method according to Ciang et al., 2008.

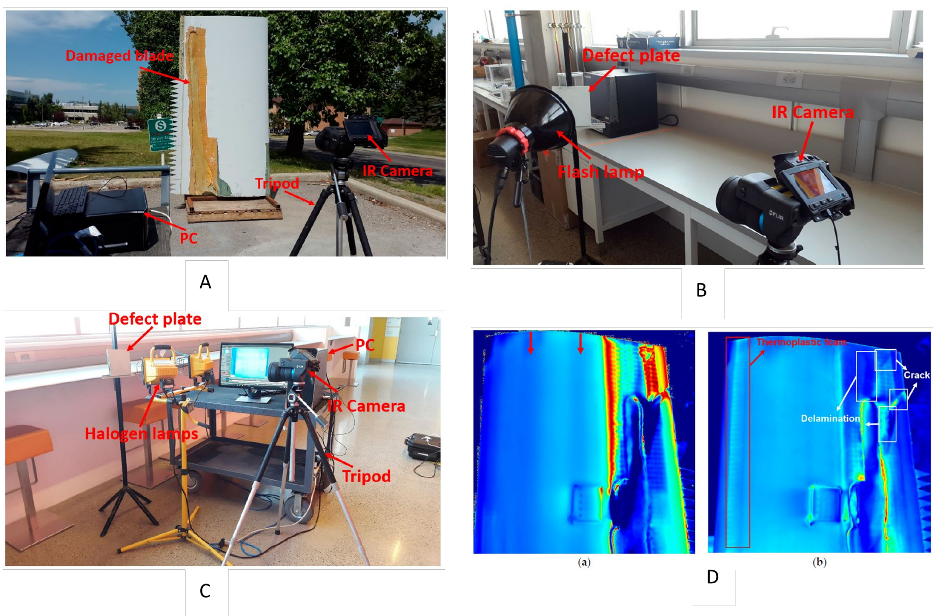

Figure. 2.19 A – set up of a passive-thermography experiment, B – set up of a pulsed-thermography experiment, C – Set up of a step-heating thermography experiment, D - Phase images of the passive thermograms captured during the morning at (a) 0.00184Hz and (b) at 0.0165Hz showing defects such as delamination crack, courced from Sanati et al., 2018

Different image processing methods are applied to the raw thermal images from IRT to improve the quality and contrast associated with internal defects. Algorithms developed specially for processing IRT images (for example, Thermographic Signal Reconstruction) and common transform-based algorithm such as Fast Fourier Transform (FFT) can convert the time domain data to frequency. This can help in better qualitative and quantitative evaluation of the subsurface defects in different materials as explained by Sanati et al., 2018.

2.2.6 Radiographic Inspection

Radiographic Inspection is a non-destructive testing technique that uses X-rays or gamma rays to examine the internal structure of wind turbine blades. By capturing images of the internal components, this method can reveal hidden defects such as voids, cracks, or other structural anomalies that could compromise the blade's integrity and performance.

X-ray Imaging (Radiographic Inspection): Márquez et al., 2012 stated that imaging and inspection of critical structural turbine components using X-rays is only rarely used although it does provide useful information regarding the structural condition of the component being inspected. X-rays can penetrate a large number of materials including composites. Hence, Ciang et al., 2008 indicated it is used for scanning the subsurface of composite material panels, in particular in detecting defects using X-ray scans on GFRP components. X-ray imaging relies on the different levels of absorption of X-ray photons as they pass through the material for impressing onto a photosensitive panel. In Martin et al., 2018, for a wind blade sample of dimension 1005 x 870 mm made of composite GFRP material, this technique has been proven to be capable of detecting damages having a diameter as small as 19 × 10-3 m on the main spar, 15 x 10^{-3}m on the trailing edge, and structural defects such as a lack of adhesive and internal irregularities. Some microfocus sources enable detection of defects less than 15 x 10^{-3}m. Furthermore, according to Ciang et al., 2008 and Martin et al., 2018, the X-ray measurement allows for obtaining quantitative information about variations in density in the targeted object, which can indicate changes in material properties or internal delamination or voids, cracks in the laminates and also non-intended orientation of fibres or kink band. Moreover, experiments carried out by Martin et al., 2018 in their study indicate that X-ray imaging is highly sensitive to thickness changes and wave/laminar defects.

X ray imaging can be used for real-time X-ray inspection for quality control during or shortly after wind turbine blade production. Main advantages of the X-ray inspection are the accuracy of the technique and utilisation for performing a large-scale investigation (utility scale size blades) of manufacturing defects as mentioned in Ciang et al., 2008 and Martin et al., 2018. Nevertheless, X-ray imaging is expensive and very compact detectors and small X-ray sources must become possible for it to be used in-service for non-rotating SHM for the wind turbine.

Terahertz inverse synthetic aperture radar (ISAR): This is another noncontact/ imaging, full-field measurement technique that can be used for assessing the condition of WT blades and highlight the presence of defects in the manufacturing process. Unlike the synthetic aperture radar which uses the movement of the radar antenna over the target area to simulate the effect of a much larger array of antennas; (this is what is meant by the term “synthetic” aperture and this technology can create highly detailed two-dimensional and three-dimensional images of landscapes) inverse synthetic aperture radar uses the movement of the target itself to generate its reading, rather than the movement of the radar emitter. ISAR is mainly used in military applications for identifying and targeting objects by their movement but can also be used for wind turbine blade structural imaging defect visualization. Detailed tests conducted via Terahertz ISAR and comparison between this methods vs X-ray and IRT are given in Martin et al., 2018.

2.2.7 Electromagnetic Measurements

Electromagnetic measurements are widely used in non-destructive testing (NDT) and condition monitoring of wind turbine blades due to their ability to detect internal flaws such as cracks, corrosion, and delamination. For example, microwave and radar-based methods utilise electromagnetic fields to identify anomalies within the blade structure. For instance, microwave testing can detect internal flaws like delamination and voids by analysing variations in the dielectric properties of the composite materials used in the blades as stated by Wang et al., 2023. Similarly, radar-based SHM employs radar systems to assess the integrity of wind turbine blades, identifying defects by detecting changes in the reflected signals caused by structural anomalies as studied by Moll et al., 2018. These electromagnetic techniques offer non-contact inspection capabilities, making them suitable for monitoring the condition of wind turbine blades. According to Cheng, 2013, electromagnetic methods provide real-time monitoring capabilities and are particularly useful for detecting early signs of wear and tear in turbine blades, enabling timely maintenance and avoiding catastrophic failures. Furthermore, as electromagnetic sensors are sensitive to material properties, their integration into wind turbine blade monitoring systems allows for continuous, remote assessment of blade integrity, enhancing the overall safety and reliability of wind turbines.

2.2.8 Other Damage Detecting Mechanisms

While a range of advanced damage detection techniques have been discussed, additional methods play a crucial role in identifying and localising damage in wind turbine blades. These alternative techniques, such as accelerometers, PZT sensors, and extensometers, offer unique advantages in terms of sensitivity, versatility, and integration with other SHM systems. The following sections delve into these methods, exploring their capabilities, applications, and limitations in more detail.

Accelerometers and PZT sensors (Lead Zirconate Titanate - PZT): Accelerometers are conventional sensors commonly used for vibrational analysis, modal analysis, or to measure structural responses in dynamic testing of wind turbine blades and components. These sensors are typically highly sensitive, tri-axial accelerometers, which may incorporate piezoceramic materials for accurate acceleration measurements. Piezoelectric, piezoresistive, and capacitive components in commercial accelerometers convert mechanical acceleration into electrical signals, enabling precise monitoring of dynamic behaviour. Additionally, PZT sensors can function as both sensors (when subject to strain or stress) and actuators (when subjected to an electric voltage). Studies, such as Li, Ho, et al., 2015, show that PZT sensors can be integrated into a Structural Neural System (SNS), which enables intelligent damage localization, providing real-time feedback for early detection of structural issues. However, challenges with accelerometers include sensitivity to external vibrations and mounting difficulties in highly dynamic environments like wind turbine blades.

Macro-fibre composite (MFC) sensors actuators: Macro-fibre composite (MFC) sensors and actuators, like PZT sensors, can both sense and act as actuators. MFCs consist of piezoelectric fibres embedded in an epoxy matrix and interfaced with polyimide electrodes, offering enhanced flexibility compared to traditional PZT sensors. MFC sensors have been successfully installed on wind turbine blades, particularly on the low-pressure side, where they function to monitor damage through impedance-based analysis. This technique involves analysing changes in impedance from both the actuators and sensors, which helps in damage diagnosis as discussed by Li, Ho, et al., 2015 at the Sandia National Laboratories. The advantage of MFCs lies in their lightweight nature and ability to conform to complex geometries, making them ideal for SHM in wind turbine blades. However, their performance may be affected by the blade's operational conditions, such as temperature fluctuations and mechanical wear.

Electrical Extensometer: Electrical extensometers are conventional devices used to measure changes in length (i.e., strain) of materials, often employed in static measurements during tensile tests. These extensometers are typically bonded to the surface of wind turbine blades to measure elongation and contraction due to strain, making them useful for detecting surface defects such as cracks or delaminations. According to Sierra-Pérez et al., 2016, the extensometer's sensitivity to surface deformations makes it a valuable tool in identifying localised damage, especially in the early stages of crack formation. Despite their utility, electrical extensometers may face challenges with attachment and environmental stability, especially on large and dynamically loaded structures like wind turbine blades.

2.2.9 Vibration Analysis

Márquez et al., 2012 observed that vibration analysis and vibration-based approaches continue to be the most popular technology in condition monitoring employed in wind turbines, especially for rotating equipment. Vibration affects the performance and strength of the wind turbine components, for example, rotor blades, gearbox and bearings etc. Typical sensors for vibration analysis may vary depending on the required frequency of the measurement. For the low-frequency range, position transducers are used, in the middle frequency range velocity sensors are used; other sensors include accelerometers in the high frequency range and spectral emitted energy sensors for very high frequencies. There are several approaches to identify, locate and quantify damage in vibration-based condition monitoring as explored by Esu, 2016. Some of these approaches are,

1. Natural Frequency Based Methods
2. Mode shape Based Methods
3. Mode Shape Curvature/Strain Mode Shape
4. Dynamically Measured Flexibility Matrix Based Methods
5. Matrix Update Based Methods
6. Non-linear Methods
7. Neural Network Based Methods

Detailed explanation of each of the above method is given in Doebling et al., 1996 and not discussed here. An overview of modal based approach is given below in this literature review to cover the subjects of modal shape/ frequency and curvature for damage detection (or bending) of wind turbine blades.

Modal-based Approach: Modal based methods are among the earliest and most common damage detection methods used, principally because they are simple to implement on any size structure. Structures can be excited by ambient energy, an external shaker or embedded actuators, and embedded strain gauges, piezoceramics or accelerometers can be used to monitor the structural dynamic responses. The basic idea behind this technology is that modal parameters, notably frequencies, mode shapes and modal damping, are functions of the physical properties of the structure (mass, damping and stiffness). Therefore, changes in the physical properties, such as reductions in stiffness resulting from the onset of cracks or loosening of a connection, will cause detectable changes in the modal properties.

Structural damage detection is based on a comparison between the response from a "pre-damage" state and that from a "post-damage" state. Since changes in modal properties, or properties derived from these quantities, are being used as indicators of damage, the process of modal-based damage detection eventually reduces to some form of pattern recognition problem (Ciang et al., 2008). The use of mode shapes to study the dynamic behaviour of structures requires a number of accelerometers be installed on the structure. Another variation is to study the curvature mode shapes and wavelet maps. The residual of a mode shape is the difference between the damaged and undamaged mode shapes. The curvature of the residual of a mode shape is the second derivative of the residual of this mode shape. This is referred to as the curvature mode shape. Next, a wavelet map is constructed for each curvature mode shape. This method can accurately predict the location of the damage. Since the wavelet number indicates the location of damage, the accuracy of this method depends on the number of wavelet coefficients contained in the signal. Similar approaches using PZT sensors and actuators are given in Ciang et al., 2008 and Li, Ho, et al., 2015 which also integrates wireless sensor networking for SHMs.

Laser Doppler Vibrometer (LDV) method: In the LDV method/ scanning LDV (SLDV) sensors can measure the vibration of many points over a wide frequency range quickly without contacting the blade. A laser beam from the SLDV is directed at the surface of a blade to allow non contact measurements of vibrations through the Doppler effect. The Doppler effect refers to the relative frequency change between the source laser and reflected laser due to movements of the blade surface with respect to the laser source. An internal laser interferometer measures the frequency change by interfering the reflected laser and a reference laser. The resulting interference is observed by a photo detector in terms of variations in light intensity, with the frequency of variation correlated with the frequency of the Doppler shift. Ciang et al., 2008 denoted that by analysing the photo detector measurements, the vibration amplitude and frequency of the blade motion can be determined.
Experiments illustrated in Li, Ho, et al., 2015, shows that operational deflection shapes and transmittance functions for damage detection were computed from velocities obtained from 114 points of an 8 feet long blade. However, to improve the reflected laser signal intensity, the research team performing the experiments had to paint a coating of retro-reflective material on to the bare fibreglass blade.

Li, Ho, et al., 2015 also added that one significant advantage of SLDV is its non-intrusive nature without mass-loading effects and can obtain operational deflection shapes or mode shapes of a turbine blade more accurately compared to conventional accelerometers.

2.2.10 Strain Measurements

Strain measurements play a crucial role in assessing the structural health and performance of wind turbine blades, as they provide real-time data on deformation. By monitoring strain, it becomes possible to detect potential damage, fatigue, or failures in critical components, ensuring timely maintenance and improving the safety and efficiency of wind turbines.
Strain Monitoring by conventional strain gauges (metal-foil): This technique is widely used in strain measurement and recognised especially in strain monitoring for the certification process of wind turbine blades. The standard procedure is to monitor the blade with strain gauges during static tests under extreme loads and subsequently during an accelerated fatigue test (Commission I E 1999). These tests are designed to ensure that all parts of the blade can withstand extreme load cases as defined in the wind turbine design and testing standards as mentioned in Li, Ho, et al., 2015. Typically, strain gauges consist of a metal foil pattern bonded onto a flexible nonconductive support. The support carrying the metal foil is then bonded to the monitored structure, usually through cyanoacrylate. Strains in the structure is transferred to the metal foil and causes a change in electrical resistivity of the metal foil. The change in resistivity is measured by a locally connected data acquisition system, commonly through the use of a Wheatstone bridge. For blades, depending on the location where the sensors are used, strain gauges can measure bending moment, shear strain and torque under high loads. This has been demonstrated in the case of an aircraft for the evaluation wing load calibration and sensing in Miller et al., 2019.

Li, Ho, et al., 2015 further stated that the disadvantages of conventional strain gauges are that they are prone to failures in the long term, even when installed in the root of the blade. The copper wiring also makes them sensitive to severe electrical disturbances, such as lightning strikes. Furthermore, conventional strain gauges suffer heavily from ambient noise disturbances and are not sensitive enough to indicate certain types of blade damage.

2.2.11 Fibre Optic Sensing Techniques

Contrary to conventional strain gauges, optical fibre sensors are not sensitive to electrical and magnetic interference and are intrinsically immune to the effects of lightning strikes, which occur quite frequently to turbine blades according to Glavind et al., 2013 and Li, Ho, et al., 2015. They are also considered to be accurate, reliable and stable in addition to their multiplexing ability and ease of embedding into structures. Geometric (size and shape) and optical (refractive index and mode conversion) changes of optical fibres due to various environmental perturbations can be converted or encoded into corresponding changes in the optical properties of the transmitted/reflected light, such as amplitude (intensity), phase, frequency, wavelength and polarization. With the appropriate demodulation systems, the coded light signal can be employed to measure external environment parameters, such as strain, temperature, moisture, corrosion and acceleration along the fibre. Fibre optical sensors can be categorized into many types according to measured physical parameters and their operating principles. This will be explored in detail in the next section 2.3.

2.3 Application of Fibre Optic Sensors for Structural Health Monitoring

2.3.1 Introduction

The rapid development in technology and communication systems has enabled the use of optical fibres and laser systems for a variety of engineering applications. In the recent decades, the wind energy solutions and services have required and relied upon cross-and-multi disciplinary knowledge exchange in order to function optimally, efficiently and increasingly autonomously. Application of optical fibres and fibre optic sensors (FOS) have penetrated in all stages of wind turbine operation such as manufacturing, installing, constant monitoring operation and successful utilisation of power generated via these renewable sources. Continuous development of wind turbines has led to increasingly large and complex structural design of components These complex structures for example, blades, platforms and towers, are constantly subjected to change in the operating environment hence reached their highest capacity for operation frequently. For example, in an offshore environment, these turbine components are susceptible to damage and defective conditions due to higher wind speed at sea, turbulence, adverse wave states and extreme weather events. These often result in reduction in power production and even lead to complete loss of turbine operation or turbine parts. Therefore, constant monitoring to alleviate unfavourable operation is imperative.

The requirements to utilise such a monitoring system depends on many factors, i.e. expected range of operation of turbine components (usually obtained from simulations), site specific conditions, shortcomings in manufacturing process introducing internal/ structural flaws and more. Typically, such systems are called structural health monitoring (SHM) or condition monitoring (CM) systems. These SHM and CM systems can lead to an increase in the turbine's operating lifetime, increase in energy production and a decrease in turbine downtime. To describe a little bit more in detail, sensors and SHM systems based on optical fibres are widely used to monitor crucial parameters such as strain, temperature, acceleration/ or vibration etc and are advantageous due to their immunity to electromagnetic interference, small size weight, robustness, high sensitivity reliability and relatively cheaper cost (sensors only). FOS are easier to implement as a multiplexed or distributed system compared to their conventional sensor counterparts such as strain gauges, accelerometers or thermocouples.

FOS systems have many functional components, each providing a specific operation. A typical FOS based system consists of gratings which are the specially fabricated regions in the fibre which does the sensing, the interrogator unit, optical spectrum analyser (OSA) or spectrometer, fibre optic coupler, a broadband light source, function generator, photo-detectors, optical connectors, and etc.
This section specifically focuses on theoretical and working principles and the practical applications of fibre optic sensors for the SHM of wind turbine blades.

2.3.2 Fibre Optic Sensing Principles, configurations and Interrogation Techniques

This section discusses the theoretical part of the FOS which is the working principle and physics behind the sensors and the associated mathematical equations. Based on the spatial distribution of the measuring parameter, the fibre optic sensors can be classified into the following – refer to Figure 2.20 and Figure 2.21.

1. **Single point sensors or interferometric sensors:** Intrinsic or extrinsic measurements of a state of a variable take place at a single discrete point in an optical channel or fibre. For example, a single Bragg grating sensor in a fibre.

2. **Quasi distributed sensors or grating based sensors:** These measure the state of a variable at several discrete points along the same fibre, for example, several Bragg gratings along the fibre.

3. **Distributed sensors:** For applications which call for the need to determine state of a variable continuously as a function of its position along the fibre with a given spatial resolution and sensitivity, the distributed fibre optic sensors are popularly used.

López-Higuera et al., 2011 along with the above three categories, mentioned another type of fibre optic sensor. The 'integrated sensors' is where the measurement is obtained by integrating all the values of the objective variable contributing to one resultant value.

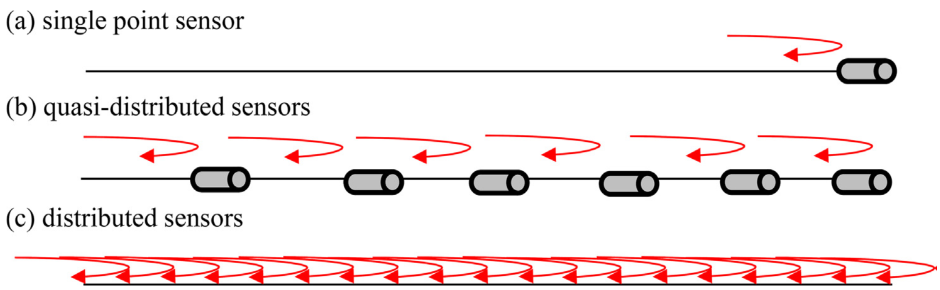

Figure. 2.20 Fibre optic sensing configurations: (a) Single point, (b) Quasi-distributed, and (c) Distributed sensors (red arrows present optical measurement signals), source: Amanzadeh et al., 2018

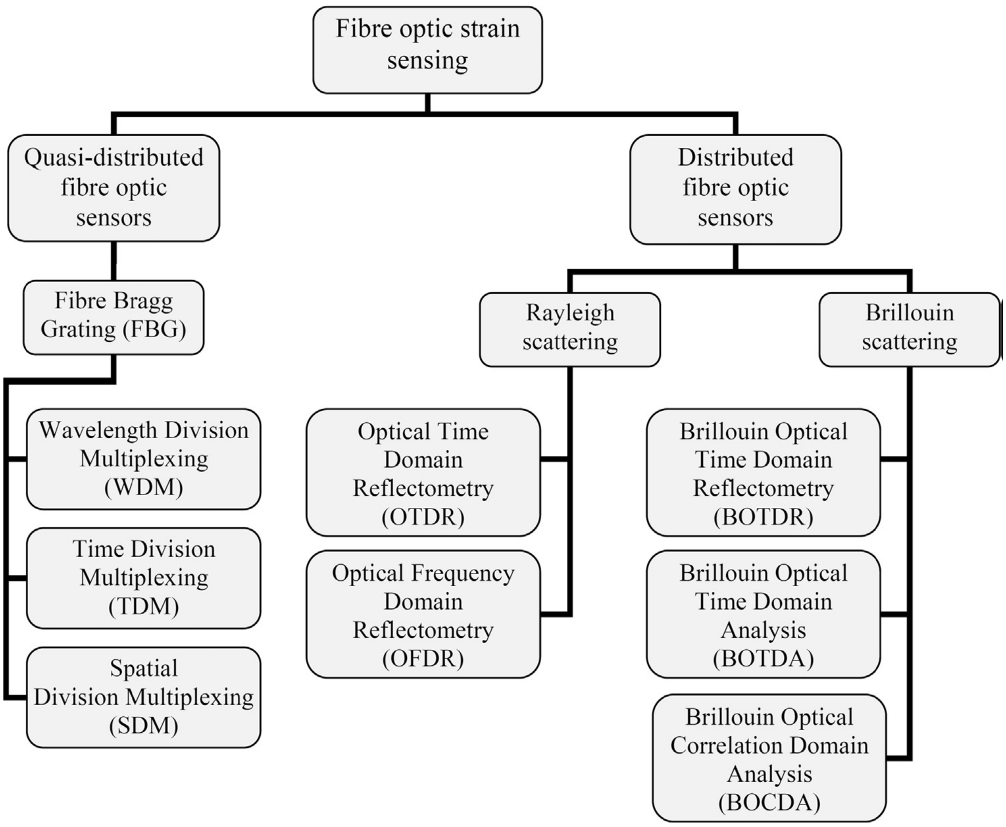

Figure. 2.21 Fibre optic strain sensing principles and techniques for fibre optic strain sensors, edited, original from Amanzadeh et al., 2018.

Quasi distributed sensors or grating based sensors: For the quasi-distributed fibre optic sensors which includes FBG, the common interrogation techniques are time division multiplexing, wavelength division multiplexing and spatial division multiplexing. Brief descriptions of each of these interrogation techniques are given below.

- Time division multiplexing (TDM)
- Wavelength division multiplexing (WDM)
- Spatial division multiplexing (SDM)

Time division multiplexing (TDM) : In a fibre optic sensing set up with TDM, a laser is used to launch light into the fibre and then the back-reflected light is collected. The signal is then resolved based on time of arrival (TOA) from each FBG in order to calculate the measured value at each singular point. The basic limitation of using TDM is that it requires the system to have the FBGs with the same Bragg wavelength and that they have a low reflectivity. But TDM allows measurements of parameters on a single fibre link with 100-1000s of FBGs of the same Bragg wavelength. Another limitation of FBG implemented via TDM is that the minimum distance between adjacent FBGs is restricted by the input light pulse length to around 200 cm.

Wavelength division multiplexing (WDM) : In a fibre optic sensing set up with WDM, the Bragg grating for example, reflects light only at a particular wavelength and transmits all other unaffected wavelengths. This allows multiple Bragg gratings to be inscribed and used in the same fibre with different designated wavelengths which can then be interrogated via different laser wavelengths. This is known as wavelength division multiplexing and is one of the simplest interrogation schemes for FBG. FBG-WDM based sensor system is widely used in both aerospace and wind turbine SHM applications.

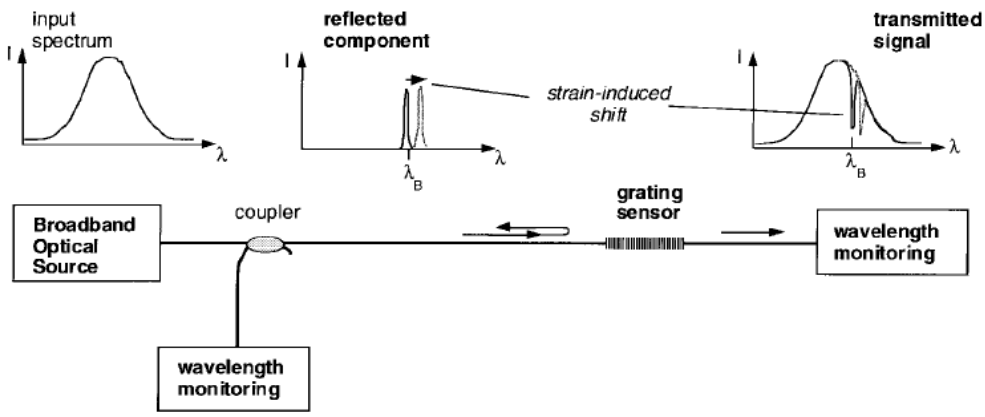

Figure. 2.22 Wavelength division multiplexing and monitoring system based on transmission/ reflection based FBG sensor system, from Kersey et al., 1997

Spatial division multiplexing (SDM): Implementing FBGs with SDM have been extensively studied in Li, He, et al., 2009 and Chen, Wang, et al., 2005. The principle of SDM allows FBGs to be utilised in parallel i.e., sensing in parallel spatial channels as illustrated in Figure 2.23 below. Application of SDM technology is not restricted to FBGs i.e. quasi distributed sensing, but often used in distributed sensing configurations as well.

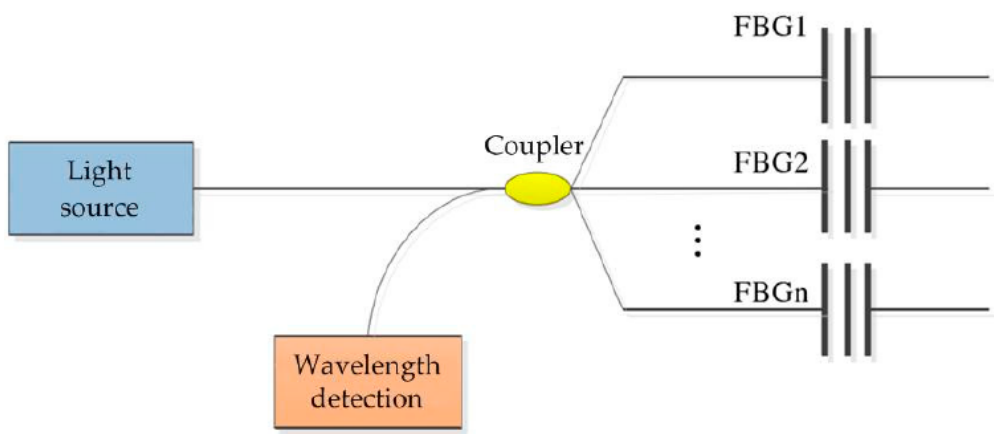

Figure. 2.23 Example of spatial division multiplexing as depicted by Di Sante, 2015

Distributed Optical Fibre Sensors (DOFS): For some sensing applications which require multi directional joints or measurements of continuous flexible structures, distributed fibre optic sensors can be utilised. These offer continuous measurement on the fibre link which are highly advantageous in a flexible mechanical structure like a wind turbine blade or tower. Based on the light scattering phenomenon, their process can be classified into three, i.e., Rayleigh, Brillouin and Raman scattering. In distributed fibre optic sensing, light scattering occurs naturally in the fibres due to the interaction of the scattering centres and the electromagnetic waves (EM). In distributed sensing scheme, the optical fibres are typically attached or embedded into the reinforcement or structure similar to a nervous system. DOFS can act simultaneously as the optical channel as well as the optical transducers. Due to these advantageous features, distributed sensing is recognised as the most promising and versatile fibre optic sensing scheme.

For the distributed fibre optic sensing configuration, the scattering of light can be measured along the fibre and there are two main categories of interrogation schemes. In an interrogation scheme based on Brillouin scattering, the shift in frequency and intensity can be used to measure the absolute strain and temperature. Interrogation scheme based on Rayleigh scattering can measure the relative change in strain and temperature. These two classifications of scattering based distributed sensing principles are explained further in detail below.

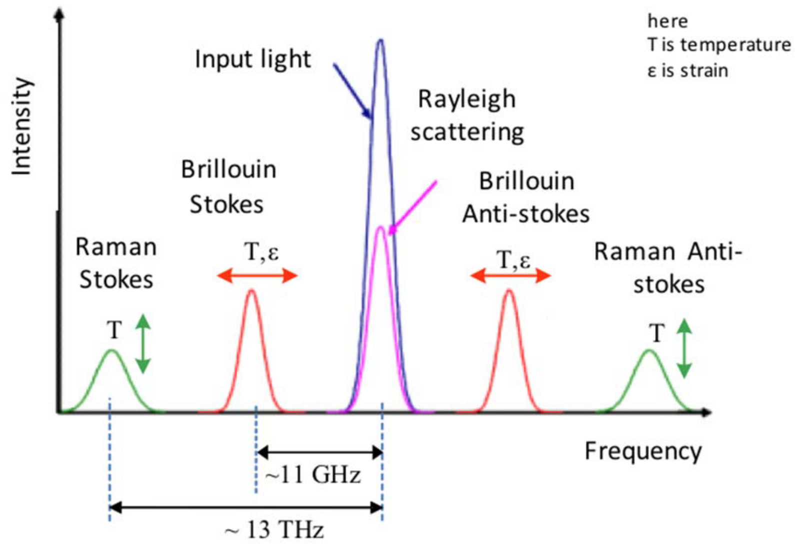

Figure. 2.24 Spontaneous backscattered light spectrum at 1550 nm as illustrated by Chen et al, 2018

Rayleigh Scattering: Distributed strain sensing based on Rayleigh scarring can be further classified into two interrogation techniques.

- Optical Time Domain Reflectometry (OTDR)
- Optical Frequency Domain Reflectometry (OFDR)

Optical Time Domain Reflectometry (OTDR) : The methodology of utilising an OTDR system is that a light pulse is launched into the fibre and the Rayleigh backscattered light from the same launching end is collected. The collected signal has a time domain (time dependent) trace and holds the information such as the round-trip time of the light pulse. This can be done for each point of the Rayleigh scattering which can represent the section of the fibre as a function of time. López-Higuera et al., 2011 stated that the Rayleigh scattered OTDR can be used to profile the fibres within structures to localise fibre breakage, connections and splices in a fibre link as well as its overall quality. Due to this capability, OTDR with both distributed sensors as well as quasi-distributed sensors can be used in SHM applications, especially in SHM systems for bend/ curvature sensing.

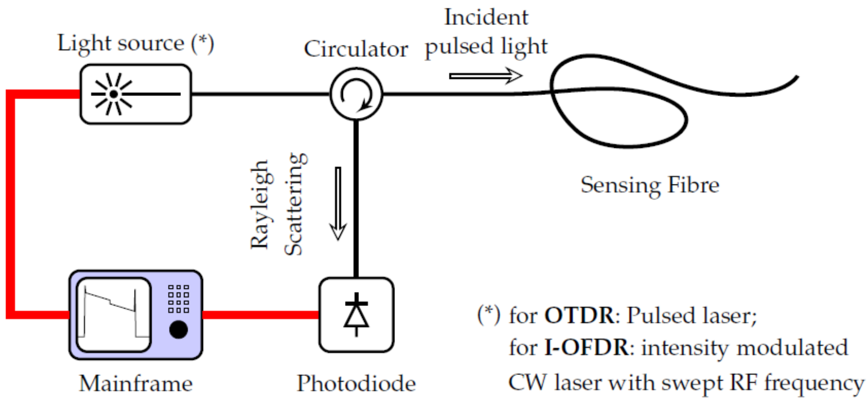

Figure. 2.25 Optical Time Domain Reflectometry operating principle, source: Schenato, 2017

Optical Frequency Domain Reflectometry (OFDR) : In the OFDR interrogation scheme, a continuous laser source is sent in frequency domain over a certain period of time. Using Fourier transform, the output data is obtained from the collected backscattered light. Similar to OTDR, the data shows the spectrum where the scattered light from each point is spatially represented by the amplitude and phase. Due to this, the OFDR system offers measurements with high spatial resolution.

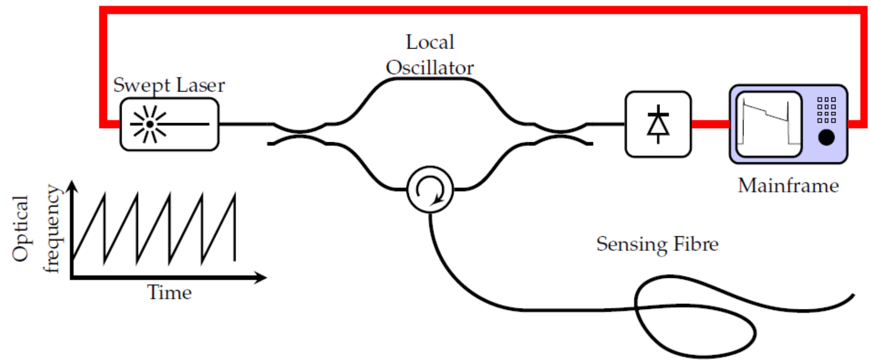

Figure. 2.26 Optical Frequency Domain Reflectometry operating principle, source: Schenato, 2017

Brillouin Scattering : Due to its beneficial features such as high sensing range, high spatial resolution, simultaneous measurement of strain and temperature, and larger order of magnitude in measurements compared to Raman scattering, Brillouin scattering based DOFS interrogation schemes are preferred and widely used technique for practical applications such as SHM. There are three major DOFS techniques based on Brillouin scattering and they are,

- Brillouin Optical Time Domain Analysis (BOTDA)
- Brillouin Optical Time Domain Reflectometry (BOTDR)
- Brillouin Optical Correlation Domain Analysis (BOCDA)

Brillouin Optical Time Domain Analysis (BOTDA) : BOTDA is commonly used for the simultaneous absolute measurement of strain and temperature. It is very similar to the OTDR technique, where the sensing principle in based on time domain interrogation of signals but depends on Brillouin backscattered light. The intensity of backscatter signal is substantially stronger in spontaneous Brillouin than Raman making the detection less-complicated, However, Schenato, 2017 stated that this interrogation technique is less sensitive to temperature as typical sensitivity coefficients of Brillouin frequency shift vs. strain and temperature in step index single-mode fibres are 0.046 MHz/$\mu\varepsilon$ and 1.07 MHz/°C, respectively. BOTDA relies on simulated Brillouin scattering (SBS) and it requires access to both ends of the fibre. The working principle of SBS is as follows; two counter propagating light pulses with different Brillouin frequencies are pumped into either ends of the sensing optical fibre. The two waves interact with each other and result in a simulation of the scattering. The propagating light with the lower frequency is amplified from the energy transfer (due to the light interaction) from the light with higher frequency. The gain from the two counter propagating waves' interaction and the time evolution (time series data) of this gain is the main parameter detected by BOTDA. The amplification of the light pulse detected at one of the ends of the sensing fibre depends on the strain and temperature applied. With appropriate application, BOTDA can be implemented over a distance of 100 km.

Brillouin Optical Time Domain Reflectometry (BOTDR): As mentioned under the section: 'Distributed sensors', the main parameters under consideration are spatial resolution, sensing range and accuracy of measurements. The Brilliouin Optical Time Domain Reflectometry (BOTDR) depends on spontaneous Brillouin Scattering (SpBS). In this optical interrogation method, the backscattered signals from the original light pulsed into the optical fibre gets measured at the same end of the optical fibre (See Figure 2.25). The main difference of BOTDA and BOTDR is the access to fibre ends, the BOTDA requires access to both ends of the sensing fibre whereas BOTDR requires only one end. Another difference is the propagating light type: BOTDA uses continuous wave in order to simulate the scattering whereas BOTDR uses light pulses. By increasing the optical power of the light pulse sent in and by improving the SNR, the accuracy in signal detection can be enhanced. Similar to BOTDA, with proper implementation, BOTDR technique can be utilised with high number of sensing points spanning over a distance of 100 km. It can be particularly useful in applications where only single-end access of sensing fibre is available, however according to Chen, Xu, et al., 2018, in applications where access to both ends of the fibre are available, BOTDA shows better performance. Over the years, several other interrogation or sensing techniques based on Brillouin scattering have been developed to increase the sensing points over the fibre. Some known examples of such techniques are Brilliouin Optical Correlation Domain Reflectometry and Brilliouin Optical Correlation Domain Analysis etc.

Brillouin Optical Correlation Domain Analysis (BOCDA): BOCDA enables measurements from millions of sensing points with resolution in the range of 1 cm and can span over 10 km. BOCDA is similar to BOTDA in the sense that it is based on SBS and uses two counter propagating continuous light waves on either ends of the sensing fibre.

2.3.3 Damage Detection System using Fibre Optic Sensors

Here in this section, a few SHM systems used for wind turbine blades which uses fibre optic sensing are discussed in detail.

Cazzulani et al., 2018 compared two surface mounted FOS systems on a scaled model of a blade with 1100 mm spanwise length and 3 mm thickness consisting of carbon fibre layers.

The first system i.e., system (A) has a total of custom etched 28 FBGs: 14 FBGs on either side of the blade surface (pressure suction side) equally spaced 62mm apart from each other on each side. This sensor configuration used a commercial DAQ and interrogator from MicronOptics. Together they have a sampling rate of 1000 Hz. The second system, i.e., system (B) is also commercially available. LUNA is a quasi-distributed/ continuous FOS comprising of 845 sensing points over a 2 m span and this fibre optic sensor is based on optical backscatter reflectometry (OBR) technique. With a sampling frequency of 250 Hz, this is classified as high-definition fibre optic sensors (HDFOS) and uses an ODiSI-B optical interrogator again from the company LUNA. Both systems measure strain and were mounted mainly to measure flap-wise vibrations/ loading under static mode and dynamic motion.

Bang et al., 2012 experimented with an arrayed sensor system comprising of FBGs on a 1.5MW wind turbine tower. To monitor the dynamic structural behaviour of the tower, 10 FBG sensors were arrayed and installed on the inner surface of the tower, which is facing the primary wind direction. The time series data for strain were collected and the bending deflection of the top of the tower were simultaneously transformed using the displacement-strain transformation (DST) matrix. The finite element model (FEM) of the wind turbine tower was created and the DST matrix based on modal approach was obtained. The authors developed a wavelength division multiplexing (WDM) interrogator with a spectrometer-type demodulator based on a linear photo detector for high-speed strain sensing. With these information, the full deflection shapes of the tower were estimated using the arrayed FBG sensors.

Lun et al., 2019 investigated an FBG sensor system embedded into a soft and flexible structure (elastomeric substrate) for the measurement of strain, bending, twisting, random deformation and deflection shape estimation. The FBG sensors on a single core fibre were embedded into a soft and flexible structure which could detect sparse local strains at high bandwidth using WDM. Machine learning modelling was then used to reconstruct its surface shape in real-time. Finite element analysis (FEA) was used to determine the design parameters and to validate the mapping of strain measurements to the continuum shape of the sensor/ reconstruct the structures surface morphology. the performance and evaluation of the FEA reconstructed displacement from the experiment and the output displacement from the trained artificial neural network is compared.

Ma and Chen, 2018 in their review paper mentioned an FBG based aircraft wing shape measurement system. The system consists of 778 densely distributed FBG sensors which are mounted on several locations of an aircraft including the aircraft wing shear web and spar cap to measure strain and then reconstruct the shape and deformation from the initial strain data. The FOS system utilises a Rayleigh scattering based OFDR interrogation technique for the FOSS function. The data acquisition (DAQ) is done via LABVIEW and deformation/ deflection reconstruction for the wing from strain is done by utilising and analysing inverse finite element method (iFEM).

Park et al., 2011 discussed the use of FBG-WDM based SHM in an operational 2-MW wind turbine blade. Four FBG sensors with different Bragg wavelengths were mounted inside the GRFP-based composite blade and parallel to the neutral axis using a unidirectional E-glass tape to laminate the acrylate-coated FBG sensors on to the surface. The sensor system measured strain at sampling rate of 100 Hz and was also used for modal analysis including flap-wise, edgewise, and torsional frequencies. Finite element and Fourier analysis were used to study the strain and mode shapes of the blade. Deviations from natural frequencies were analysed using Fast Fourier Transform (FFT) and were compared to the FEM results.

Similar to this, Schroeder et al., 2006 studied the use of surface mounted FBG-WDM system for a 53 m long blade of an operational E112 4.5 MW wind turbine. Six FBGs covering the leading and trailing edge of the blade were attached to sensor pads made from a GRFP substrate and then stuck to the blade surface using an adhesive. These sensors were used for spatially distributed load monitoring, strain measurements and flap-wise bending. The system utilises a compact polychromator based on a spectral read out principle which ensures the simultaneous processing of all sensor signals in the network and provides momentary states of vibrational strain modes.

2.3.4 Embedded vs Surface Mounted Fibre Optic Sensors

Extensive literature review of both embedded and surface mounted FOS systems are described in detail under section subsection 2.3.5. This section specifically focuses on common current practices in both systems, physical/ mechanical coupling of FOS within and on top of the composite materials and challenges in such procedures. There are several aspects that must be taken into consideration before and after embedding fibre optic sensors into composite materials or reinforcements. Measures, 1993 provided a detailed description on the criteria and selection of FOS based on the mechanical physical properties of both the FOS and the composite material possess. Some of these criteria are given below.

- **Influence of embedded FOS on the material properties:** For FOS to be utilised into an efficient embedded SHM system, they must not compromise the structural integrity, tensile/ compressive strength of the reinforcement, increase the susceptibility to damage/ degradability and decrease the fatigue life of the materials involved. However, in composite materials, the FOS embedding process itself give rise to micrographic imperfections such as resin cavities (voids dry spots), change in adjacent ply directions (misalignment) etc.

- **Sensor-host interface and performance life of the FOS system:** Due to the heterogenous nature of FOS and composite materials, careful consideration must be given to both components' combined performance lifetime. The main factor in sensor-host interface is the interfacial shear strength between the sensors and the host resin matrix. This determines the degree of adhesion between the two and in turn determines the reliability and the performance life of the embedded sensors. High stress concentration in and around the area where the FOS are embedded could give rise to debonding between the sensors and the host resin-matrix and eventually delamination between the plies of the composite structure. FOS properties such as the diameter of the embedding optical fibre, type, and possibility of coating of the embedding fibre, stiffness of the fibre and etc play a significant role in ensuring sensor performance, sensitivity, and proper function. The presence of coating for the optical fibres have a significant influence on the sensor – host interface and aids in its optimisation by reducing the high stress concentration in and around the embedded fibres' location.

- **FOS system architecture and multiplexing:** Any practical applications of FOS based SHM system for smart structures such as WTBs would require the sensors to be robust. Since FOS are amenable to networking, the robustness of such system is enabled by the sensor system architecture and multiplexing within the composite structure. The type of sensor and the requirement or type of measurement determines if the sensors should be localised and or distributed. The nature of the sensor architecture (localised or distributed) will then determine if the system is multi-layered or limited to a single-layered form in a specific location. Some of the physical considerations and constraints are the orientation and placement of the embedded fibres, spatial resolution, ease of fabrication, length, bend radius of the embedded fibres, supplementary physical components (for example, interrogator unit, light source, amplifiers, couplers) etc. Some of the considerations and constraints for multiplexing in terms of data transmission are the multiplexing type (wavelength, time, frequency, space, phase), channel capability (data rate resolution), interrogation techniques, fibre loss (connector, splice etc) among others.

- **Structural interconnection/ interface:** Generally, it is ideal if the FOS based embedded SHM interface has minimal structural perturbation and if the sensor system can be easily fabricated during the manufacture/ fabrication of the structure. Hence the structural interconnection/ interface largely depends on the nature of the input/output signals used by the FOS system. for an embedded FOS system, the signals can be either electrical or optical.

2.3.5 Applications of Embedded vs Surface Mounted Fibre Optic Sensors

Di Sante, 2015 discussed the prospects of embedded FBG based sensors with different interrogation techniques for SHM of composite structures used in aerospace industry. Like most FOS based SHM systems for aircraft components, they measure strain, and based on that data, the deflection/ deformation shape is reconstructed. Shape estimation is crucial for aircraft wing structures as the industry demands with the highest safety and reliability monitoring requirements. Additionally, the author explored the use of advanced image processing and pattern recognition techniques for impact-based damage assessment. Detailed description of typical issues present in sensor integration in composites were also explored. They include mechanical coupling, fibre protection at critical locations of the composites (ingress and egress) and spectral response of the FOS during the embedding process. Under mechanical coupling, the author compared the diameter of the embedded optical fibre (typically 125 μm for standard telecommunication fibres and 50 μm for fibres designed specifically for sensing in aerospace composites) with that of a unidirectional, a cross-ply and woven fabrics as the host materials. Demonstration showed that fibres with small diameter do not significantly change the mechanical properties of the host properties and that it has minimal intrusive behaviour when the fibres are embedded parallel to the reinforcing fibre mats.

Considering the physical movement of the substrate and critical location of the embedded fibres, i.e., the ingress and egress points of the fibre in the composite material, in a structure such as a WTB, the embedded fibres experience high stress concentration/ sharp pressure gradient leading to severe bending during the manufacturing process (and later during the operational phase with different wind loading conditions). To mitigate these, the author mentions a technique other the typical coating: i.e., the usage of small tubes made from either polytetrafluoroethylene (PTFE aka, Teflon) or polyvinylidene fluoride (PVDF) materials. The fibres, along with these tubes can be reinforced additionally with metal coils. Strain transfer between the substrate and the sensing fibre and protective reinforcement are the primary concerns when utilising this technique. Furthermore, the opening of the tubes must be sealed properly to avoid the resin seeping in. Typically, some WTB manufactures carry out surface polishing after manufacturing the composite structures therefore, the location of these fibres (inlet and outlet), if they are embedded closer to the surface, must be clearly marked to avoid loss of sensing fibre. Another important factor to consider according to Di Sante, 2015 is the resin escaping from substrate plies due to the presence or embedding of the FOS system.

The primary technique to check if the FOS are functioning properly is to check their pre-embedding and post-embedding or post-manufacture spectral response. Generally, the spectral sensitivity of an embedded FOS deviates from that of the FOS that is un-embedded. The WTB manufacturing process is exothermic in nature hence the sensing fibres undergo non-uniform and transverse stress variations at the bonding area between the fibre and the composite plies. The stress generated during the resin-infusion phase was released only partially during the composite cooling phase resulting in residual strain operating on the fibre and the substrate. These result in a modified or distorted spectral response of the embedded sensors. Di Sante, 2015 in his study mentioned that such distorted spectra result in inaccurate strain measurements and in some cases prevents longitudinal strain measurements. The coating of the fibre again plays a vital role in reducing these adverse effects of the residual strain. Several studies mentioned in Di Sante, 2015, for example: the work conducted by Di Sante et al., 2014 and Okabe et al., 2002 indicated that an acrylate or polyimide coating shows shifts in transmission/ reflection spectrum of the FOS due to longitudinal or transverse strain but does not distort the spectrum. For wind turbine blades, assuming ideal strain transfer between the blade's composite layups and the embedded FOS across the coating, accurate calibration of the embedded FOS after their fabrication and WTB manufacturing process and critical evaluation of the measured data in the operating wind conditions will ensure an effective and reliable SHM.

The distorted spectrum albeit being a result of imperfect embedding process, can be useful in damage detection mechanisms. The information from a bare embedded FOS can indicate possible cracks, delamination and debonding in different types of composite matrix. The distortion can be compared with the characteristics of a specific localised damage or defect or impact-based damage and this mechanism can be extended to embedded distributed sensing systems to cover a larger area of the blade. However, basic requirements such as proximity of the FOS to the defect location, utilisation of an FOS interrogator with full spectrum detecting capability, priori knowledge of the defect and its position need to be satisfied to ensure the distributed sensors contribute to an advanced WTB SHM.

In recent years, WTB manufacturers have turned to Vacuum assisted Resin Transfer Moulding (VaRTM) to fabricate composite WTB structures. The VaRTM process uses vacuum pressure to drive the resin and impregnate the preform. Access to one side of the mould (of the structure) is enough to employ VaRTM and the mould is closed off using a vacuum bag and sealant tape. Despite some advantages such as low cost for process and tools, high fibre volume content, fume free process, and low void occurrence, there are some considerable disadvantages in applying VARTM for wind turbine blades. Resin shrinkage, dry spots, non-uniform resin flow and hence unimpregnated parts uneven dimensional stability are some of the easily identifiable issues in VaRTM. Therefore, effective process (and or resin flow) monitoring of VaRTM and cure monitoring of the WTB manufacturing should be conducted. Eum et al, 2007 studies the means of process and health monitoring of a WTB by fabricating a highly strong and stiff WTB specimen using VaRTM. The SHM system has embedded long gauge FBG sensors based on OFDR. These long gauge FBG sensors are about 100 mm in length each (roughly 10 times longer than regular FBGs) and are utilised as distributed sensors inside the blade. The aim of their experiment was to monitor both the VaRTM/ resin flow and use the same embedded sensors post manufacturing for SHM purposes (mainly via a 3-point bending tests as shown in Eum et al, 2006. Depending on the embedded FBG location, for some sensors, acrylic plates were used to protect the FBGs from breaking under the vacuum pressure. Like the work conducted by Di Sante, 2015, the sensors were put into protective tubes installed through the acryl plates and then tube-ends were sealed off by a sealant tape to prevent air from leaking into the vacuum bag. Following the curing, the WTB specimen was subjected to several 3-point bending tests during which the top and bottom part of the FBGs embedded measured the compressive and tensile strain, respectively. The wavelength shift due to temperature and strain changes in the obtained spectra of the long-gauge FBGs were studied using Fourier Analysis.

Higgins and Meissner, 2010 and Sotoudeh et al., 2010conducted extensive research on FBG based interrogation schemes particularly for in-situ, real time defect detection for WTB as means for a non-destructive evaluation. Their focus is the detection localisation and quantification of damage with a 1.5 kHz sensor interrogator with embedded FBGs and associated instrumentation tested on small scale composite material coupons and on WTB. The FBG sensor interrogator module is composed of an optical interface port for connecting to the multiplexed FBG sensors, sensor-specific front-ends modifiers, a parallel-architecture Photonic Spectral Processor (PSP) engine with customised Array Waveguide Gratings (AWGs), micro controllers and wired or wireless network interfaces. The PSP interacts with a broadband light source that sends light to the FBG sensors. The sensors reflect light with varying wavelengths depending upon the measurands (strain, temperature, acceleration, etc). The PSP then processes the returned light that is then converted to electrical signals and then is processed by the electronics signal processing subsystem and finally interpreted by the algorithmic software subsystem.

2.4 Summary of SHM for Wind Turbine Blades

The previous sections have outlined various sensing schemes for wind turbine blades. These are summarised in the following two tables. The first table categorizes defects and damages in wind turbine structures and maps them to the detection techniques and methods capable of identifying them. Defects are classified into manufacturing defects and operation-induced damages, listed in the first row, while detection techniques are organized in the first column. Each technique is correlated with the defects it can detect, with an ‘x’ indicating a successful detection capability. This summary is supported by published literature referenced throughout this chapter.

Building on this analysis, a second comparison table focuses specifically on fibre optic sensors (FOS) and their role in SHM of wind turbine blades. This table compiles information from published studies and categorizes FOS types, their placement within the turbine structure, whether they are surface-mounted or embedded, the measurands they capture, the interrogation techniques employed, and the data analysis methods used. The final column provides references to the relevant studies. This structured overview highlights the application of FOS in SHM and their advantages in defect detection for wind turbine blades.

Table 2.3 Overview of NDT Monitoring for Wind Turbine Blades

Technique	Manufacturing Defects	Operation-induced Damages
Visual Inspection	Misalignment, Voids, Wrinkles	Cracks, Deformation, Panel Breathing and Peeling Stress
Acoustic Emission	Detects crack initiation, delamination, void formation, and debonding. Capable of identifying early-stage damage.	Monitors crack propagation, adhesive joint failure, and fatigue effects
Ultrasonic Testing	Ideal for detecting internal defects like voids, delamination, and debonding by measuring wave reflection.	Can identify cracks, fatigue damage, and adhesive joint failure due to stress.
Laser Ultrasonic Imaging	Detects internal voids, delamination, and debonding, often with high resolution and minimal impact on the material.	Helps identify cracks or deformations caused by external impacts and stress.
Infrared Thermography	Sensitive to surface temperature variations, useful for detecting misalignment, voids, or inclusions, especially near the surface.	Detects deformations, buckling, and internal stresses like cracks from thermal variations.
X-ray Imaging	Provides detailed internal inspection, detecting voids, inclusions, and delamination at a microstructural level.	Identifies cracks, especially those deep in the material, and failures in adhesive joints.
Terahertz ISAR	Capable of non-destructive inspection for voids, inclusions, and debonding at both the surface and subsurface level.	Used for detecting cracks, adhesive joint failures, and deeper damage during operation.

Technique	Manufacturing Defects	Operation-induced Damages
Laser Doppler Vibrometer Method	Monitors vibration patterns to detect misalignment, voids, and wrinkles through changes in vibration response.	Helps detect damage, fatigue, and cracks due to shifts in vibrational behavior during operation.
Strain Gauges	Can monitor local deformations caused by misalignment, voids, or wrinkles by measuring the strain response.	Monitors fatigue-related strain, deformation, and adhesive joint failure.
Vibrational Analysis	Identifies performance issues like misalignment, voids, or wrinkles through abnormal vibrational patterns.	Detects fatigue damage, cracks, and changes in structural stiffness over time.
Modal Analysis	Detects changes in modal frequencies and shapes, useful for identifying delamination, voids, and misalignments.	Can identify cracks, fatigue damage, and structural issues leading to deformation.
Accelerometers	Measures vibration and displacement, detecting misalignment, voids, and minor wrinkles.	Identifies deformation, fatigue, and crack progression in operation.
Electrical Extensometer	Detects elongation and contraction in areas with misalignment, voids, or wrinkles, especially under load.	Measures cracks, deformation, and localised damage during operational loading.
Fibre Optic Sensors	Provides real-time, continuous monitoring for manufacturing defects like misalignment, voids, and delamination through strain and temperature sensors.	Monitors cracks, fatigue, adhesive joint failure, and deformation with high accuracy over time.

Table 2.4 Overview of Structural Health Monitoring for Wind Turbine Blades - I

Damage Identification Techniques	**Manufacturing Defects**							
	Delamination	Improper Curing	Wrinkles	Dry Spots	Mislaignments	Debonding	Voids	Inclusions
Visual Inspection			x	x	x	×		
Acoustic Emission	×	×				x		
Ultrasound testing	×	×		×		×	×	
Laser Ultrasonic Imaging	×					×		
Infrared thermography	×					×	×	×
X-ray imaging			x	x			x	×
Terahertz ISAR	×		×	×				×
Accelerometers	x							
Electrical Extensometer			x		x			
Optical Sensors	x	x	x	x	x	x	x	

Table 2.5 Overview of Structural Health Monitoring for Wind Turbine Blades - II

Damage Identification Techniques	**Operational Defects**						
	Adhesive Joint Failure	Deformations	Panel Breathing & Peeling Stress	Buckling	Brazier Effect	Cracks	Fatigue
Visual Inspection	×	×				×	
Acoustic Emission	x			x		x	
Ultrasound testing	×					×	
Laser Ultrasonic Imaging	x					x	
Infrared thermography	×			x		×	
X-ray imaging		x	x		x	x	
Terahertz ISAR							

Table 2.6 Overview of Structural Health Monitoring for Wind Turbine Blades - II contd

Damage Identification Techniques	**Operational Defects**						
	Adhesive Joint Failure	Deformations	Panel Breathing & Peeling Stress	Buckling	Brazier Effect	Cracks	Fatigue
Laser Doppler vibrometer method							
Strain Gauges	x	x	x	x	x	x	x
Vibrational Analysis		x	x	x			
Modal Analysis		x	x	x	x		
Accelerometers		×	x		x	x	x
Electrical Extensometer							
Optical Sensors	x	x			x	x	x

Table 2.7 Fibre Optic Sensors based Structural Health Monitoring I

FOS Type	Location in Blade/ Turbine/ Structure	Surface Mounted/ Embedded	Measurand	Interrogation Techniques	Data Analysis Methods	References
FBG-arrayed sensor system	Tower of an 1.5MW wind turbine	Surface Mounted	Strain and bending deflection shape estimation	Developed a WDM interrogator with a spectrometer-type demodulator based on a linear photo detector for high speed strain sensing	FEM of the wind turbine tower was created and the displacement-strain transformation (DST) matrix on the basis of modal approach was obtained	(Bang et al., 2012)
FBG based sensor system	Soft Flexible Structure	Embedded in elastomer	Measurement of strain and bending/ twisting/ random deformation/ deflection shape estimation	Wavelength division multiplexing (WDM)	Using ANN (artificial neural network)- the performance and evaluation of the FEA simulated displacement in the experiment and the output displacement from the trained network were conducted	(Lun et al., 2019)

Table 2.8 Fibre Optic Sensors based Structural Health Monitoring II

FOS Type	Location in Blade/ Turbine/ Structure	Surface Mounted/ Embedded	Measurand	Interrogation Techniques	Data Analysis Methods	References
Densely distributed FBG strain sensors (778 FBGs)	Aircraft wing shear web, spar cap	Surface Mounted	shape sensing, strain measurements, reconstruct deformation from strain measurements	Optical Frequency Domain Reflectometry (OFDR) - Rayleigh Scattering for fibre optic strain system (FOSS)	LabVIEW, Inverse Finite Element Method (iFEM) analysis, modal analysis	(Ma and Chen, 2018)
FBG	Blade	Embedded	Strain	Principle Component Analysis (PCA)	Strain based deformation shape reconstruction	(Di Sante, 2015)
FBG	Blade	Embedded	Manufacturing defects: Curing, effect of vacuum pressure, resin or matrix shrinkage/ residual stress, resin flow edge, and strain change of laminates.	Optical Frequency Domain Reflectometry (OFDR)	The spectra of the long gauge FBGs were determined by Fourier analysis.	(Eum, Kageyama, Murayama, Ohsawa, et al., 2006)

Table 2.9 Fibre Optic Sensors based Structural Health Monitoring III

FOS Type	Location in Blade/ Turbine/ Structure	Surface Mounted/ Embedded	Measurand	Interrogation Techniques	Data Analysis Methods	References
FBGs (at 4 locations with 3 Bragg wavelengths)	Blades of a 2 MW wind turbine	Surface Mounted	Strain Measurements, Flap-wise/ Edgewise and Torsional frequencies	Wavelength division multiplexing (WDM)	FE modal analysis and FFT	(Park et al., 2011)
FBG	53 m Blade of a E-112 4.5 MW wind turbine	Surface-Mounted	spatially distributed load monitoring and strain measurements, flap-wise bending strain	wavelength division multiplexing (WDM)	Compact polychromator based spectral read out for simultaneous processing of all sensor signals and provides momentary states of vibrational strain modes.	(Schroeder et al., 2006)
FBG	Blades	both	cure monitoring and strain monitoring	wavelength division multiplexing (WDM) and Time Division Multiplexing (TDM)		(Schubel, Crossley, et al., 2013)

Table 2.10 Fibre Optic Sensors based Structural Health Monitoring IV

FOS Type	Location in Blade/ Turbine/ Structure	Surface Mounted/ Embedded	Measurand	Interrogation Techniques	References
FBG	Wind Turbine Blades	Embedded	matrix cracks/ delamination, strain in static, dynamic tests of wind turbine blades	The FBG interrogator module is composed of an optical interface port for connecting to the multiplexed FBGs, sensor-specific front-ends modifiers, a parallel-architecture Photonic Spectral Processor (PSP) engine with customized Array Waveguide Gratings, micro controllers and wired/wireless network interfaces.	(Sotoudeh et al., 2010)
Brillouin-Based FOS (SMF)	14 m composite Wind Turbine Blade configured as a cantilever beam	Surface-Mounted	Distributed strain and vibration measurements	Brillouin Optical Time-Domain Analysis (BOTDA)	(Coscetta et al., 2017)

Table 2.11 Fibre Optic Sensors based Structural Health Monitoring V

FOS Type	Location in Blade/ Turbine/ Structure	Surface Mounted/ Embedded	Measurand	Interrogation Techniques	References
Combination of FBGs	Scaled Model of a blade with 1100 mm span length and 3 mm thick carbon fibre layers.	Surface-Mounted	Flap-wise loading strain and vibrations (both static and dynamic tests)	Sensor configurations use commercial DAQ and interrogation systems. (a) uses an optical sensing interrogator from MicronOptics and (b) is a high definition fibre optic sensing (HDFOS) with a LUNA fibre and ODiSI-B optical interrogator again from LUNA.	(Cazzulani et al., 2018)
FBG	Flat beam	Embedded	Resin flow monitoring	Optical Frequency Domain Reflectometry (OFDR)	(Eum, Kageyama, Murayama, Uzawa, et al., 2007)
FBG and LPG	Blade	Embedded	FBGs: Strain and Load Sensing and LPGs: Strain and Directional Bend Sensing		(Glavind et al., 2013)

2.5 Conclusion

This literature review has highlighted the growing importance of SHM systems in ensuring the optimal performance and longevity of wind turbine blades. As wind turbines are integral to the generation of renewable energy, their reliable operation is paramount. The key focus of this review has been on various sensing methods, with a particular emphasis on fibre optic sensing, which has proven to be a powerful tool in monitoring the health of wind turbine blades.

Several conventional and modern Non-Destructive Testing (NDT) methods such as Acoustic Emission (AE), Ultrasonic Testing, Thermographic Methods, Radiographic Inspection, and Electromagnetic Measurements were discussed in relation to their role in wind turbine blade monitoring. These methods contribute significantly to detecting damage such as delamination, fatigue, cracks, and other structural failures that may compromise the integrity of turbine blades. Each of these techniques has its merits, but also limitations, especially concerning their application to large-scale, complex structures like wind turbine blades and in-field deployment.

Fibre optic sensing (FOS) was identified as a highly promising method for SHM in wind turbines, owing to its sensitivity, ability to provide real-time data, and capacity for integration into the composite materials used in blade construction. Key FOS systems, such as FBG and distributed fibre optic sensing, were presented as capable of measuring strain, temperature, vibration, and other parameters that are critical for monitoring the dynamic behaviour of the blades. These sensors offer several advantages over traditional methods, such as their ability to be embedded directly into the composite structure, providing continuous, high-resolution data over large areas of the blade surface. They can detect small changes that might otherwise go unnoticed, potentially preventing catastrophic failures.

Despite the advantages of fibre optic sensors, there remains a research gap in the integration of these systems into operational wind turbines. Several challenges persist in optimising sensor placement, durability, and the ability to monitor large turbine structures in real-time. Additionally, while fibre optic systems offer high sensitivity, the embedding process can introduce stress concentrations affecting structural integrity and resulting in potential measurement distortions, which could affect the reliability of the data. These challenges highlight the need for further research and development in the following areas:

Limited Experimental Validation in Defect Detection and Bridging the Gap Between Numerical/Analytical Modelling and Experimental Data: Existing research lacks systematic experimental studies focusing on laboratory-scale composite blades with defects that represent reduced stiffness and structural strength. Additionally, there is a gap in correlating numerical and analytical models with experimental data for defect detection. This research aims to address these gaps by investigating defect detection under low loads, specifically to monitor the minimum detectable change in strain due to the presence of defects. Fibre optic sensors, particularly FBGs, will be employed to assess their capability in detecting defects while numerical/analytical models will be used to validate and enhance experimental findings.

Multiplexing and Data Integration: This research focuses on wavelength division multiplexing (WDM) of FBG sensor arrays to maximize bandwidth utilisation and enable multi-point sensing, allowing for more sensing points within a single fibre. Additionally, advanced data collection and integration techniques will be explored to extract and interpret the maximum amount of information with high accuracy, particularly under low static loading conditions, where detecting subtle strain variations due to defects is critical. While this study focuses on laboratory-scale validation, the findings will contribute to future advancements in large-scale wind turbine monitoring, where efficient data handling and interpretation are essential for real-world applications.

Correlation Between Sensor Configuration and Detection Sensitivity: There is limited understanding of how the configuration and placement of FOS impact their accuracy and sensitivity in detecting defects. This gap will be bridged by exploring different sensor configurations, including sensor length and placement, and examining how they affect the detection of specific defects.

In conclusion, while fibre optic sensing has shown immense potential for SHM in wind turbine blades, there is still significant room for improvement. In the upcoming chapters, these gaps will be addressed through systematic experiments, numerical modelling, and the development of practical SHM frameworks for fibre optic sensing in wind turbine blades. By investigating these research questions, this work aims to advance the field of SHM and contribute to the development of more efficient, accurate, and cost-effective monitoring systems for the maintenance of wind turbine blades.

Chapter 3

Application of Fibre Optic Sensors: Characterisation and Calibration

3.1 Introduction

The previous chapter elaborates on the different types of fibre optic sensors used for wind turbine structural damage and defect detection. Out of them, the fibre Bragg gratings (FBG) are the simplest, most economical optical sensor option used for SHM systems and applications Wen et al., 2020 Schroeder et al., 2006. However, there are some challenges in sensing for defect detection, especially for geometrically large structures such as wind turbine blades. Typical challenges include sensitivity to small, localised variations in strain which can indicate defects at an early stage, high sensitivity strain measurements with appropriate positioning and suitable spatial resolution of sensors.

To investigate the required spatial resolution and sensitivity of these FBG, an experimental campaign was conducted in which the FBGs were first checked for their sensitivity on their own for strain as well as temperature, which is also known as characterisation. Building upon that, a series of further investigations using successive structures approaching that of a full scaled blade were done by surface mounting/ bonding these sensors on (a) Aluminium cantilever beam with and without known defect and (b) a composite cantilever beam with and without defect. These cantilevered beams were used in a static loading test setup to further investigate the potential of the FBGs for defect detection. In order to validate the experiment results, a series of finite element analysis (FEA) simulations were performed using ANSYS workbench software. The simulated strain results vs experimental strain obtained from the FBG sensors results were then compared. Following this, as described

in the next few Chapters (4-6), a scaled 1.8 m long defect-free healthy blade and a blade with a known defect present were tested under varying static loading conditions and different mounting orientations. Suitable preliminary sensitivity analyses and sensor characterisation were also performed. These are explained in detail in the upcoming sections.
In this Chapter, the type of optical sensor, suitable data interrogation technique and the design of data acquisition system which are part of a simple SHM system are explained. The preliminary sensitivity analysis, sensor characterisation and secondary characterisation based on numerical FEA simulations and experimental methods are also explored in further sections. The design and manufacturing of the scaled blade is explained in Chapter 4 - 5 and experiments, methodology and results of blade loadings tests are explored in Chapter 6-7.

3.2 Draw Tower Gratings - DTG

Draw Tower Gratings (DTG) are FBGs for which the manufacturing process of the optical fibre combines with the inscription of the gratings. The manufacturer of the DTG used in this thesis FBGS, 2022 elaborates the production of these type of DTG-FBG. This starts with step 1: heating the glass preform using an oven. The next step involves pulling the glass into optical fibre form, during which, the inscribing laser is positioned so that the optical axis of the laser and the interferometer crosses the fibre being pulled and the interferometer creates the periodic UV-light interference pattern which ultimately makes the Bragg grating. The third step involves coating the grating with the fibre via a coating reservoir and finally the coating allowed to cure. Figure 3.1 illustrates the manufacturing process of DTG. Key advantage of DTG is that it has higher strength compared to other FBG technologies such as FemtoSecond Grating (FSG) as stated by FBGS-Technologies, 2022. As these fibres are drawn, inscribed and coated within the same process rather than the conventional stripping, inscribing and re-coating fibres which result in poorer strength of the fibres, the tensile strength as well as the tensile breaking load of DTG fibres are very high (> 50 N corresponding to > 5% strain FBGS, 2022). Another benefit of this process is the feasibility of producing splice-less array of DTG sensors in a single fibre at relatively low cost. Figure 3.2 show the size and scale of the optical fibre and Figure 3.3 show the wavelength division multiplexed-FBG arrays purchased from FBGS International NV used for the sensor characterisation as well as the blade loading experiments. The design specification of these arrays are explained in detail under Chapter 6.

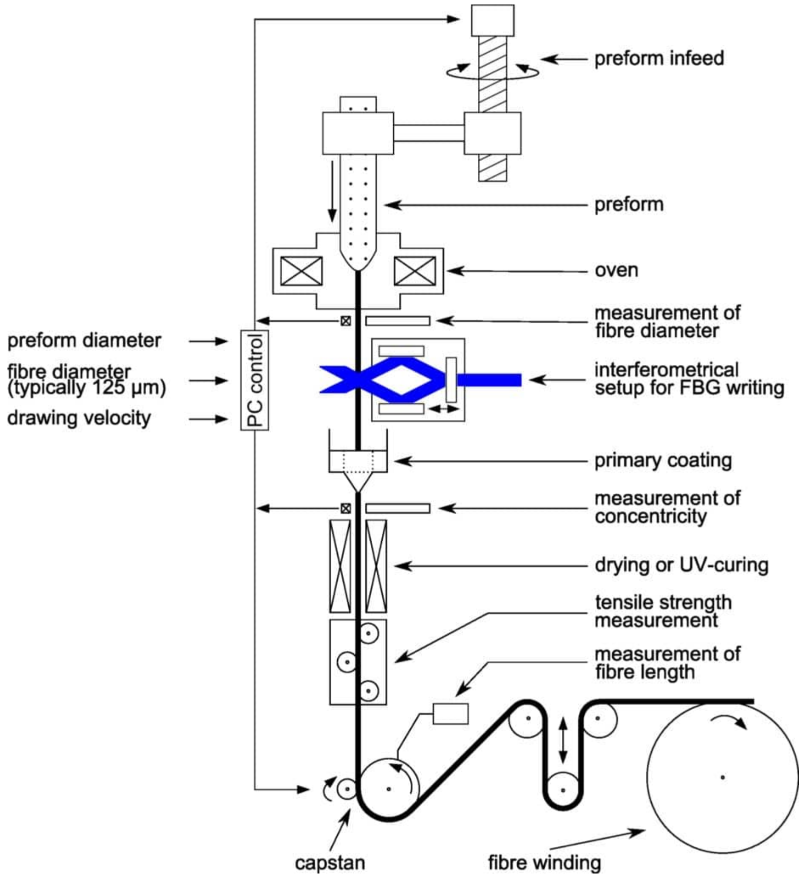

Figure. 3.1 Manufacturing Process of DTG-FBG illustrated by FBGS, 2022

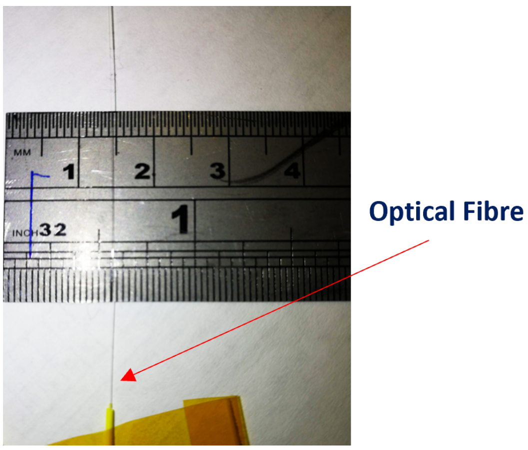

Figure. 3.2 size and scale of optical fibre

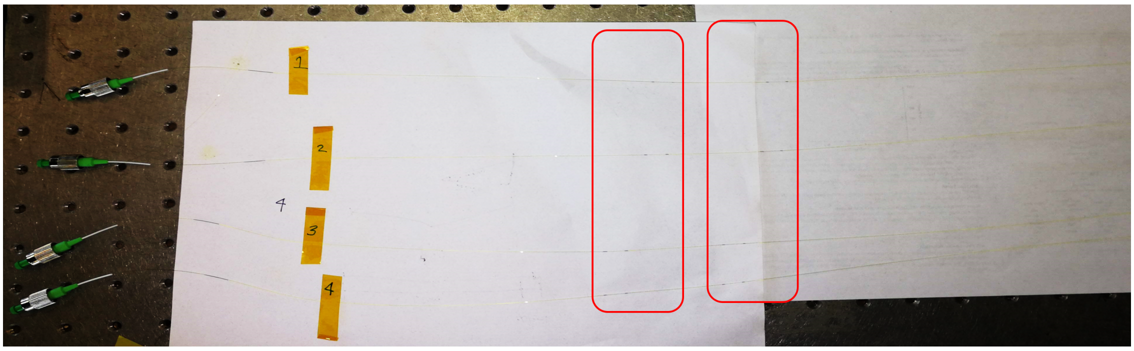

Figure. 3.3 Fibre Optic cable with FBG sensor Arrays

3.3 Development of the Data Acquisition System

Typically, most optical spectrum analysers (OSA), spectrometers or optical interrogators come with a manual device-user-interface where the bandwidth (starting and stopping wavelength and range), display frequency, number of sampling points, averaging and repeat scanning process can be defined on the front panel of the device. This limits the usage of the OSA for any amount of large repetitive or multiple scanning of the spectra or for dynamic measurements systems. When the application requires lots of sensors, consisting of multiple arrays and additional equipment such as an optical switch, the OSA could be integrated along with these devices into an efficient user interface. Hence, having external automated data acquisition system which can dynamically change the above settings while measurements are taken and saved within the scanning process while also incorporating multiple devices is beneficial. This increases the robustness of the overall sensor system.

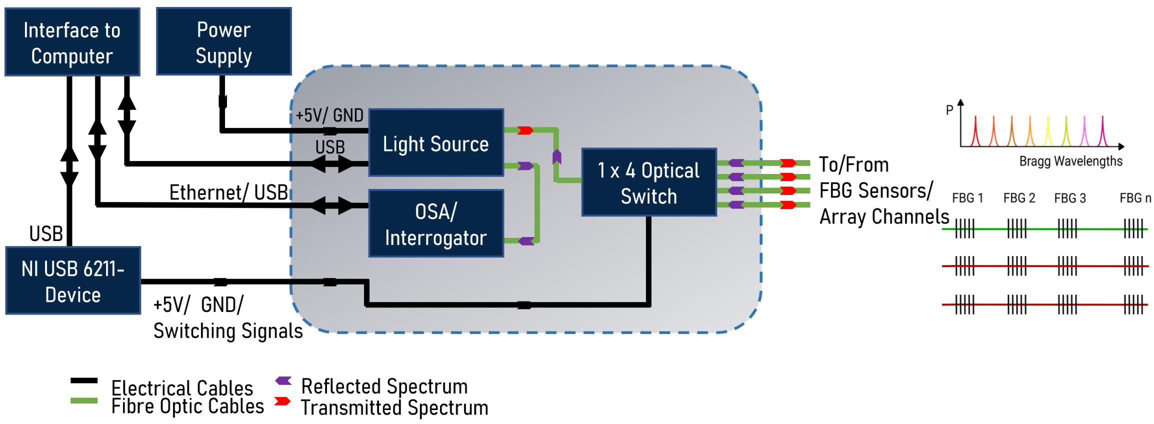

Figure. 3.4 Schematic Diagram of Data Acquisition System and Devices

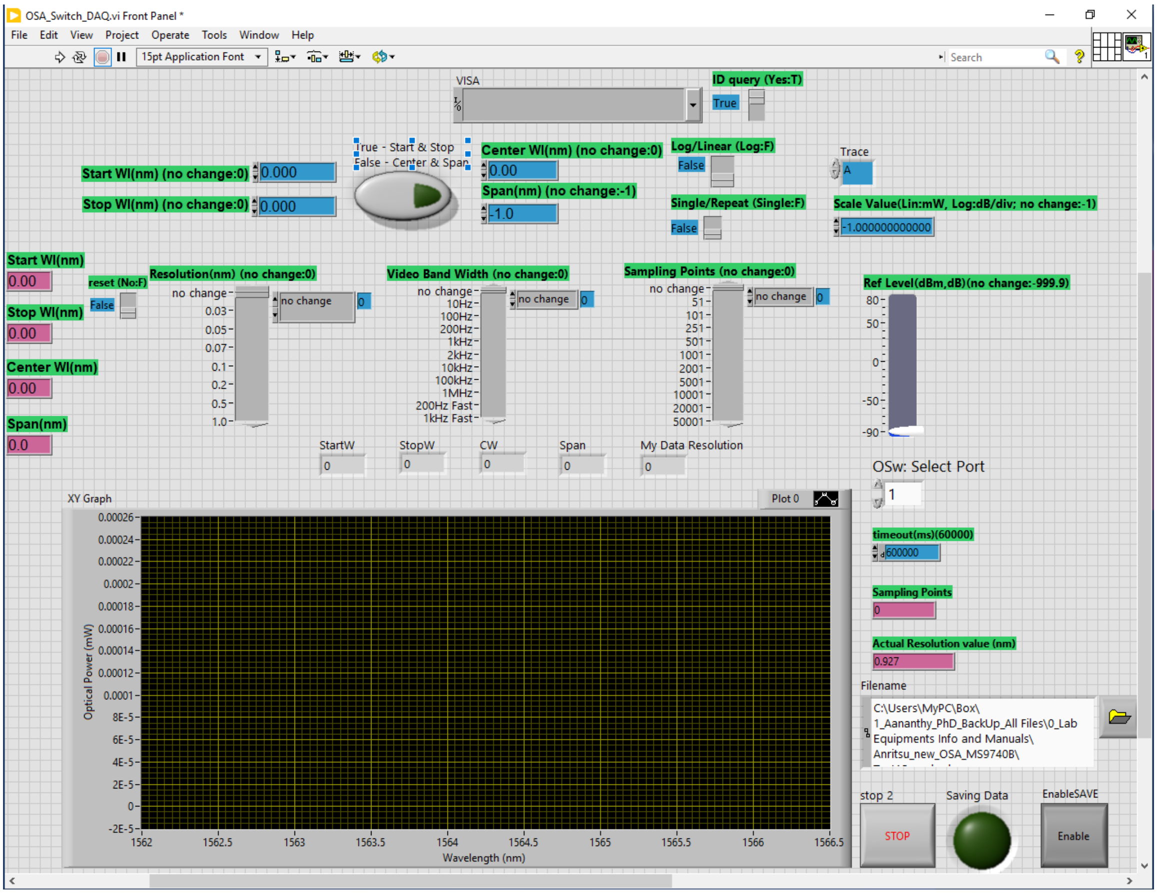

Figure. 3.5 Front Panel of LabVIEW Data Acquisition System

For the FBG sensor system, i.e., wavelength division multiplexed FBG sensor arrays, an automated data acquisition and interrogation system was designed in National Instruments LabVIEW software package. This interfaces the computer to automatically scan and record the reflected spectra of the WDM-FBG arrays from the Anritsu MS9740B optical spectrum analyser (OSA) via Ethernet connection. A super-luminescent light emitting diode (S-LED) with a built-in optical circulator by Denselight Semiconductors from Singapore DenseLight-Semiconductors, 2022 was used as the light source. The optical power for the light source can be set with its own software user interface and this is used in conjunction with the rest of the DAQ devices. An 1x4 optical switch by Sercalo Microtechnologies Switzerland SercaloMicrotechnologyLtd, 2022 was also used to switch between arrays with all of them connected to the light source via the switch. This covers a broad wavelength range of 1240 nm to 1600 nm and works with a maximum switching time of $\simeq$1 ms and has a 1.0 dB insertion loss. Figure 3.5 shows the design of the front panel of the data acquisition system designed on the computer to interface the OSA and the PC. A separate LabVIEW based task was developed with the use of National Instruments DAQ module NI USB-6211 for the optical switching and source selection function. The computer is utilised to control both through the USB interfaces. This data acquisition and optical ports switching task is then fed into the larger DAQ system for the OSA. Figure 3.4 shows the schematic/ system block diagram for the devices connected in the DAQ system along with the sensor arrays. Table 3.1 shows the electrical specification for selecting the desired optical port. This is used in the design of the LabVIEW based DAQ as well as physical connection to the sensor arrays to the optical switch.

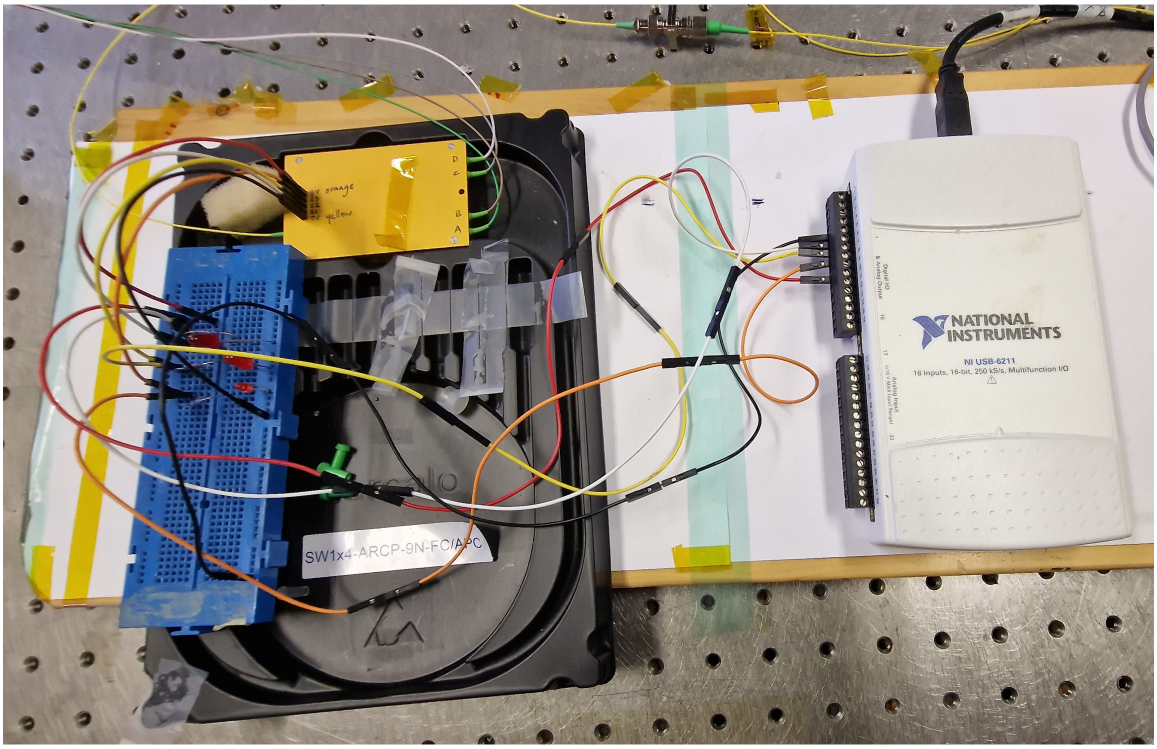

Figure. 3.6 Optical Switch connected to DAQ device NI USB 6211

Table 3.1 Electrical Specifications for Optical Port Selection

Port	**S1**	**S2**	**S3**
A	0V	0V	X
B	5V	X	5V
C	5V	X	0V
D	X	5V	X
Supply: 4.5 - 5.5 V, 10 mA max			
S1 – S3: CMOS or TTL levels, 0 mA			

3.4 Development of Automatic Gaussian Fit

Static measurements were recorded for each FBG in each of the four sensor arrays purchased from FBGS. Data sheet of these DTG-FBGs state that these have a nominal strain sensitivity of 1.2 pm/$\mu\varepsilon$, that is 1.2 pm wavelength shift for every $\mu\varepsilon$ unit of strain applied on the fibre (Typical range 1.15 pm/$\mu\varepsilon$ - 1.25 pm/$\mu\varepsilon$). Throughout this chapter, the unit of strain is taken as micro strain denoted as $\mu strain$ or $\mu\varepsilon$ which is defined as strain multiplied by 10^{-6}. The key parameter required to interrogate a quasi-distributed WDM-FBG system is the reflected centre wavelength of the gratings, which is then used to determine the Bragg wavelength shift to estimate the physical parameter such as strain, temperature etc. Due to the low-resolution limitations of the optical spectrum analyser (OSA) at 0.07 nm, the minimum detectable strain (MDS) thus becomes 58.3 $\mu\varepsilon$ (70 pm/1.2 pm/$\mu\varepsilon$) for FBGs with a calibrated sensitivity of 1.2 pm/$\mu\varepsilon$. This sensitivity can also be found in numerous strain FBG calibration work conducted in Liang et al., 2020, Li, Tan, et al., 2019 and Kreuzer, 2006. Due to this limit of detection posed by the OSA as the optical interrogator, small changes in wavelength shifts corresponding to tiny variations in FBG strain needs to be improved in post-processing. Typical approaches in determining the Bragg wavelengths as explained in Tosi, 2017, Lee, Park, et al., 2007 and Wolfgang, 2008 includes finding the peak wavelength of the FBG spectrum, centroid wavelength or the central wavelength of the FBG peak after fitting a Gaussian function over it. However, from these studies conducted, the problem in determining the reflected wavelength either peak/ centroid or the central wavelength of the reflected FBG peak are the limitation in resolution, increased noise (or amount of background noise), presence of spectral distortion (skewing of the FBG peak which is not a feature of manufacture). These lead to false measurements of the spectra as mentioned in Tosi, 2017 as they only applied the Gaussian fit to the peak region upto a threshold/reaching FWHM and not to the entire peak. As the proposed DTG sensors were used for in-field/ laboratory based applications where the sensors are bonded to the surface of structures, any improper bonding or embedding may lead to broadening of the FBG peak spectra or distortion of the spectra Lee, Park, et al., 2007. The results were analysed with the assumption that the entire peak reflected spectra of a single FBG may be modelled as a 1^{st} order Gaussian function with amplitude corresponding to the peak/centre wavelength and arbitrary amplitude and bandwidth (Tosi et al., 2012). For this, an automatic Gaussian fitting function developed in MATLAB was used to accurately calculate the centroid wavelength shift with an increase/ high resolution which is needed for the accurate strain estimation.

$$y = \sum_{i=1}^{n} a_i e^{\left[-\left(\frac{x-b_i}{c_i}\right)^2\right]} \tag{3.1}$$

Equation 3.1 was used to represent the FBG peak; where a is the amplitude, b is the centre (location) or the mean, c is related to the peak width, i.e. standard deviation and n is the number of peaks to fit, in this case of a single grating, n=1 representing single peak. By using this approach and by fitting the Gaussian function over the entire peak from the baseline of the signal, the accuracy of the wavelength shift improved. Finally, with the sensitivity and the wavelength shift, the experimental strain were calculated. Application of this fitting function is included in the next few sections.

3.5 Preliminary Sensor Characterisation

Optical fibre based strain sensors for structural monitoring on wind turbine blades is a mature and highly developed technique (Glavind et al., 2013). There are a lot of reports based on different structures of optical fibre sensors for general applications, such as FBG, long period gratings (LPG), tilted gratings, chirped or asymmetrically inscribed or phase-shifted grating etc but for wind turbine blades which undergo larger loading conditions, larger deflections and larger curvatures under varying operating conditions, FBG and LPG are more commonly used.

Generally, the longer the grating or 'sensor' length is, the larger the curvature sensitivity is. Fabricating longer gratings require special photonic facilities and are rather expensive. Commercially available sensors tend to be in the range of 4-10 mm of grating length and are relatively cheaper and easier to custom-manufacture for specific applications. In view of this, for this PhD work, uniform FBG were characterised for their sensitivity for strain and temperature. Fibre optic sensors are transducers that respond to the quantity of a particular parameter that is being measured, i.e., *measurand*. To put it simply, the response of the sensor should ideally be a linear function of the measurand and strictly a single valued parameter without hysteresis and can be expressed by the following equation, (Kashyap, 2009),

$$s = k(\omega)x \tag{3.2}$$

where s is the output of the sensors, x is the measurand, and $k(\omega)$ is the sensor's sensitivity of the transfer function, which is a function of frequency ω. Any deviation from linearity causes errors and should be quantified for the sensor or transfer function. However, for most experiments, the transfer function is typically linear and deviates as a function of time by a minimum or maximum value. This value is generally parallel to the ideal curve and can be determined at the time of calibration of the sensors. The DTG-FBG used for this preliminary characterisation investigation offer excellent wavelength to temperature and wavelength to strain linearity as they are coated with Ormocer coating (Kreuzer, 2006).

3.5.1 Axial Strain Sensitivity Calibration of DTG-FBG Sensor

Typically, FBGs do not come with accurate calibration charts or values like conventional or piezoelectric sensors. FBG sensor manufacturers usually provide a range and sensitivity values for both strain and temperature observed under standard laboratory conditions (Technica, 2021). FBGS International BV (Germany) who supplied the FBG arrays and sensors for this investigation provide a strain sensitivity value of 1.2 pm/$\mu\varepsilon$ determined by applying a constant displacement of 30 mm at each increment at room temperature as per the IEC-60793-1-31 standard (FBGS, 2022).As the temperature and the measurement conditions vary from place to place, accurate calibration is crucial to define the meaning of reflected wavelength to load/ strain experienced by the FBG, furthermore it is also a prerequisite for subsequent experiments, performance and quality measurement of the sensor.

It should be noted that no two types of FBGs sensors or FBGs manufactured using the same technology would have the same sensitivity values as there will be difference in the coating material, uniformity of coating which contribute to the photo-elastic coefficient. The relationship between wavelength shift, axial strain sensitivity and the applied strain are governed by the following equations,

$$\varepsilon_A = \frac{\Delta L}{L} \tag{3.3}$$

$$\Delta\lambda_B = (1 - P_e)\,\lambda_B \varepsilon_A \tag{3.4}$$

$$P_e = \frac{n_{\text{eff}}^2}{2}\left[P_{12} - \nu\left(P_{11} + P_{12}\right)\right] \tag{3.5}$$

$$\frac{1}{\lambda_B}\frac{\Delta\lambda_B}{\Delta\varepsilon} = 0.78 \times 10^{-6}/\mu\varepsilon \tag{3.6}$$

Equation 3.3 expresses the applied axial strain ε_A in terms of the length of the fibre L and the change in the length of the fibre ΔL. As strain is a ratio of length vs length, it is dimensionless. Equation 3.4 describes the amount of Bragg wavelength shift $\Delta\lambda_B$ in terms of the applied strain ε_A with the use of effective photo-elastic coefficient of the fibre P_e and this can be calculated using Equation 3.5 where n_{eff} is the effective refractive index of the core of the fibre and ν is the Poisson's ratio of the fibre material and P_{11} and P_{12} are the Pockel's piezo coefficient of the stress optic tensor. For an FBG made out of fused silica centred around the wavelength 1550 nm, typical values for P_e is approximately 0.22, ν is 0.17, P_{11} is 0.121 and P_{12} is 0.271 and at a constant temperature (1-P_e) in Equation 3.6 yields a normalised Bragg wavelength shift of 0.78 x 10^{-6} per $\mu\varepsilon$. This is regardless of the Bragg wavelength of any FBG sensor and its indicated wavelength shift.

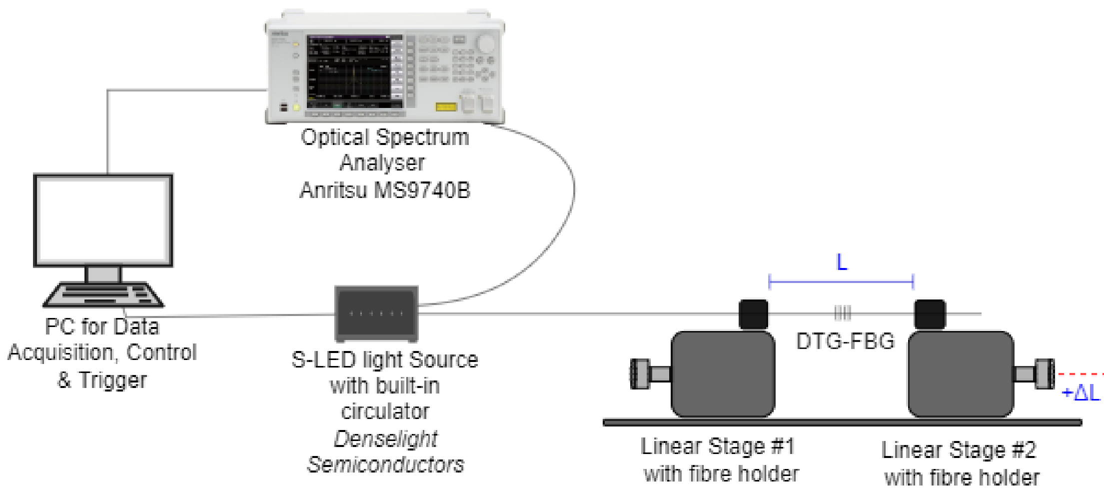

Figure. 3.7 Axial Strain Characterisation & Calibration Setup

In order to determine the strain (and temperature) sensitivity of the specific FBG arrays, the following experiments were conducted. Several papers (Ahmed and Jun, 2014), (Liang et al., 2020) and (Leal-Junior et al., 2019) described the typical setup for axial strain sensitivity measurement. The array considered for this calibration test consisted of 7 uniformly spaced FBGs with a 1 m lead-in and 0.5 m lead-out distance as illustrated in Figure 3.8. Each 10 mm gratings are spaced out by 260 mm between them and have reflectivity between 26% to 35% and full width half maximum (FWHM) bandwidth of 80 pm. A description of the array specifications is given in Table 3.2. Further details of these arrays can be found in Chapter 6.

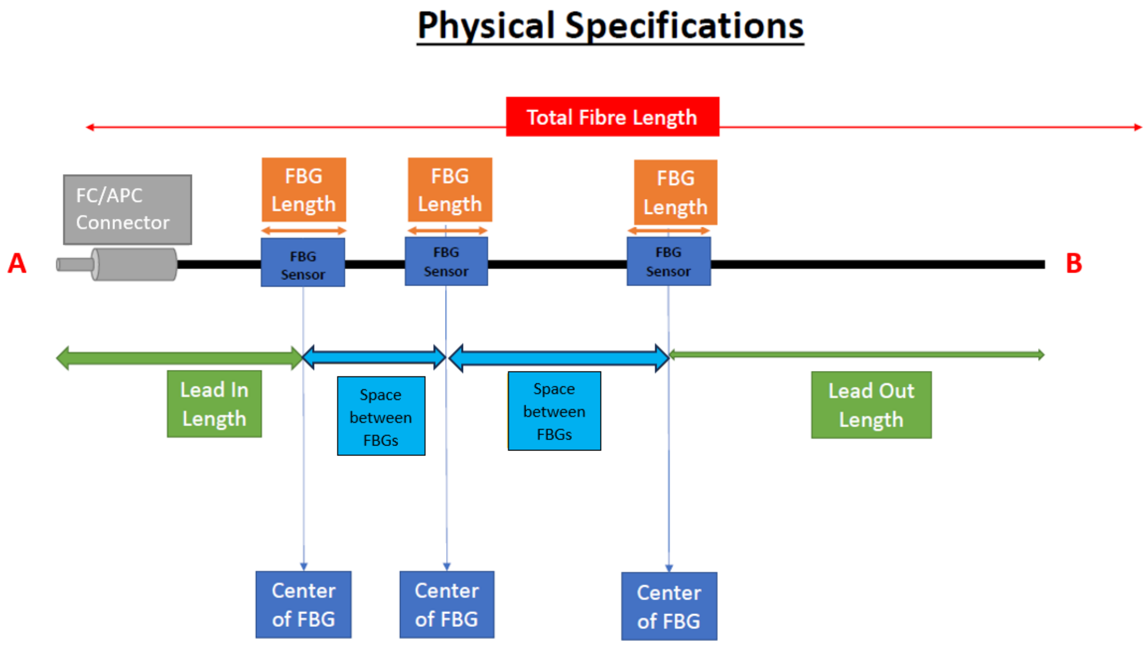

Figure. 3.8 Physical Specification FBG Array

Table 3.2 Array 4 Specifications for Axial Strain Characterisation

Specification	**DTG N°**	**Position (mm) Absolute**	**Position (mm) Relative**	**Wavelength (nm) Nominal**
	Lead In	0	0	N/A
	1	1070	1070	1531
	2	1330	260	1536
	3	1590	260	1541
Array 4	4	1850	260	1546
	5	2110	260	1551
	6	2370	260	1556
	7	2630	260	1561
	Lead Out	3130	500	N/A

Using the setup as illustrated in Figure 3.7 and shown in experimental setup in Figure 3.9, the fibre was secured in two fibre holders on top of two manual translating stages. The length of fibre with the 7 FBGs were characterised in three stages, first with FBGs 1-3 and then with next two 4-5th FBGs and finally with the last two remaining FBGs 6-7. These were fixed at different lengths covering the number of FBGs considered (For eg, for 2 FBGs, the fixed length between the two stages were 600 mm) and was stretched by steps of 10 μm using the linear stage-micrometer applying strain on the fibre, finally concluding the extension at 200 $\mu\varepsilon$. To avoid the fibre slipping from the fibre holders as well as to avoid breakage of the fibre, the strain was limited to well below 1 %. It should be noted that initially, the fibre between the two stages may be slack and a strain (application of pre-strain before the strain for the characterisation) needs to be applied by moving the linear stage to get the fibre taught. For this strain characterisation campaign, the temperature in the laboratory was assumed to be at a constant temperature 25 degree Celsius to avoid the cross-sensitivity effects, or from temperature influencing the wavelength shift due to applied strain.

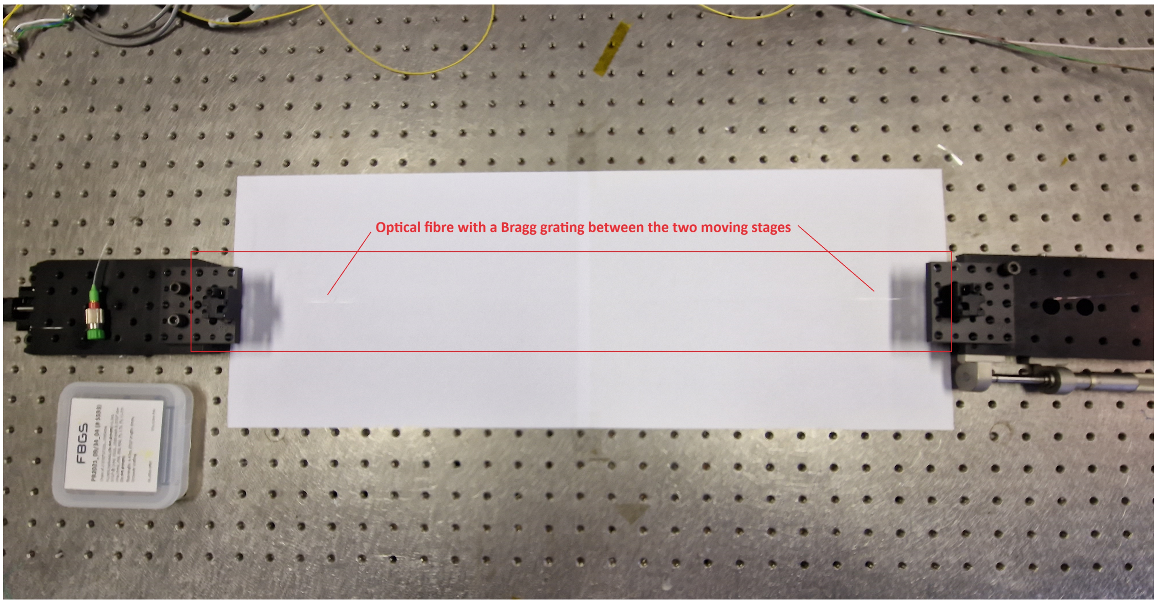

Figure. 3.9 Experimental setup for FBG Axial Strain Characterisation & Calibration

Figure 3.11 shows the spectral response (raw-data) of Sensor 1 in the array with 1531 nm Bragg wavelength under increasing applied strain from 0 $\mu\varepsilon$ to 170 $\mu\varepsilon$. The first couple of spectra do not move as much as expected as they were captured during the pre-strain application. This can be monitored at the OSA interface display and can be evaluated by looking at the spectrum moving when the pre-strain is applied. Looking at the spectra in Figure 3.11 which show the change in reflected spectrum with increasing applied strain, it can be seen that the FBG show good strain response with the applied extension, i.e, wavelength shifts to the right indicating that the fibre is experiencing tensile strain. For this raw-data, the Gaussian fit was applied for the entire peak using the equation Equation 7.1, rather than the full-width-half maximum (FWHM) to improve accuracy of the peak and to capture as much information as possible from the original raw-data peak. For the initial fitting, using the equation/ function in MATLAB, the numerical fitting was done and for this fitted data, the centroid Bragg wavelength, b was finally extracted for each FBG spectrum. Figure 3.10 shows the raw-data peak and the Gaussian fit for the sensor with Bragg wavelength of 1531 nm.

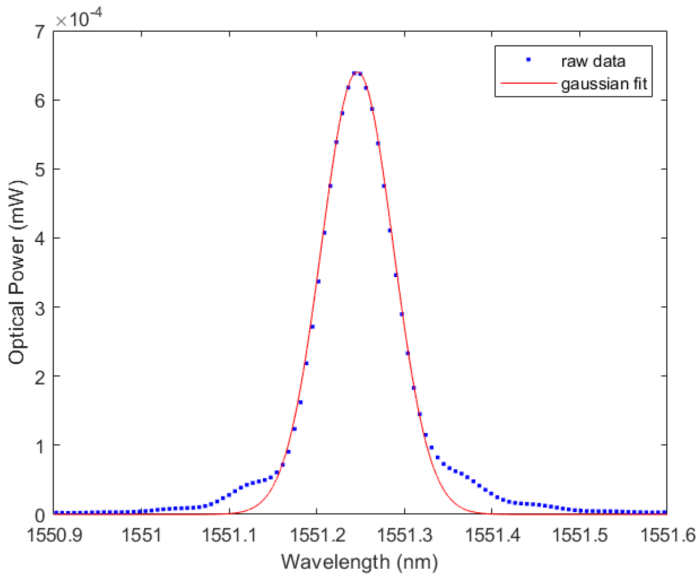

Figure. 3.10 Gaussian fitted data vs Raw Data for FBG-1531 nm

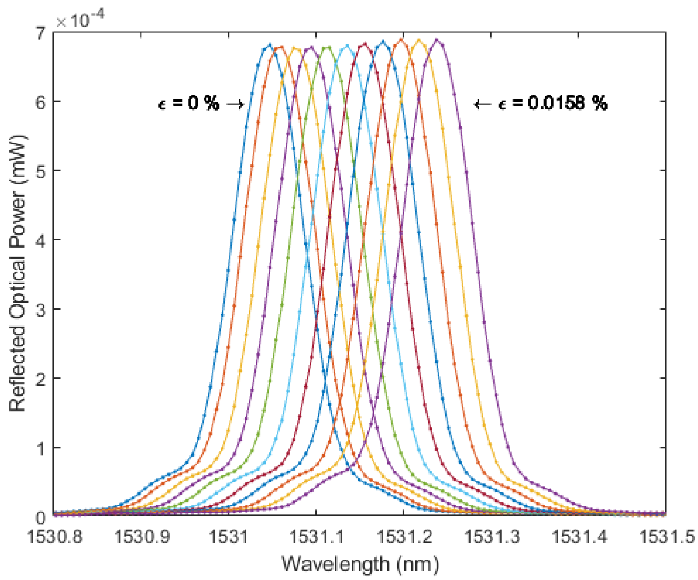

Figure. 3.11 1531 Axial Spectrum Spectra

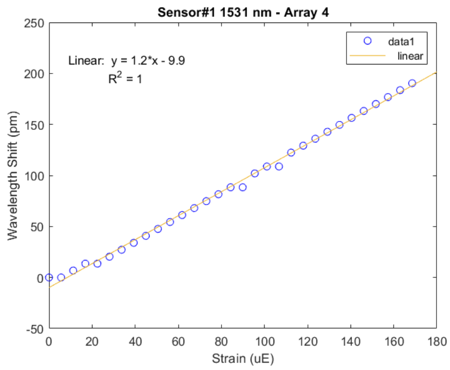

(a) S1 FBG at 1531 nm

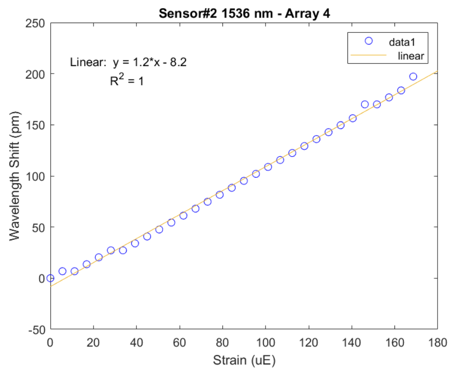

(b) S2 FBG at 1536 nm

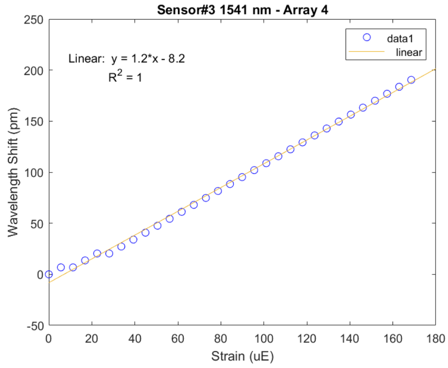

(c) S3 FBG at 1541 nm

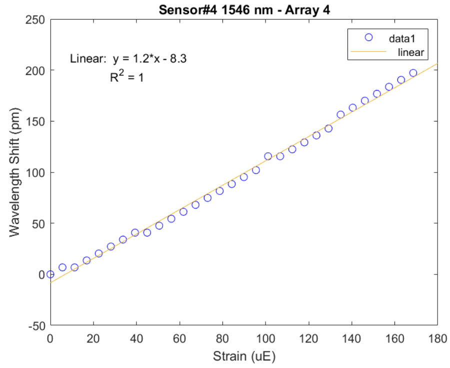

(d) S4 FBG at 1546 nm

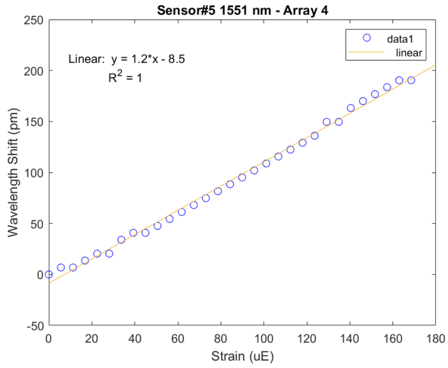

(e) S5 FBG at 1551 nm

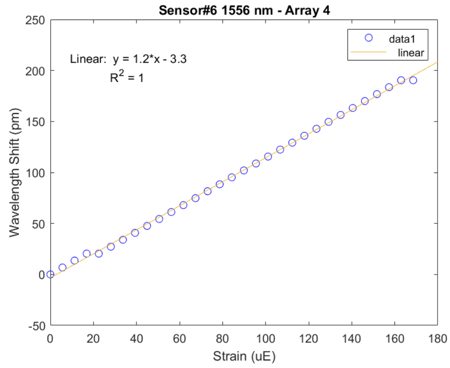

(f) S6 FBG at 1556 nm

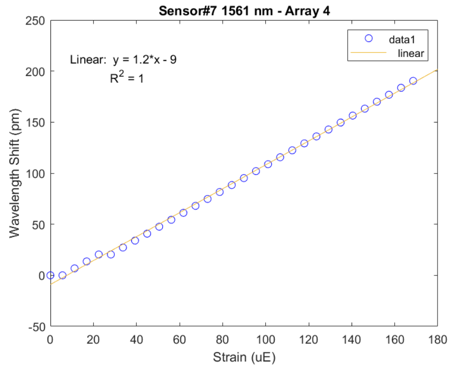

(g) S7 FBG at 1561 nm

Figure. 3.12 Linear fit of FBGs Centroid wavelength with respect to Strain Variation for (a) 1531 nm (b) 1536 nm (c) 1541 nm (d) 1546 nm (e) 1551 nm (f) 1556 nm (g) 1561 nm

The strain vs wavelength shift results for each FBG in the array considered are plotted in Figure 3.12 For this set of data, using the Equation 3.4, the axial strain sensitivity was calculated. It can be seen that the strain sensitivity for all FBGs result in 1.2pm/ $\mu\varepsilon$. There could be minor variations (i.e., 1.19 or 1.21) if the results are approximated to three or four significant digits however, as majority of the FBG spectra follow the expected linear trend on average for the extracted wavelength shift with respect to applied strain, a final value of 1.2pm/ $\mu\varepsilon$ is considered for the strain calculations for the analysis from here onwards in this thesis. Based on the in-depth literature review conducted in Chapter 2, the FBG is widely known to be sensitive to both strain and temperature. Looking at Equation 3.7 below, it can be seen that the total wavelength shift of an FBG is affected by both the axial sensitivity as well as the temperature sensitivity. Furthermore, according to the strain measurement campaign conducted by (Kreuzer, 2006), FBGs show high temperature dependence, where $\Delta\lambda/\lambda_0$ caused by ± 1.00°C results in $\Delta\lambda/\lambda_0$ caused by 8 μm/m mechanical strain. Therefore, it is important to conduct a temperature characterisation for FBGs. This is discussed in the next section.

$$\ln\frac{\lambda}{\lambda_0} = S_\varepsilon \Delta\varepsilon + S_T \Delta T \tag{3.7}$$

3.5.2 FBG Temperature Characterisation

The sensitivity of the FBG to temperature was investigated by immersing the sensor in a hot water bath and monitoring the wavelength as the water cooled. The FBG under investigation was secured inside a vessel with two supporting blocks and two k-type thermocouples were secured inside next to the fibre grating as shown in Figure 3.13. With the LabVIEW based data acquisition program for the OSA and an independent temperature data acquisition device (PicoUSB TC-08 Thermocouple Data Logger) running continuously recording the sensor's response spectrum and the temperature respectively, hot water was slowly poured into the vessel covering the entire depth plus a few centimetres from the fibre and both the thermocouples. Data from both devices were taken automatically at 10 second intervals. Additional support blocks and tacky tape were used to ensure that all 3 sensors are secured in the same depth/ level so that they would experience the same temperature. This also ensured that the sensors were fully submerged not floating on the surface of the water or coming loose when hot water is poured into the vessel. shows the schematic diagram of the experimental setup. Any micro strain induced by the taping or the blocks were constant throughout the experiment, therefore was assumed to have no significant effect in the change in wavelength compared to wavelength shift due to change in temperature. The temperature varied from 80°C to 30°C and was recorded with a resolution of 0.001°C provided by the data logger and an accuracy of ±1.00°C provided by the thermocouple.

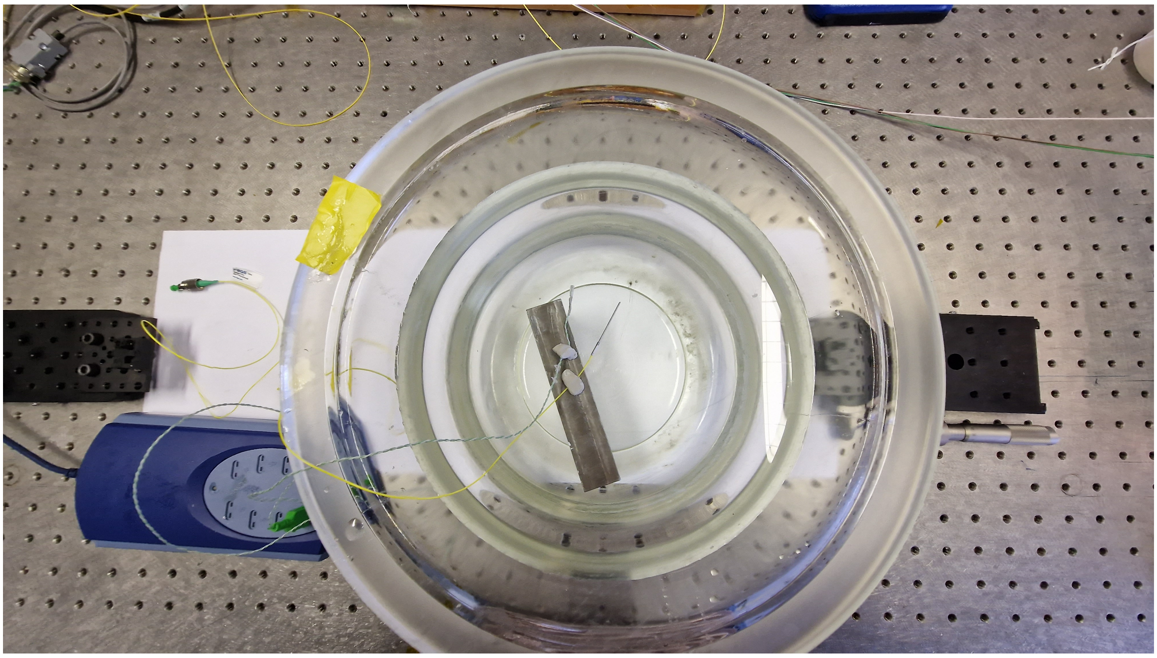

Figure. 3.13 Experimental setup for FBG temperature characterisation with both FBG and K-type thermocouple

3.5.3 Temperature Characterisation of TP-01 DTG-FBG Sensor

A Fibre Bragg Grating (FBG) sensor is sensitive to both strain and temperature changes. The relationship between the wavelength shift due to the change in strain and change in temperature is given the in Equation 3.8 below.

$$\ln \frac{\lambda}{\lambda_0} = S_\varepsilon \Delta\varepsilon + S_T \Delta T \tag{3.8}$$

For the purpose of using with the draw tower grating (DTG) based FBG array sensor system, a single DTG-FBG temperature probe manufactured by FBGS Technologies has been used. This particular grating is 40 mm in length and is sensitive to temperature only. It comes in a tiny steel casing so that it is not sensitive to any strain imposed on it and can be integrated easily into existing FBG sensor systems. A summary of specifications is given below in Table 3.3 and the detailed data sheet is attached under Appendix: Technical Data Sheets.

Table 3.3 TP-01 Temperature FBG Configuration

Parameter	Value
Total sensor length	40 mm
Pigtail length	1 m
Pigtail material	PVDF
Connector type	FC/APC
Number of sensors	1
Housing material	SS316
Typical temperature precision	0.2°C
Temperature accuracy	1°C
Temperature range	-22.5°C to 110°C
Nominal wavelength at 22.5°C	1564.061 nm

For the sensor's calibration, a similar approach mentioned under subsection 3.5.2 is followed, where the wavelength of the sensor is monitored under a hot water bath. An independent temperature measurement unit Picolog with a k-type thermocouple attached is also taken simultaneously. The response of the sensor to the change in temperature is described in Equation 3.9 below.

$$\ln\frac{\lambda}{\lambda_0} = S_1 \cdot (T - T_0) + S_2 \cdot (T - T_0)^2 + k \cdot \varepsilon \tag{3.9}$$

where λ is the wavelength; λ_0 is the nominal wavelength at zero strain and at a fixed temperature T_0; S_1 and S_2 are the temperature sensitivities and k is the strain sensitivity or the gage factor. The strain ε is the mechanical strain experienced by the fibre grating. Due to the quadratic nature of the relationship between the grating to strain and temperature Equation 3.9, the calibration parameters S_1 and S_2 depends on the reference temperature used. In this case, the parameters S_1 and S_2 of the sensors supplied by FBGS are determined with the reference temperature of 22.5°C. When temperature T is expressed in °C and strain ε is expressed in $\mu\varepsilon$ (micro strain), typical values for S_1 = 6.37E-06, S_2 = 7.46E-09, $k = 0.772$ and the thermal expansion coefficient α_f is 0.5 $\mu\varepsilon$/°C.

In this investigation, the temperature varied from 86°C to 36°C over a period of 160 minutes and was recorded with the resolution of 0.001°C provided by the data logger and an accuracy of ±1.00°C provided by the thermocouple - Picolog software. The Figure 3.14 shows the response of the FBG i.e, reflected spectra of the FBG as the temperature cools down with time.

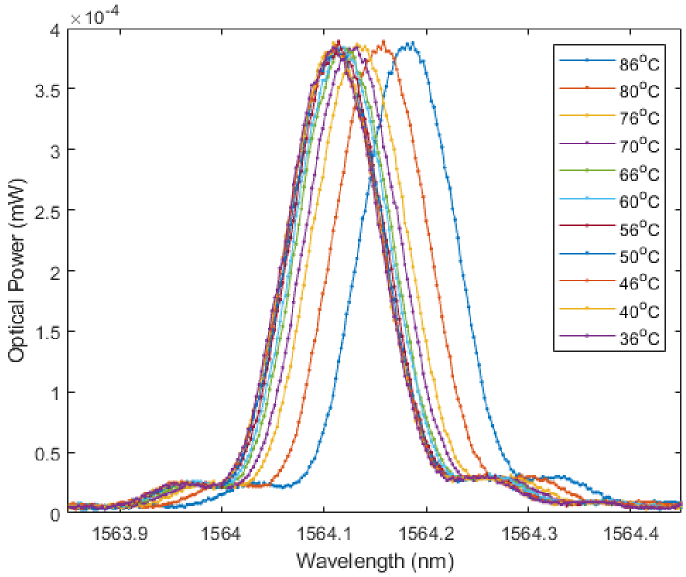

Figure. 3.14 FBG response as a function of temperature changes

The Figure 3.15 below shows the temperature measured by the thermocouple vs. the temperature estimated using Equation 3.9. The estimation of the FBG's temperature was based on the centroid wavelength reading taken by applying a first-order Gaussian fit to each recorded spectrum from the optical spectrum analyser. Detailed implementation is given in Section 3.4 and the MATLAB code developed for this post processing can be found under Appendix B.

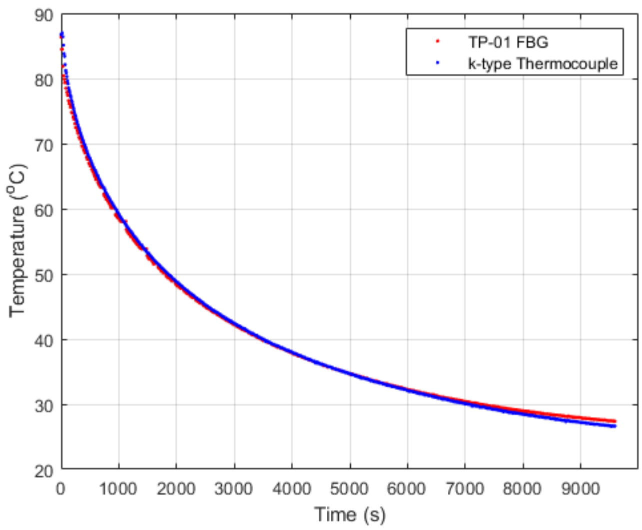

Figure. 3.15 Measured Thermocouple Temperature vs Measured TP-01 FBG Temperature

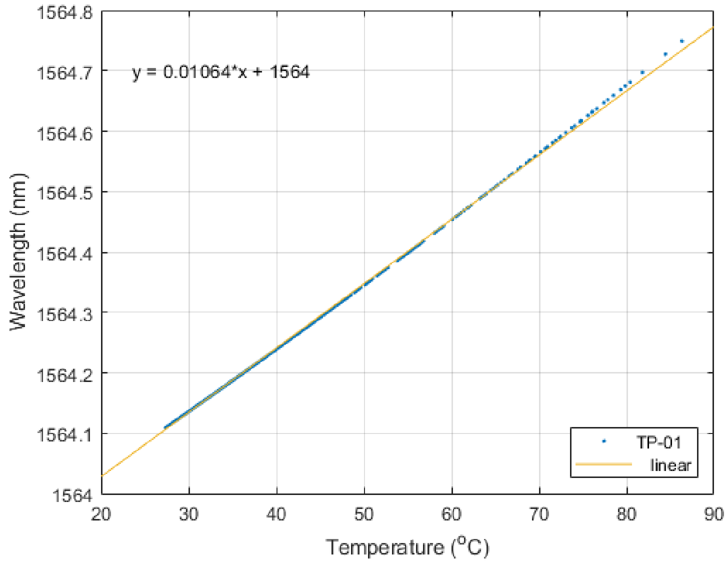

Figure. 3.16 Linear fit of Centroid wavelength with respect to Temperature Variation

By fitting a linear line to the plot obtained from the calibration i.e., centroid wavelength with respect to temperature variation shows that the sensitivity of the TP-01 FBG is approximately 10.64 pm/°C in Figure 3.16. This comes close to the standard sensitivity of an FBG at 1550 nm nominal wavelength for most bare single mode fibre (SMF-28) (Abushagur et al., 2021).

3.5.4 Bonding FBGs on Different Materials

Before the fibre optic sensors could be tested on structures such as beams or blades, the Ormocer-coated fibre was first evaluated for bonding on different materials, including an aluminium plate, a 3D-printed polylactic acid (PLA) plate, and a composite plate made of resin and a few layers of glass.

The adhesive chosen for this task was Cyanoacrylate, as it provided a strong yet temporary bond that could be easily removed with an adhesive remover, enabling the sensors to be used at multiple locations and orientations. This flexibility was particularly important for experiments that required the repositioning of sensors to optimize strain measurement or validate results across different configurations. While industrial two-part adhesives could have provided a stronger, permanent bond, they were deemed unsuitable for this investigation due to the inability to debond them without damaging the sensor or the structure. Thus, the use of Cyanoacrylate ensured reliable adhesion while maintaining the adaptability needed for testing across a variety of materials and conditions. For this, a reel of just Ormcoer coated fibre without any gratings inscribed was purchased from FBGS so that the usability of this special coated fibres could be checked before purchasing arrays of fibres with gratings inscribed.

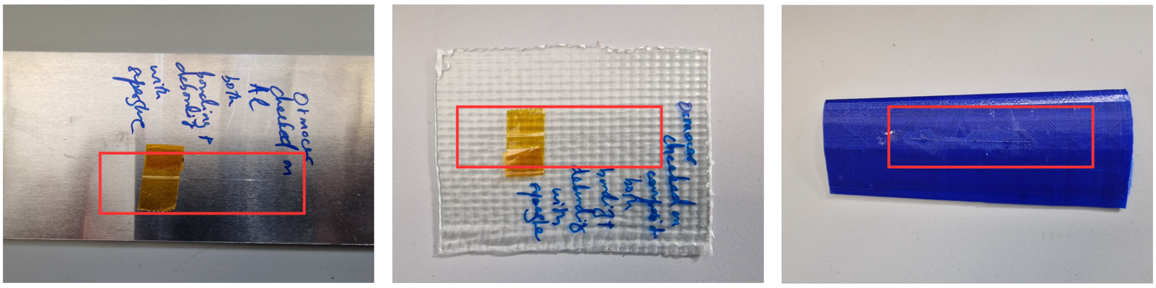

(a) Aluminium plate (b) Composite plate (c) 3D printed PLA

Figure. 3.17 Testing Cyanoacrylate bonding and debonding on (a) Aluminium plate (b) composite plate (c) 3D printed PLA material

Figure 3.17 shows the Ormocer coated fibre after being bonded and debonded. It can be seen that the fibre coating has responded well to the adhesive as well as the adhesive debonding liquid. Whereas the last figure in the same series, shows the fibre bonded to the PLA surface, also shows the debonding has failed and the fibre remains bonded to the PLA surface.
Based on the above experiment on bonding and debonding on different materials, it was determined that Ormocer coated fibres can only be tested with either Aluminium or composite materials using Cyanoacrylate.

3.6 Secondary FBG Strain Characterisation on Aluminium Cantilever Beam

Esu, 2016, Heaney et al., 2018, Feng et al., 2016 and Hwang et al., 2011 have conducted sensor strain characterisation based on cantilever beam experiments. In this section, one of the main objectives is to investigate the performance and demonstrate the use of quasi-distributed fibre optic grating-based sensor system for load monitoring (based on strain measurements) and defect detection.

Wind turbine blades can be viewed as beam-like or plate-like structures. Based on classical Euler-Bernoulli beam theory and simple beam theory, analytical methods of evaluating cantilever beam behaviour under varying static loads were carried out for a uniform Aluminium beam and a non-uniform beam with a notch. Both Euler-Bernoulli and simple beam theory were used to predict the behaviour of the cantilever beam; however, Euler-Bernoulli is better suited for uniform beams, whereas Finite Element Analysis (FEA) was necessary for validating the behaviour of the defective beam. It is worth noting that Euler-Bernoulli is often referred to as simple beam theory, as they share the same fundamental assumptions. Finite element models were also developed in ANSYS for both types of beam with the appropriate boundary conditions. In order to characterise the FBGs under static loading experimentally and validate the performance, a series of simulations were conducted using ANSYS Workbench, so that the experimental results can be compared with the numerical/ analytical results from simulations. The main difference between Euler-Bernoulli and simple beam theory lies in their assumptions: Euler-Bernoulli predicts bending stress/strain and deflections based on linear elasticity assumptions and neglects shear deformation, whereas simple beam theory ignores complexities such as non-uniform cross-sections and localised stiffness variations, focusing instead on an average approximation. The first set of simulations were conducted for a uniform beam with the physical dimensions and properties mentioned in Table 3.4 and the second set of simulations were conducted for the same beam specimen with a known defect present. The known defect in this case is a 2 mm deep, 2 mm wide 'V' notch on top of the beam at 30 mm from the fixed end as depicted in the Figure 3.19 in subsection 3.6.2. Finally, the measured strain results from FBG, both on the defect and other FBG locations on the beam from on the experiments with the cantilevered setup with static loads were compared and validated with the expected strains/ strain profile for those locations based on the simulations for both beam cases.

For this investigation, the assumptions made to utilise the simple beam theory/ Euler Bernoulli beam theory are as follows,

1. The beam material is isotropic and homogeneous and obeys Hooke's Law. i.e. linear elastic.

2. The beam is long relative to its width and depth. Hence the stress observed perpendicular to the beam's length is much smaller than the stress observed parallel to the beam length, hence the perpendicular stress can be ignored.

3. The beam's cross section throughout its length is constant.

4. The beam is symmetrical about the Y-Y axis (runs width-wise along the beam), hence there is no twist or torsion.

5. Plane sections remain plane. This is true when a beam is subject to pure bending, and experiences zero shear deformation.

6. The deflections of the beam are small. (A quantitative definition of "small" means that the maximum deflection is much smaller than the beam's length (or smaller than its depth). $\frac{\delta_{\text{max}}}{L} \leq \frac{1}{10}$, where δ_{max} is the maximum deflection L is the beam length. Craig Jr and Taleff, 2020; Boresi and Schmidt, 2002)

However, real life structures deviate from the above assumptions and depend on the following points. But typically, these factors are approximated well enough for the simple beam theory to be fairly accurate.

- The geometry of the beam i.e. length, width, depth as well as the cross section.
- The type of material and its properties, for example, Young's modulus
- The internal equilibrium of the structure/ beam.
- The beam's deformations/ curvature.

It should also be noted that Assumption 3, which states that the beam's cross-section is constant throughout its length, may no longer be valid in the case of a beam with a V-notch. The V-notch introduces a localised discontinuity in the cross-sectional area, leading to a significant reduction in stiffness and the formation of stress concentrations near the notch. These factors can no longer be accurately represented using simple beam theory alone. In such cases, Finite Element Analysis (FEA) becomes necessary to capture the complex stress and strain distributions caused by the geometric irregularity of the V-notch. FEM allows for a more detailed and accurate representation of the beam's response, accounting for stress concentrations, localized deformations, and other effects that are ignored in the assumptions of simple beam theory.

3.6.1 Theoretical Analysis of Aluminium Beam - ANSYS Workbench

For the theoretical analysis of the expected strain, both the Aluminium beams with and without the defect were modelled in ANSYS Workbench/mechanical. The beam is 550 mm long and 50 mm of it is fixed and 500 mm is free. Static loads of upto 3.2 kg or 31.392 N is applied by hanging weights at 35 mm on the centre line of the beam, as shown in Figure 3.18a For the numerical simulations, the 3D geometry was designed in SpaceClaim.

Table 3.4 Material and geometric properties of the uniform beam

Parameter	Variable	Value
Material		Aluminium
Total Mass	m	685 g
Density	ρ	2770 kg/m^3
Elastic Modulus	E	71 GPa
Poisson's ratio	ν	0.33
Total Length		550 mm
Free Length	l	500 mm
Width	b	75 mm
Height	h	6 mm

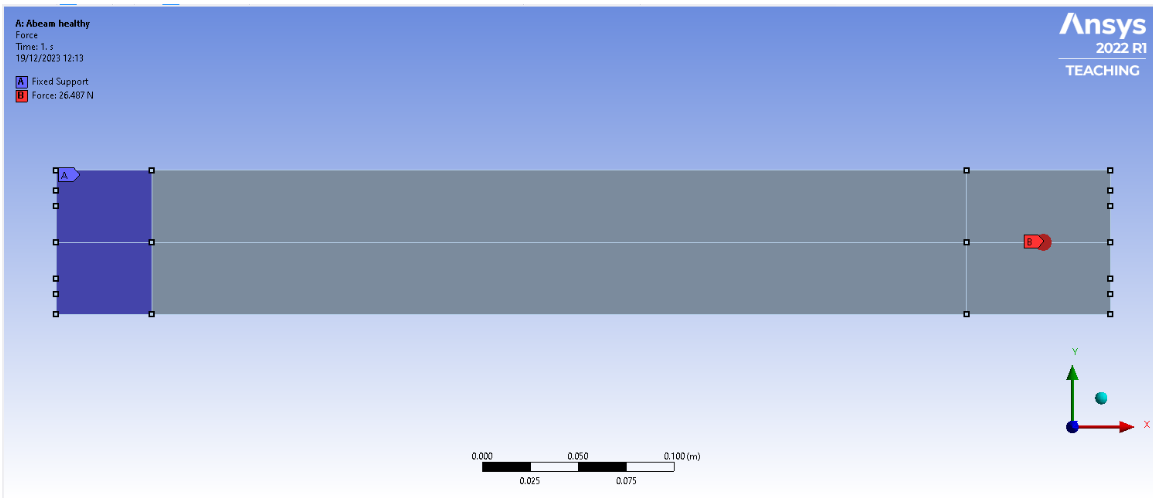

(a) Aluminium healthy beam

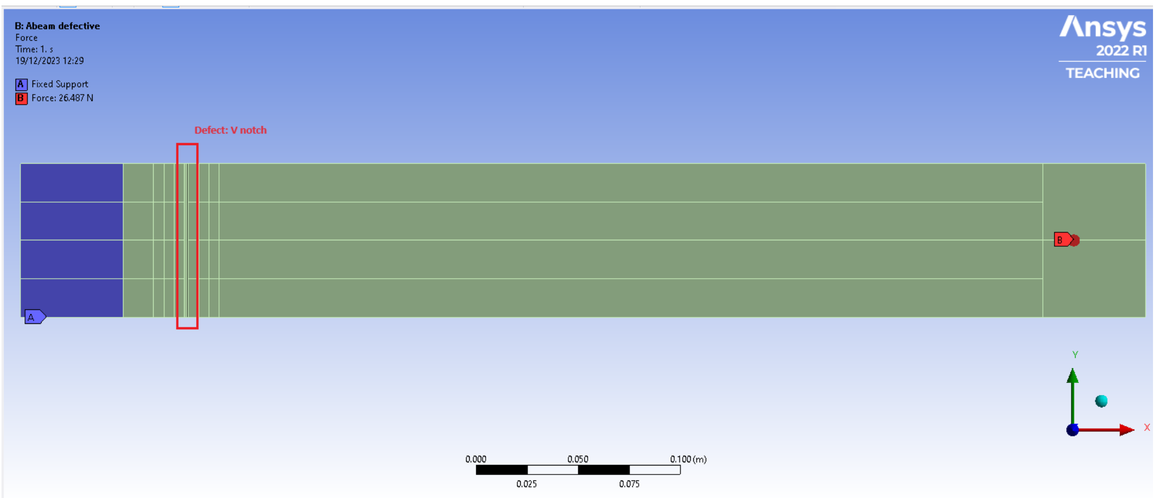

(b) Aluminium beam with defect

Figure. 3.18 ANSYS illustration of Aluminium (a) healthy beam (b) beam with V-notch defect

The mesh of the volumetric beam model was created using the software package ANSYS Mechanical v.19.2 and the material Aluminium Alloy was characterised with homogeneous, isotropic and linear elastic properties as defined under Engineering Data. The detailed information can be found under general materials listed under the Engineering Data Sources. The beam was assigned with a Young's modulus (E) value of 71 GPa and a Poisson's ratio (ν) of 0.3. Additional construction geometry paths were created to accurately predict the elastic strain and directional deformation of the beam along that path. These paths were created so that they coincide with the proposed FBG mounting locations. For the meshing method, a uniform hex-dominant mesh was selected with quadrilateral free face mesh type. This resulted with the beam having uniform element size of 0.002 m which is defined under "mesh". This generated a mesh with approximately 240,000 nodes and 45,000 elements. Since this set of studies were not concerned about the number of elements, a separate mesh dependency test was not conducted.
A convergence study is typically required to ensure that numerical results are independent of the mesh size and adequately represent the physical behaviour of the model. However, in this study, the chosen mesh density was sufficiently fine for the problem at hand. Specifically, the selected element size of 0.002 m was significantly smaller than the smallest structural feature of interest, such as the sharp edges and reduced cross-sectional thickness near the V-notch, ensuring adequate resolution of stress and strain gradients in these regions. The mesh was also sufficiently dense to accurately capture the curvature and deformation of the beam under loading.

A 50 mm section at the root was selected to be the fixed support/ clamped end under static structural analysis settings. The settings for the force applied were defined by 3 components X, Y, Z with the Z negative component pointing towards the ground. A vertex point located at 35 mm from the tip (along the centreline perpendicular to the upper face of the beam) was then defined as the location at which the force would be applied. X and Y force components remained zero as there are no edgewise and or torsional force applied to the beam directly. Figure 3.18b depicts the fixed support i.e., clamped section of the cantilever beam and the force applied direction with respect to the global coordinates of the ANSYS simulations.

By parametrising the Z force component, a series of force (N) values starting from 4.41 N up to 31.39 N, with an interval of 5 N input and respective strain and displacement results were calculated as output. To obtain the solution for the beam, several equivalent elastic strain along the construction geometry paths were drawn along with the directional deformation of Z axis along those selected paths. The displacement results were later used to compare with

the tip deflection measured experimentally. For the beam with the defect, the same setup as above was applied for the geometry without the defect present. The presence of the V notch prevented the bonding of the FBGs directly above the "defect" due to the absence of material, therefore as an alternative, FBGs were bonded right underneath the defect. In this case, the construction geometry paths were created predominantly on the bottom of the beam so that they coincide with the practical FBG mounting locations.
A total of 10 separate of FE analyses were conducted for both beam cases, one for each tip loading case i.e., force applied at the tip.

3.6.2 Experimental Analysis - Aluminium Beam

The Aluminium beam experiments were conducted to validate the accuracy and reliability of the FBG sensing system under controlled conditions, leveraging Aluminium's isotropic and homogeneous properties for straightforward comparisons between experimental and numerical results. This material provides a consistent baseline to evaluate the sensors' sensitivity to localized defects, ensuring the system's effectiveness before applying it to more complex materials like composites. Additionally, Aluminium's predictable strain behaviour and cost-effectiveness make it an ideal choice for refining the experimental setup and understanding the sensors' performance in detecting early-stage damage. These experiments establish the foundation for scaling the methodology to more advanced materials and structures. The FBGs are bonded to the beam's surface using Cyanoacrylate at various lengths along the beam as depicted in Figure 3.19 below. The locations of the sensor bonded on the beam are given in Table 3.5 and Table 3.6.

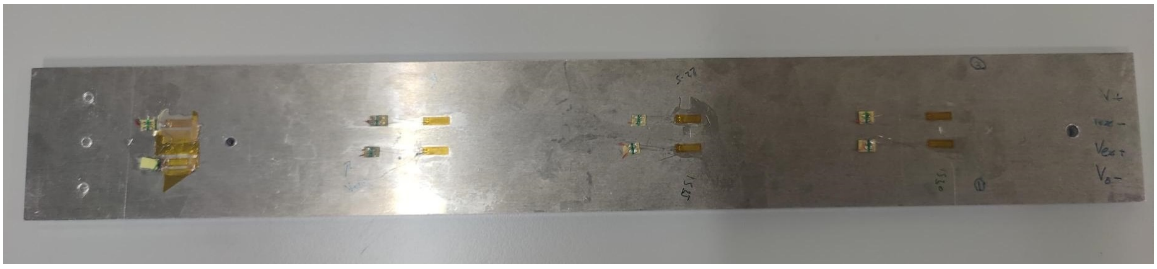

(a) Aluminium beam without notch

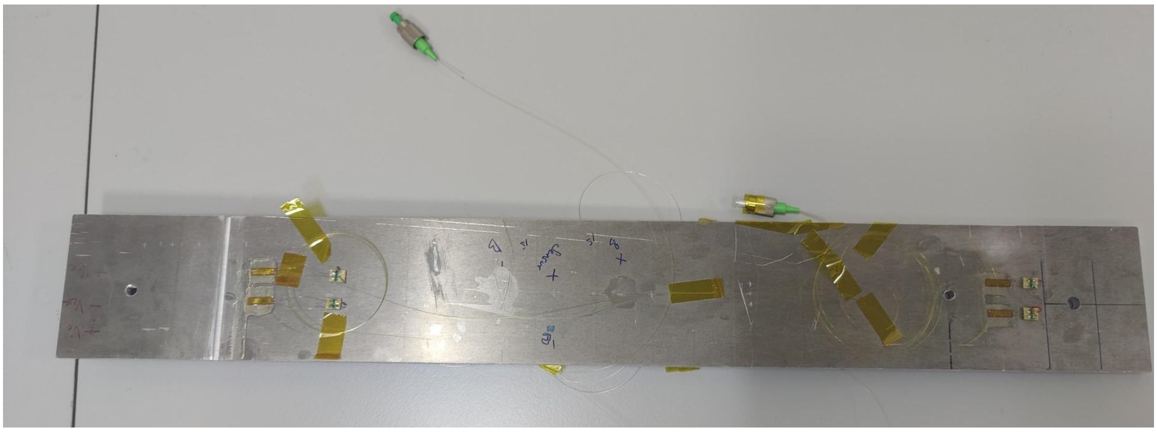

(b) Aluminium beam with ’V’ notch

(c) top view

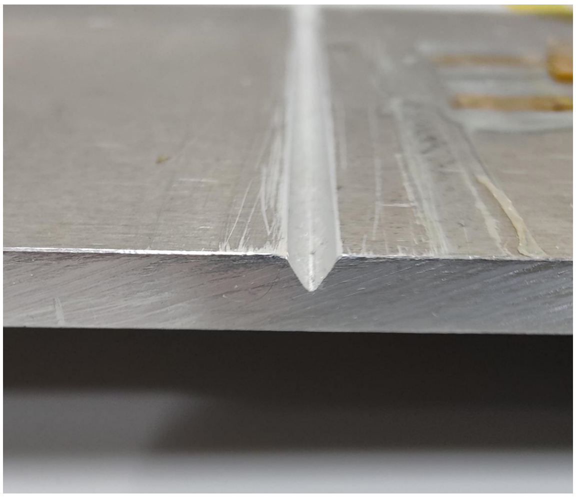

(d) side view

Figure. 3.19 Aluminium beams used for FBG-strain characterisation (a) beam without notch (b) beam with V-notch defect (c) top view of V-notch (d) side view of V-notch

To measure the tip deflection experimentally, a Mitutoyo 2050-08 dial gauge with a magnetic base fixed on a separate stand was used. The maximum measurement of this device was 20 mm with a maximum resolution of 0.01 mm. During each strain measurement campaign, the weight was hung off the cantilevered beam and was left to settle down so that there are no vibrations affecting the reading of the FBGs as well as the dial gauge.

For the static loading test, measurement of the Bragg wavelengths was performed at a low frequency of 100 Hz and a high resolution of 0.002 nm so that the scanning process doesn't pick up any random noise or vibrations. On the optical spectrum analyser's LabVIEW based data acquisition system, 1000 sampling points per scan was selected for a spectrum spanning 2 nm. For each load applied, measurements were taken for 3 minutes each spectrum scan lasting for 10 seconds, resulting in approximately 18-20 spectra and then later averaged for further data analysis.

A simplified annotated schematic diagram of the beam with the sensor locations is given in Figure 3.20. A super-luminescent light emitting diode (LED) by Dense Light Semiconductors, centred at a wavelength of 1550 nm, with a built-in optical circulator is used as the broadband light source. To switch between the different FBG arrays or sensors, a 1x4 fast fibre Micro-electro-mechanical Systems (MEMS) opto-mechanical switch by Sercalo Microtechnology was used.

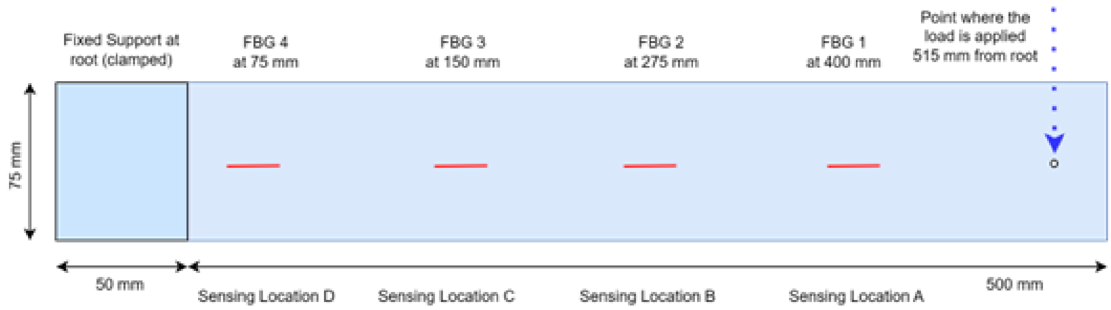

Figure. 3.20 FBGs bonded to the top surface at different span lengths of the healthy beam

The measurement campaign started with zero strain without any weights/ loads applied on the beam, i.e., the beam without anything attached to it. The second loading case was conducted with just the aluminium rod secured to the beam's tip. The third and the rest of the measurements were taken by hanging weights off this rod one by one (increasing in load) attached to the beam. After conducting the load-on measurement campaign, i.e., going from zero strain to max strain/ load applied, the load-off measurement campaign was conducted to check for any hysteresis effect present. To start off, this was done with the highest load attached and then went down to zero load by decreasing the weights one by one. A total of 10 measurements were taken for both load-on and load-off measurement campaigns. This whole process were repeated three-times to ensure repeatability.

The static loading tests for the beam with the defect follows a similar experiment methodology as above, with the main difference being the mounting locations of the FBG sensors. To characterise the strain of this beam, two sensors were chosen to be bonded to the surface. One FBG with central (Bragg) wavelength 1545 nm was mounted right underneath the defect i.e., the "V" notch, at the bottom surface of the beam 80 mm from the root. The other FBG with a central wavelength of 1535 nm was mounted on the top surface of the beam, 250 mm from the root, coinciding with the middle line of the beam. Refer to Figure 3.21 below.

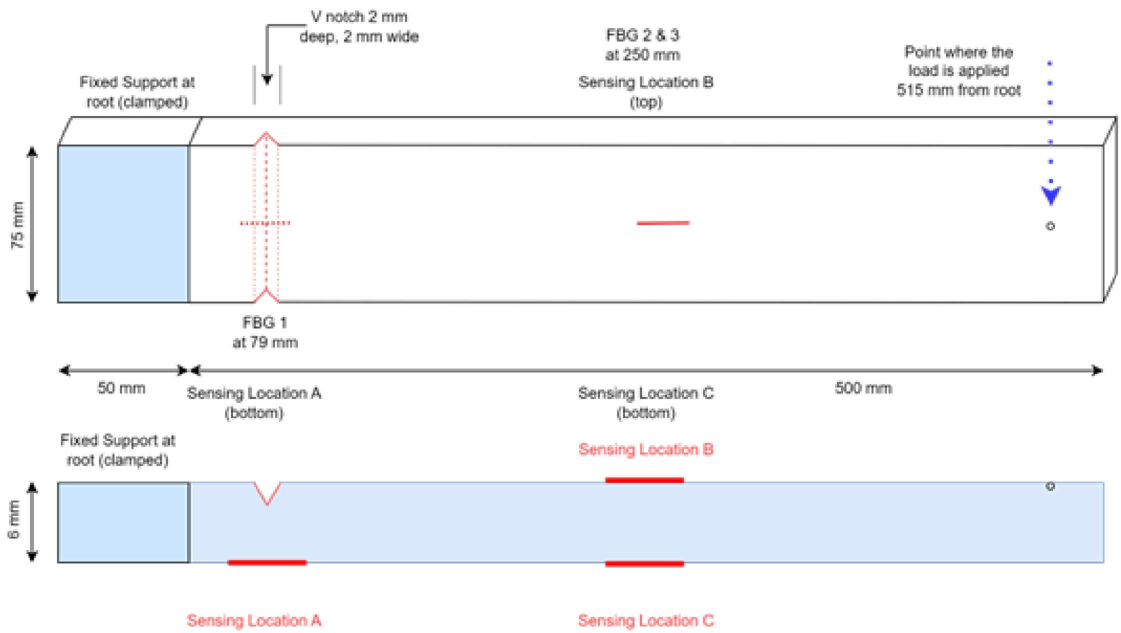

Figure. 3.21 FBGs bonded to the top and bottom surface of the beam with defect

The location of the surface bonded FBGs and their respective Bragg wavelengths for the healthy aluminium beam is given in Table 3.5 and photos of the experimental setup are shown in Figure 3.22.

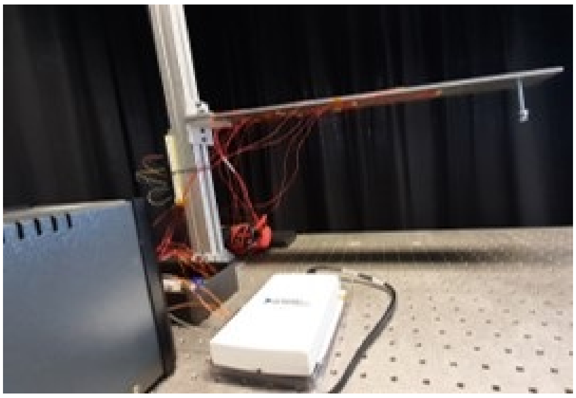

(a) side view

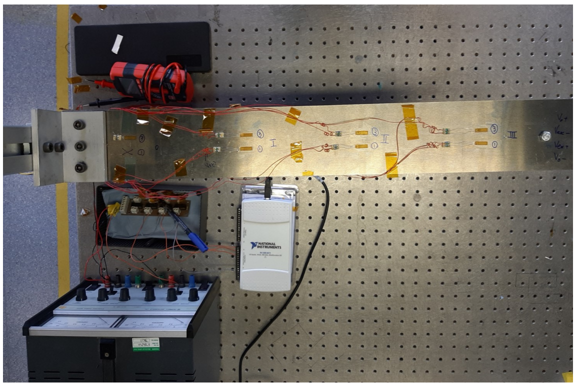

(b) top view

Figure. 3.22 Cantilever set up with Aluminium beam (a) side view (b) top view

Table 3.5 Sensing Location and FBG Wavelengths Healthy Aluminium Beam

Sensing Location	Distance from root	FBG sensor wavelength
A	400 mm	1530 nm
B	275 mm	1535 nm
C	150 mm	1540 nm
D	75 mm	1545 nm

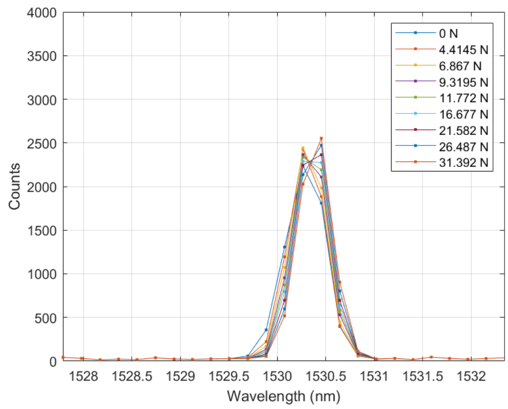

(a) Location A

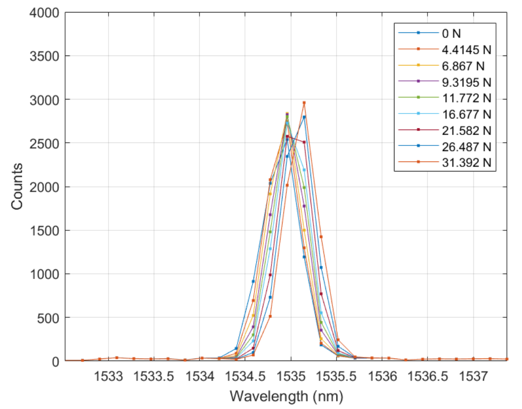

(b) Location B

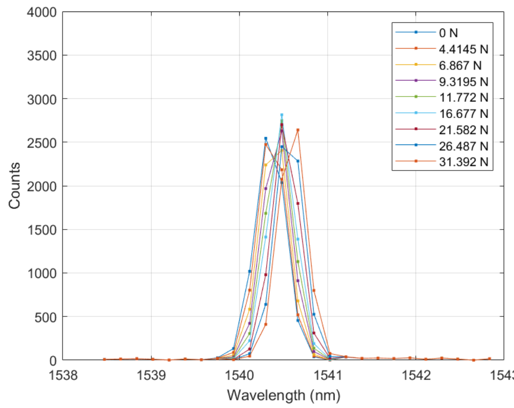

(c) Location C

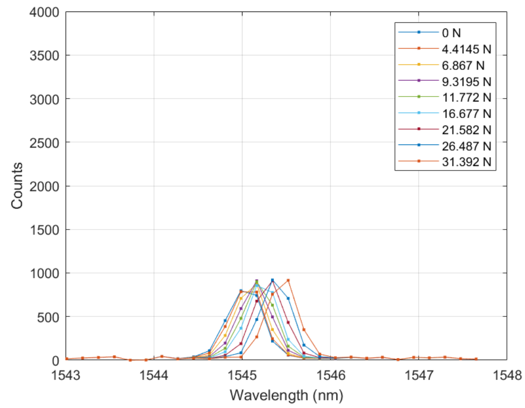

(d) Location D

Figure. 3.23 FBG Spectra for healthy Aluminium beam at (a) Sensing Location A (b) Sensing Location B (c) Sensing Location C (d) Sensing Location D

Figure 3.24 shows the strain measured by the FBGs from the static loading experiments and the strain estimated by the FEA simulations for that specific sensor location. Figure 3.23 shows the raw data spectra obtained from healthy Aluminium beam loading measurements. Here, it can be observed that FBG peaks are not smooth as they are limited by the measurement resolution. With the 1st order Gaussian fit however, this issue becomes resolved and the spectra becomes smoother and easier to estimate the Bragg wavelength. This is done for the FBG spectra for the defective beam and is shown in Figure 3.25.

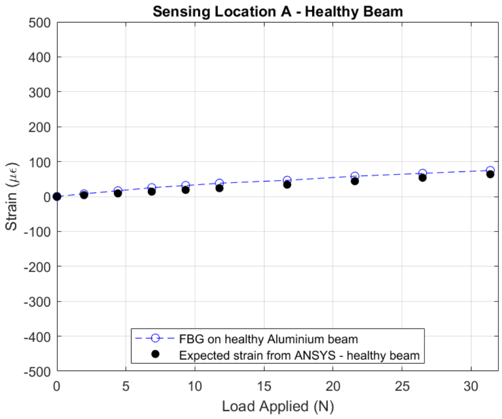

(a) Location A

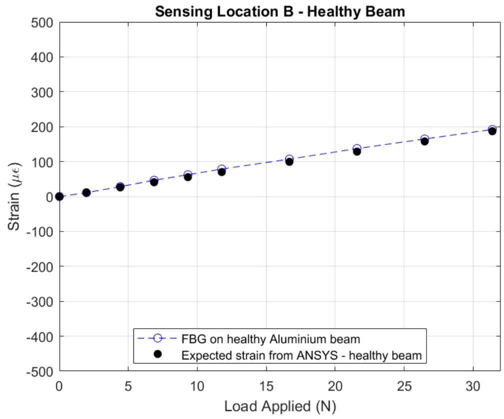

(b) Location B

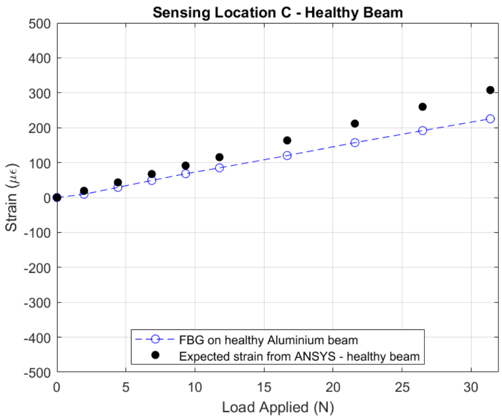

(c) Location C

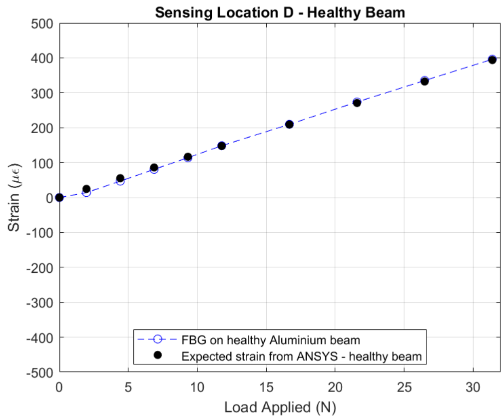

(d) Location D

Figure. 3.24 Measured vs expected strain for healthy Aluminium beam at (a) sensing location A (b) sensing location B (c) sensing location C (d) sensing location D

To accurately compare the strain sensed by the bonded FBGs with the simulated results, the strain values over the corresponding mounting locations were averaged over the bonded length. If the grating was mounted at 250 mm from the root, and the grating length was 10 mm, bonded at 15 mm on either sides, the strain expected from the ANSYS simulations were taken from 235 - 265 mm and then averaged so that a single strain value could be obtained. For each transverse load applied, multiple strain readings were taken by PC with the aid of the automated DAQ developed for the OSA therefore, those were averaged for the post processing. The measured strain of the FBG was determined from the estimated Bragg wavelength shift from the zero strain position to the strain position corresponding to the respective load applied. The automatic Gaussian fitting function developed in section 3.4 was used to accurately calculate the centroid wavelength shift. Based on the previous strain calibration experiment mentioned in subsection 3.5.1, a strain sensitivity value of 1.2 pm/ $\mu\varepsilon$

was used to estimate the strain in microstrain.

Table 3.6 Sensing Location and FBG Wavelengths Defective Aluminium Beam

Sensing Location	Distance from root	FBG sensor wavelength
A - bottom surface	79 mm	1545 nm
B - top surface	250 mm	1535 nm
C - bottom surface	250 mm	1560 nm

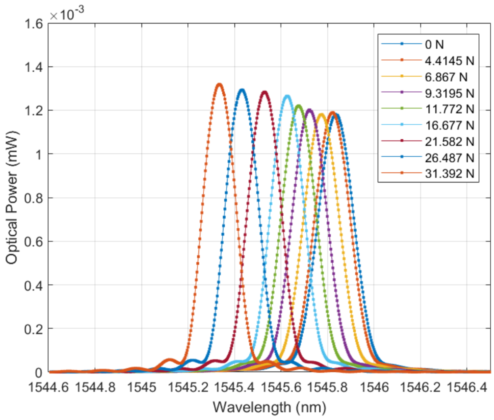

(a) Location A

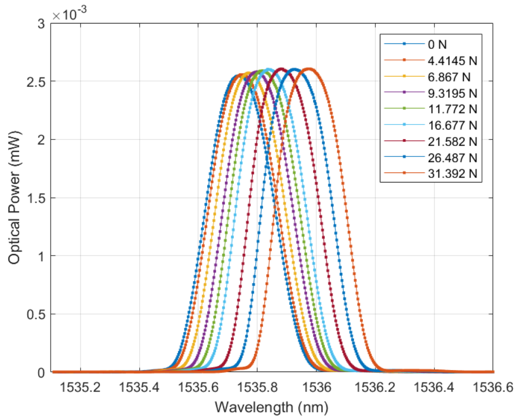

(b) Location B

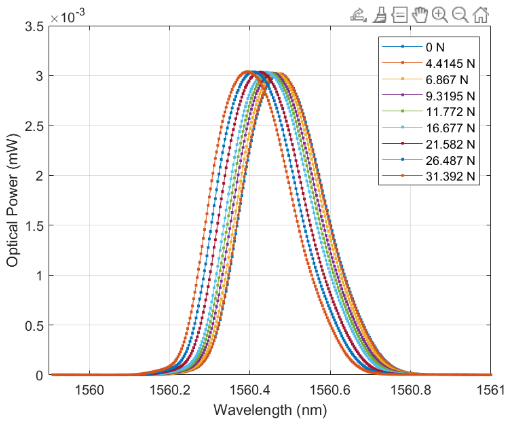

(c) Location C

Figure. 3.25 FBG Spectra for healthy Aluminium beam at (a) Sensing Location A (b) Sensing Location B (c) Sensing Location C

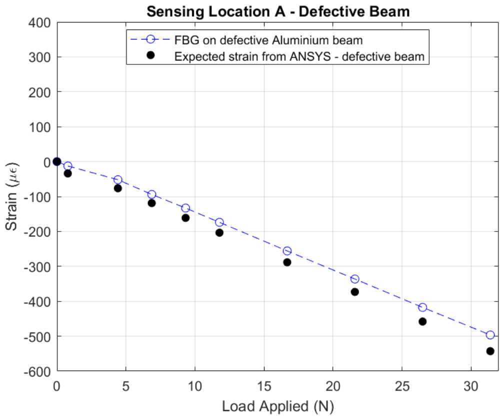

(a) Location A

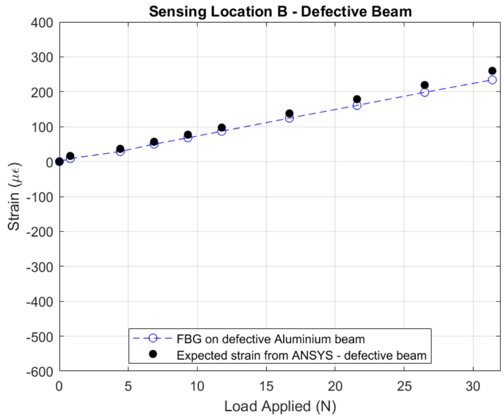

(b) Location B

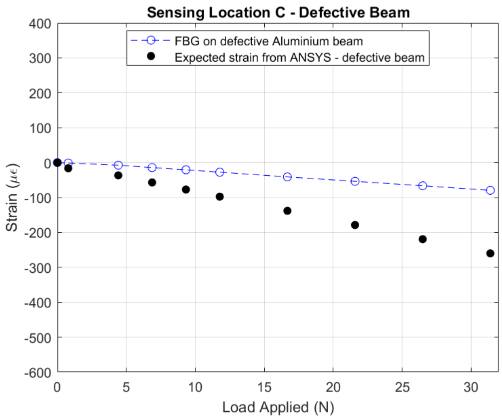

(c) Location C

Figure. 3.26 Measured vs expected strain for defective Aluminium beam at (a) sensing location A (b) sensing location B (c) sensing location C

Looking at the healthy beam results in Figure 3.24, it can be seen that measured FBG strains are almost perfectly linear and align with the expected results from the simulations. There are a few instances where the measured values deviate from the expected strains in, particularly at Location C at higher loads and this could be due to the fibre being slack more at those particular loads leading to a slight decrease in tensile strain. Comparing the defective beam's results i.e. measured FBG strain vs expected strain, it can be said that on the bottom of the defect, at location A, the FBG measures almost close to the expected strains for that location as shown in Figure 3.26 and the same observation can be made for the sensing location B. The sensing location C measures significantly lower strains compared to the expected values and this could be attributed to the slack in the fibre bonded at that particular location.

3.6.3 Tip Deflection: Aluminium Beams

The expected tip deflection taken from the simulations and the measured tip deflection for both the Aluminium beams with and without defect have been plotted in Figure 3.27. It can be seen that due to the defect being present, i.e. absence of material, the deflection of the defective beam is expected to be slightly higher than the defect-free healthy beam. Looking at the measured results, it can be said that the results for the healthy beam albeit being lower than the defective case, are not perfectly linear as expected.

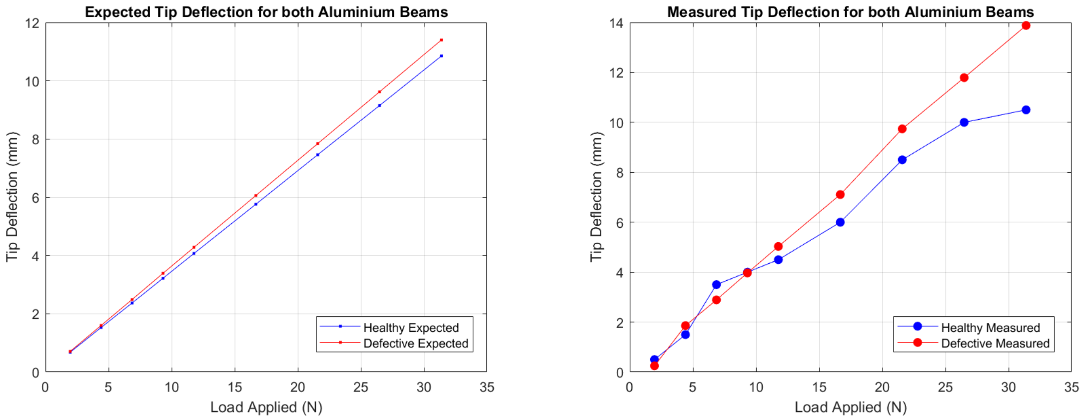

(a) Expected Tip Deflection (b) Measured Tip Deflection

Figure. 3.27 Comparison of tip deflection of both Aluminium beams (a) Expected (b) Measured

Comparing each beam expected vs measured results in Figure 3.66, it can be said that the measured values are higher than the expected values by a few millimetres in the defective case. This could be due to unsteady spring in the dial gauge, however, the measured values are not too far off and still indicates that due to the presence of a defect, the deflection would be higher at the tip.

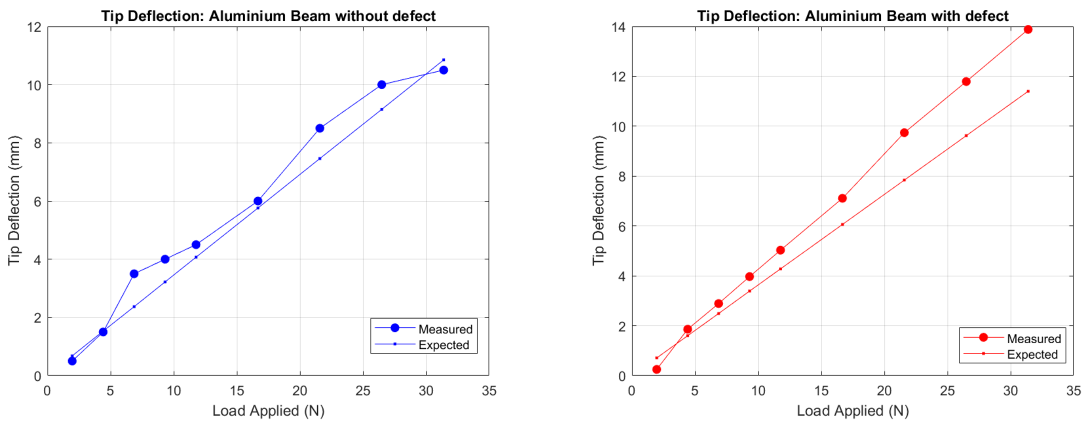

(a) Healthy Aluminium beam (without defect)   (b) Aluminium beam with defect

Figure. 3.28 Expected vs Measured tip deflection of Aluminium beam (a) without defect (b) with defect

3.7 FBG Strain Characterisation on Composite Beam With and Without Defect

Unlike the homogeneous material Aluminium (homogeneous in all three axes), characterising the FBGs for a composite defect is complicated. Blades are large scale, geometrically complex and constructed from composite materials with complex structural properties, making predictions of behaviour difficult. As a step towards studying defects on these structures, tests have been conducted on a composite cantilever beam with a known defect since the blades can be viewed as a beam-like structure from a numerical calculations' perspective as mentioned in Nicolas et al., 2016. The approach is very similar to the one discussed in section 3.6 where static loading tests have been conducted for two Aluminium beams; Here in this section 3.7, a "healthy" defect-free composite beam and a second beam with a known defect present were considered for FBG-Defect characterisation under static load tests. The strain measured by the FBGs bonded to the composite beams are compared to the strain estimated by the ANSYS simulations. The defect was pre-defined as a small resin-rich patch with reduced fibre-volume-fraction (FVF), i.e. modifying the composition of reinforcement (fibre) in the defect location, compared to the rest of the composite material.

In the above study utilising the Aluminium beams, the notch was an obvious defect which represents the absence of material and results in the high variation in strain compared to the healthy Aluminium beam. In the composite material beam however, the defect introduced is intended to be representative of any manufacturing induced defect or operational induced damage that results in a less-stiff material at the defect location. For example, Heinecke and Willberg, 2019 explore that, a dry spot or a void, both typically occurring at the manufacturing stage may be represented by this defect. Additionally, an impact damage on the blade during the operational phase of the turbine, which causes the impacted area to be less-stiff as discussed in Katsaprakakis et al., 2021, could also be represented by this defect. Hence, introducing a defect this way serves two main purposes: (1) represents a broad array of defects and operational damages which may result in a less-stiff material and (2) ease of testing the application of FBG sensor system in detecting the variation in strain due to the presence of the defect compared to the healthy beam case. The key assumptions here are, firstly that the healthy, defect-free composite beam is free of any manufacturing defects and is uniform, and the cured composite material is homogeneous in X and Y axes throughout the beam structure and secondly that the defective beam is also free of any variation in material properties and is homogeneous in X and Y axes of the beam, apart from the "defect" location which is introduced intentionally to test the FBG sensors. It should be noted that both healthy and defective composite materials considered are homogeneous in X and Y direction but non-homogeneous in Z direction due to the reinforcement (chopped strand fibre) lay-up. The X, Y and Z coordinate system considered for these beams are the same for both healthy and the defective beams and can be referred to in Figure 3.41 and Figure 3.42.

The predicted strain pattern was simulated by defining the composite material for the healthy (defect free) beam having a fibre-volume-fraction (FVF) of 0.491 while the defect was represented by a series of second composite material with reduced volume fraction of fibre representing the material of the defective area, these values are shown in Table 3.9. The calculation of these FVF values is explained in the following sections using Equation 3.24 - Equation 3.25. A series of finite element analysis (FEA) simulations were conducted for different transverse tip loads (0.7876 N - 11.772 N) in ANSYS Workbench. Both the beams were cast at the University of Hull composites laboratory and as explained in detail in subsection 3.7.2.

3.7.1 Composite Beam's Material and Stiffness Behaviour

Making a custom composite beam fundamentally requires predicting the elastic behaviour i.e. strain characteristics in the axial, transverse and torsional directions based on the material's mechanical properties which, in turn, depends on how much of its constituent materials are used i.e. amount of fibre reinforcement and matrix (epoxy). The reinforcement is usually designed to enhance the stiffness and strength of the matrix. (Clyne and Hull, 2019). Using this, the simplest way to estimate the elastic behaviour of the resultant composite is to consider it as a composite with aligned long (continuous) fibres. This essentially leads to high stiffness and strength in the direction of the fibre. For this section of the chapter, complete curing and perfect bonding at the reinforcement-matrix interface is assumed. Another assumption for the aligned long fibre composite is called the "slab model" where the resultant composite material can be treated as if the two constituent materials are bonded together in parallel with the relative thickness of each material is proportional to the volume fractions of the reinforcement (fibre) and the matrix. This is illustrated in the following Figure.

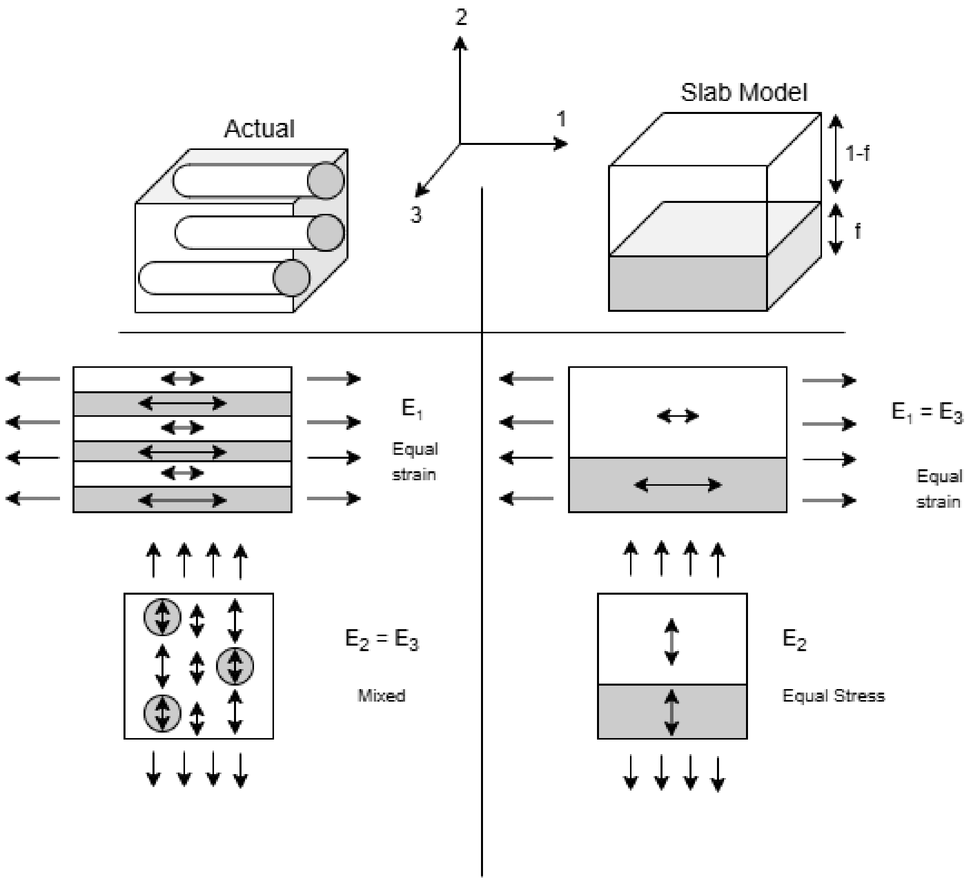

Figure. 3.29 Schematic Illustration of loading geometry and distributions of stress and strain for the slab model representation - source: Clyne and Hull, 2019

To derive the Young's modulus of the composite, the following equations from Clyne and Hull, 2019 have been applied. The axial strain in the fibre and the matrix must correspond to the ratio between the stress and the Young's modulus for each of the two components hence this can be represented by Equation 3.10. The overall composite stress can be expressed as shown in Equation 3.11 where the fibres are much stiffer than the matrix $(E_{\mathrm{f}} >> E_{\mathrm{m}})$ and the reinforcement bears a much higher stress than the matrix $(\sigma_{\mathrm{f}} >> \sigma_{\mathrm{m}})$. A table of symbols used in these equations and their description is given in Table 3.7.

Table 3.7 Table of Symbols: Composite Manufacture

Symbol	**Description**
ε_{f}	Strain of fibre
ε_{m}	Strain of matrix
ε_{c}	Strain of resultant composite
$\mathrm{E_f}$	Young's Modulus of fibre
$\mathrm{E_m}$	Young's Modulus of matrix
$\mathrm{E_c}$	Young's Modulus of resultant composite
σ_{f}	Stress of fibre
σ_{m}	Stress of matrix
σ_{c}	Stress of resultant composite
f	Volume of fibre
1-f	Volume of matrix
FVF	Fibre-Volume-Fraction
w_c	Weight of composite
w_f	Weight of fibres
w_m	Weight of matrix
W_f	Weight fraction of fibre
W_m	Weight fraction of matrix

$$\varepsilon_c = \varepsilon_{\mathrm{f}} = \frac{\sigma_{\mathrm{f}}}{E_{\mathrm{f}}} = \varepsilon_{\mathrm{\ m}} = \frac{\sigma_{\mathrm{\ m}}}{E_{\mathrm{m}}} \tag{3.10}$$

$$\sigma_{\mathrm{c}} = (1-f)\sigma_{\mathrm{m}} + f\sigma_{\mathrm{f}} \tag{3.11}$$

With these two equations derived, the Young's modulus of the composite can be written as Equation 3.12. Using the ratio between the stress in the two constituents, this can be further simplified in to Equation 3.13. This well-known "rule of mixtures" from Clyne and Hull, 2019 indicates that the composite stiffness can be defined as weighted mean between the Young's moduli of the two components i.e. fibre and matrix, and this depends only on the volume fraction of fibres. With the equations derived and resultant composite material's Young's modulus in the axial direction, similar approach was followed for derivation for the strain transverse directions, density, Poisson's ratio.

$$E_c = \frac{\sigma_{\mathrm{c}}}{\varepsilon_{\mathrm{c}}} = \frac{(1-f)\sigma_{\mathrm{m}} + f\sigma_{\mathrm{f}}}{\sigma_{\mathrm{f}}/E_{\mathrm{f}}} = E_{\mathrm{f}}\left[\frac{(1-f)\sigma_{\mathrm{m}}}{\sigma_{\mathrm{f}}} + f\right] \tag{3.12}$$

$$E_{\mathrm{c}} = (1-f)E_{\mathrm{m}} + fE_{\mathrm{f}} \tag{3.13}$$

Before the composite beams with and without defect can be manufactured, a few additional validations were conducted. The key point is that with a presence of the composite defect, the neutral axis will shift from a uniform beam case along with the cross-sectional properties i.e. second moment of area about the X-axis, denoted by I_{xx} and second moment of area about the Y-axis, denoted by I_{yy} will change resulting in the change in expected strain over the defect. To evaluate this, the defect was defined as mentioned in section 3.7, where a small resin-rich (low in fibre reinforcement) patch with reduced stiffness selected to be on top of the beam with half the depth of the composite beam. Next, the fibre-volume-fraction (FVF) for the healthy composite beam and the defective composite beam were defined based on the composition of the materials required, geometry and the dimension of the defined defect. In this case, both beams were 550 mm in length, with 75 mm width and a thickness of 6 mm. The defect was defined as follows. 20 mm in length, 15 mm in width and with a thickness of 3 mm. With these parameters defined, the following equations for surface strain, location of neutral axes, I_{xx} and I_{yy} and were estimated for both the healthy and the defective composite beams.

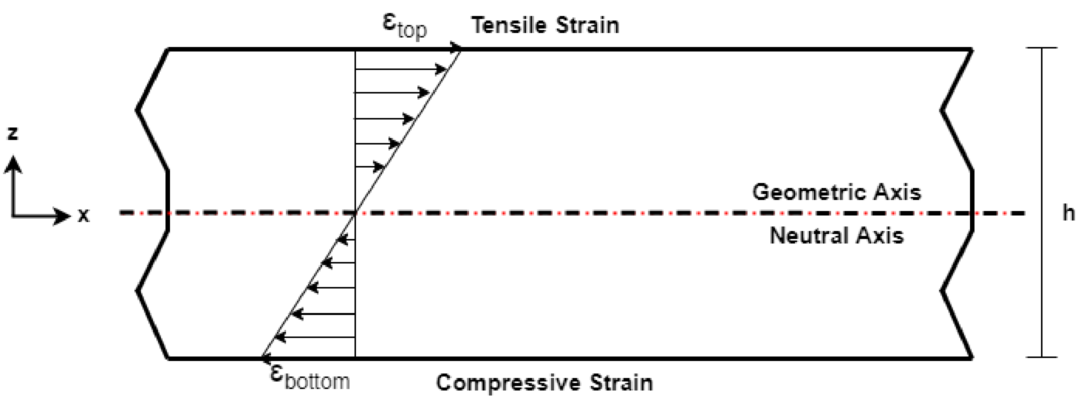

Figure. 3.30 Strain distribution through uniform, homogeneous composite cantilever beam in Z-X plane

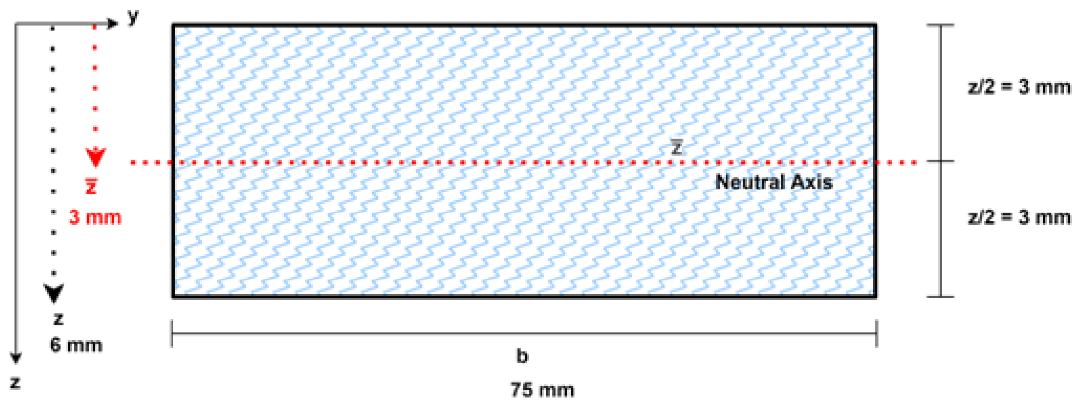

Figure. 3.31 Cross section of uniform, homogeneous composite cantilever beam in Z-Y plane

For a homogeneous, uniform composite beam, the neutral axis, I_{xx} and I_{yy} and the surface strain can be determined in a straightforward manner using the equations below. Figure 3.30 and Figure 3.31 show the schematic used for these estimations. The following equations are standard derivations taken from (Craig Jr and Taleff, 2020) for rectangular beams.

$$\varepsilon_{\text{top}} = \frac{Fl\bar{z}}{EI} \tag{3.14}$$

$$I = \frac{bh^3}{12} \tag{3.15}$$

$$I_x = \frac{bh^3}{12} \text{ and } I_y = \frac{b^3h}{12} \tag{3.16}$$

For the healthy composite beam, applying these equations gives:

$$I_x = \frac{bh^3}{12} \text{ and } \text{ mm}^4, \quad I_y = 210,937.5 \text{ mm}^4 \tag{3.17}$$

For the defective composite beam, however, these equations are no longer directly applicable due to the non-uniform material distribution. Instead, a sectional analysis was performed, dividing the beam's cross-section into four regions for calculating the new neutral axis location and updated I_{xx} and I_{yy} values. The neutral axis was found to shift downward from 3 mm (for the healthy case) to 3.26 mm due to the reduced stiffness in the defective region:

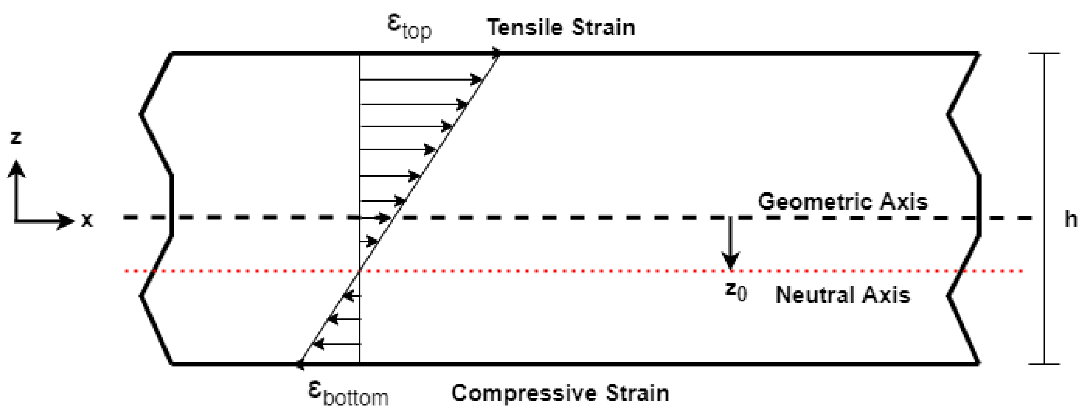

Figure. 3.32 Strain distribution through non-uniform, heterogeneous composite cantilever beam

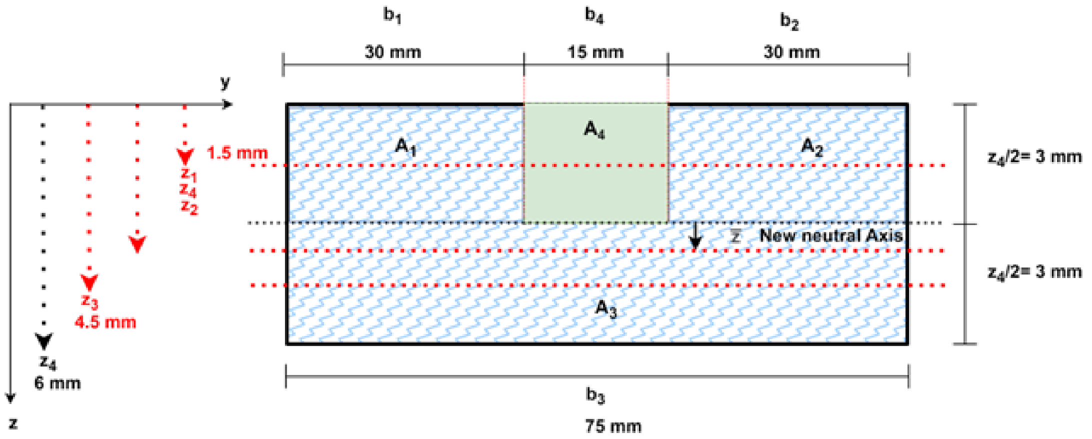

Figure. 3.33 Cross Section of non-uniform, heterogeneous composite cantilever beam through Z-Y plane

Table 3.8 Geometry specification of defective composite beam

	Part 1	Part 2	Part 3	Part 4 (defect)
Breadth (mm)	b1 = 30	b2 = 30	b3 = 75	b4 = 15
Height (mm)	h1 = 3	h2 = 3	h3 = 3	h4 = 3
Neutral axis (mm)	z1 = 1.5	z2 = 1.5	z3 = 1.5	z4 = 4.5
I_{xx} mm^4	$I_{xx}1$ = 347.93	$I_{xx}2$ = 347.93	$I_{xx}3$ = 334.08	$I_{xx}4$ = 313.3
I_{yy} mm^4	$I_{yy}1$ = 7030.43	$I_{yy}2$ = 7030.43	$I_{yy}3$ = 105,746.58	$I_{yy}4$ = 2723.62
Total thickness	z = 6 mm			
Ratio between the two Young's moduli	n = 11.602 GPa / 4.1914 GPa = 2.768			

$$\bar{z} = \frac{A_1 z_1 + A_2 z_2 + A_3 z_3 + n\left(A_4 z_4\right)}{A_1 + A_2 + A_3 + nA_4} \tag{3.18}$$

$$\bar{z} = 3.2652mm \tag{3.19}$$

Using this adjusted neutral axis, the revised second moments of area were calculated as:

$$I_{\text{total },xx} = 1343.24 \text{ mm}^4 \tag{3.20}$$

$$I_{\text{total },yy} = 122,531.06 \text{ mm}^4 \tag{3.21}$$

These values provide key insights into how stiffness properties change due to the defect and offer a reference for understanding the variations in strain distribution over the defective region. The derived parameters serve as a basis for evaluating stiffness-related effects and could be further applied in detailed structural analyses.

3.7.2 Composite Beam Manufacture

With the equations derived, the manufacturing and casting of the composite beams were first tested using 3-D printed PLA mould. These practise runs served as a way of perfecting the composite casting method and identifying the required tools and techniques needed for a effective moulding and demoulding process. Figure 3.34 shows the computer aided design (CAD) done using Solidworks for the 3D printed mould and the top (lid) and bottom parts 3D printed PLA mould as well as the composite beam made using this mould. Here, it can be seen that the sides of the composite beam have come out covering and sticking to the sides as random, uneven pieces of chopped strand fibre were used and this trial composite beam requires trimming. Hence as a solution to eliminate the need for trimming which may result in uneven edges of the beam, the chopped strand mat was measured and cut to match the geometry of the beam.

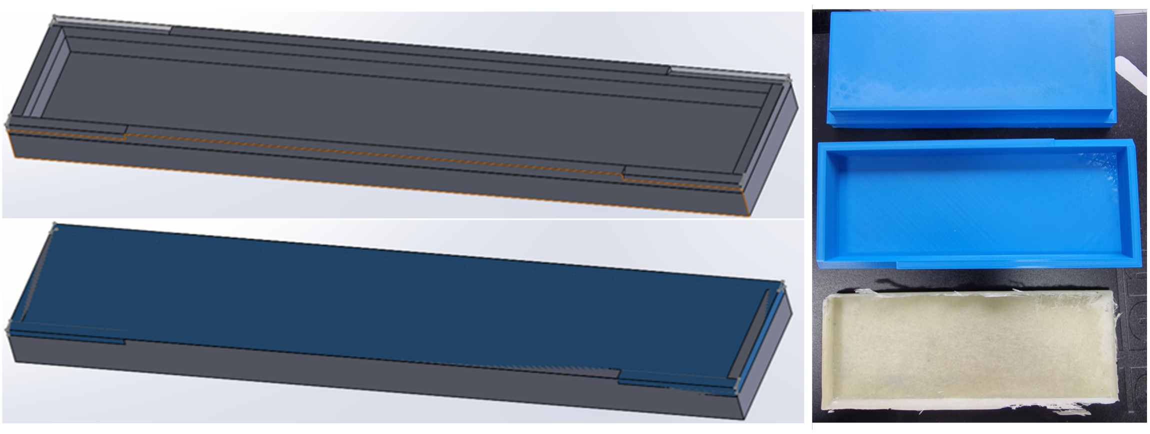

Figure. 3.34 CAD model and 3D printed PLA mould

Once these practice test runs were successful, the actual manufacture and casting of both the composite beams were done using an Aluminium mould. The convenience of using this mould, was that the mould could be assembled and de-assembled for the purpose of making the composite and after curing, de-moulding the composite respectively. For this purpose, the aluminium mould was designed in Solidworks (See Figure 3.35) and was then machined off and manufactured at the mechanical workshop at the University of Hull. The parts of the de-assembled aluminium mould are shown in Figure 3.36. Assembly was complete with the mould parts screwed in place. The methodology followed for the casting was wet-laying the chopped strand mats and using the laminating resign purchased form Easy Composites, UK (Composite, 2022). To prepare for the wet-laying process, the chopped strand fibre mats were measured and cut into the required dimension in multiple layers and weighed. For the defective composite beam, half of the layers were kept as they were and for the other half of the layers, the defect area were cut out from the mats using a box cutter knife for precision. The aluminium mould was cleaned with ethanol thoroughly of dust and debris, then mould release liquid was painted five times totally in 30 minutes intervals leaving each layer of mould release to dry off. The two part epoxy component was mixed with the hardener at appropriate ration, in this case, 100 parts of epoxy resin to 30 parts of fast-type-hardener. As the fast hardener was used, the entire wet-laying process had to be fast as the hardener starts reacting and accelerates the curing process in about 30 minutes after mixing with the epoxy.

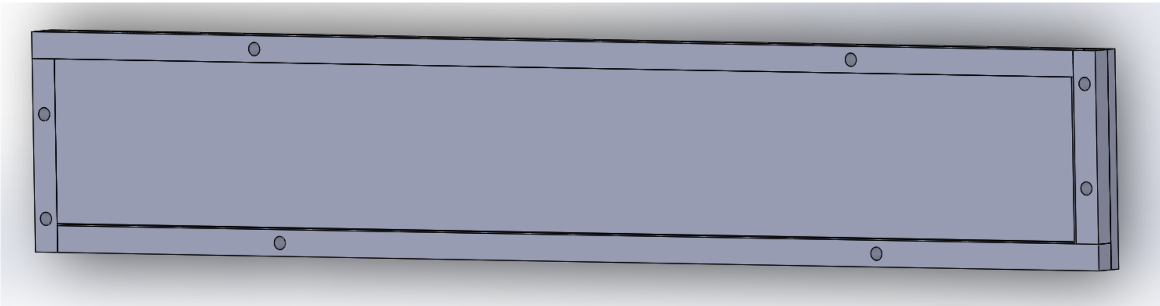

(a) CAD model top view

(b) CAD model bottom view

Figure. 3.35 CAD model for the Aluminium casting mould (a) top view (b) bottom view

Figure. 3.36 Aluminium mould used for composite beam casting

Figure. 3.37 Chopped strand fibre layers with defect area cut out

Figure. 3.38 Wet-laying composite beam: mould with chopped strand and resin

Figure. 3.39 Aluminium mould clamped to the table with weights on top

The wet-laying process involved placing each layer of reinforcement fibre and then pouring some of the resin in to the mould. A small brush was used to spread the resin across the entire layer and to the corners of the mould. For the healthy composite beam, this process was repeated for each layer until the number of reinforcement fibre layers were finished, making sure that each layer is fully coated and drenched with the epoxy resin. As depicted in Figure 3.38 to fabricate the composite beam with the defect, the first half the reinforcement fibre layers were wet-laid using the same method as the healthy case and then the remaining reinforcement fibre layers with the defect area cut out were used in the same manner. Finally, the remaining resin was poured on top, and the mould lid was placed on top and the mould was screwed in tight and sealed in. Additionally, to make sure that the lid on top was laying flat and sealed properly, weights were placed on top and the entire mould was wrapped in vacuum bag and then using a 3 G clamps, it was clamped to the table top. This is shown in Figure 3.39.

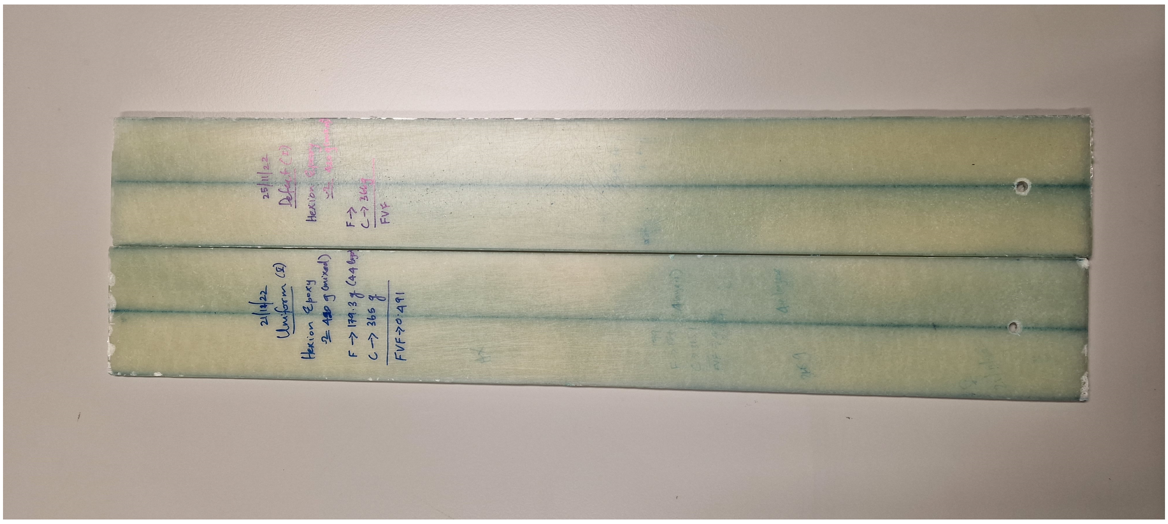

Figure. 3.40 Cured composite beams: Defect-less and Defective beam

$$W_f = \frac{w_f}{w_c} \tag{3.22}$$

$$W_m = \frac{w_m}{w_c} \tag{3.23}$$

$$w_c = w_f + w_m \tag{3.24}$$

$$FVF = \frac{w_c - w_m}{w_c} \tag{3.25}$$

To determine the final fibre-volume-fraction (FVF) of the resultant composite beam, the weight of the total fibreglass layers was measured pre-casting and the weight of the final cured composite beam was measured. With this, the weight of the cured, hard resin can be found out. Using these values, based on equations from Gikunoo, 2019 and Jones, 2018, the final FVF can be determined (refer equation above). For this calculations, it is assumed that there are no voids in the resultant cured composite beam. These were determined and the values were then included for the calculations in subsection 3.7.1.

3.7.3 Numerical analysis of composite defects with varying volume fraction

The analysis of the composite beam depends on the assumptions about the manufacturing process of the laboratory scale beam for experimental work. For example, it is assumed that the composite beam made without any intentional defect ("healthy" composite beam) is actually defect-free and the material stiffness is homogeneous throughout the beam and that the composite beam with the "defective" area is also homogeneous apart from the "defective" area which was introduced intentionally. In order to maintain the integrity of the research, it is important to keep these assumptions as realistic as possible. The manufacturing process of the composite beam discussed above gives rise to a few uncertainties regarding the true stiffness value of the resultant composite material which has been produced. Observing the scale of the defective area, which is pre-determined to be 20 mm long x 15 mm wide x 3 mm deep, in a 600 mm long x 75 mm wide x 6 mm deep rectangular beam, precise control of the manufacture of the defect is difficult and uncertain. Keeping the layers of chopped strand reinforcement in place without wrinkling and bending to maintain the through thickness uniform in the healthy beam is comparatively straightforward. However, in the defective region, because there is a gap and the chopped strand layers discontinue at the defect location, keeping them in place without the layers moving or shuffling during the casting procedure is tricky. Moreover, the size of the defect gives rise to its edges being frayed and for the chopped strand to stick out into the defective region. Consequently, the amount of fibre reinforcement within the defect location becomes unreliable and needs validation to determine its fibre composition. Nevertheless, any fraying leading to uncertainty is contained within the defective region, with the fraying roughly accounting for 1 mm, and its effect being mostly concentrated along the defective edge rather than significantly affecting the entire defective region. However, when considering the fibre volume fraction (FVF) of the entire defective region, the overall reduction remains consistent with the intended modification. While local variations may exist due to fraying at the defect edges, these effects are minimal and do not significantly alter the average FVF of the defective area.

Due to the limitation of the laboratory facilities, i.e. unavailability of conducting a computed tomography (CT) scan on a component of this size, as well as restriction on availability of reinforcement and matrix material, to verify whether these assumptions are logical/ practical, a comparison study of the beam with different stiffness models at the defect have been conducted numerically using ANSYS. This was carried out so that both beams that were manufactured could be used for the experiments without needing to produce multiple composite beams. For this, FEA simulations were done using six different composite materials as defined in the Table 3.9. The composite material 1 was the material chosen for the healthy beam case with homogeneous material all around the beam and FVF of 0.491. The subsequent composite materials 2 - 6 were considered for the defective beam case where the FVF has been modified leading to modified stiffness at the defect location predefined in the beam geometry. For all the cases considered, apart from the defective location, the rest of the beam consisted of the unmodified composite material (composite material 1 with nominal stiffness value) throughout the beam. This is illustrated in the Figure 3.58 and in Figure 3.54. Detailed explanation on the FEA simulations conducted and the theoretical analysis of the composite beams considered are given in the next section.

3.7.4 Theoretical Analysis of Composite Beam - ANSYS Workbench

The geometry of both composite beams with and without defect were modelled in ANSYS workbench using Spaceclaim. The first beam used for the test without any defect ("Healthy case") had no structural deformities and was 550 mm long, 6 mm thick and 75 mm wide. Similarly, the composite beam with known defect was designed to have the same length, thickness and width but an area/ volume of 20 mm (length) x 3 mm (thickness) x 15 mm (width) with the material with reduced stiffness was introduced ("Defective case"). This defect was modelled to be at the top surface 80 mm from the root where the beam was clamped. Figure 3.41 shows the defect on the top surface of the beam. Additional construction lines and points were drawn on top and bottom surface of the beams covering various lengths to investigate the strain profile further.

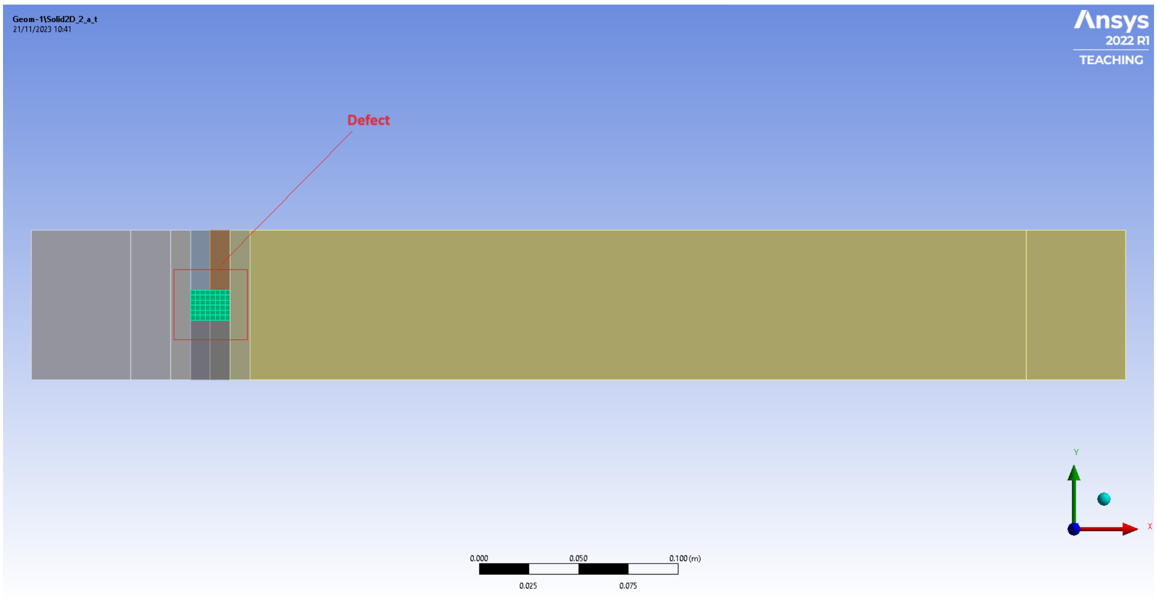

Figure. 3.41 Defective Composite Beam with defect on top highlighted in green

For the FEA simulations of the composite beam with and without the defect, six custom materials were defined in the engineering data section of the ANSYS workbench software. For the fault-free composite beam, properties of a resultant composite material where the FVF is 0.491 i.e., 49.1% glass to 50.9% resin by volume were used using the equations from Gikunoo, 2019 and Jones, 2018 depicted in subsection 3.7.2 - this is mentioned as Composite Material 1 in Table 3.9. As chopped strand glass was used for the experiments, the elastic properties of the composite used in the FEA simulations were assumed to be isotropic and homogeneous in all directions. For the localised defect defined as a 20 mm x 15 mm x 3 mm deep patch within the composite beam, the same composite material where the stiffness is reduced by certain percentages were used (resin-rich, n% less glass) - these are mentioned as Composite Materials 2,3,4–6 in the same table. The rest of the beam/ the area without the defect or reduced FVF was designed with the healthy case's material previously defined. Detailed properties of these materials used are given in Table 3.9.

Table 3.9 Material properties of the composite beam specimen

	Composite Material 1	**Composite Material 2**	**Composite Material 3**	**Composite Material 4**	**Composite Material 5**	**Composite Material 6**	**Unit**
Description	healthy	defective					
Material	chopped strand and resin						
% of FVF modified	—-	80% reduced	85% reduced	90% reduced	95% reduced	100% reduced	
FVF	0.4910	0.0982	0.0737	0.0419	0.0246	0.0000	
Density	1520.1	1304	1290.5	1273	1263.5	1250	kg/m^3
Isotropic Elasticity							
Derived from	Young's Modulus and Poisson's Ratio						
Young's Modulus	1.16E+10	5.12E+09	4.72E+09	4.19E+09	3.91E+09	3.50E+09	Pa
Poisson's Ratio	0.3407	0.3721	0.3741	0.3766	0.3780	0.3800	
Bulk Modulus	1.21E+10	6.67E+09	6.24E+09	5.66E+09	5.33E+09	4.86E+09	Pa
Shear Modulus	4.33E+09	1.87E+09	1.72E+09	1.52E+09	1.42E+09	1.27E+09	Pa

With the geometry and material selection defined for both the composite beams, a series of FEA simulations were conducted for different transverse tip loads applied. These were 0.7876 N, 4.4145 N, 6.867 N, 9.3195 N, 11.772 N. These were representative of the weights applied experimentally starting from 0.08 kg, 0.45 kg, 0.7 kg, 0.95 kg and 1.2 kg. Figure 3.42 shows the "cantilevered" composite beam with the root clamped and the location and the direction where the force is applied as defined in ANSYS Mechanical. Within the same ANSYS module, meshing was done by dividing the beam into several sections or parts and assigning a mesh method and size for those different sections separately.

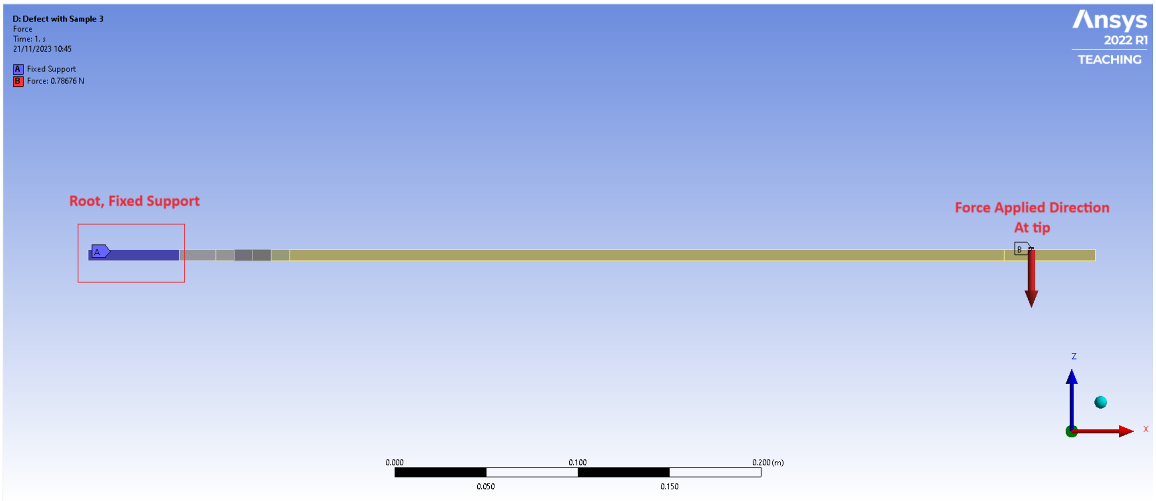

Figure. 3.42 Locations of fixed support at root and force applied at tip

In Figure 3.43, it can be seen that for the fixed support/ root, the mesh is quite coarse as the strain profile for that particular section was not of interest for this investigation. For this root/ fixed supports section an element size of 0.002 m was selected and for the rest of the beam including the defect, an element size of 0.001 m was used. By defining a small element size, the localised variations in strain could be looked into in detail along with the added construction paths solved for strain distribution. It should be noted that for the healthy beam case, the same meshing method was applied so the results from both the beam cases can be compared while only the material of the defect has changed. Altogether, both beams were meshed with 1715793 elements. Results obtained from this analysis are discussed below.

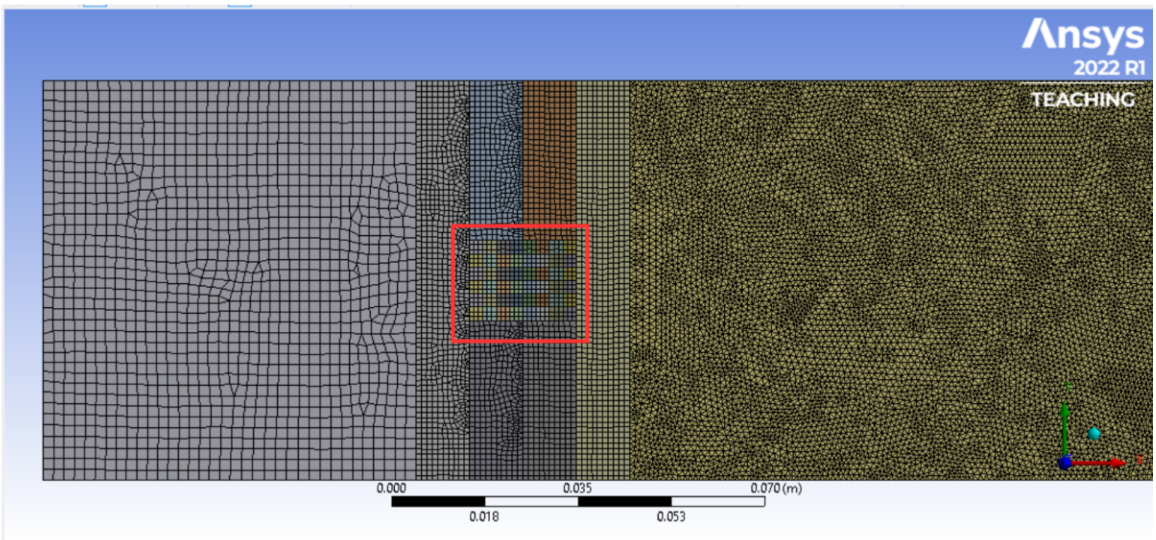

Figure. 3.43 Composite beam mesh for defect marked with red rectangle

Results obtained from the top and bottom middle line of the both beams are shown in Figure 3.49a and Figure 3.49b below. The location of these lines in the beam is shown in Figure 3.44 and Figure 3.45 below. As the first 50 mm of the beam was for section that was clamped at the root, the strain for the first 50 mm was zero in all loading cases for both composite beam cases considered. The peaks shown at 515 mm indicates the point where the force was being applied.

Comparing the first loading case 0.7876 N, the elastic strain along the middle line of the top surface of the healthy beam, indicated by continuous blue line in Figure 3.49a and the red dashed line for the same loading case showing the results from the defective composite beam clearly illustrates a significant change in strain pattern at the location of the defect. Due to the reduced stiffness in the defect area, at the boundary of the defect, precisely at the starting point 80 mm, a small dip and a sharp increase in strain followed by a broader dip ranging over the length of the defect can be seen. At the other boundary of the defect, i.e., ending point 100 mm, another sharp increase followed by a small dip was observed. From about 100 mm up to 515 mm (loading point), the strain behaviour is quite as expected for a cantilevered beam. This behaviour can be repetitively seen in the other loading cases as well, except at the defect location, the significant change or the sharp rise in strain is larger and is in proportion to the force being applied. The dips near the first and last boundary of the defect are larger (20 mm and 100 mm respectively, length-wise) as well as the dips in between those two points of interest. Apart from the first loading case, for the rest of the loads, comparing the distribution of elastic strain across the beam from 100 mm to 515 mm, the defective composite beam measures lower strain compared to the healthy composite beam. the irregular lines can be attributed to the way the meshing was done using tetrahedron method and the shift from hex-based mesh to tetrahedrons can also be clearly seen at 110 mm.

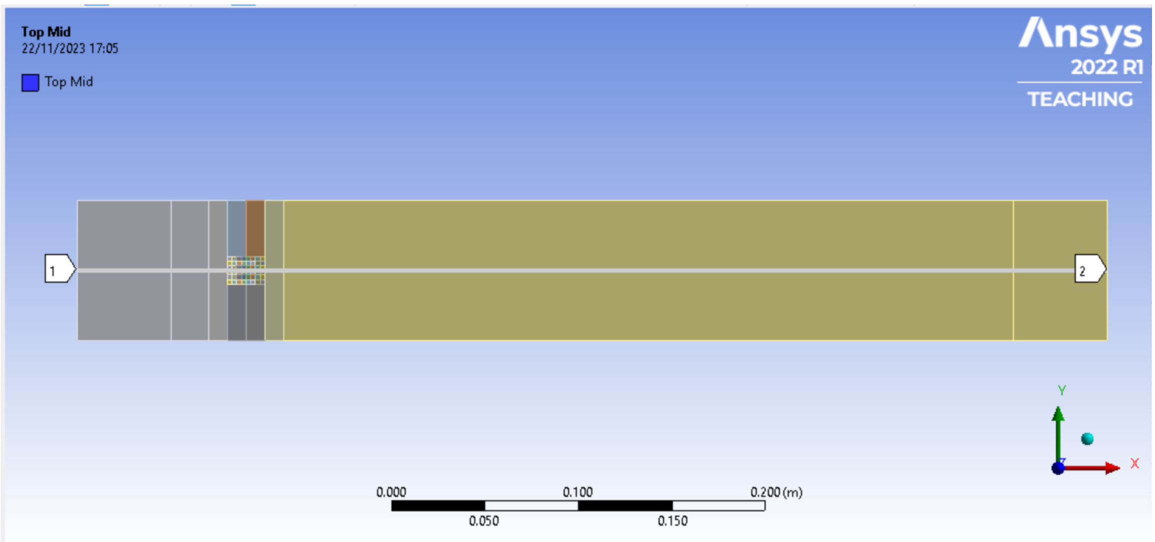

Figure. 3.44 Construction path modelled on top of beam for elastic strain analysis

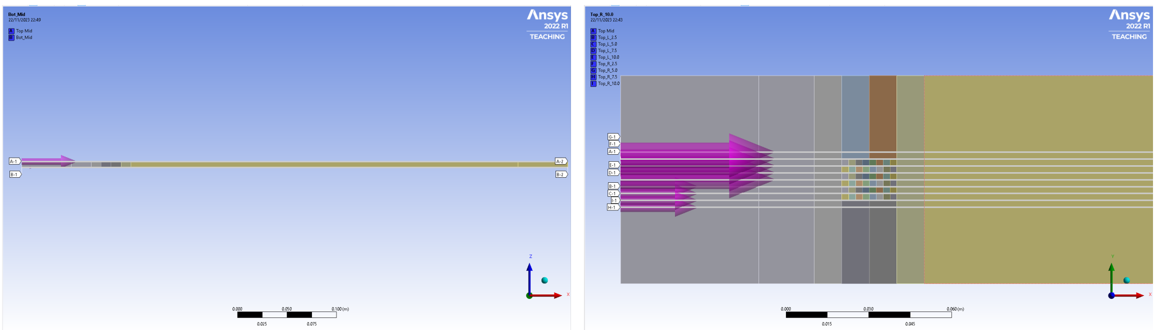

(a) Construction paths modelled on top and bottom of beam

(b) Construction Paths at various distances from middle line

Figure. 3.45 Construction path modelled on (a) top and bottom of beam (b) at various distances from middle line, for elastic strain analysis

The surface strain on top of the beam for the healthy and defective composite beams considered under varying static tip loads have been plotted and are compared below.

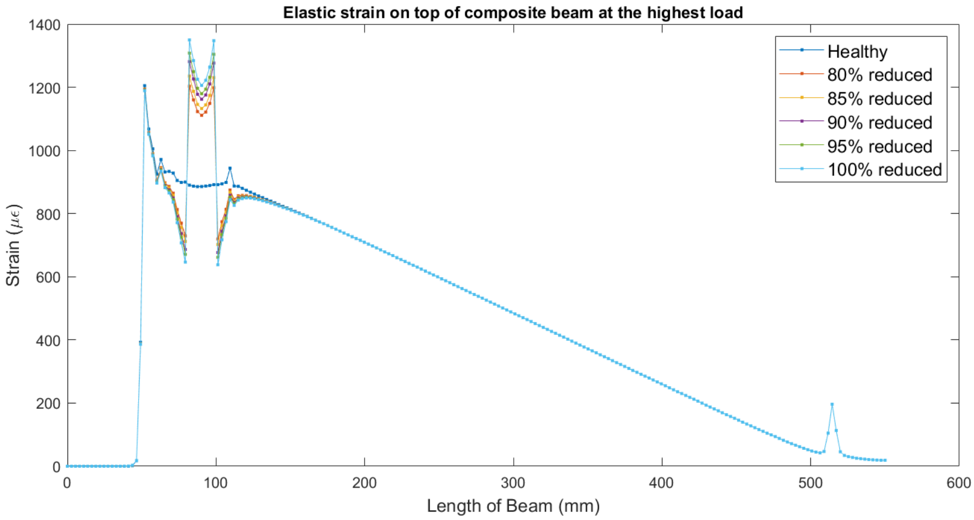

(a) Elastic strain for entire beam span

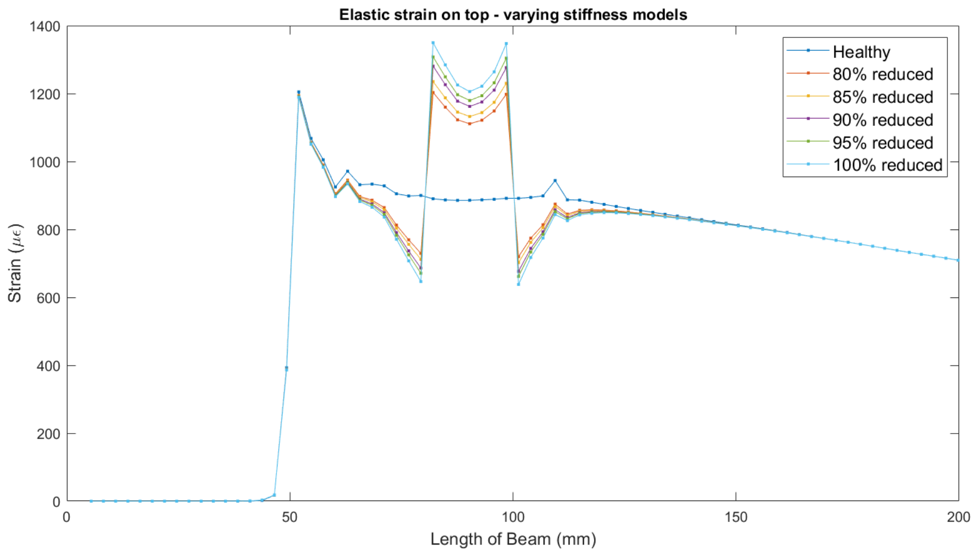

(b) Elastic strain for x = 0-200 mm

Figure. 3.46 Elastic strain on top of composite beams of varying stiffness at 11.772 N tip load (a) for entire beam span (b) for x = 0-200 mm

Looking at the above Figure 3.46, it is evident that, except for the healthy beam case, the elastic strain on the top surface of the beam increases as the fibre volume fraction (FVF) reduction in the defective region becomes more severe. Specifically, the beam with a 100% fibre-free, resin-rich patch (100% FVF reduction) in the defective region exhibits the highest strain values, with a strain difference of approximately 100–150 $\mu\varepsilon$ compared to the 95% FVF reduction case around the defect location. Similarly, the 95% FVF reduction case shows higher strain than the 90% FVF reduction case, with strain differences of about 70–100 $\mu\varepsilon$. This trend continues across the other cases, with changes in strain values decreasing as the FVF reduction becomes less pronounced. The strain variations are most prominent near the defect edges, highlighting the localised impact of FVF reduction.

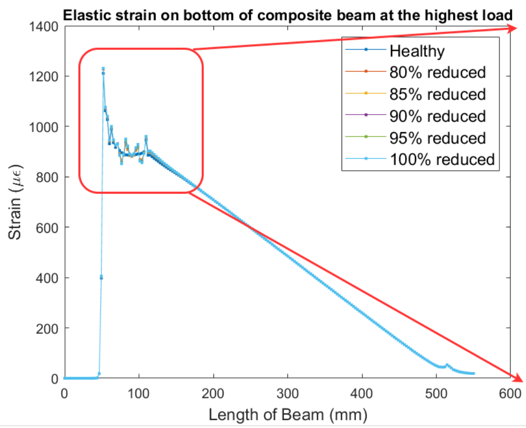

(a) Elastic strain on bottom middle surface covering entire span of beam

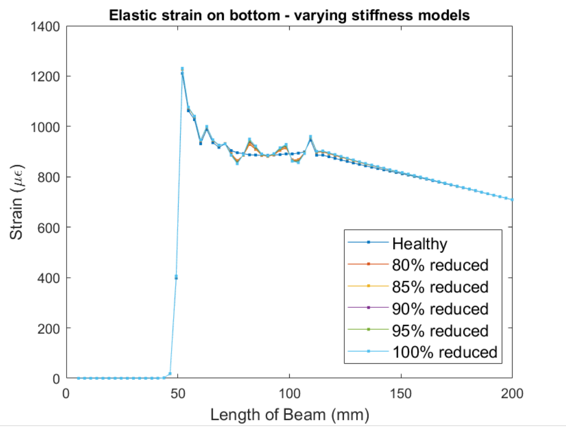

(b) Elastic strain on bottom middle surface covering the first 200 mm of beam

Figure. 3.47 Elastic strain on bottom for 11.772 N tip load - varying stiffness models

Figure 3.47 shows the elastic strain distribution along the bottom surface of the composite beam under the highest applied tip load. The strain is plotted for various stiffness reductions in the defective region, and it is evident that the strain values remain relatively unchanged across the bottom surface. This suggests that, unlike the top surface, which experiences more significant strain changes due to bending tension and the presence of the defect, the bottom surface is less affected by stiffness reductions. The strain distribution on the bottom is mostly consistent across all cases, indicating that defects in the top surface of the beam have minimal impact on the bottom surface strain compared to the top surface.

The divergence in strain between the healthy beam and the defective beams in the figure likely arises from the differences in stiffness. The healthy beam retains its full material stiffness, leading to a more uniform strain distribution. In contrast, the defective beams, with reduced stiffness (due to defects like voids or resin-rich patches), experience localised stress concentrations, altering the strain pattern. These stiffness reductions cause changes in the overall strain distribution, particularly where defects are present, and result in the healthy beam having higher strain in certain areas. This behaviour is consistent with findings in other composite material studies i.e. as discussed in Schubel and Crossley, 2012 and Jensen et al., 2023, where even small stiffness reductions can cause significant shifts in strain distribution due to localised material degradation and non-uniform stress under load.

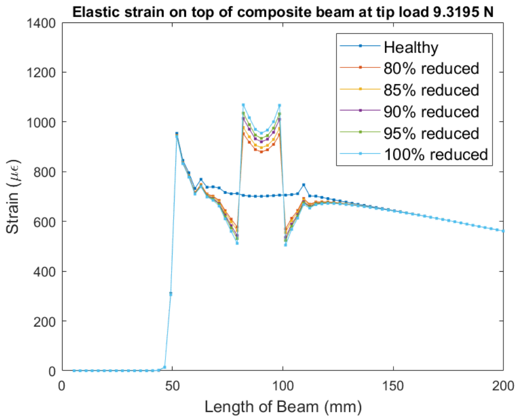

(a) at 9.3195 N

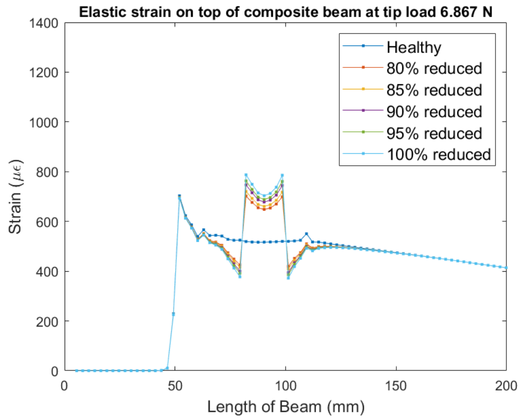

(b) at 6.867 N

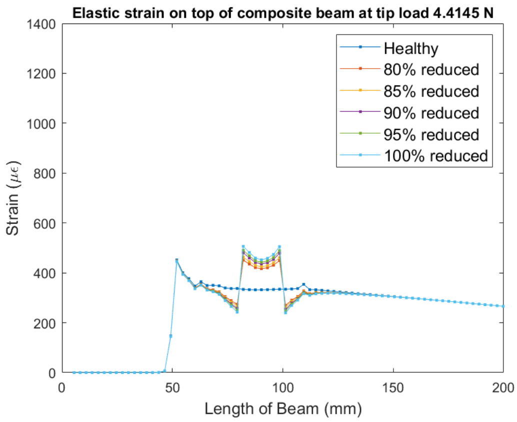

(c) at 4.4145 N

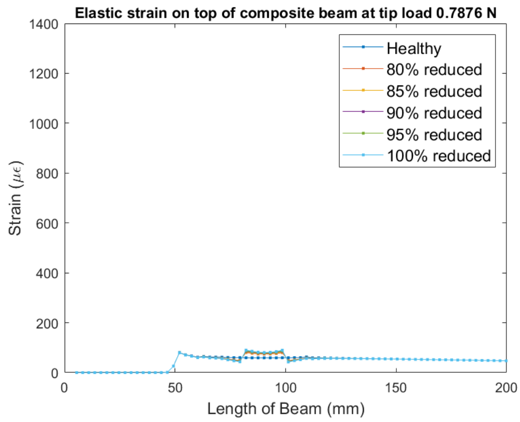

(d) at 0.7876 N

Figure. 3.48 Elastic strain on top of composite beam for x = 0-200 mm at (a) 9.3195 N (b) 6.867 N (c) 4.4145 N (d) 0.7876 N tip loads

Figure 3.48 shows the elastic strain on top of the different composite beams, both healthy and defective cases at various tip loads. The strain distribution at the highest tip load applied is given in Figure 3.46b. The aim here is to determine the impact of varying fibre volume fraction (FVF) reductions within the defective region on the elastic strain distribution of the composite beams. To account for uncertainties in the exact FVF of the defective location, an average FVF reduction is considered for the defective area. Based on the strain measurements, the defective region is assumed to have approximately 90% reduced FVF compared to the healthy composite material. For instance, at the highest tip load applied (11.772 N), the strain difference at the defect location (80–100 mm lengthwise) between the 100% FVF reduction case (1011 $\mu\varepsilon$) and the 80% FVF reduction case (975 $\mu\varepsilon$) is only 36 $\mu\varepsilon$. Similarly, at the lowest tip load (0.7876 N), this difference reduces further to just 2.4 $\mu\varepsilon$. This small variation in strain values across defective cases, as depicted in Figure 3.46b, indicates that the defective area's strain response is relatively consistent, even when the FVF reduction varies. Consequently, an average FVF reduction of 90% is used to represent the defective area for further analysis.

The surface strain on top of the beam for the healthy composite beam case under varying static tip loads have been plotted along with the strain obtained from the average 90% defective case and are compared below. Here in the comparison figure below, it can be seen that the strain away from the defect (from 100 mm - nearly 500 mm from the defect) in the non-defective regions are almost the same in both the healthy and the defective beam cases. With the same FEA parameters selected for the non-defective regions in both beam cases, i.e. material properties (Young's modulus, Poisson's ratio and density), mesh properties (element size, density and type), applied load, boundary conditions and fixed support, the primary differences in strain can be attributed to the presence of the defect, leading to localised strain concentration and load redistribution i.e. effect of defect can be seen clearly. This also reinforces the significance of considering structural defects and discontinuities in FEA simulations, as their effects propagate either side of the defect location as well, i.e. near 80 mm and 100 mm.

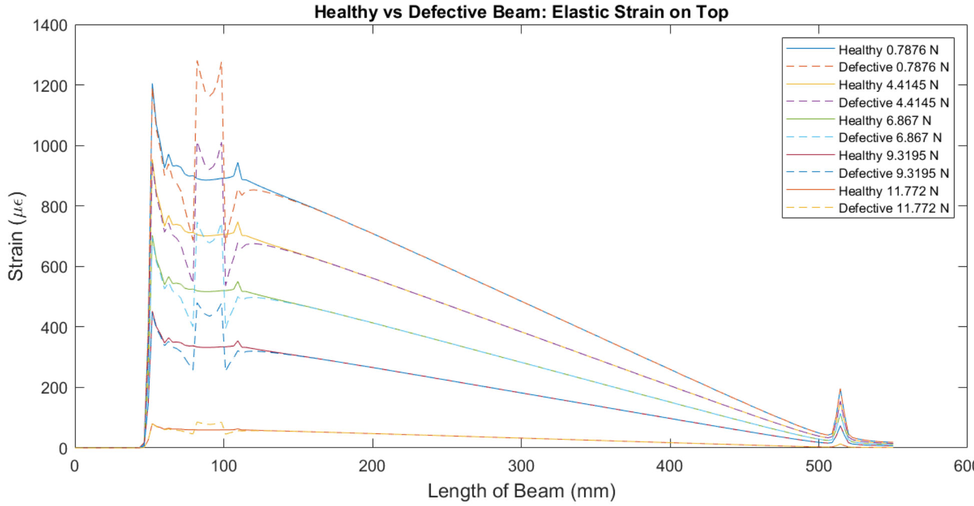

(a) top surfaces of both beams

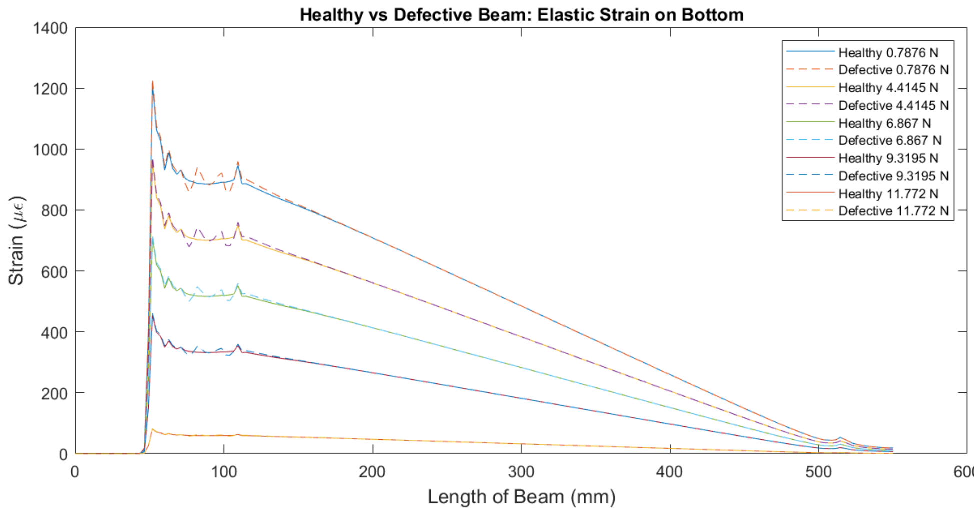

(b) bottom surfaces of both beams

Figure. 3.49 Compressive strain on both beams (a) top surface (b) bottom surface

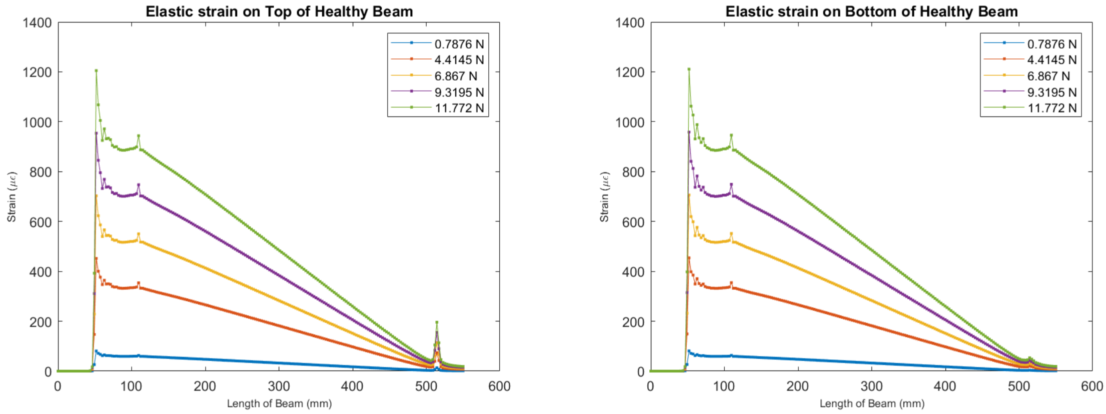

(a) on top surface (b) on bottom surface

Figure. 3.50 Compressive strain on healthy beam (a) top surface (b) bottom surface

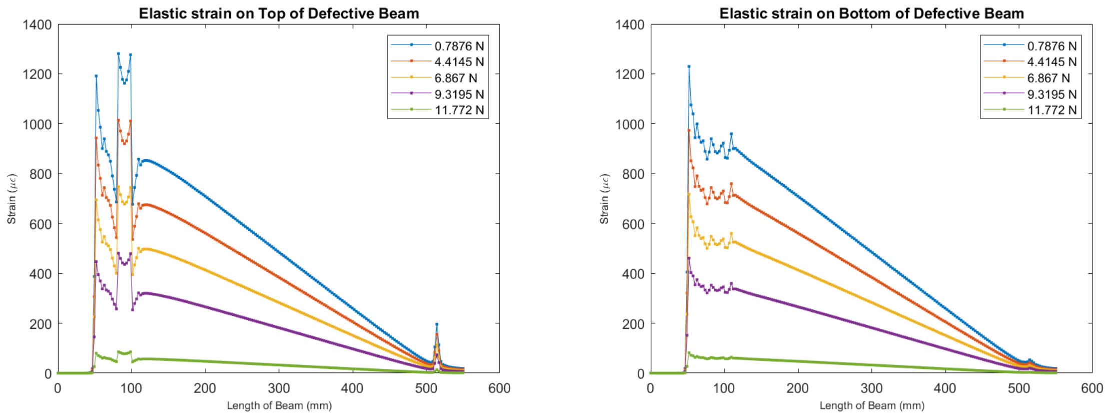

(a) on top surface (b) on bottom surface

Figure. 3.51 Compressive strain on defective beam (a) top surface (b) bottom surface

Using the additional construction path modelled (See Figure 3.45), further analysis regarding the location of the defect i.e. strain profile at locations away from the defect and the centreline was carried out.

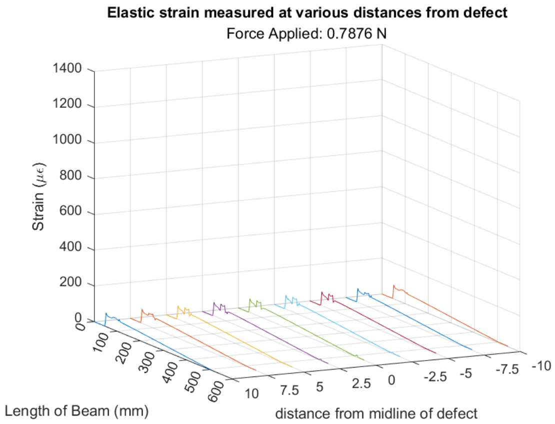

(a) at 0.7876 N

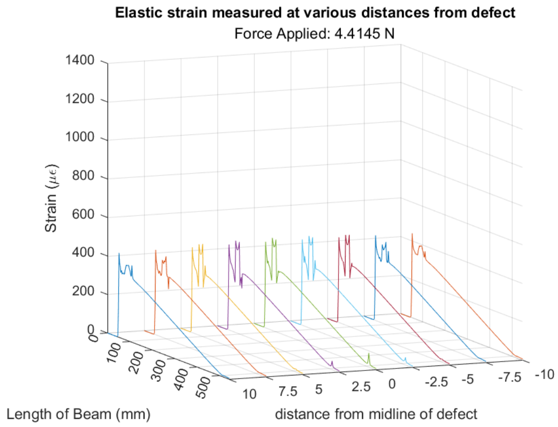

(b) at 4.4145 N

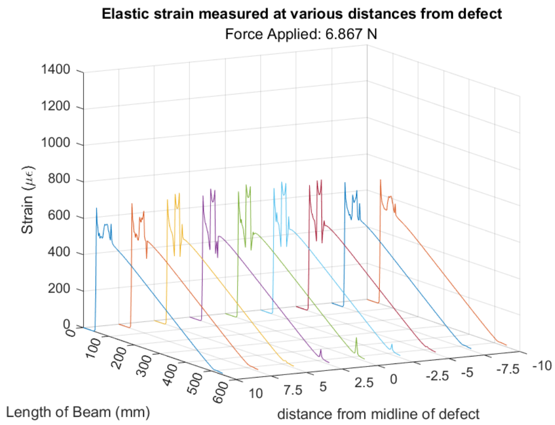

(c) at 6.867 N

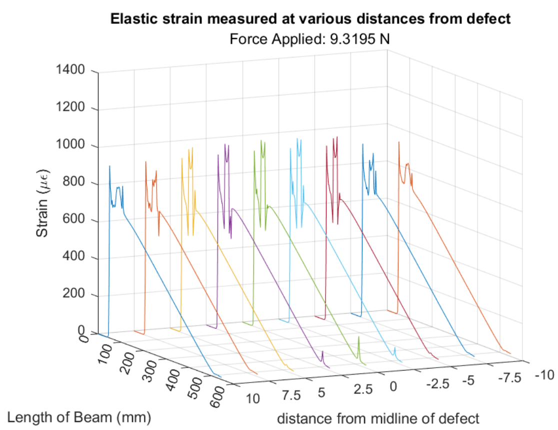

(d) at 9.3195 N

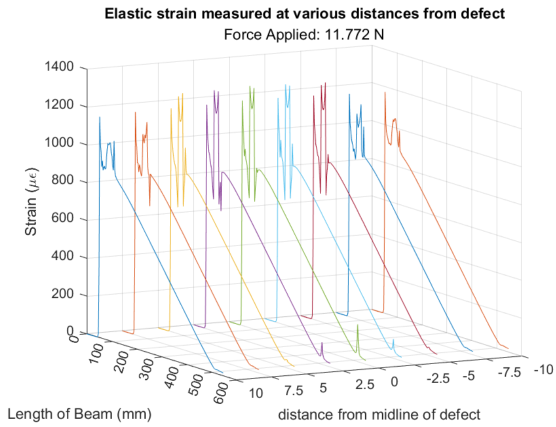

(e) at 11.772 N

Figure. 3.52 Elastic strain measured at various distances from defect at (a) 0.7876 N (b) 4.4145 N (c) 6.867 N (d) 9.3195 N (e) 11.772 N on top of the beam

Figure 3.52 depict the results in three- dimensional axis where in addition to the top surface strain distribution for the overall length of beam, results from each construction path at various distances from the middle line of the defect on the beam have been plotted. Zero distance plots in green indicates the middle line of the defect which is also the middle line of the beam. For each graph, at zero distance from the defect, it can be seen that the force applied is represented by a sharp peak at 515 mm of the beam. A slight effect of this can be seen at 2.5 mm from the defect, however, for the rest of the distance from the defect on either side, this effect disappears as expected. For each set of distances from the defect, i.e. 10 mm on either side, 7.5 mm on either side, and 5 mm, the strain pattern from 80 mm - 100 mm of beam length are symmetric as expected but as one moves close to the edge of the defect, the strain profiles are smoother with smaller peaks and dips. A similar observation can be made for the Figure 3.53, where the bottom surface strain is plotted, again for the middle line of the beam and various distances away from the middle line of the beam, at both left and right of the line.

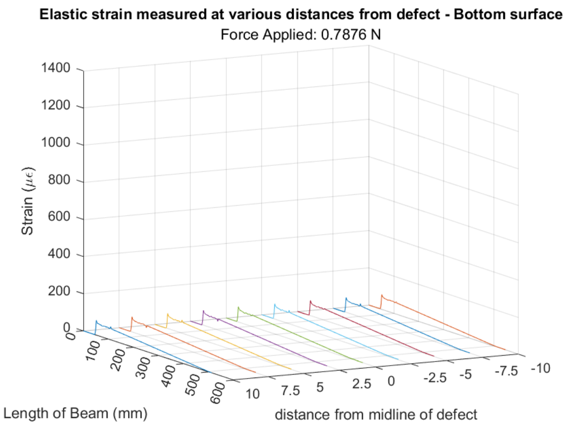

(a) at 0.7876 N

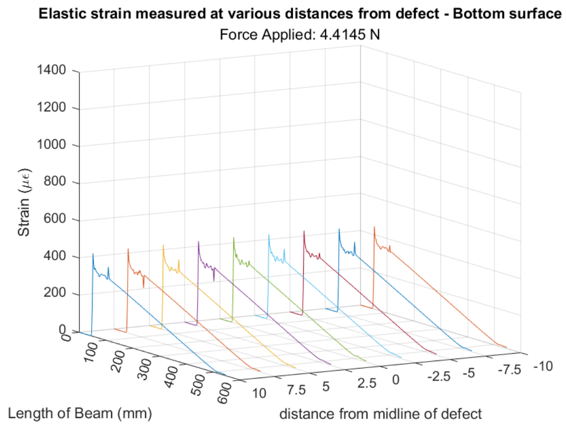

(b) at 4.4145 N

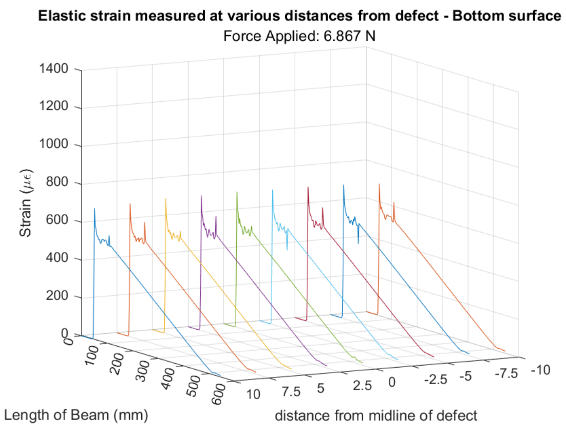

(c) at 6.867 N

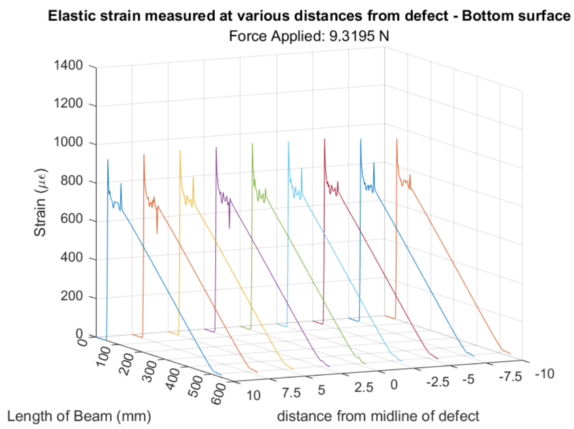

(d) at 9.3195 N

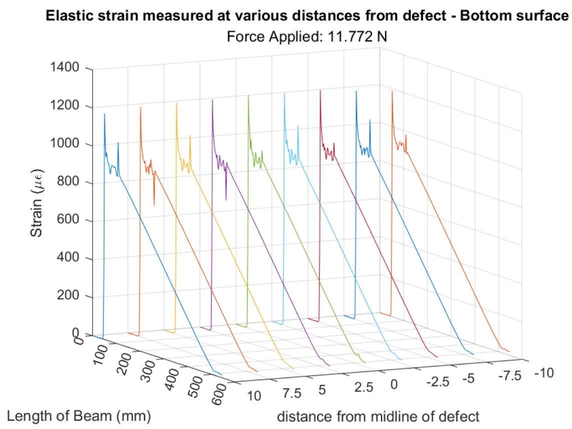

(e) at 11.772 N

Figure. 3.53 Elastic strain measured at various distances from defect at (a) 0.7876 N (b) 4.4145 N (c) 6.867 N (d) 9.3195 N (e) 11.772 N on the bottom of the beam

3.7.5 Experimental Analysis of Composite Beam

Looking at the schematic Figure 3.54 and the Figure 3.49a, where the strain profile over the defect has been plot, the trend shows that the stiffer material (composite material with FVF 0.491 throughout the beam - i.e. the healthy beam case) does not extend/ undergo strain a much at the edge of the defect and the softer material (with reduced stiffness) moves more. This indicates that the measured strain for the defective beam depends on where the sensor is bonded over the defective region and how long that sensor is.

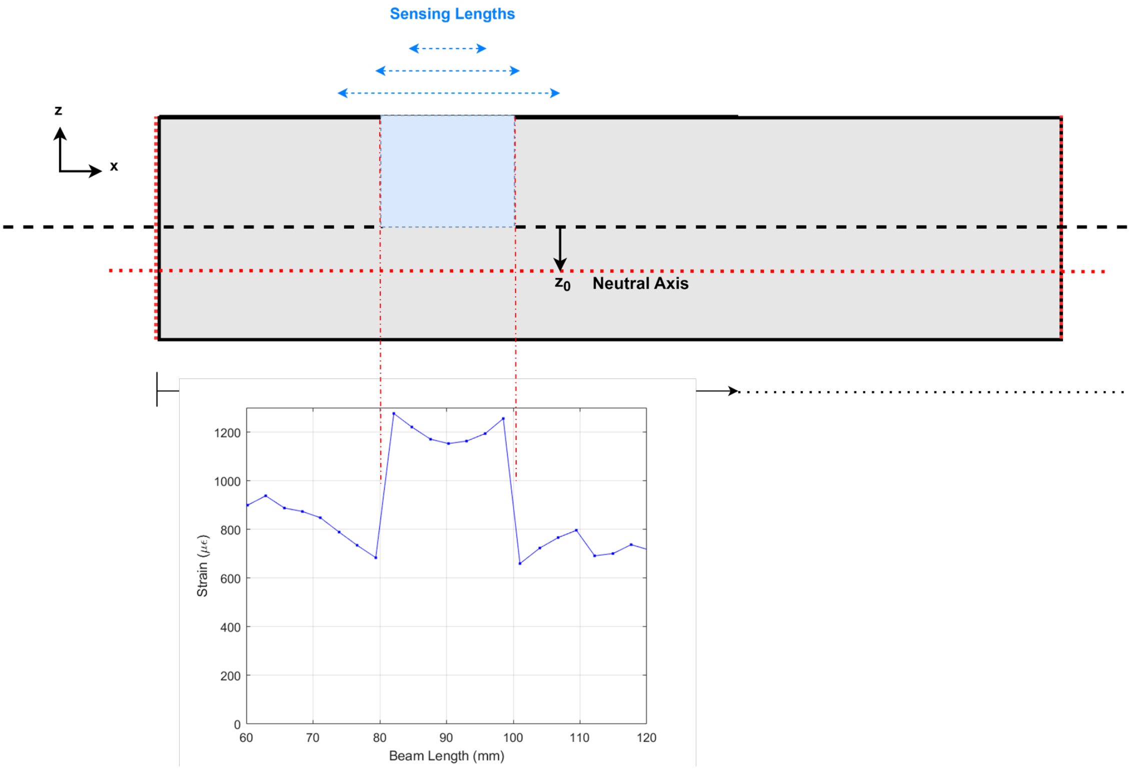

Figure. 3.54 Schematic diagram of composite defect and strain profile over the defect

For the experimental analysis of the FBG strain characterisation on composite beams, altogether 4 DTG-FBG sensors were bonded to the top and bottom surfaces of the composite beam. Figure 3.55 shows the defect on the composite beam and Figure 3.56 shows the experimental setup used for both the beams, cantilevered and clamped and the FBGs connected to the beam. The bonding was done similar to the previous approach i.e. if the grating is 10 mm, the sensor was bonded at 15 mm from either side of the centre of the grating making this a bonded length/ sensing length of 25 mm.

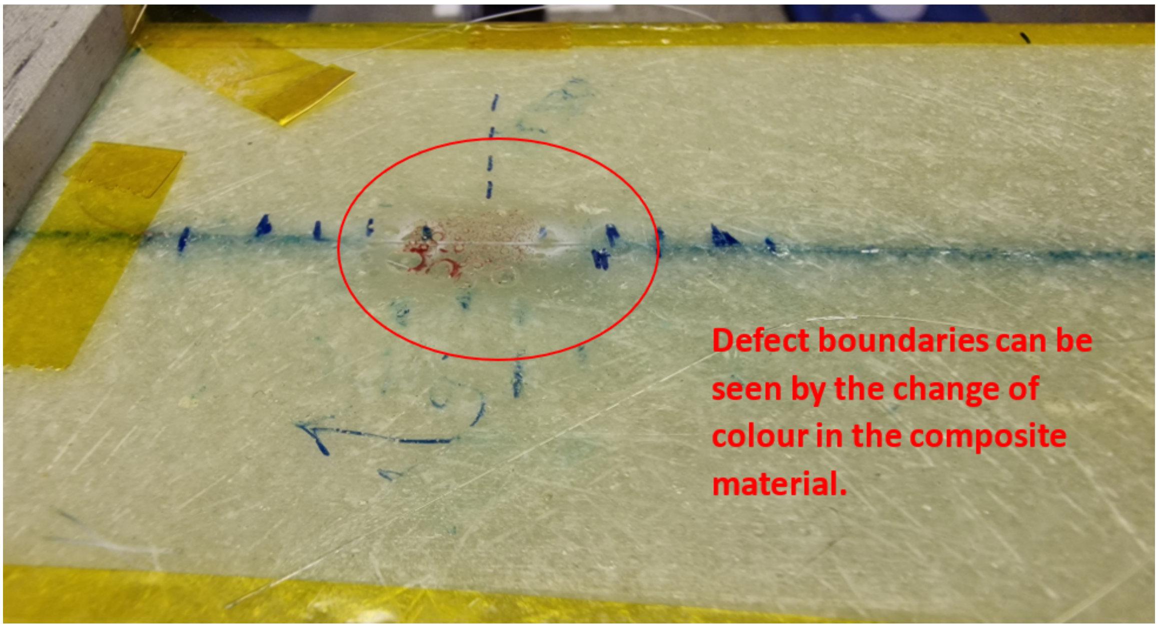

Figure. 3.55 Defect on top surface of the composite beam

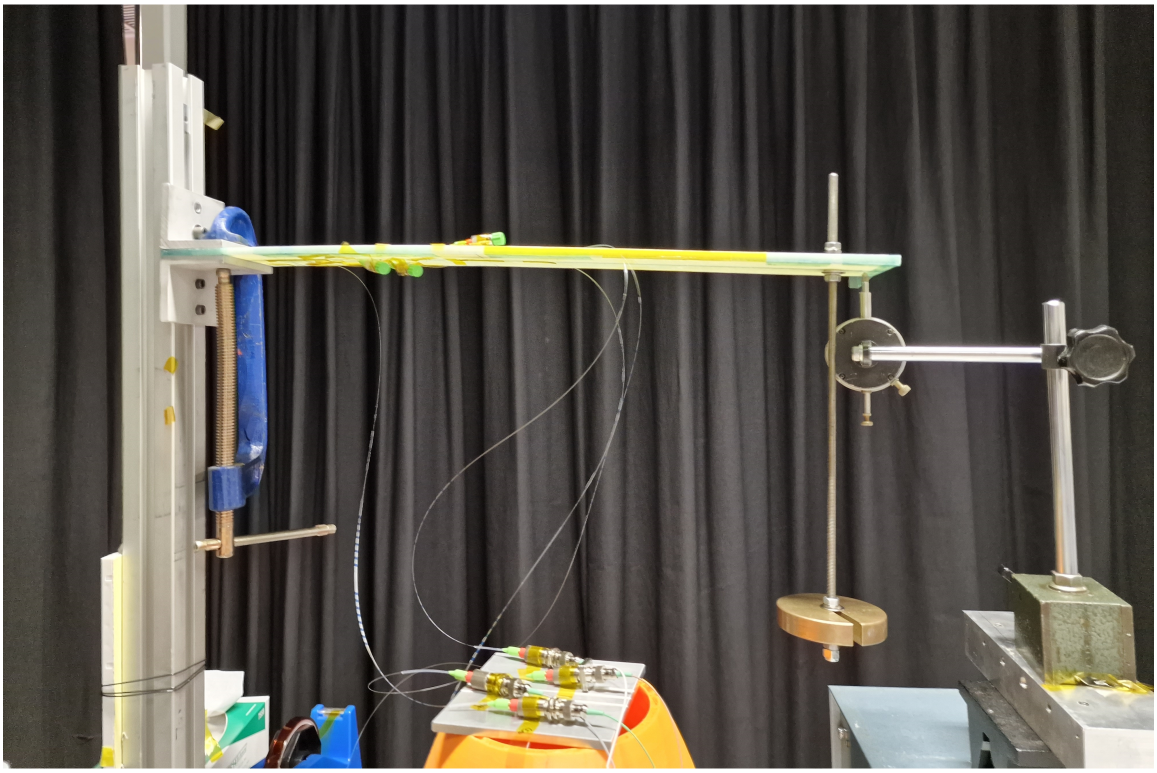

Figure. 3.56 Photograph showing experimental setup of cantilevered composite beam

As seen in Figure 3.56, the beam was firmly held to the stand using a G clamps and two additional small L plates. The distances and the bonded location of the FBGs is illustrated in Figure 3.57, Figure 3.58 and Figure 3.59. Tip deflection was measured using a Mitutoyo 2050-08 dial gauge at 535 mm from root. Using the same data acquisition and measurement devices used for the experimental analysis on FBG strain characterisation for aluminium beams described in subsection 3.6.2, the experiments using the composite beam were also carried out. However, since the composite material/ beams are less dense and more flexible compared to Aluminium, both composite beams were loaded with lower weights, starting from 0.08 kg (0.7876 N), 0.45 kg (4.4145 N), 0.7 kg (6.867 N), 0.95 kg (9.3195 N) and 1.2 kg (11.772 N) in this increasing manner. For the entire set of measurements during this experiment, temperature was assumed to be steady and constant.

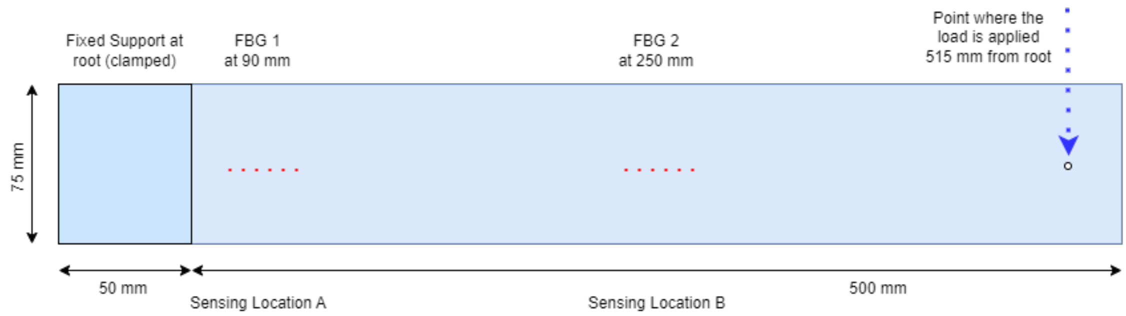

Figure. 3.57 Schematic diagram of healthy composite beam - top surface

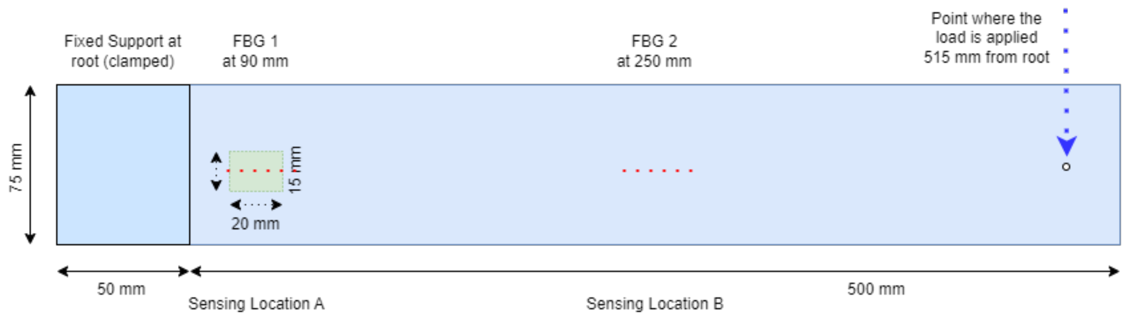

Figure. 3.58 Schematic diagram of defective composite beam - top surface

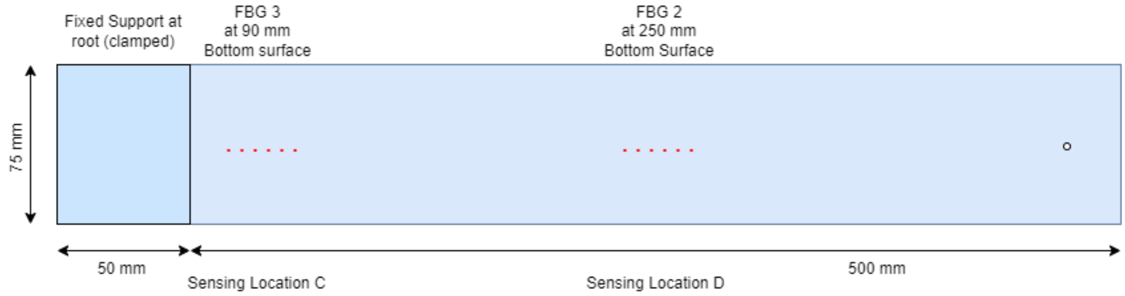

Figure. 3.59 Schematic diagram of both healthy and defective composite beam - bottom surface

For each load applied, the FBG wavelengths were recorded using the automated data acquisition and post processing was done in MATLAB using the previously developed automatic Gaussian peak fitting function (section 3.4). The following figures show the spectra of the four FBGS bonded recorded for increasing weights/ load applied for both beams.

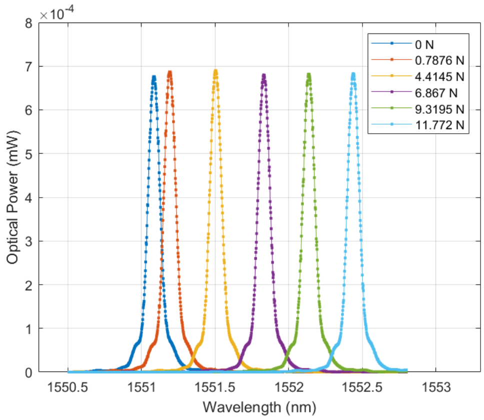

(a) Location A

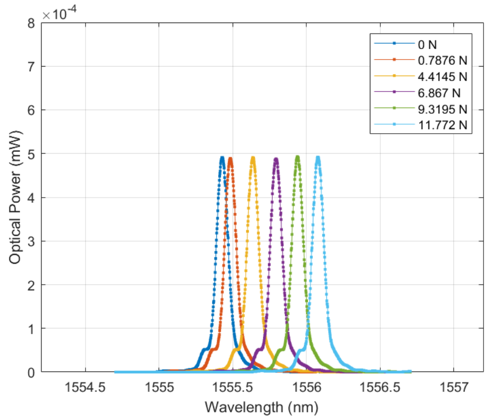

(b) Location B

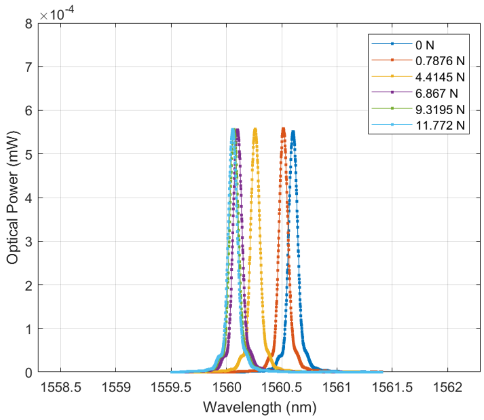

(c) Location C

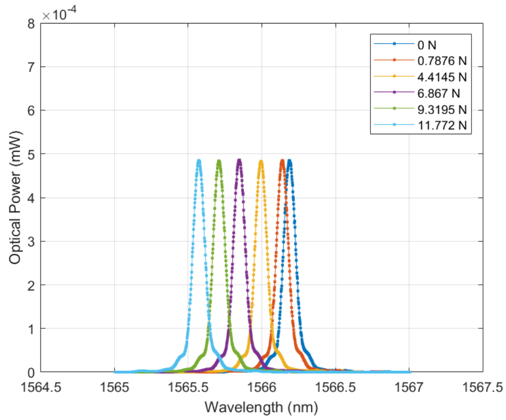

(d) Location D

Figure. 3.60 FBG Spectra for defective composite beam at (a) Sensing Location A (b) Sensing Location B (c) Sensing Location C (d) Sensing Location D

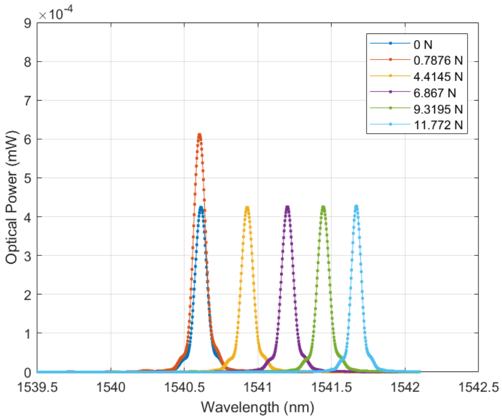

(a) Location A

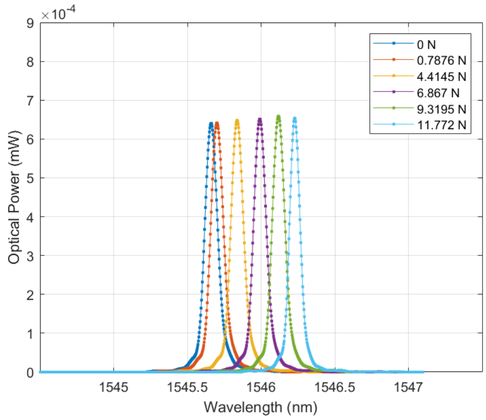

(b) Location B

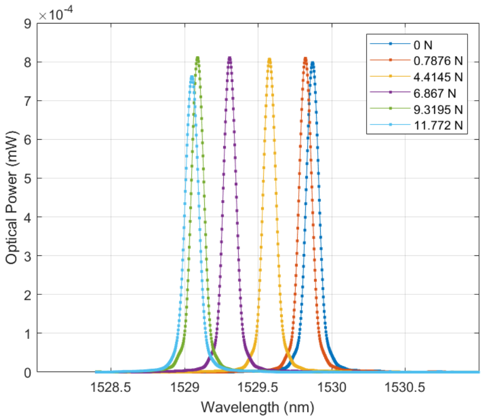

(c) Location C

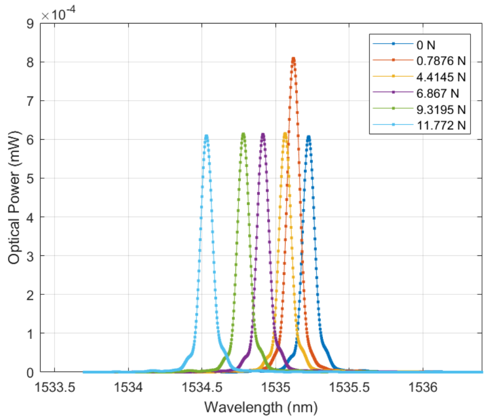

(d) Location D

Figure. 3.61 FBG Spectra for healthy composite beam at (a) Sensing Location A (b) Sensing Location B (c) Sensing Location C (d) Sensing Location D

Similar to the previous approach, to accurately compare the strain sensed by the bonded FBGs with the theoretical results obtained from ANSYS workbench, the strain values over the corresponding mounting locations were averaged over the bonded length. For example, if the grating was mounted at 90 mm from the root right on top of the defect, and the grating length was 10 mm, bonded at 15 mm on either sides, the strain expected from the ANSYS FEA simulations were taken from 75 - 105 mm and then averaged so that a single strain value could be obtained from the FEA results. This was compared with the strain obtained from FBG measurements from applied load and is shown in Figure 3.62 for healthy composite beam and Figure 3.63 for defective composite beam. To determine the measured strain from the FBG's wavelength shift, the previously calibrated strain coefficient 1.2 pm/$\mu\varepsilon$ has been used.

Table 3.10 Sensing Location and FBG Wavelengths

Sensing Location	Distance from root	Healthy Beam	Defective Beam
		FBG sensor wavelength	
A - top surface	90 mm	1530 nm	1550 nm
B - top surface	250 mm	1535 nm	1555 nm
C - bottom surface	90 mm	1540 nm	1560 nm
D - bottom surface	250 mm	1545 nm	1565 nm

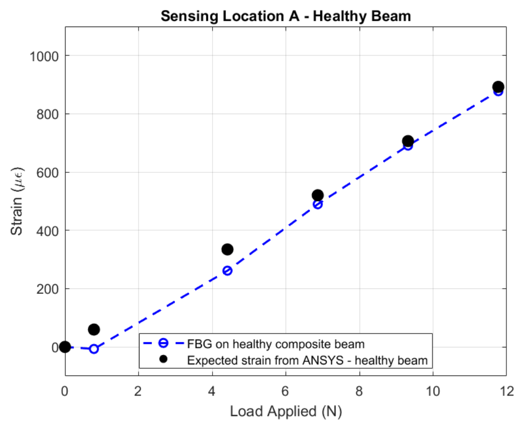

(a) Location A

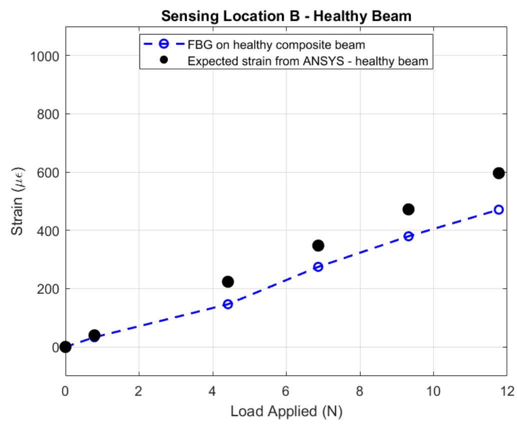

(b) Location B

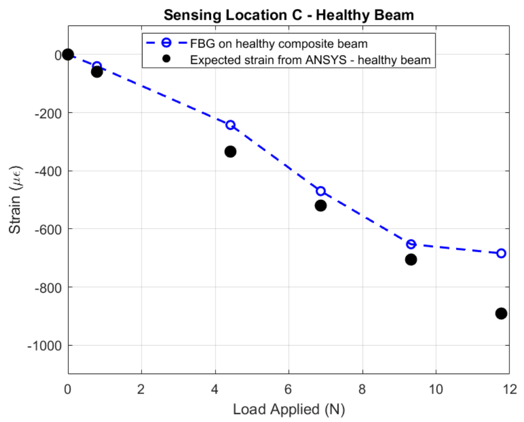

(c) Location C

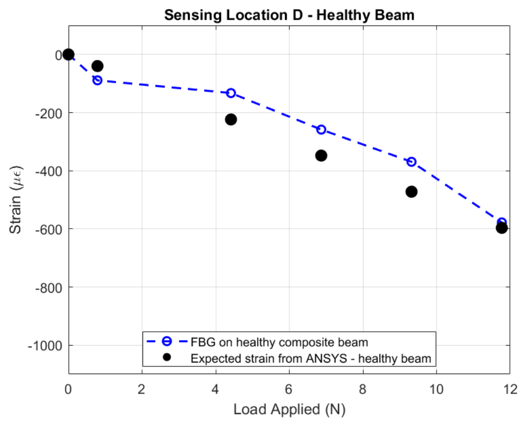

(d) Location D

Figure. 3.62 Measured vs expected strain for healthy composite beam at (a) sensing location A (b) sensing location B (c) sensing location C (d) sensing location D

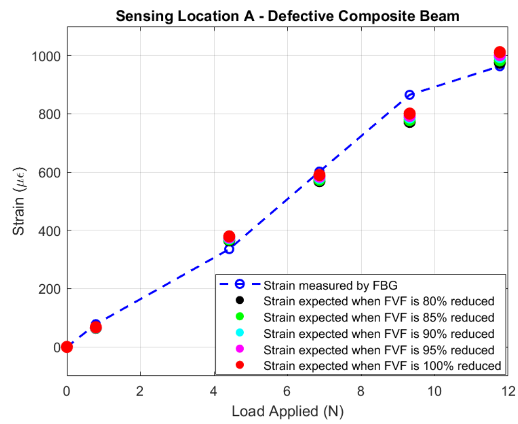

(a) Location A

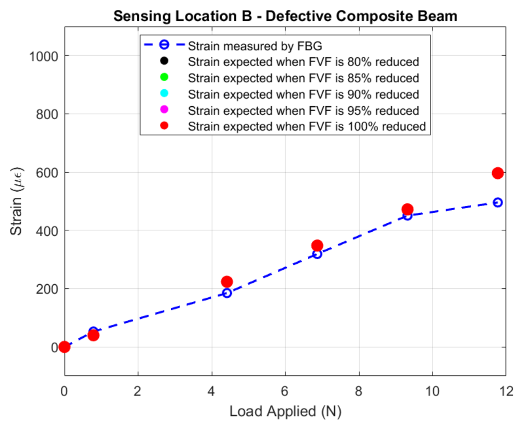

(b) Location B

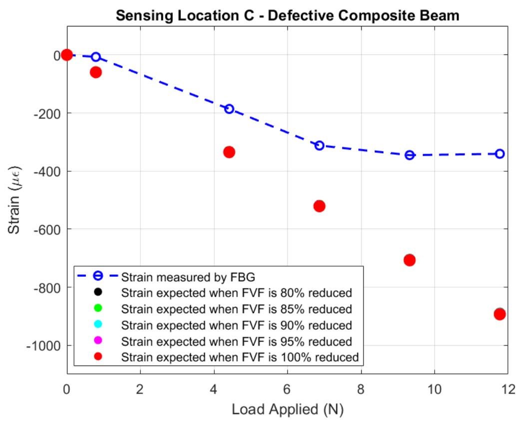

(c) Location C

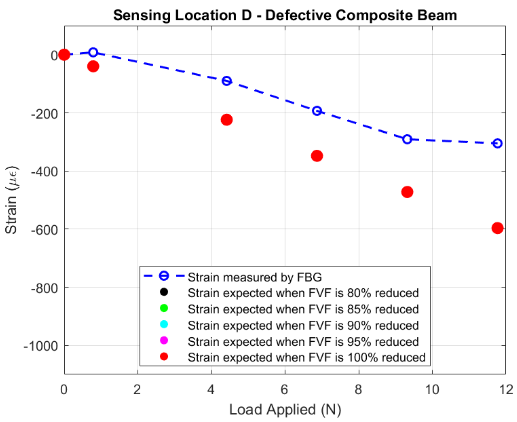

(d) Location D

Figure. 3.63 Measured vs expected strain for defective composite beam at (a) sensing location A (b) sensing location B (c) sensing location C (d) sensing location D

Looking at the results from the defective cases at all sensing locations, the strain trends indicate tension and compression appropriately. At sensing location A (the defect location), the FBG measurements show strain values that fluctuate slightly above and below the expected strain from all defective, FVF-reduced ANSYS models at a load of 9.3195 N. Despite these minor fluctuations, the agreement between the experimental FBG strains and expected strains is the highest at location A. The expected strains from the numerical analysis are very close to each other across all defective cases, with the differences being small and negligible. While the alignment remains strong at sensing locations B, C, and D, location A shows the most consistent match (strongest agreement). At location C, the match is good for lower loads, but as the loads increase, the FBG records significantly lower strains compared to the expected strains, as seen in Figure 3.63. One potential explanation for this is the non-uniformity in the composite beam's cross-section at the defective location (90 mm from the root), where the stiffness changes dramatically between the top and bottom 3 mm halves of the beam. Despite these minor discrepancies, the overall trend shows that if a straight line were fitted to the experimental results, it would likely fall in the middle of the FEA results, indicating overall good agreement between the measured and expected strains.

Looking at the results from the defective cases at all sensing locations, the strain trends indicate tension and compression appropriately. However, at sensing location A (the defect location), the FBG measurements show strain values that fluctuate slightly above and below the expected strain from all defective, FVF-reduced ANSYS models at a load of 9.3195 N. The expected strains from the numerical analysis are very close to each other across all defective cases, with the differences being small and negligible. The agreement between the experimental FBG strains and expected strains is the highest at location A and generally better at sensing locations B, C, and D, where the FBG strains align very closely with the expected strains, with minimal variation among the defective cases. At location C, the match is good for lower loads, but as the loads increase, the FBG records significantly lower strains compared to the expected strains, as seen in Figure 3.63. One potential explanation for this is the non-uniformity in the composite beam's cross-section at the defective location (90 mm from the root), where the stiffness changes dramatically between the top and bottom 3 mm halves of the beam. Despite these minor discrepancies, the overall trend shows that if a straight line were fitted to the experimental results, it would likely fall in the middle of the FEA results, indicating overall good agreement between the measured and expected strains.

When both healthy and defective composite cases are compared at sensing location A, the strain measured by the FBG sensors in the defective case is consistently higher than that of the healthy, non-defective case. This behaviour can be explained by the stiffness reduction at the top surface of the composite material, as previously discussed in subsection 3.7.1. This finding confirms the ability of FBG sensors to accurately detect increased strain caused by stiffness reductions, demonstrating their efficacy in identifying structural defects if suitably placed.

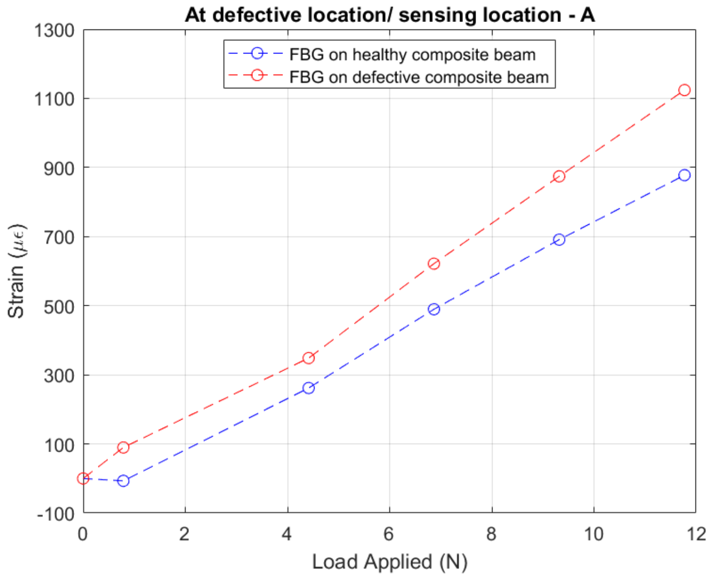

Figure. 3.64 Comparison of measured strains of healthy vs defective beam at sensing location A

3.7.6 Tip Deflection: Composite Beams

Similar to the analysis done for the Aluminium beam, here the tip deflection of the two composite beams are discussed. The expected deflection at the tip for both the composite beams with and without the defect are plotted in Fig (a) in Figure 3.65 and the measured results for both beams are given in Fig (b) Figure 3.65. Here, just like the Aluminium beam case, due to the presence of the defect i.e. region with reduced stiffness, the tip deflection for the composite beam with the defect is higher than the tip deflection of the beam without the defect. Looking at the deflection range, it can be said that, due to these beams being made out of a more flexible material i.e. composite, compared to a rigid material like Aluminium, the deflection is in the higher range.

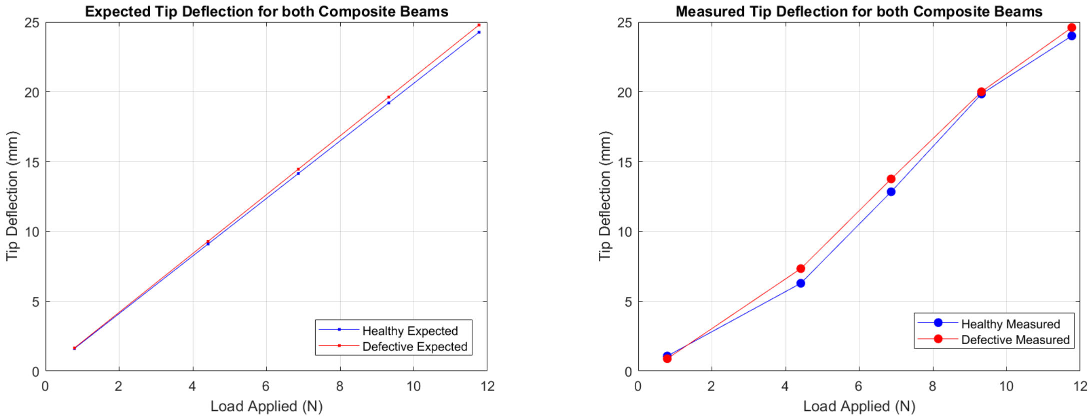

(a) Expected tip deflection

(b) Measured tip deflection

Figure. 3.65 Comparison of tip deflection of both composite beams (a) Expected (b) Measured

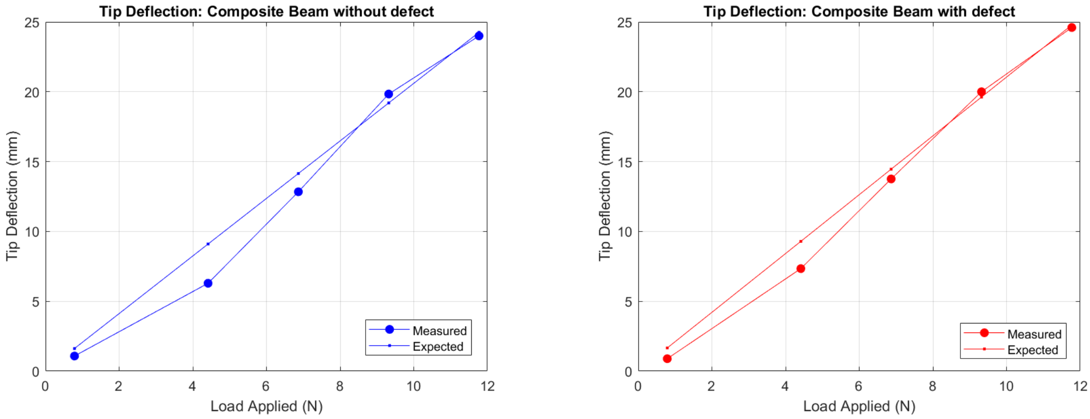

(a) Composite beam without defect

(b) Composite beam with defect

Figure. 3.66 Expected vs Measured tip deflection of composite beam (a) without defect (b) with defect

However, when each of the different composite beams are compared, the measured values are very slightly lower than the expected values. A similar trend can be seen in Fig (b) of Figure 3.65 for both the beams measured values. Here again, the defective case is slightly higher than the non-defective composite beam case.

3.7.7 Sensing Length vs Average Strain

To further explore the applicability of FBGs to assess the effect of localised defects, the bonded length of the FBG on top of the defect was changed multiple times to incorporate different sensing lengths and the same loads were applied at the tip. This was to see if as the bonded length increased, whether the average strain measured over that bonded length increases or decreases. As the defect size doesn't change, this novel experiment on analysing the optimum sensing length required to measure the smaller change in strain was carried out. This was done in the same manner as the previous method, with the use of both ANSYS simulations as well as testing this out experimentally. This was also to determine the spatial resolution of sensors required to detect a defect of this size. Additional construction lines were drawn in 10 mm, 20 mm, 30 mm, 40 mm and 50 mm distances over the defective region on the beam geometry in ANSYS mechanical and the elastic stain was extracted for the load cases considered. For the physical experiments, as the fibre was bonded using cyanoacrylate, it was debonded at the defective region and re-bonded at 10 mm, 20 mm, 30 mm, 40 mm and 50 mm intervals over the defect on top of the beam. For each bonded length, the experiments were carried out in order and then the FBG was debonded and rebonded at the next bonded length interval and measurements will be carried out. in this order, starting from 10 mm to 50 mm, all measurements were recorded. The figures below show the construction lines considered for the strain averaging from ANSYS simulations. For the rest of the sensing locations B, C and D, the bonded length were kept as before at 30 mm.

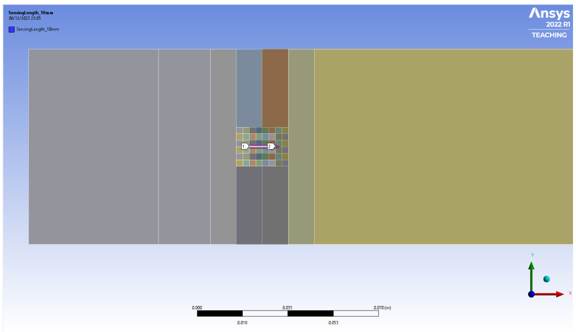

(a) Construction line over 10 mm

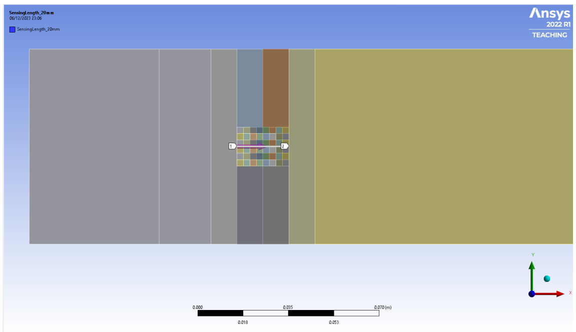

(b) Construction line over 20 mm

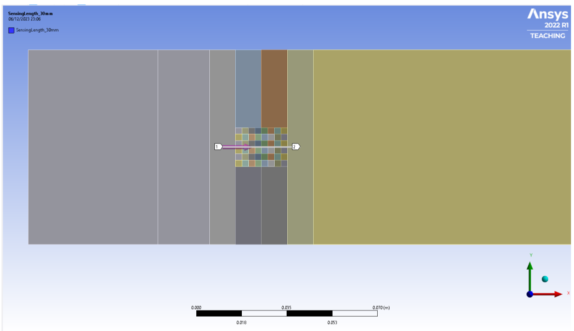

(c) Construction line over 30 mm

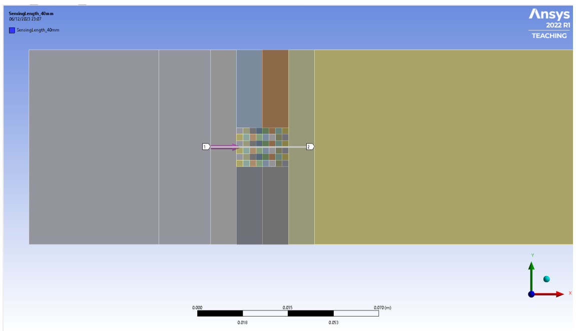

(d) Construction line over 40 mm

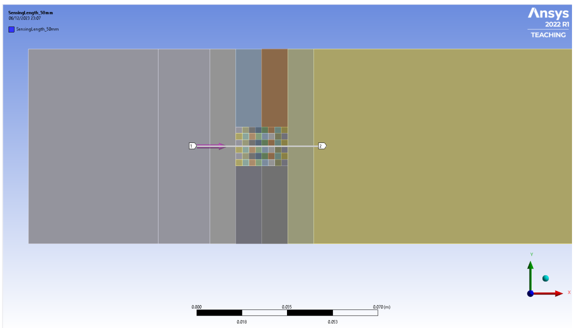

(e) Construction line over 50 mm

Figure. 3.67 Construction lines over (a) 10 mm (b) 20 mm (c) 30 mm (d) 40 mm (e) 50 mm for strain analysis

The spectra of the FBG at each bonded length, for each load applied were recorded and by using the Gaussian fitting function on the FBG data and by finding the centroid, then wavelength shift, the final measured strain were determined. These are shown in Figure 3.68. It should be noted that during the re-bonding of the FBG on the defect for the 50 mm bonded length experiment after performing the 40 mm bonded length measurements, the FBG broke right on the grating region and was rendered unusable. Therefore as an alternative solution, a single FBG with wavelength 1540 nm was used instead of broken 1550 nm. Hence a difference in wavelengths in the X-axis can be seen in the last figure in Figure 3.68 compared to the rest of the FBG wavelength vs strain figures.

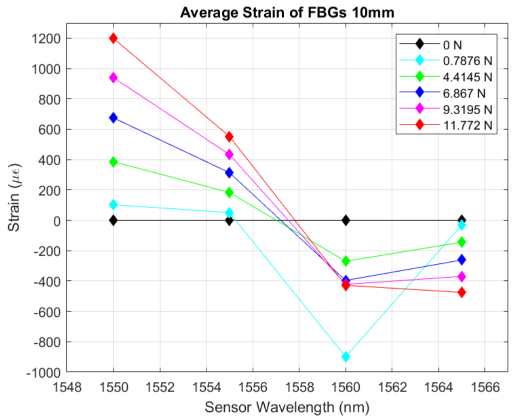

(a) Sensing length = 10 mm

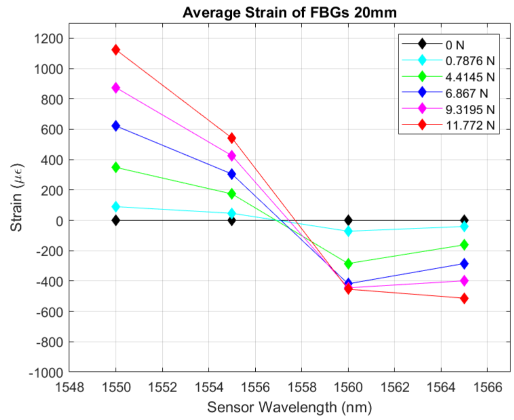

(b) Sensing length = 20 mm

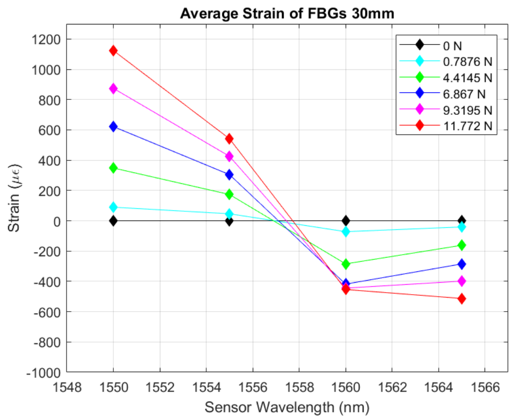

(c) Sensing length = 30 mm

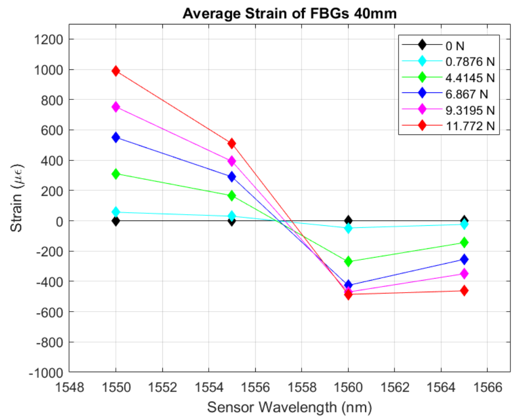

(d) Sensing length = 40 mm

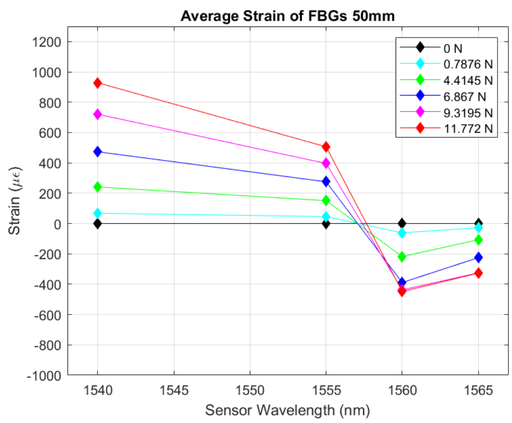

(e) Sensing length = 50 mm

Figure. 3.68 Average strain measured over (a) 10 mm (b) 20 mm (c) 30 mm (d) 40 mm (e) 50 mm bonded length

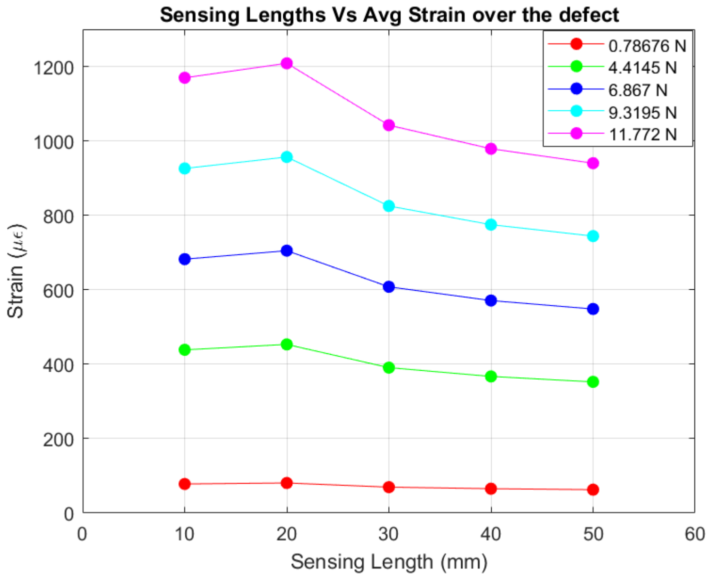

Figure. 3.69 Average strain over defect experimentally measured by different sensing lengths

If only the FBG bonded on top of defect is considered, looking at Figure 3.69 starting from 10 mm, going up to 50 mm bonded length, it can be seen that the average strain measured by the FBG for the smallest bonded length is much higher than the longest bonded length. As the length of the grating was 10 mm and the length of the defect is 20 mm, for the 10 mm bonded length, as the loads are applied at the tip, the strain measured in this case is not limited by the change in material stiffness. In the 50 mm case, however, the length of the fibre over the top covers beyond the 20 mm defect length and covers the two different materials. Hence the strain measured is lesser than the other cases, especially compared to the results for 10 mm and 20 mm bonded lengths. The average strain difference in this case is around 200-230 $\mu\varepsilon$ between the 50mm case and 10/20 mm case. By analysing this, it can be inferred that to detect defects, and to measure the smallest variations in strain accurately, the smaller the sensing length or bonded length in this case is much preferred that a longer sensing length.

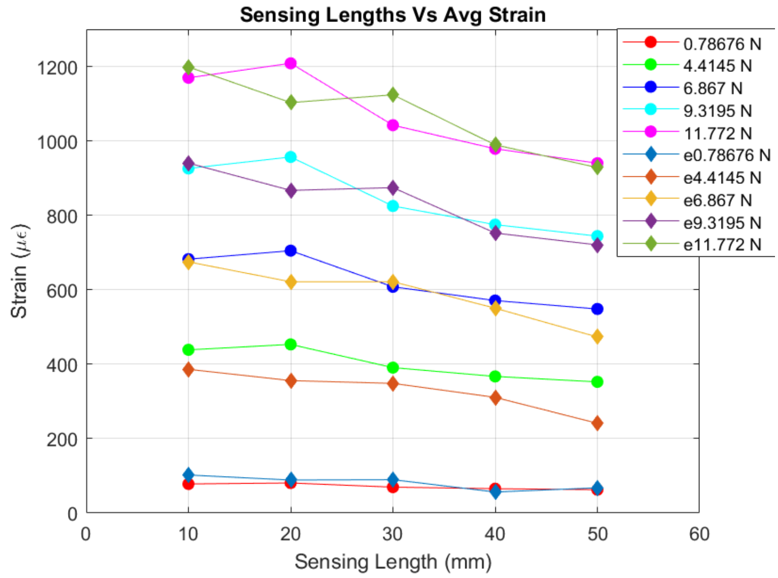

Figure. 3.70 Measured experimental vs Expected FEA average strain over defect with different sensing lengths

Figure 3.70 shows the comparison of the experimentally measured and FEA expected average strain taken for each sensing lengths. From the FEA results, the expected average strain for the 10 mm bonded length aligns closely with the peak strain values over the defect, demonstrating its ability to capture localised variations. Similarly, the 20 mm bonded length follows the trend predicted by the FEA, capturing strain variations effectively, although some minor deviations are observed at specific loads. For the 50 mm bonded length, the strain values are notably lower due to the averaging effect over a larger region, which includes both defective and non-defective material. The difference in average strain between the 10 mm and 50 mm bonded lengths for the highest applied load (11.772 N) falls within the range of 200-230 $\mu\varepsilon$, highlighting the superior sensitivity of shorter sensing lengths to defect-induced strain variations. However, among the shorter lengths, based on the measured results, the 20 mm sensor offers a balanced advantage; it maintains high sensitivity while requiring only half as many sensors as the 10 mm case. Meanwhile, the 50 mm bonded length, though less sensitive, remains viable and would require only one-fifth of the sensors, making it a more practical choice for broader structural coverage.

3.8 Conclusion

In this chapter, the primary and secondary characterisation of FBG for measuring strain was thoroughly explored. The potential of FBGs to detect small changes in strain resulting from structural defects in different materials i.e. Aluminium and Composite was demonstrated, alongside the data acquisition system and data processing techniques that can be integrated into a sensing system. A novel investigation was conducted to examine the effect of FBG sensing length on the average strain measured. The results highlighted that smaller sensing lengths are more effective in detecting strain variations over defects, providing valuable insights into how sensor configuration can optimise the detection of localised defects.

The experimental analysis of composite beams, both healthy and defective, confirmed that FBG sensors can successfully capture strain variations caused by defects, even in materials with complex stress distributions. It was observed that the defect region, characterised by reduced stiffness (FVF modified), exhibited higher strain levels than the healthy portions of the beam. While there was some minor discrepancy between the measured and expected strains, especially at sensing locations closer to the defect, the overall trend and correlation with theoretical predictions were strong. Notably, the agreement at location A (on the defect) was better than at locations B, C, and D, reinforcing the reliability of strain measurements directly over the defective region. This shows that FBGs are capable of reliably monitoring strain in composite materials under varying load conditions.

Additionally, the analysis of different bonded lengths of FBGs revealed that shorter sensing lengths, such as 10 mm or 20 mm, provided more precise measurements of localised strain changes, while longer sensing lengths averaged the strain over a larger area, thereby reducing sensitivity to smaller defects. This insight emphasises the importance of sensor resolution in detecting small structural changes, optimising the application of FBGs for SHM. However, there is a trade-off to consider: assuming the location of the defect is not known, shorter sensor lengths require more sensors to cover the entire structure, while longer sensors, though less sensitive to small defects, offer broader coverage. Among the tested lengths, the 20 mm sensing length emerged as the most effective, as it maintains a balance between sensitivity and coverage, providing higher precision in detecting defects compared to longer lengths while requiring half as many sensors as the 10 mm configuration to monitor the full structure.

The findings from this chapter lay the foundation for the application of FBGs in the detection of defects in composite structures. These results are particularly relevant to wind turbine blade monitoring, where early detection of structural flaws is crucial for maintaining performance and safety. The concept of optimized sensing lengths and their impact on defect detection is further developed for a 1.8 m scaled composite wind turbine blade, with additional results and analysis presented in Chapter 7.

Chapter 4

Aerodynamic, Structural Simulations and Modelling of Blades

4.1 Introduction

The previous chapter discusses the characterisation of the sensors on their own as well as bonded to Aluminium and Composite beams and also explains how the data acquisition and the post processing algorithm were developed. The current chapter covers two main topics: firstly, the work explained in section 4.2 was conducted following the primary sensor characterisation and prior to the secondary sensor characterisation described in Chapter 3. This was done primarily for the purpose of identifying the type of defect which can be replicated/ reproduced physically in the beams mentioned above. The second topic covered in this chapter includes the design and modelling of the 1.8 m scaled down blade which was used for the final sensor validation experiments. The selection of a 1.8 m blade for the scaled model is based on practical considerations related to the scaling process, where the blade size is approximately 1/35th of the reference blade (126 meters) to ensure accurate simulation results. This size allows for a manageable experimental setup while capturing key characteristics of the full-sized blade, such as aerodynamics and structural behaviour. The design follows established scaling laws for maintaining a sufficiently accurate representation of the blade's aerodynamics, structural behaviour, and potential defects Hansen, 2015 Canet et al., 2021. The scaling laws, the mathematical equations demonstrating the dependency of the scaled down model to the reference turbine model, and the working principle of the scaled down features are also described.

4.2 Simulations of Healthy vs Defective Blade for Defect Determination

For the purpose of determining the type and configuration of the defect that ultimately undergoes the investigation of the performance of FBGs on a healthy vs defective blade for this thesis, the Aero-Servo-Hydro-Elastic-Simulation (ASHES) software developed by Simis, 2022 was used. This is comparable to the other wind turbine simulation tools in the wind energy industry such as OpenFAST or QBlade except where that this software provides a user friendly interface. Another advantage of using this simulation tool is that it provides a real-time 3D visualisation as the turbine operates under the wind field conditions applied. A variety of results can be extracted for data analysis, but also these results and measurement parameters such as Blade moment, out of plane or in plane tip deflection, acceleration, the distributed lift and drag forces etc. can be viewed real-time in graphical format both in time domain as well as for the entire blade span. Moreover, the parameters for the applied wind field can also be changed according the user's requirement. For example: the wind speed and type (for example: uniform, turbulent, extreme wind), the turbulence intensity, direction, shear can be modified and can be changed real-time or can be pre-set.

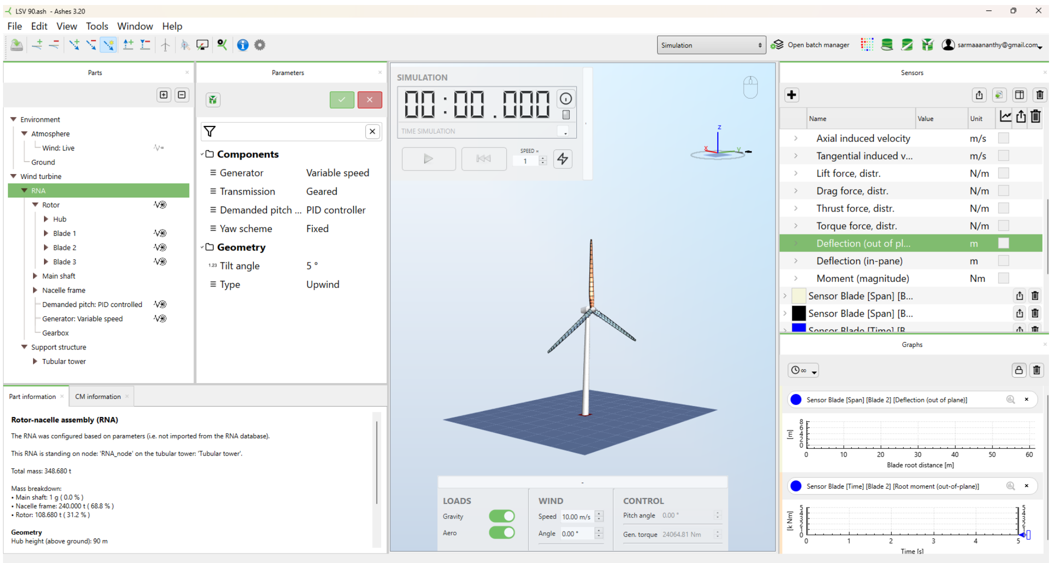

Figure. 4.1 Sample window of ASHES wind turbine simulation tool

A figure showing some selected sensors and the simulation window is given above. A few classical reference wind turbine and blade models such as the DTU-10 MW from Bak et al., 2013, the IEA-15MW wind turbine model from Gaertner et al., 2020 and lastly the NREL-5 MW from Jonkman et al., 2009 have already been installed in the software however, newer blade models and user-defined custom blade models can also be added into the software. This can be done by defining the distributed shape (external geometry) and structural parameters as shown in subsection 4.3.2 and subsection 4.3.3 in the blade database in the simulation tool.

4.2.1 Simulation Setup

A series of ASHES simulations were performed using the NREL 5MW reference turbine model. For this study, a healthy, flawless blade model was chosen, while a second "defective" blade was defined in the blade database. The defect was introduced by modifying the structural parameters of the selected blade. Specifically, the blade's structural integrity was compromised by altering its stiffness properties, rather than introducing manufacturing flaws such as material defects. This approach allows for simulating the effects of a loss of optimal structural performance due to changes in the stiffness distribution. Among the structural parameters, flapwise stiffness was selected for modification because of its significant impact on the blade's bending response to aerodynamic loads. Flapwise bending is a critical mode of deformation for wind turbine blades, and a reduction in flapwise stiffness represents a substantial alteration in the blade's ability to withstand these loads. In this investigation, the flapwise stiffness was reduced by 90% at 30% of the blade length from the root, specifically between 20-22 m from the root. This local change in stiffness is referred to as the Localised Stiffness Variation (LSV). This method of stiffness reduction was chosen based on studies that have used stiffness modification in the flapwise direction to model blade degradation and damage; Sheibani and Akbar Akbari, 2013 this is regarding stiffness reduction in the root but a similar approach can be taken by following the same theory.

Another type of defect was considered, where the blade's stiffness was uniformly reduced by 15% along the entire length of the blade, from root to tip. This is representative of a more global reduction in blade stiffness, termed Global Stiffness Variation (GSV). The 15% reduction was selected based on findings from similar studies that examined the effects of more gradual, uniform stiffness degradation, which can occur due to long-term operational wear or fatigue Vassilopoulos, 2023 and Kensche, 2006.

In the ASHES tool, the defective blade model was re-imported as the first blade of the NREL 5MW turbine's configuration, while the second and third blades were kept unchanged, using the original structural files of the NREL 5MW turbine blade model. The results of these simulations aim to quantify the effects of both localised and global stiffness variations on the turbine's overall performance.

Once the structure of the wind turbine and the blades have been sorted, the simulation parameters were selected. Since the investigation was focused only on the performance of the two different kinds of blades; the simulations were conducted for three different wind speeds: (1) Under the rated wind speed i.e. 8 m/s (2) At the rated wind speed 12.1 m/s and finally (3) At a wind speed above the rated value i.e. 18 m/s. For each blade station/ blade node spanning from root to the tip of the blade, angle of attack, lift coefficient, drag coefficient, moment coefficient, ratio of lift over drag coefficients (Cl/Cd), local wind speed, relative velocity, Reynolds number, lift and drag forces, thrust, torque, out-of-plane and in-plane deflections and finally moment can be extracted as blade span sensor data. The time series sensor provides the following fields as data; root force, root moment (both out-of-plane and in-plane), pitch angle, out-of-plane and in-plane tip deflection and the root torque.

These simulations were conducted for 2-minutes without interruptions; this time period was considered as the optimum time taken for the turbine to start operating, hit the cut-in speed of 3.5 m/s so that any of the turbine-start effects can be excluded from the analysis. Following this, a number of results were extracted, out of which the out-of-plane deflection was chosen to be evaluated for the simulation cases above for both the defective and healthy blades. As the second and the third blade belong to the original healthy case of the reference turbine, blade 2's results were taken and were plotted and compared against blade 1's (defective case) results.

4.2.2 Results from Simulations and Discussion

The results from the simulations based on the local stiffness variation are plotted below. The mean out-of-plane deflection were taken for the three wind speeds while keeping the pitch control mechanism unchanged. When the defective vs the healthy blade results were compared for the entire blade length, it can be seen that due to the defect present, the mean deflection has increased by approximately 1.7 m at the tip. At the rated wind speed of 12.1 m/s, the difference was even higher (2.15 m), where the defective blade measures 6.15 m and the healthy blade out-of-plane deflection measures 4 m at the tip. At the wind speed of 18 m/s which is above the rated speed, the pitch control began to take effect and due to this, the out-of-plane deflections can be seen to reduce, even below the values obtained from the 8 m/s simulations. Up to 22 m length measured from the root, both out-of-plane deflections were very similar for all three wind speed cases as on the figures below.

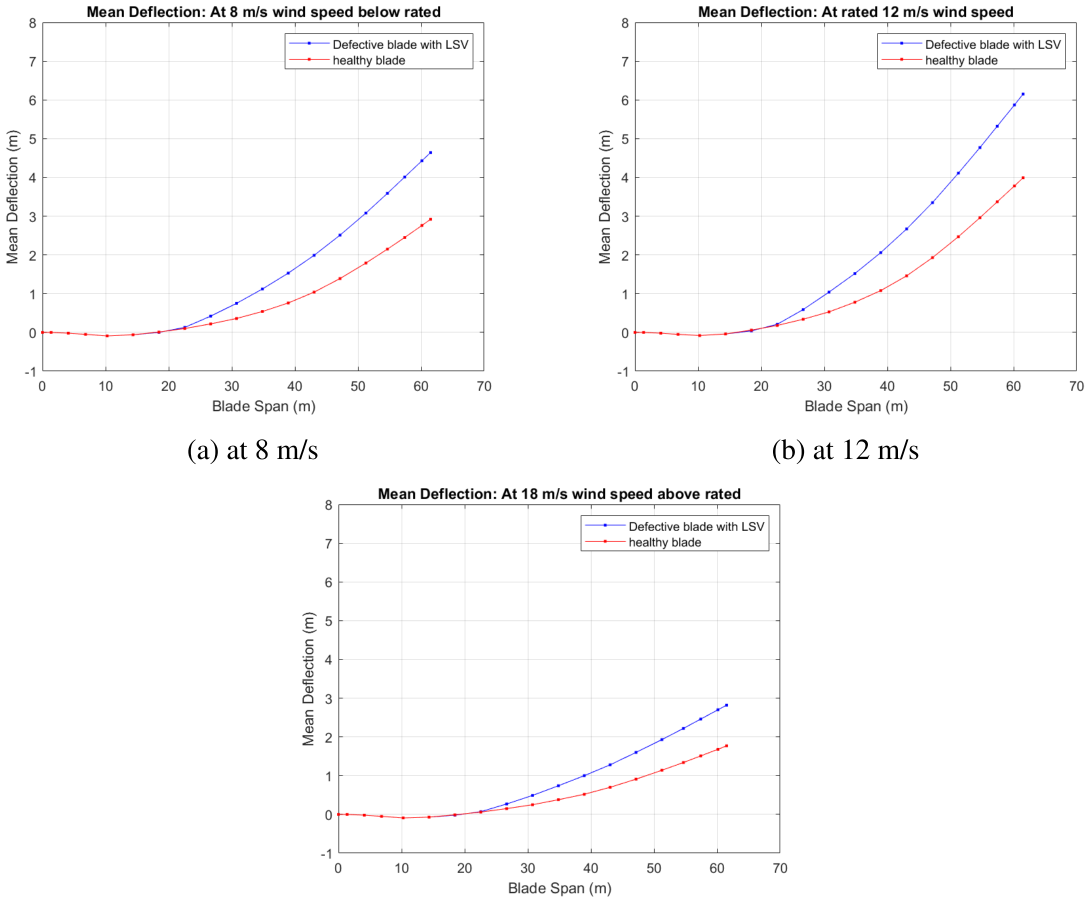

(a) at 8 m/s

(b) at 12 m/s

(c) at 18 m/s

Figure. 4.2 Mean deflection with LSV simulated at wind speeds (a) 8 m/s (b) 12 m/s and (c) 18 m/s

The results from the simulations based on the global stiffness variation (GSV) are plotted below. The "defect" in this case is featured as reduction in the flapwise stiffness in the entire blade's span. Here, similar to the same three wind speeds considered for the effect of LSV in the blade's out-of-plane deflection previously, the results have been obtained without changing any of the parameters or working conditions. At 8 m/s which is below the rated wind speed, the defective blade measures 3.4 m and the healthy blade measures 2.9 m, and the difference was much less compared to the same simulation case with the local stiffness variation. For the subsequent simulations done, at rated wind speed of 12.1 m/s, these measurements were 4.6 m for the less-stiff i.e. defective blade and 4 m for the healthy blade. i.e. for a 15% reduction in overall stiffness, there is 15% increase in deflection for the defective blade. At 18 m/s, these out-of-plane deflection measurements were 2 m for the less-stiff/ defective blade and 1.8 m for the healthy blade at the tip as it can be seen on Figure 4.3.

Another observation is that the difference between the defective and the healthy case is much lesser than the LSV case and as expected, near the tip, the out-of-plane deflections at rated wind speed is the highest out of the three sets and the deflections above rated wind speeds are much lower because of the pitch control taking over the turbine rotor.

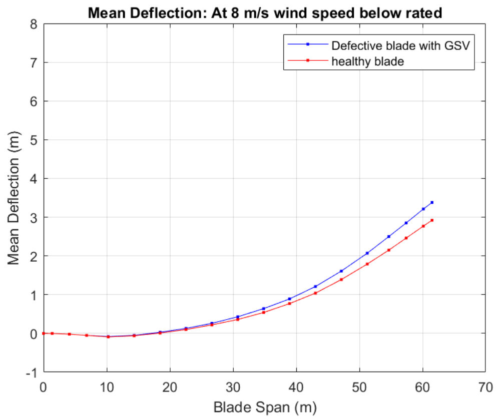

(a) at 8 m/s

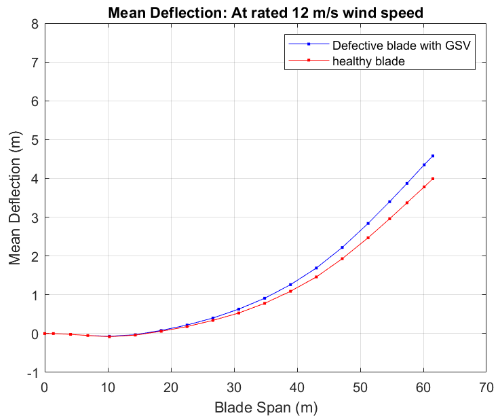

(b) at 12 m/s

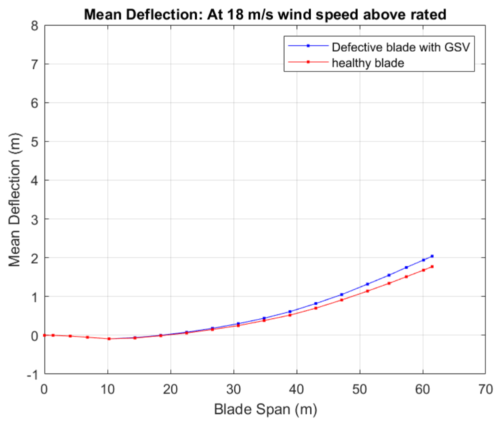

(c) at 18 m/s

Figure. 4.3 Mean deflection with GSV simulated at wind speeds (a) 8 m/s (b) 12 m/s and (c) 18 m/s

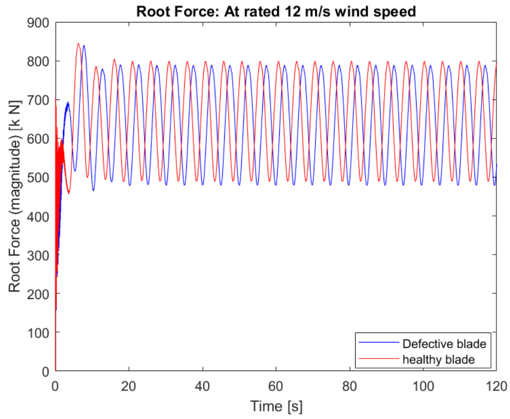

Figure. 4.4 Root Force (Magnitude only): At rated 12 m/s wind speed

Looking at the root force sensor from the time series data for the defective and healthy blades, it can be seen that in Figure 4.4, both the blades act similarly even though there's a presence of defect in one of the blade and do not show any distinction between the two types of blades. This can be seen throughout all the simulation cases considered for the different wind speeds. The turbine start-up effects are also apparent in the first few seconds. There is a 60-degree phase angle difference between the 1st blade (defective) and the second blade (healthy) as expected as well. This analysis showed that distributed measurements throughout the blade prove to be more useful compared to local measurements such as the root. Using a single sensor or using sensors at a singular, localised location on the blade typically leads to extrapolation of measured results in order to estimate any damage inducing parameters. Even though there are some data-riven methods such as the work conducted in García and Tcherniak, 2019 to make use of the single sensor's signals for SHM, evaluation of damage and its progression could be tricky. Hence, comparing the sensors covering the entire blade span vs a single sensor at the root (from the time series data) highlights the need for multi-point and distributed sensing, particularly for blades.

4.3 Blade Design and Modelling

The objective of this design and modelling is to produce a scaled blade which can then be used to mount sensors and for laboratory testing and validation. However, due to the scaling process itself, not all non-dimensional numbers can be maintained, hence the scaling process has been modified wherever necessary. The blade model was aimed for investigations in the area of experimental static loading. This also served the characterisation of defects with laboratory validation using experimental measurements with surface-mounted fibre optic sensors compared with the expected strain for the blade. For this, following up from the previous ASHES simulations, the NREL- 5 MW reference turbine model was selected to be scaled down.

4.3.1 Scaling laws

Based on the NREL 5MW baseline turbine blade and practical limitations involving physical scope of sensors system and blade, the length and time scale factors were determined. With these, the rest of the main parameters were estimated. This evaluation is based on the work of Berger et al., 2018, Sieros et al., 2012 and most notably Chaviaropoulos, 2007. Typically, for a scaled turbine, the rotor diameter is scaled with a length scaled factor n_L as in equation Equation 4.1 below,

$$n_L = \frac{D_{\text{scaled}}}{D_{\text{reference}}} = \frac{3.6 \text{ m}}{126 \text{ m}} = \frac{1}{35} \tag{4.1}$$

The main limiting factor for the time scale factor n_T is the rated rotational speed of the turbine. Even though the blade was not intended to be used with an entire scaled wind turbine set-up in a rotating environment or in a wind tunnel, scaling of the main turbine parameters depend on the time scale factor Equation 4.2. For this, a rotational speed for the scaled blade is taken as an arbitrary value of 600 RPM.

$$n_T = \frac{n_{\text{scaled}}}{n_{\text{reference}}} = \frac{6001/\text{min}}{12.11/\text{min}} = 49.6 \tag{4.2}$$

It should be noted that the rotor diameter of 3.6 m directly corresponds to the blade length of 1.8 m because the rotor diameter is twice the blade length in a typical wind turbine design. This is due to the fact that the rotor diameter measures the full span of the circular sweep area, which includes the lengths of two opposite blades extending outward from the hub. Thus, for a turbine with two blades, the rotor diameter is simply 2 × blade length.

Table 4.1 Scaling of main turbine parameters

Rated Values	Factor	Reference	Scaled
Rotor Diameter	n_L	126 m	3.6 m
Rotor Speed	n_T	12.1 1/min	600.16 1/min
Tip Speed	n_L . n_T	80 m/s	113.37 m/s
Power	n_L^5. n_T^3	5 MW	11.61 kW
Torque	n_L^5 . n_T^2	3.95 MNm	0.0024 MNm
Wind Speed	n_L . n_T	11.4 m/s	16.18 m/s
Thrust	n_L^4 . n_T^2	700 kN	1.15 kN
Max.Chord Reynolds Number	n_L^2 . n_T	1.1 * 10^7	22.088 * 10^6

4.3.2 External Geometry

For the external geometry of the scaled rotor blade, the geometric similarity is assumed so that scaled blade's characteristics scale up proportionally with the length factor n_L with the reference turbine blade. The radius of the blade, the local radius, length; also known as the span of the blade, chord distribution and maximum thickness distribution of airfoils use the length scale factor and are dependant. The twist distribution and the airfoil type remain the same as the reference blade whereas the non-dimensional spanwise distance, non-dimensional chord distribution and the non-dimensional maximum thickness distribution remain independent of the scaling factors.

The original distributed aerodynamic and geometrical properties of the NREL-5MW blade and the same parameters for the 1.8 m scaled Hull Blade are given in tables Table 4.3 and Table 4.4 respectively below.

The NREL 5MW baseline turbine blade uses eight airfoils throughout its span. The two airfoils at the root of the blade (nodes 1-4) are cylinders: cylinder 1 and cylinder 2 and have a designed drag coefficient of 0.50 and 0.35 respectively. Since both are located at the root, they do not have any lift coefficient and have a relative thickness ratio t/c of 100 %. The transitional region spans from node 5-7 and comprises of DU 99-W-405 and DU 99-W-350 with a relative thickness of 40.50 % and 35.10 %. The midspan or the aerodynamic region spans from nodes 8-12 and are covered by DU 97-W-300, DU 91-W-250 and DU 93-W-210 and consist of relative thickness ratios of 30.00 %, 25.00 % and 21 % respectively. Finally, the tip region extending from node 13 to node 18, represents the shape with the same airfoil NACA-64-618 and relative thickness ratio of 18 % throughout the tip nodes. The three-dimensional coordinates and the detailed lift and drag coefficients with respect to the

Table 4.2 Scaling Dependency for External Geometry of the Blade

Symbol	**Defining Formula**	**Description**	**Size Dependency**
R		Blade Radius	Dependent
r		Local Radius	Dependent
L	$L = R - r_0$	Blade Length	Dependent
c(r)		Chord Distribution	Dependent
t(r)		Maximum Thickness distribution of airfoils	Dependent
x	x = r / R	Non-dimensional spanwise distance	Independent
$c^*(x)$	$c^*(x) = c(r)/R$	Non-dimensional chord distribution	Independent
$t^*(x)$	$t^*(x) = t(r)/c(r)$	Non-dimensional Max-Thickness distribution	Independent
twist(x)		Twist distribution	Independent
airfoil(x)		Airfoil Type	Independent

angle of attack range for each airfoil used are included in Appendix A.

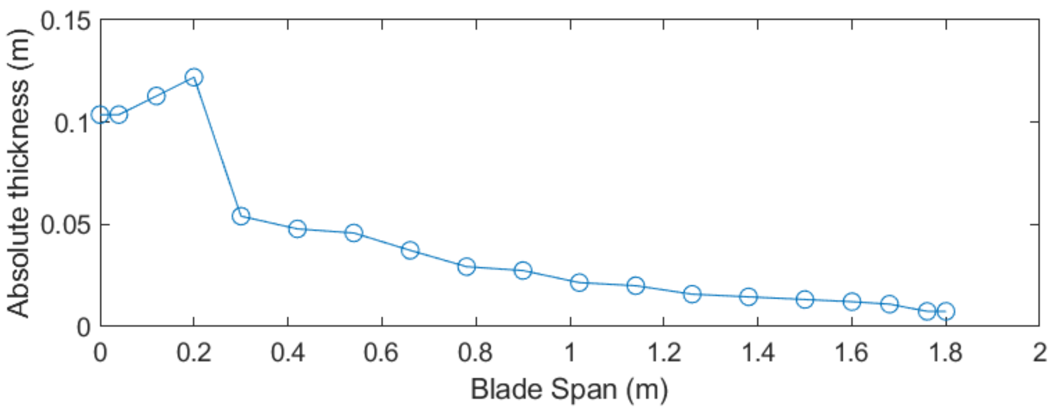

Figure. 4.5 absolute thickness distribution

Table 4.3 Distributed Aerodynamic & Geometrical Properties of NREL 5MW Blade

Node (-)	Blade Span (m)	Blade Element Length (m)	Aerodynamic Twist (°)	Chord (m)	Airfoil Type
1	0.000	0.000	13.308	3.542	Cylinder 1
2	1.367	1.367	13.308	3.542	Cylinder 1
3	4.100	2.733	13.308	3.854	Cylinder 1
4	6.833	2.733	13.308	4.167	Cylinder 2
5	10.250	3.417	13.308	4.557	DU 99-W-405
6	14.350	4.100	11.480	4.652	DU 99-W-350
7	18.450	4.100	10.162	4.458	DU 99-W-350
8	22.550	4.100	9.011	4.249	DU 97-W-300
9	26.650	4.100	7.795	4.007	DU 91-W-250
10	30.750	4.100	6.544	3.748	DU 91-W-250
11	34.850	4.100	5.361	3.502	DU 93-W-210
12	38.950	4.100	4.188	3.256	DU 93-W-210
13	43.050	4.100	3.125	3.010	NACA 64-618
14	47.150	4.100	2.319	2.764	NACA 64-618
15	51.250	4.100	1.526	2.518	NACA 64-618
16	54.667	3.417	0.863	2.313	NACA 64-618
17	57.400	2.733	0.370	2.086	NACA 64-618
18	60.133	2.733	0.106	1.419	NACA 64-618
19	61.500	1.367	0.106	1.419	NACA 64-618

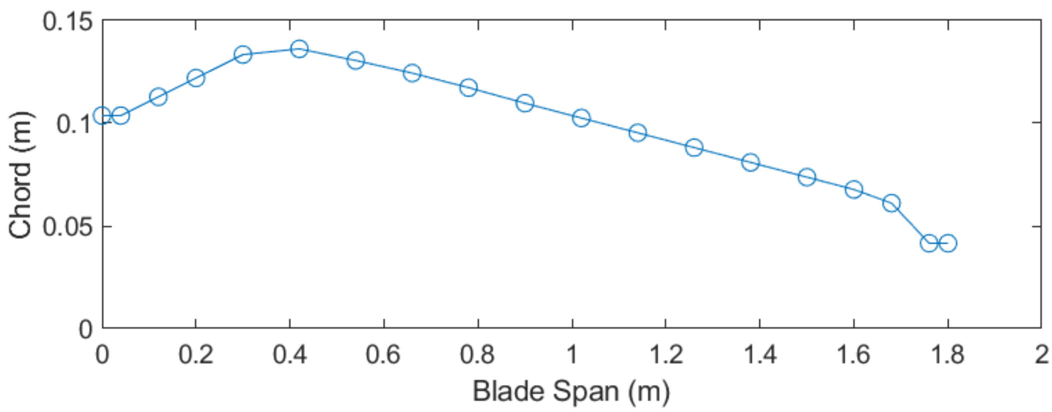

Figure. 4.6 chord distribution

Table 4.4 Distributed Aerodynamic & Geometrical Properties of Hull Blade - 1.8 m

Node (-)	**Blade Span** (m)	**Blade Element** Length (m)	**Aerodynamic** Twist (^{o})	**Chord** (m)	**Airfoil** Type
1	0.000	0.000	13.308	0.104	Cylinder 1
2	0.040	0.040	13.308	0.104	Cylinder 1
3	0.012	0.080	13.308	0.113	Cylinder 1
4	0.200	0.080	13.308	0.122	Cylinder 2
5	0.300	0.100	13.308	0.133	DU 99-W-405
6	0.420	0.120	11.480	0.136	DU 99-W-350
7	0.540	0.120	10.162	0.131	DU 99-W-350
8	0.660	0.120	9.011	0.124	DU 97-W-300
9	0.780	0.120	7.795	0.117	DU 91-W-250
10	0.900	0.120	6.544	0.110	DU 91-W-250
11	1.020	0.120	5.361	0.103	DU 93-W-210
12	1.140	0.120	4.188	0.095	DU 93-W-210
13	1.260	0.120	3.125	0.088	NACA 64-618
14	1.380	0.120	2.319	0.081	NACA 64-618
15	1.500	0.120	1.526	0.074	NACA 64-618
16	1.600	0.100	0.863	0.068	NACA 64-618
17	1.680	0.080	0.370	0.061	NACA 64-618
18	1.760	0.080	0.106	0.042	NACA 64-618
19	1.800	0.040	0.106	0.042	NACA 64-618

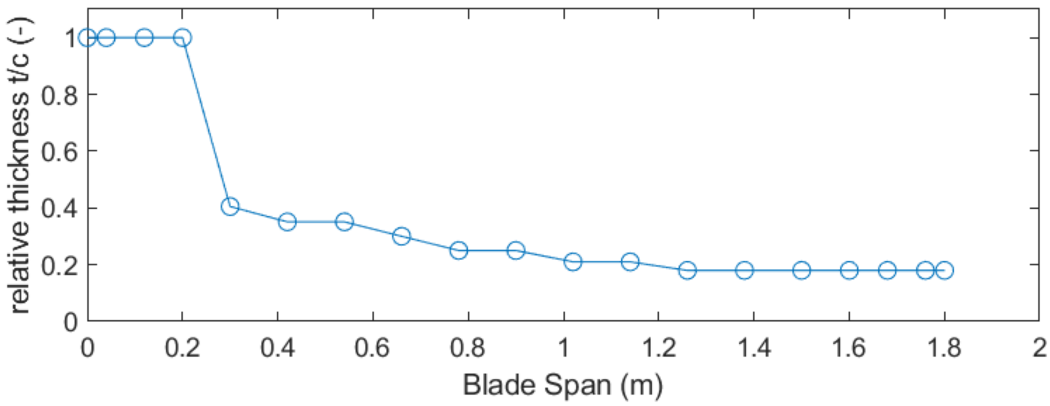

Figure. 4.7 relative thickness distribution

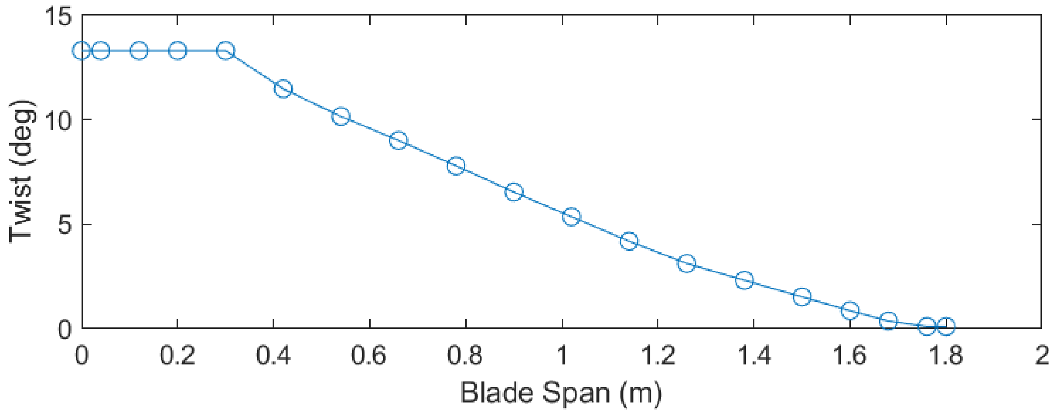

Figure. 4.8 twist distribution

4.3.3 Blade Structural Properties

For the scaled blade, we assume the geometric scaling of the internal blade structure is proportional and uses the length scale factor in 2nd or 4th order as depicted in the following table. Some sectional properties ignore the possible second order effects but is proportional when it comes to number of layers of the material.

Table 4.5 Scaling Dependency for Sectional Properties of the Blade Structure

Symbol	Defining Formula	Description	Size Dependency
A(x)	$=\mathrm{R}^2 \int ds^* = R^2.A^*(x)$	Effective Area	${n_L}^2$
$\mathrm{I(x)}=\begin{pmatrix} \mathrm{Iyy}(x) & \mathrm{Iyz(x)} \\ Izy(x) & \mathrm{Izz}(x) \end{pmatrix}$	$= R^4 \begin{pmatrix} \int z^{*2} ds^* & -\int y^* z^* ds^* \\ -\int z^* y^* ds^* & \int y^{*2} ds^* \end{pmatrix}$ $= R^4.I^*(x)$	Moments of Inertia - Tensor	${n_L}^4$
$\mathrm{I}_p(x)$	$\mathrm{R}^4.I_p^*(x)$	Polar Moment of Inertia	${n_L}^4$
J(x)	$\mathrm{R}^4.J^*(x)$	Torsion Constant	${n_L}^4$
$\mathrm{W}_y(x)$		Section Moduli – Y Bending	${n_L}^3$
$\mathrm{W}_z(x)$		Section Moduli – Z Bending	${n_L}^3$
$\mathrm{W}_t(x)$		Section Moduli – Torsion	${n_L}^3$
$\overline{\rho_m}(x)$		Mean Material Density	Independent
$\overline{E}(x)$		Mean Young's Modulus	Independent
$\overline{G}(x)$		Mean Rigidity modulus	Independent
$\overline{\rho}(x)$	$\overline{\rho_m}(x).A(x)$	Linear Density	${n_L}^2$
$\mathrm{EI}_(x)$	$\mathrm{E(x).I}_(x)$	Bending Stiffness - Tensor	${n_L}^4$
GJ(x)	G(x).J(x)	Torsional Stiffness	${n_L}^4$

4.3.4 Operational Conditions

To determine the operating condition of the scale blade with respect to the reference turbine, we follow the scaling rules mentioned in Table 4.1 but only the rotor or rotational speed, Reynold's number and derivative parameters which depend on these change proportionally to the turbine size. Rated wind speed for the scaled turbine model uses the scaling factor however, the wind speed at which the turbine operates in the real world is independent of the scaling laws and depends purely on environmental conditions.

Table 4.6 Scaling Dependency for Operational Conditions of Scaled Blade

Symbol	Defining Formula	Description	Scaling Dependency
ρ_a		Air Density	Independent
U		Wind Speed	Independent
ω		Rotational Speed	Dependent
ωR	$\omega R = function(U)$	Tip-Speed	Dependent
p	p = $function(U)$	Collective Pitch	Independent
V(x)	V(x) = $function(U,x)$	Effective Wind Speed	Independent
Re(x)	Re(x) = V(x) *c (x)/ ν	Reynold's Number	Dependent
M(x)	M(x) = V(x) / a	Mach Number	Independent

where a is the speed of sound and ν is the kinematic viscosity of air.

It should be noted that the local wind speed of the blade depends on the scaling factors as shown in Table 4.1 but the operating wind speed mentioned in Table 4.6 is independent of the size/ type of blades/ turbine and scaling factors as it depends purely on the operating environmental conditions.

4.3.5 Loads and Stresses

For the scaled wind turbine blades, the loads and stresses can also be scaled. However, the centrifugal stresses and the aerodynamic stresses are independent of the size of the turbine model. Any stresses relating to the weight of the turbine is proportional to the length scale factor. However, the longer the blade is, the more likely the blade is susceptible to buckling. This also triggers a low cycle fatigue failure due to the weight when scaling up.

4.3.6 Elastic Deformations

When it comes to elastic deformations, mainly deflections, the normalised deflections when produced by aerodynamic forces/ loads are independent of the both the length and time scale factors. The deflections produced by the weight of the structure however, depend on the length scale factor and is proportional. This has a direct effect on the maximum edgewise/ in-plane deflections. Pre-deflected blades (made for tower clearance) and tilted rotors follow the scaling laws, however, as the length of the blades increase, the tower-clearance set by the turbine designers gets complicated and is prone to deformations and other damages. This is explained further in Chaviaropoulos, 2007.

4.3.7 Blade Modelling in Solidworks

With the above parameters defined, the design of the 1.8 m scaled down blade was done in computer aided design (CAD) tool Solidworks. For this, the global coordinates system was selected accordingly and 19 planes were added based on the distance of each blade stations. With the airfoil coordinates already obtained from the NREL-5 MW turbine model, they were imported on to each plane by using the function plot curve through XYZ points as shown in Figure 6.1a. With these plots imported on to each plane, these were then connected via the leading edge and the trailing edge. Each of these were then lofted from one plane to the next and the blade was finally made with lofted surfaces from root to tip as shown in Figure 4.11. This essentially results in the shell model of the blade without any thickness for the pressure side/ suction side.

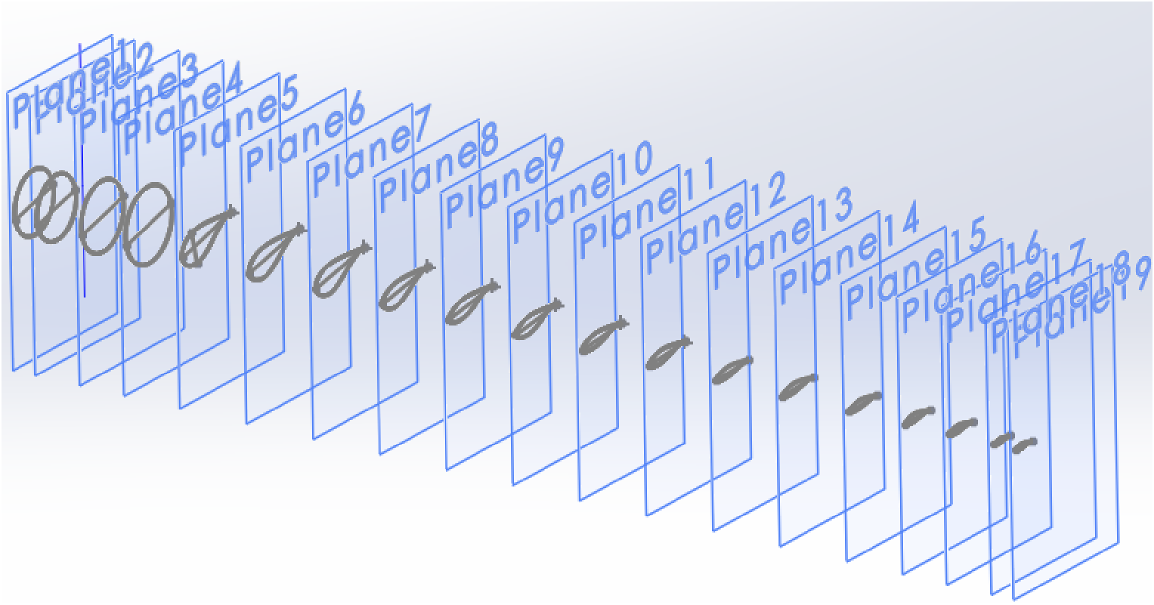

Figure. 4.9 Planes and Airfoils of 1.8 m Hull Blade Model in Solidworks

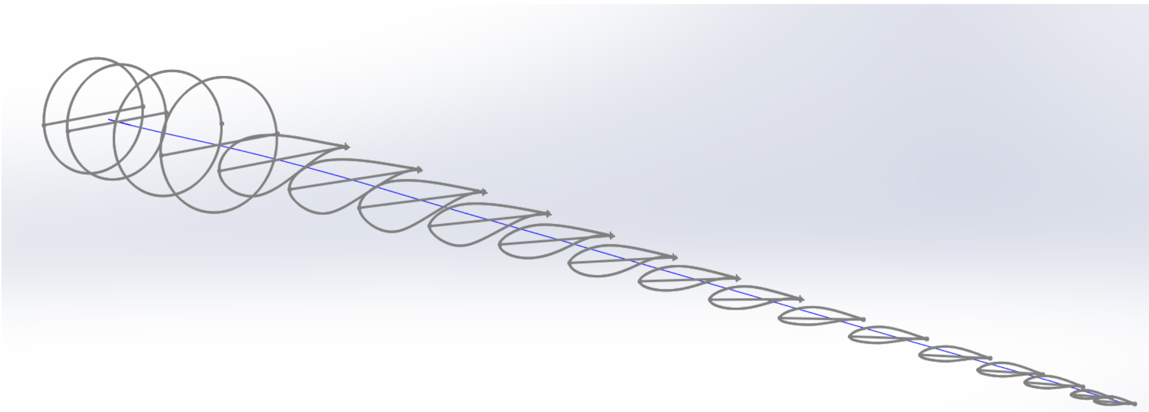

Figure. 4.10 Airfoils and chord-lines of 1.8 m Hull Blade Model in Solidworks

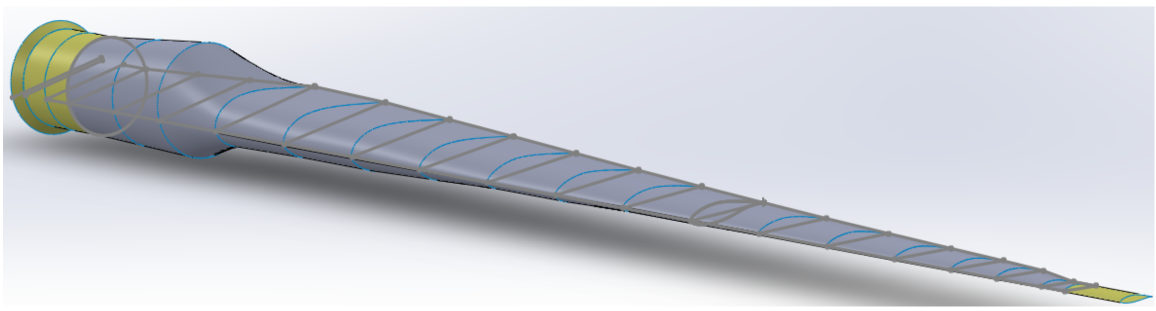

Figure. 4.11 Blade Lofted Surfaces Solidworks

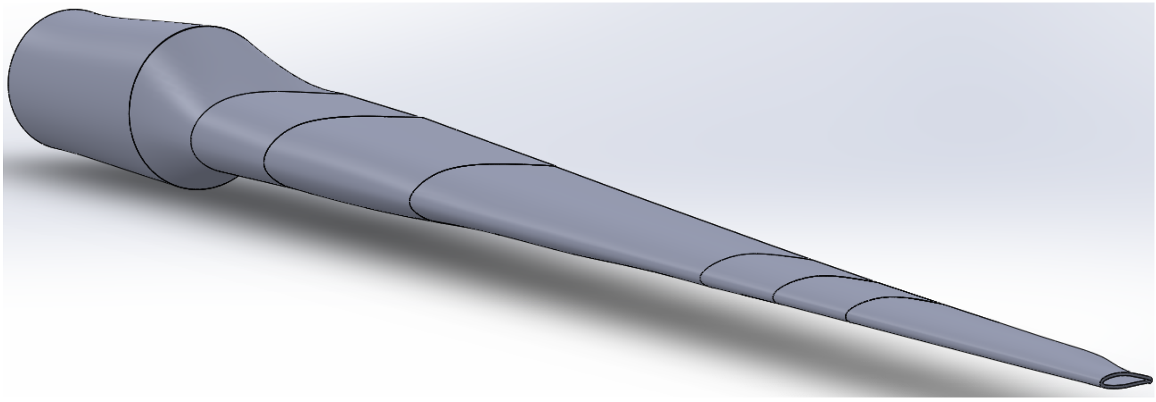

Figure. 4.12 Blade with thickness Solidworks

For the shell model, the thickness was introduced using the "extrude" the function. With this, a 3 mm realistic thickness was added all throughout the blade. This is shown in Figure 4.12, however, this thickness can be changed later to match the thickness of the composite manufacturing process. For the final blade design, this design was amended slightly and the thickness was set to 2.3 mm to match the manufacturing process for this blade. Several minute adjustments were done in Solidworks where the interfaces of airfoils/ blade stations and the surfaces did not meet each other and were not connected seamlessly.

4.4 Conclusions

The first section of this chapter demonstrated the simplest way to introduce a "defect" was by modifying the structural parameters of a blade model, a method that can be replicated physically via composite manufacturing (discussed in the next chapter). Structural parameter changes, such as localised or global stiffness reductions, effectively simulate real-world defects like delamination or material ageing, and simulations using the ASHES tool show that these defects lead to higher distributed deflections compared to a healthy blade. Results further indicate that distributed sensing is more effective for quantifying damage than relying solely on root measurements.

The second section of this chapter emphasizes the practical application of scaling laws to develop a feasible scaled model from the reference design. The adjustments made, such as simplifying conditions and disregarding Reynolds number variations, ensure the model remains both accurate and manufacturable. This chapter offers valuable insights for manufacturing the scaled blade by detailing the scaling process, highlighting the importance of maintaining aerodynamic and structural properties, and providing a clear pathway for experimental validation. These considerations make the scaled blade design including the

CAD model ready for practical implementation in manufacturing and testing.

Chapter 5

Composite Scaled Blade Manufacture

5.1 Introduction

This chapter explores the manufacturing process of composite wind turbine blades as basis for selecting the best method to construct a test scaled blade. Starting with typical commercial size wind turbine blades manufacture, then with newer, unconventional composite manufacturing techniques to the methodology of producing the 1.8 m scaled composite Hull Blade, this part of the thesis explains the design and manufacturing of the entire test rig in detail. The previous chapter explains the blade design and modelling in detail including the scaling laws utilised to achieve 1:35 scale model of the National Renewable Energy Laboratories (NREL) 5 MW wind turbine blade design. The methodology for constructing the physical composite structure of the 1.8 m Hull Blade, including the techniques used for both the "healthy" and "defective" blades, has been outlined in section 5.3, with the blade's geometrical and structural properties from root to tip already pre-defined. section 5.4 provides an introduction to the composite defect introduced in the "defective" blade. Finally, a simple validation of the design and the physical blade has been made by comparing the blade's cross-sectional properties for both blade cases with additional calculations of the expected strain profile at several selected paths along the blade.

5.2 Manufacturing Composite Wind Turbine Blades Structures

In recent times, wind turbine manufacturers produce rotor blades using the two common practices: (a) prepreg and (b) vacuum assisted resin transfer moulding (VARTM) in place of the much laborious wet layup method. The latter process starts with fabricating female moulds which then are used to lay up the fibre reinforcement mats. This is done for both pressure side (PS) and suction side (SS) separately and then the two sections are adhesively bonded along both the leading and the trailing edge. During this process, the spar cap in-between the PS and SS shells is also placed and bonded using adhesive. The typical construction process for making blade is illustrated below.

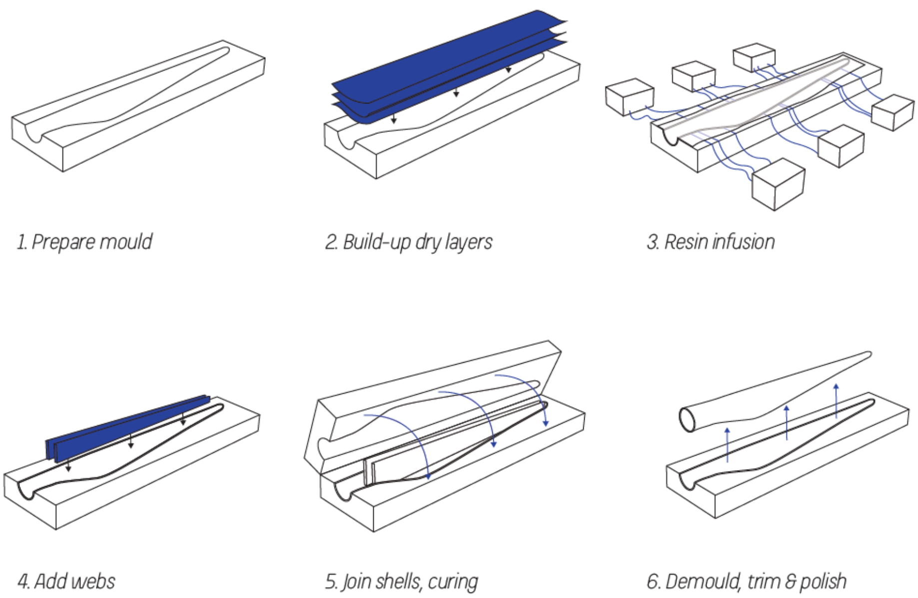

Figure. 5.1 Composite Blade Manufacture Process as shown in Bladena, 2021

Figure. 5.2 Typical Mould Layup Process, original source: Cairns et al., 2011

Bladena, 2021 have published a blade handbook which describes the concept and methods which go into manufacturing a blade. In most cases, the composite blade is made using two female moulds, one for pressure side and one for suction side shell. Manufacturing of the moulds include CNC machining of foam plugs, applying a gel-coat as tool surface and building up the mould with fabrics and (presumably) resin. Inclusion of heating systems in the mould and incorporation of other parameter-monitoring systems are also carried out during the infusion and curing process. Preparation of the mould for each subsequent infusion includes, cleaning the mould of dirt, grime and dust and applying mould release agent.

Next, the individual casting processes start with the building up of the fibreglass layers, either using dry glass layers (a combination of unidirectional and bi-directional fibre lamina) or by using prepreg glass laminates such as the Danish wind turbine manufacturer, Vestas Mishnaevsky et al., 2017. This is conducted along with the assembly of the required sandwich materials such as balsa wood and polymer foam on the mould. This is then covered with vacuum bag and made air tight using vacuum pumps as the majority of the composite blades are now made using the VARTM method. Prepreg (pre-impregnated) laminates contain the reinforcement material, i.e. fibre glass layers and a little amount of the matrix (resin) bonding the fibres together. After the application of the vacuum, the resin is injected via several inlets and low-viscosity resin flows in and wets the fibres as illustrated in Figure 5.3 . Depending on the scale of the composite structure, the number of resin inlets and the vacuum suctions points can be increased to make the infusion process faster and more effective.

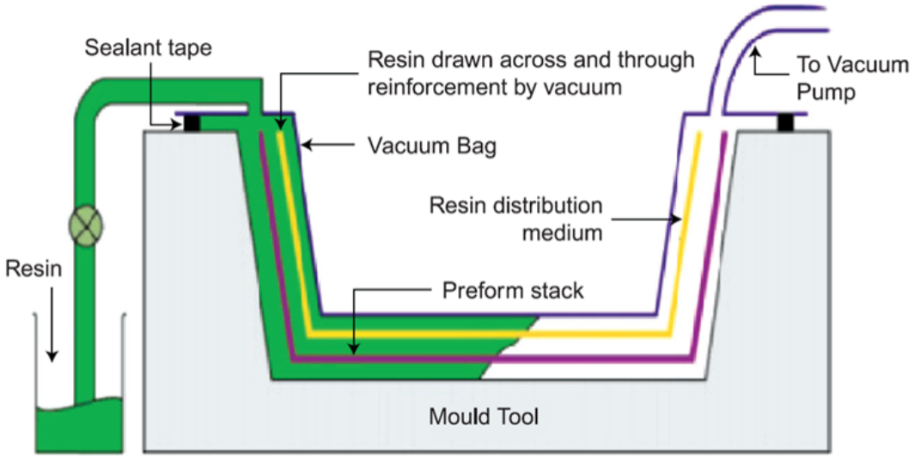

Figure. 5.3 V acuum assisted resin transfer moulding (VARTM) process, original source: NationalAerospaceLaboratoriesIndia, 2020

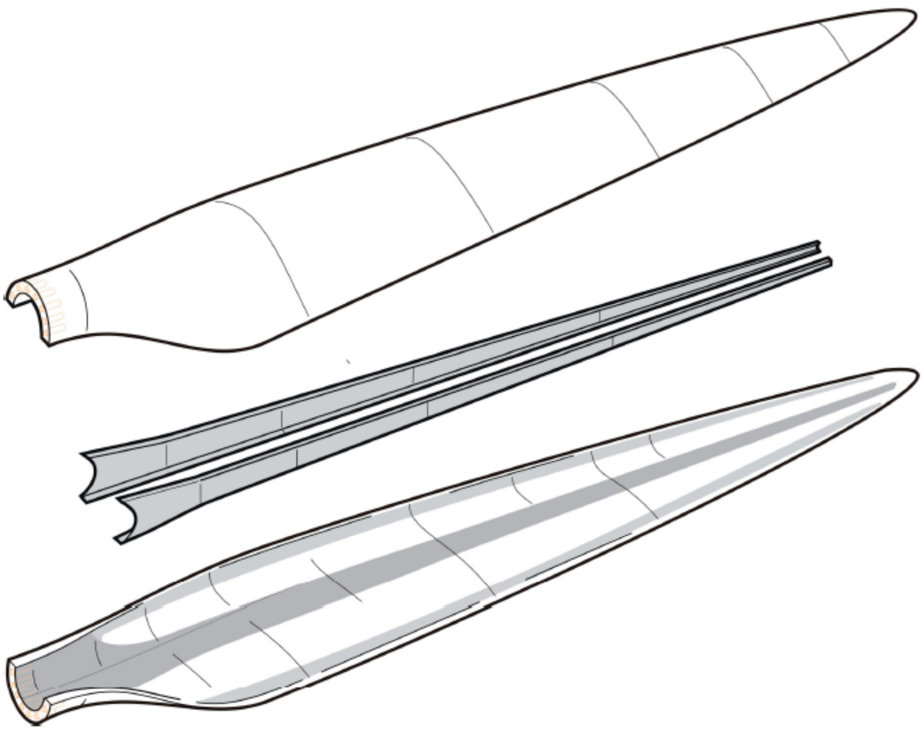

Figure. 5.4 Assembly of blade shells and addition of shear webs, original source: Mishnaevsky et al., 2017

After resin infusion, the blade shells are let to cure at room temperature. In some cases, the temperature is elevated i.e., the composite is post-cured by increasing the ambient temperature; this is a typical practice followed in resin transfer moulding (RTM), another variant of VARTM. Once the two halves or the PS and SS shells have cured completely, they follow one of two procedures (1) de-moulded separately and the shear webs are added and then the two shells are bonded together. or (2) shear webs are added to one-half and then the other mould with the shell folds over the shell with the shear webs and then the two shells are adhesively bonded. The procedure is demonstrated in Figure 5.4. Finally, the blade is taken out of the mould for trimming and polishing, sometimes finishing with a gel coat. For commercial and industrial sized blades, additional monitoring is conducted for quality control and to repair any manufacturing defects (wherever necessary). At present, with the development of technology and involvement of artificial intelligence (AI) practices, the composite manufacturing process with automated lay-up of tapes, automated fibre placement along with enhanced infusion, cure monitoring, damage and quality control techniques and finishing technologies are being explored. It is worth noting that two of the four top wind turbine manufactures, Vestas Wind Systems and Siemens Gamesa (SGRE) manufacture their rotor blades using the one-shot blade method where the blade is cast using single infusion process without any bonding with adhesives and shear webs as mentioned in Damiano and D'Ettore, 2018. Having explored these commercial manufacturing methods for operational scale wind turbine blades, these methods are not readily available or not suitable for laboratory scale blade manufacture. To explore this further, alternative manufacturing methods and procedures have been investigated in subsection 5.2.1 and section 5.3.

5.2.1 Solrun-Andri method of producing airfoils

The Solrun-Andri Method or male mould method developed at the University of Iceland uses a solid blade-like structure which is used to wrap the composite layers around to make the outside shell of the actual blade as described in Solrun Traustadottir, 2017. This layup is then covered with vacuum bag and infused with resin. After the infusion is completed and subsequently the part has been cured, the vacuum bag is then removed and the part is slowly and carefully pried out of the male mould manually. Typically, a wind turbine blade made using this method would then have to be adhesively bonded at the trailing edge joint running along the root to the tip of the blade. The main challenge in this method is that the performance of an aerofoil will be a combination of the surface finish and the fidelity/ accuracy of the leading edge shape. With this Solrun-Andri method the exterior surface of the airfoil/ blade part is outside and is determined by the vacuum bag, so is not as smooth as that of a blade produced using female moulds. To test this methodology, a 1.9 m long 3D printed blade like structure, printed using Leapfrog Xcel from Leapfrog, 2020 2 m long 3D printer was used. To begin this trial-run of the composite manufacture of the blade shell, a section starting from root to about 40% of the blade length was selected to be replicated using the male mould method. The rest of the process have been divided into several steps to allow for detailed explanation. A schematic diagram (See Figure 5.5) as well photos taken during the manufacturing process are provided below,

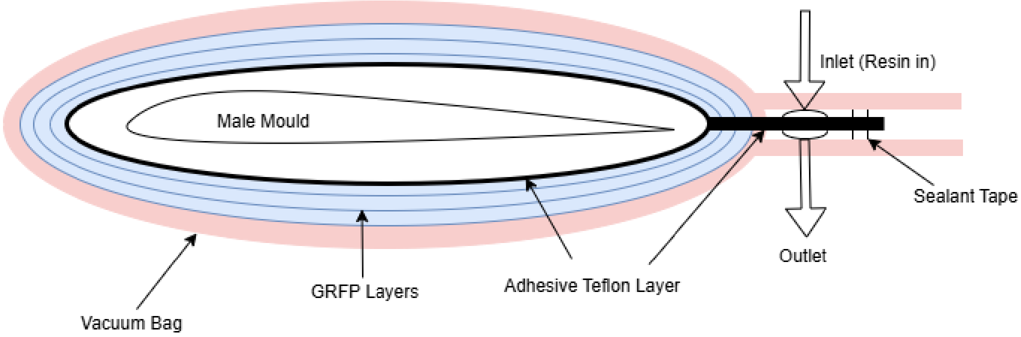

Figure. 5.5 Schematic Diagram for Solrun-Andri (Male Mould) Method

- To start this, step one covers the preparation process of the male mould itself. To elaborate, this structure was first wrapped with adhesive Teflon paper as shown in Figure 5.6 running from leading edge from the suction side to the leading edge of the pressure side. To remove the cured-composite shell later on, a few inches of extra Teflon tape was stuck together and left hanging. This would protect the male mould structure as well as create a space along the leading edge so that the shell can be popped off the male mould. Next, some tacky (sealant) tape was placed around the edges of the Teflon sheet for the vacuum bag to stick on later. This layer of Teflon sheet were wiped several times with mould release in 20 minute intervals so that the final composite can be popped out of the mould easily.

- Next in step 2, the fibre reinforcement assembly is done; i.e. three layers of bi-axial woven glass fibre is measured and cut to fit the selected section of the Teflon wrapped male mould. These layers are wrapped around the male mould as shown in Figure 5.7.

- In step 3: the inlet and outlet points for the resin transfer were marked and the pucks were added in the middle of the leading edge on the suction side and the leading edge of the other side (pressure side). Along with this, the vacuum bag was applied to the edges and sealed off with the use of the already attached sealant tape. After this, the inlet and outlet pipes were attached to the inlet and outlet pucks and were secured with more sealant tape to prevent air from going in and to maintain the vacuum inside. The whole structure was laid horizontally securing the root and tip section so that there was no twist or turn which would make the fibre layers inside slide off. This was implemented particularly to keep the fibre layers in place instead of leaving the structure normally on the ground, this can be seen in Figure 5.8.

- Step 4: With the resin mixed in with the hardener at the correct proportion, and with the vacuum pump running to maintain stable pressure inside the casting mould, the composite casting process was begun. Figure 5.10 shows the resin infusion on the reverse side.

- Step 5: Once the entire infusion process was completed, the pump was turned off and the composite was left to cure at room temperature. For the thickness and length of the composite, using a fast hardener with the resin, about 24 hours were enough for complete curing.

- The final step is the de-moulding process which was done carefully by prying the cured blade shell apart using hands. As the male-mould and the Teflon tapes were coated multiple times with the release agent, this helped in the part popping off the mould easily. Figure 5.11 and Figure 5.12 show the cured blade shell out of the male mould and the uneven, non-uniform surface finish on the outside of the blade shell.

Figure. 5.6 Step 1: Teflon tape around male mould

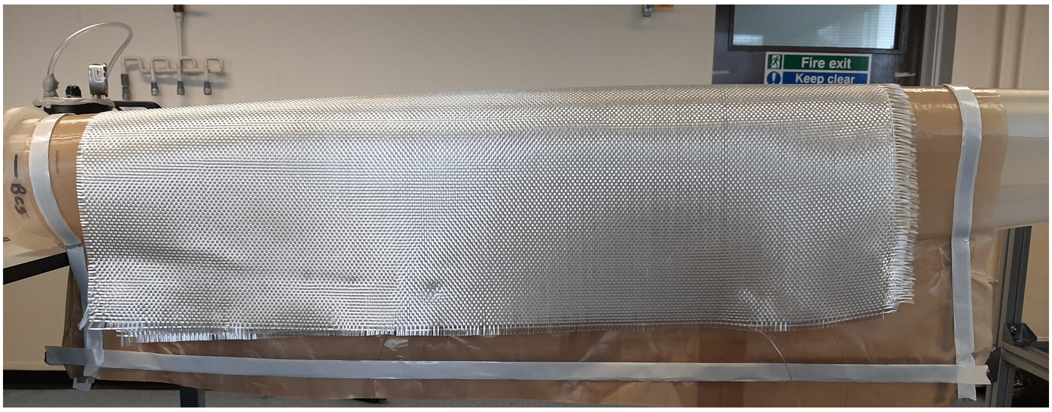

Figure. 5.7 Step 2: Fibre glass layers around male mould

Figure. 5.8 Step 3: Selection of inlet and outlet and application of vacuum bag

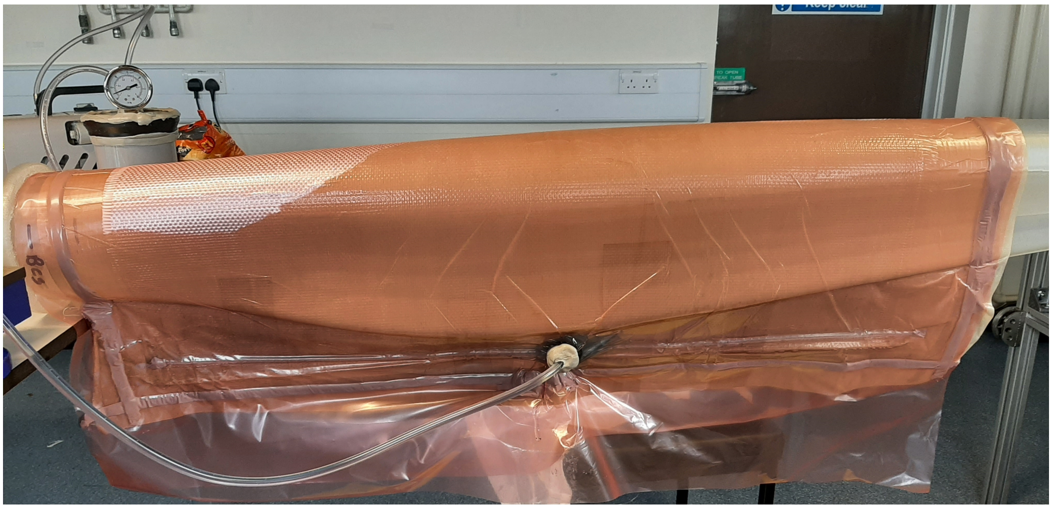

Figure. 5.9 Step 4: Resin flow over the surface from inlet going towards outlet on the other side

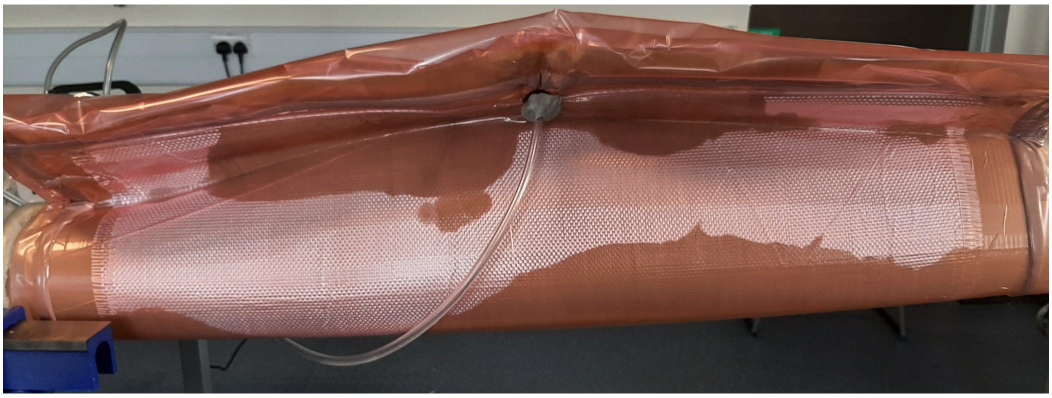

Figure. 5.10 Step 5: Resin reaching the outlet on the other side

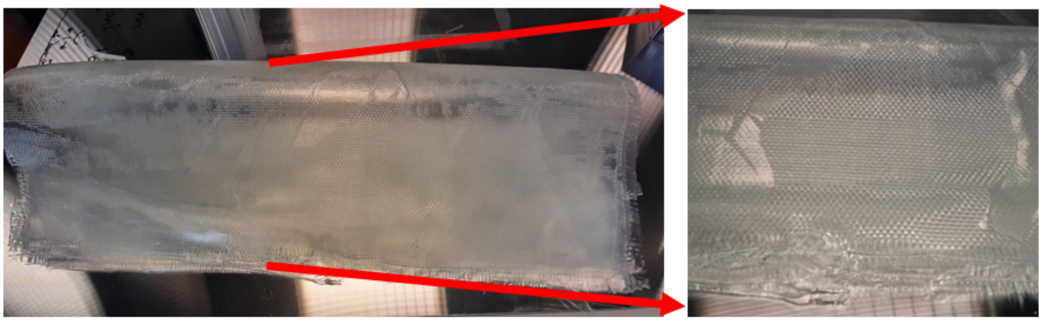

Figure. 5.11 Non-uniform surface finish on cured composite shell

Figure. 5.12 Cured composite blade shell removed from male mould showing the airfoil shape in the middle and the un-bonded trailing edge on the right

As mentioned earlier, the main challenge with this male-mould method is the surface finish of the blade structure as has been pointed out by the trial-run described above. This makes the use of an existing male mould and using this, it is theoretically possible for a scaled blade to be made in one piece, provided there are some changes in the methodology and design. Additionally, for smaller, aerofoil sections and wings, this method is much more feasible and efficient. However, for the design of the 1.8 m Hull Blade, with the trials shown above, making a male mould (inside structure) in one shot as well as the composite structure (blade/ outer shell) is a tricky process as the design is not straight and has got curvature at each blade station-geometry locations. This two-dimensional curvature of the blade leads to wrinkles in the reinforcement and the vacuum bag, causing unevenness in the blade surface. Removing the shell from the mould while keeping the lightweight, thin shell intact is also quite challenging once the structure has cured. This is susceptible to breakage where there is complex curved geometry. Furthermore, manufacturing a 1.8 m long scaled blade using this method also introduces new defective regions such as regions where resin hasn't reached, i.e. dry spots and voids and misalignment due to the unstable positioning of the male-mould during the infusion process. Along with this, to achieve a flawless fully infused and cured, full blade shell (as opposed to the half the blade length as shown in the trials above), this male-mould method needs additional refining and fine tuning. Due to these identified drawbacks of this method, the proven, generic method of making a blade using female mould has been followed to make the 1.8 m scaled blade.

5.3 Methodology: Hull Blade 1.8m Manufacture

The manufacturing of the 1.8m long Hull Blade started with the making of female moulds. These were designed in Solidworks and Spaceclaim and were based on the blade design described in detail in Chapter 4. A rectangular solid model with an extended edge was designed built around the blade part. Then, the core and cavity based on the blade was taken out to make the female mould. This was then split into two halves: pressure side (PS) and suction side (SS) parts to make two halves of the female mould. These two Solidworks models of the female moulds were then split and sliced in eleven sections radially and were 3D printed. These 3D printed sections were then arranged in the correct sequence and were bonded using adhesives. This process is less complicated than the typical computer numerical control (CNC) manufacturing method which is highly precise and accurate but very expensive and bulky during production. Generic Polylactic acid or polylactide (PLA) material was used for 3D printing of the mould as its parameters were somewhat suitable for printing these parts and PLA is the cheaper options compared to Acrylonitrile Butadiene Styrene (ABS) etcetera. The potential issues around porosity, infill density, and resolution were overcome by manually selecting these print settings for each parts individually so that the parts are strong and sturdy.

Figure 5.13 shows the 3D printed parts of the female mould stacked on a table in order and Figure 5.14 shows these printed parts adhesively bonded together and secured tightly so the parts are not moving during adhesive-drying/bonding.

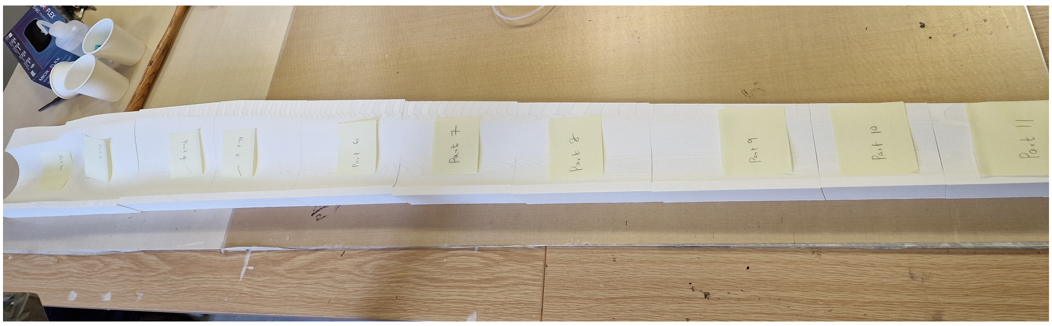

Figure. 5.13 3D printed female mould parts arranged in order

For both the PS and SS female moulds, the 3D printed parts were setup on an MDF board and after marking out each of the part's outline on the board, these parts were bonded with an industrial strength adhesive (Loctite Hysol 9466 Adhesive) to the board as well as to the adjacent parts. They were then clamped to secure any movement or gap that may occur which can cause misaligned sections within the female mould (refer to Figure 5.14). The use of the MDF board serve the purpose of easy handling during blade manufacture and moving/transfer between laboratory spaces. After the adhesive has completely cured and both the PS and SS female moulds have completely set as two individual parts, additional support were added using a few MDF board parts to create an extended top surface along the leading and trailing edges as well as the root and tip sections. This extension all around the core cavity of the blades was necessary to provide additional space during the fibre lay-up and vacuum bagging processes. The gaps between the PLA parts and the MDF boards were filled with special sealants to keep the moulds watertight so no resin would leak through as well as airtight to prevent the loss of vacuum. Additional support materials and fillers were used in the form of Polyfilla to make the extended supports sturdy. The inside of the 3D printed parts were sanded to make them smooth, so the fine lines of the 3D print were not creating any rough waves of resin flow or crevices on the outer surface of the blade shells. Additionally, a thin coat of laminating resin was painted on to the inside of both the female mould to smooth any imperfections after sanding. Final sanding of the female mould was done using sandpapers of finer grit to produce smooth, glossy finish on the inside of the moulds. Necessary lab-safety procedures were carried out and followed during female mould manufacturing process.

Figure. 5.14 Female mould parts adhesively bonded together

Next, both the prepared female moulds were treated with polishing compound by applying a bit of the polish on the inside surface and rubbing it on the surface. These surfaces were next cleaned with mould cleaner four times in 20 minute intervals, to remove any residual polish, dirt and other impurities left during mould preparation. With both the pressure-side and suction-side moulds cleaned and prepared, the final step before the fibre layers are carried out with the application of the mould release. Similar to the application of the mould cleaner, the mould release agent was applied to the entire surface of the mould and all corners for five times in 20-30 minute intervals letting each application dry off before applying the next coating of mould release agent. Subsequently, the fibre mats to build the composite layer were assembled.

For the composite layer, chopped strand mats were cut to fit the blade shell design. As the blade shells have curves incorporated in their geometry, this task was carried out using Solidworks by flattening out the female mould model/ design and by accurately measuring the area of the fibre mat that is required. Cutting lines wherever necessary were identified using this Solidworks flattened model. For both the "healthy" and "defective" blades, 4 layers of chopped strand were cut for each blade shell/ blade. In the "defective" region of interest (ROI) which has an area of reduced stiffness, no chopped strand fibre was used. The making of the defect is described in detailed in the next section section 5.4. Apart from the chopped strand mats and resin, the other two materials used to make up the composite layers were the peel ply and flow distribution media. These materials were assembled in this particular order; (1) Peel-ply (2) Chopped strand glass fibre layers (3) Flow distribution media and then (4) Vacuum bag layer. Before applying the vacuum bag, these layers were kept in place by dabbing a little bit of the prepared resin in and around the dry peel-ply, fibre glass layers.

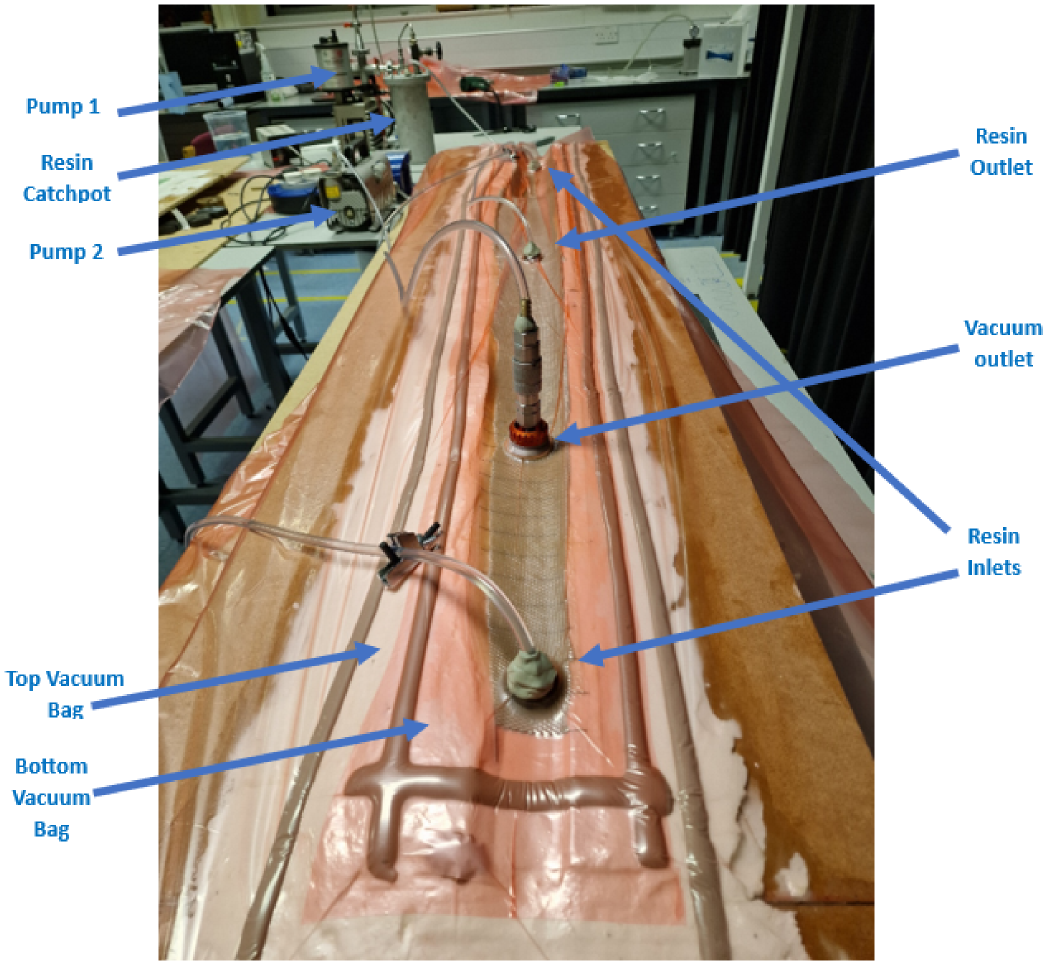

Figure. 5.15 Components used for resin infusion of blade shell

Before starting the infusion process, a few key steps were followed. To increase the effectiveness and the efficiency of the resin flow during infusion, two layers of vacuum bags were utilised and two pumps were used. The first boundary of tacky tapes were taped around the female mould for the vacuum bag which comes in contact with the resin and composite layers. The second set of tacky tapes were applied around bigger boundary around the first boundary of tacky tapes to be used for a bigger vacuum bag area to ensure a good vacuum which in turn ensures fast infusion and good quality finish of the blade part. Both vacuum bags were sealed carefully with the use of the tacky tapes and pressed on further to prevent air from coming in/ vacuum pressure leaking. These components can be seen in Figure 5.15. The resin was then mixed with slow hardener in 100:30 ratio as mentioned in the IN2 Epoxy Infusion Resin's data sheet supplied by Easy Composites UK. For the slow hardener, the mixed resin provides about 95-115 minutes pot-life which was deemed enough time for the whole infusion/ resin flow to be complete. The two components were measured accurately using a digital weighing scale and mixed thoroughly for 2 minutes using a mixing stick. The mixed resin was then let to stand for 5 minutes to allow air bubbles to escape. This process is known as degassing. For one half of the blade, i.e. either PS or SS shell, about 400 g of resin and about 120 g of slow hardener was used The temperature in the lab was kept stable between 22°C to 25°C as the recommended working ambient temperature suggested by resin manufacturers were 20°C to 25°C. The lab windows were kept open to aid ventilation and avoid overheating of resin in the pot during the whole infusion process. Again, for the whole infusion process, necessary lab safety practices were followed by wearing gloves, goggles and lab coats. The data sheets can be found in Appendix E.

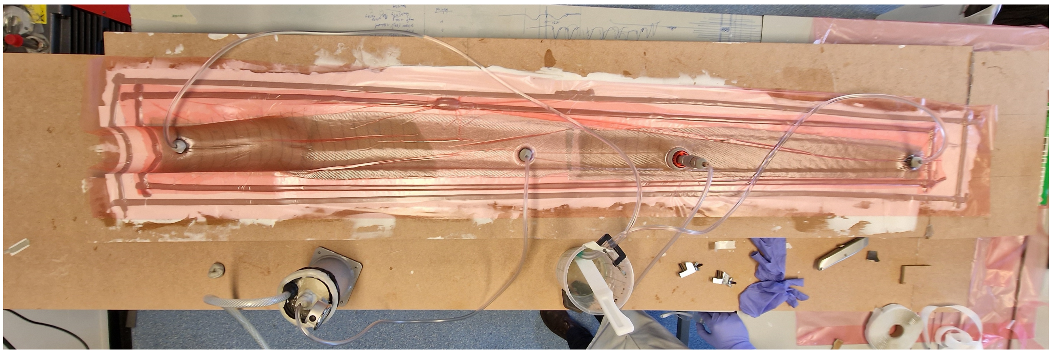

Figure. 5.16 Infusion using female mould

For the composite-vacuum bag set, two inlets were taken at the root and tip of the blade shell respectively and one outlet was selected to be in the middle of the blade. One outlet for the bigger vacuum bag (top vacuum bag layer) was also selected to be between the 1st vacuum bag layer (bottom vacuum bag layer). Additionally, the inlets and outlets were inserted with the tubes for resin transfer and all tube ends were secured with the tacky tape to prevent air from coming inside the vacuum bags. As seen in Figure 5.15, both inlet tubes were also secured with clamps to control the resin inflow as well as excess resin from going in after resin inflow was complete. This resin flow process were monitored by eye, i.e. the wetting of the composite layers and the resin coming out of the outlet after reaching all surfaces and corners of the composite layer. This is depicted in Figure 5.16.

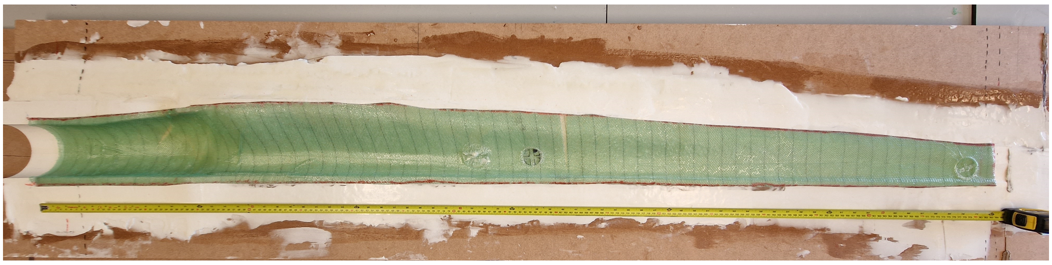

Figure. 5.17 Cured composite blade shell

Once the infusion process was complete and the inlets were sealed off with the outlet still open for the flow of excess resin out of the mould, both the pumps were kept running overnight to maintain the vacuum pressure constant and to aid in the efficient transfer and flow of resin to all corners and surfaces of the mould. After about 10-12 hours since the start of the infusion and maintenance of the vacuum pressure using the pumps, the pumps were turned off and the composite structure was let to cure. For this scale of structure, since the resin was mixed with the slow hardener, about 24 hours were required for complete composite cure. The temperature of the lab was increased slightly to 25°C to 27°C to aid faster curing time.

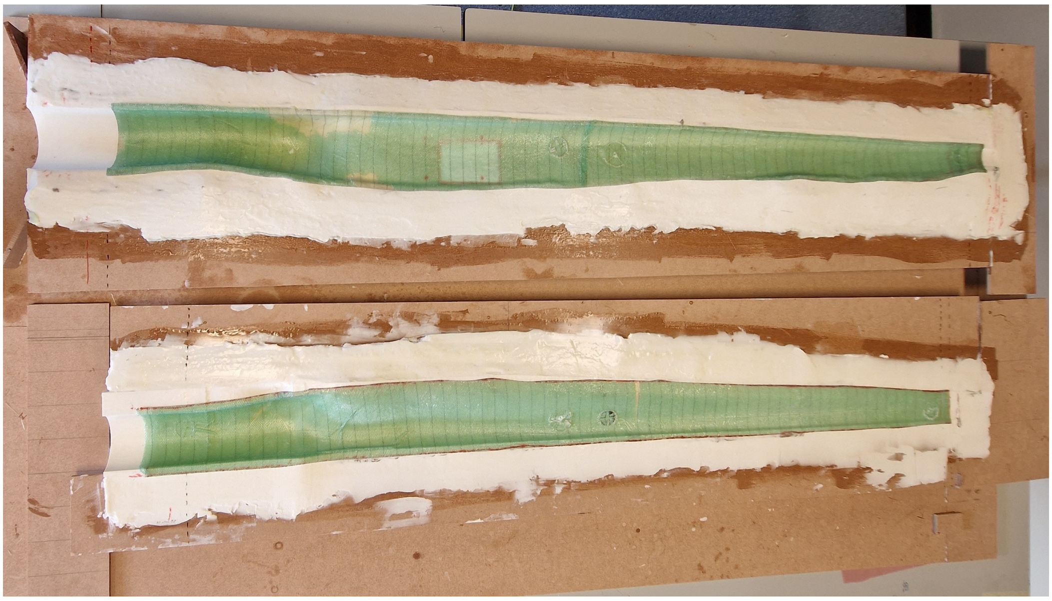

Figure. 5.18 Cured composite blade shell both PS and SS

After the PS and SS shells have completely cured, both shells were de-moulded carefully by removing the vacuum bag layers. The peel-ply on top of the shell was peeled off and the two shells were carefully joined together temporarily using scissor/ spring clamps along the leading and trailing edge. This was implemented to arrange the LE and TE of both shells aligned with each other to maintain the correct airfoil profile from root to tip. Once these two are aligned perfectly, using the two-part adhesive epoxy both shells were joined and clamped again using spring clamps to secure the shells from moving and prevent misalignment. As the flow distribution media does not have any impact on the structural strength inside the shell/ blade, it was left on the shell. Thereafter, the bonded blade was taken to the mechanical workshop and excess composite along the leading and trailing edge was trimmed off. Gaps found along the leading and trailing edge were sealed again with the two part epoxy wherever necessary. The excess length at the root were trimmed and then bonded to the adapter plate using the same two-part epoxy. Furthermore, the surface of the blade was then sanded with a fine grit sandpaper/ sanding blocks to remove dried resin residue, and trimmed edges were sanded and filed manually using hand-held flat engineers files to smooth the roughness as seen in Figure 5.19.

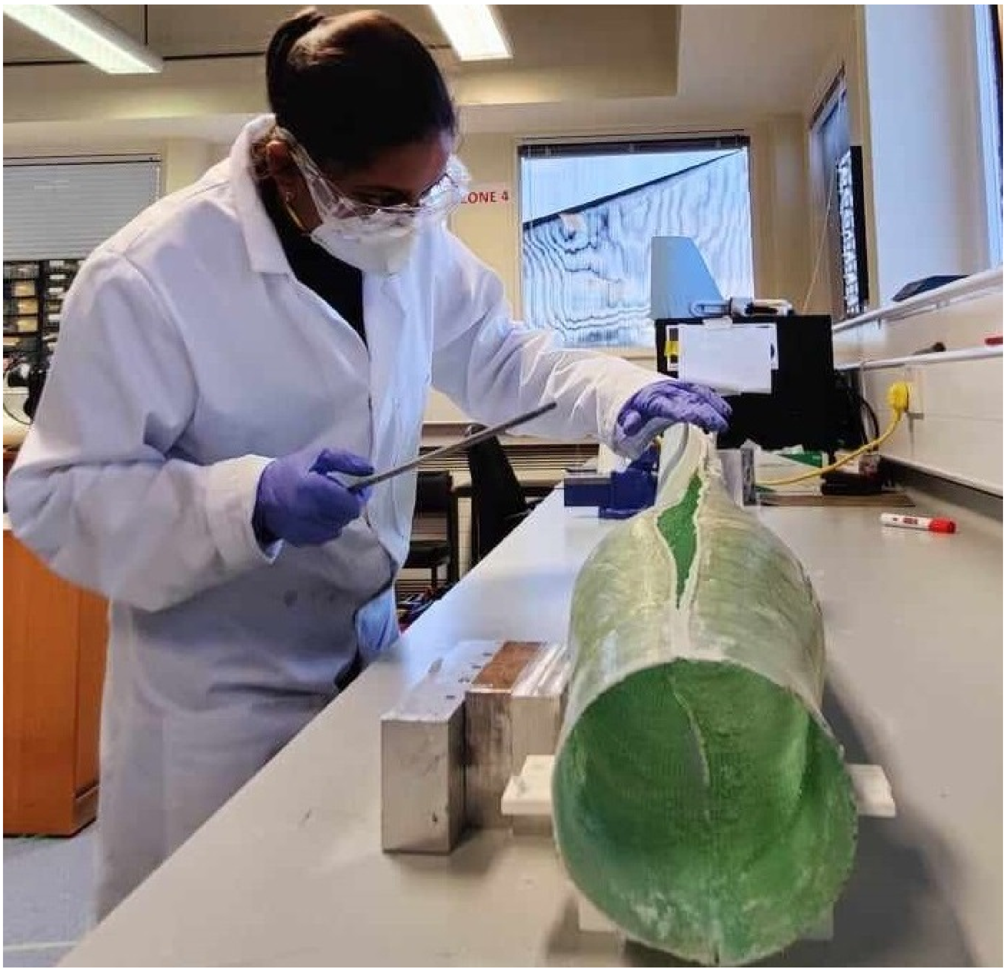

Figure. 5.19 Sanding and filing the Leading and trailing edge

In a typical wind turbine blades or even in scaled blade structures, spar caps are found and play an integral role in load bearing. Primarily, the pressure side shell works in tension and the suction-side shell works in compression from root to tip and transfer them to the cylindrical section at the blade root. Shear webs also important as they keep the PS and SS shells separate and away from each other while allowing the blade to behave as a beam and to retain its global stiffness Bladena, 2021. In commercial-scale wind turbine blades, spar caps and shear webs are essential for maintaining the mechanical integrity and load-bearing capacity of the structure. Spar caps, located along the tension and compression sides of the blade, resist bending moments and enhance the blade's strength under loading. Shear webs, positioned between the spar caps, help keep the pressure and suction sides of the blade from separating and ensure uniform load distribution, preventing structural failure (Bladena, 2021, Veers et al., 2023). These components are particularly important for large blades subjected to high operational loads, where their absence would significantly reduce the blade's stiffness and performance. However, in the design of the 1.8 m Hull Blade, spar caps and shear webs were intentionally excluded. This decision was driven by the blade's specific testing purpose: to evaluate the performance of FBG for strain measurement and defect detection when surface-bonded. The small size of the blade (1.8 m) and the low applied loads (0-50 N) make spar caps and shear webs unnecessary, as they do not significantly affect the load-bearing behaviour under these conditions. As long as the blade's design remains similar, with the only difference being the defect at a specific location, the load-bearing capability is unaffected. Therefore, spar caps and shear webs are not needed, and their absence does not influence the mechanical performance of the blade for the intended testing purposes (Bladena, 2021, Veers et al., 2023). Nevertheless, for advanced testing using the same blade design, i.e. fatigue testing under cyclic loads, or dynamic testing/ modal analysis at higher frequencies, spar caps and shear webs should be included in addition to the current design/ model.

5.4 Methodology: Introduction of Defect

Most composite structures are inevitably built with defects, However, not all defects are identical or lead to critical damages. Defects can have different shapes and characteristics, which may lead to different damage severity if they grow as mentioned in Chen, Semenov, et al., 2021 and Phelps and Singleton, 2011. This is discussed in detail in Chapter 2 of this thesis. Typically, there are a few considerations when designing artificial defects in wind turbine blades for the sake of testing the performance of sensors and SHM systems. Some of these factors are listed below,

- The type of defect should be typical and appropriate for the wind turbine blade structures.
- The defect should be easy to reproduce by other researchers, i.e. the defect specifications/ characteristics should be well documented.
- The defect initiates damage that grow under fatigue loads (only if fatigue tests are being conducted as part of the investigation)

Some of the typical types of defects found in wind turbine blade testing are laminate wrinkles in spar caps, skin laminates and core material de-bonding in sandwich panels or adhesive joint de-bonding in leading or trailing edge or between the shear web and spar caps. These are however, typical for defects that grow under fatigue loading or which can be testing under cyclic loading test set-ups. Other types of defects are patches that are improperly cured/ dry spots which have weak infusion of resin and voids which have trapped air/ air pockets embedded within the composite layers. These structural defects which occur during the manufacturing process can either grow during the operational phase may lead to sudden serious damage or cracks or breakage during operational phase due to cyclic, inertial and stochastic loads. Further description of manufacturing defects and their behaviour is explained in Chapter 2.

For the purpose of testing the fibre optics sensors for this PhD work, following the preliminary sensor characterisation described in Chapter 3, a resin rich or an area with no fibre glass material present was chosen as the artificial defect introduced in the blade. From a numerical simulations perspective, the area with no glass material can be considered as an area with modified stiffness. This type of defect was selected as it can be easily produced/ introduced in the blade during the composite manufacture of the blade and it can be reproduced for any future investigations as well.

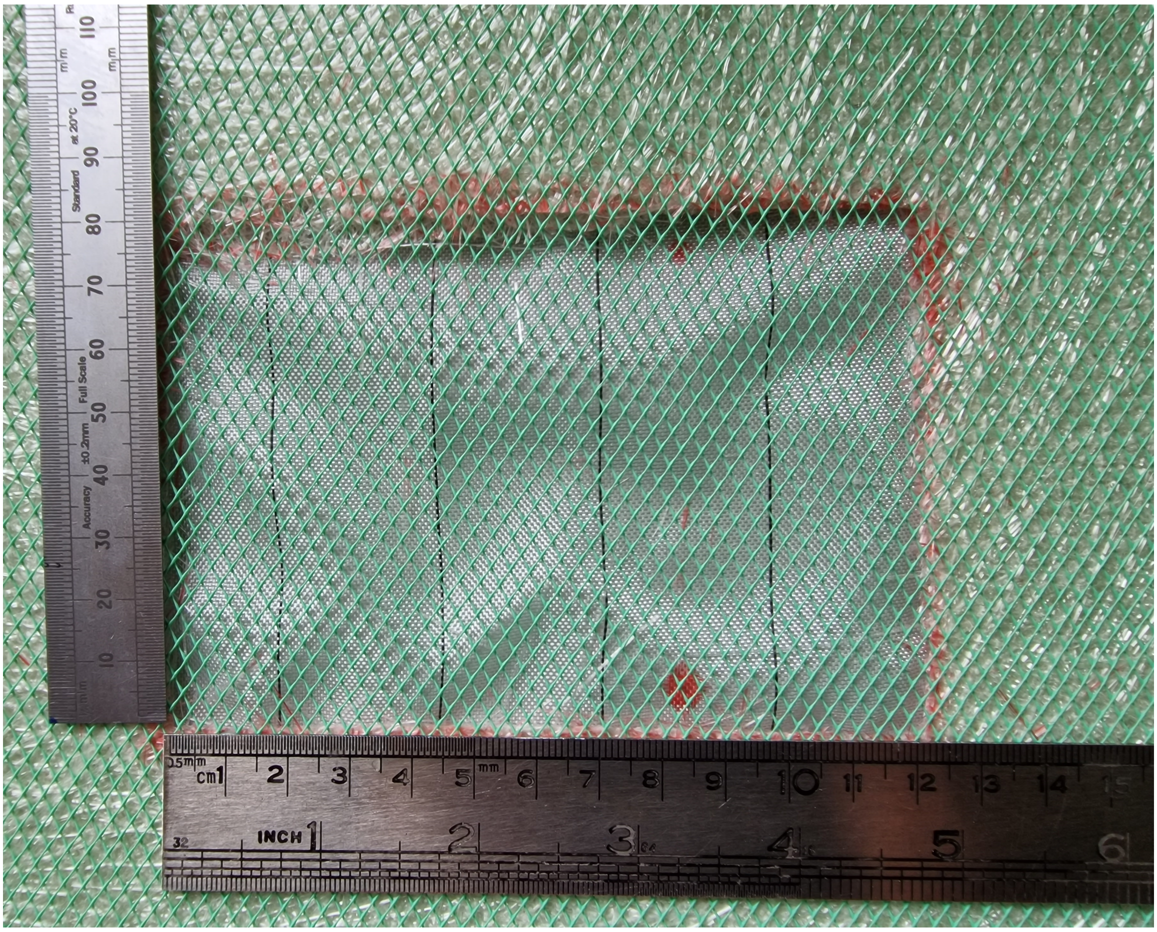

Figure. 5.20 Dimension of composite defect

The defect area was determined as a 80 mm x 140 mm area with no glass fibre material as shown in Figure 5.20. To achieve this, the area was measured and cut off from the fibre glass layers selected for the pressure side. This defect was designed to be at a distance of approximately 600 mm from the root (about 1/3 of the total blade length) and 30 mm from the leading edge. Typically, in a wind turbine blade, the transition region, i.e. the region where the geometry of the blade take the form from cylinder to airfoil shape, shows the highest strain when tip loaded as mentioned in Batay et al., 2023 and Schubel and Crossley, 2012 and the bending moment is the largest at the root. This is true regardless of the presence of the internal spar caps or shear webs. As mentioned previously, these internal structures do most of the load bearing compared to the rest of the blade span. This has also been verified using the cantilevered composite beam set-up previously, where the strain measured high values near the region close to the fixed end when the load was applied near the free end (tip). Therefore, this 600 mm location was chosen for the blade experiments in particular so that during tip-loading, the FBGs bonded later on would read a higher strain as the defect is close to the root of the blade and the smallest variations in strain can be easily monitored. It should be noted that the smallest variation in strain is not the same as small strain values. Based on the previous FBG characterisation experiments on the composite beam with and without a defect, the FBG should be able to detect large strain (magnitude) under applied loads while also capturing small variations in strain caused by the presence of the defect. These small variations are determined by subtracting the strain measured in the absence of the defect from the strain measured in the presence of the defect, allowing for a precise evaluation of the defect's influence on the structural response. As the peel ply and the flow distribution media do not provide any structural strength, both those components were left as they were throughout the investigation and were not taken out pre-infusion or post-curing.

Then, the typical steps for composite manufacture as mentioned in the previous Section 5.3 were followed.

Unlike the composite beams manufactured for the FBG characterisation explained in the Chapter 3, the scale of this blade as well as the defect is much bigger compared to the scale of the composite beam and its defective region. The main advantage of working with a bigger structure is the the ease of controlling the edges of the defined defective region when it is being introduced or manufactured. Any fraying of the edges would only affect a small portion of the defective area, making it relatively easier to keep the reinforcement layers in place and achieve a completely fibre-free, resin-rich patch compared to the composite beam case, primarily due to the size of the defective region. The application of vacuum bag and the vacuum sealing was carried out carefully as not to disturb and move the adjacent glass layers into the determined defective area. By dabbing some mixed resin to keep the layers in place aided in executing this without any complications. Figure 5.21 shows the difference in thickness after the application of the vacuum, clearly showing the structural "defect" and its edges. This thickness was measured using a digital calliper before the blade shell was bonded to the other blade shell.

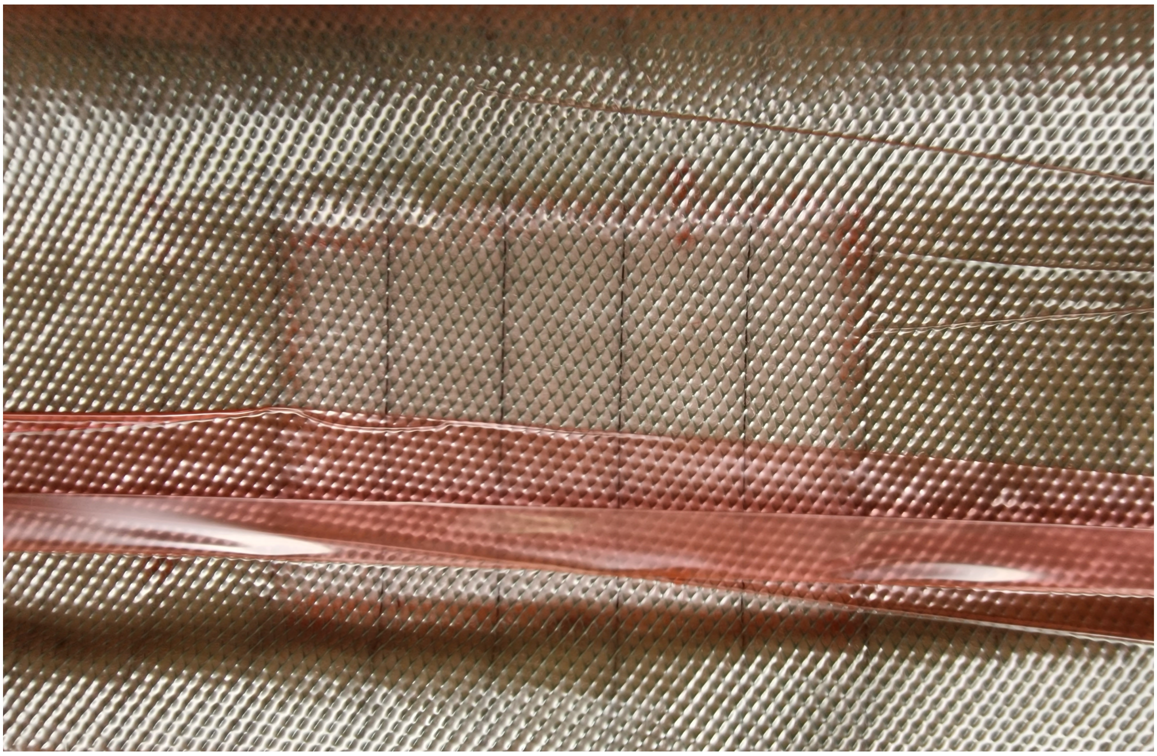

Figure. 5.21 Composite defect

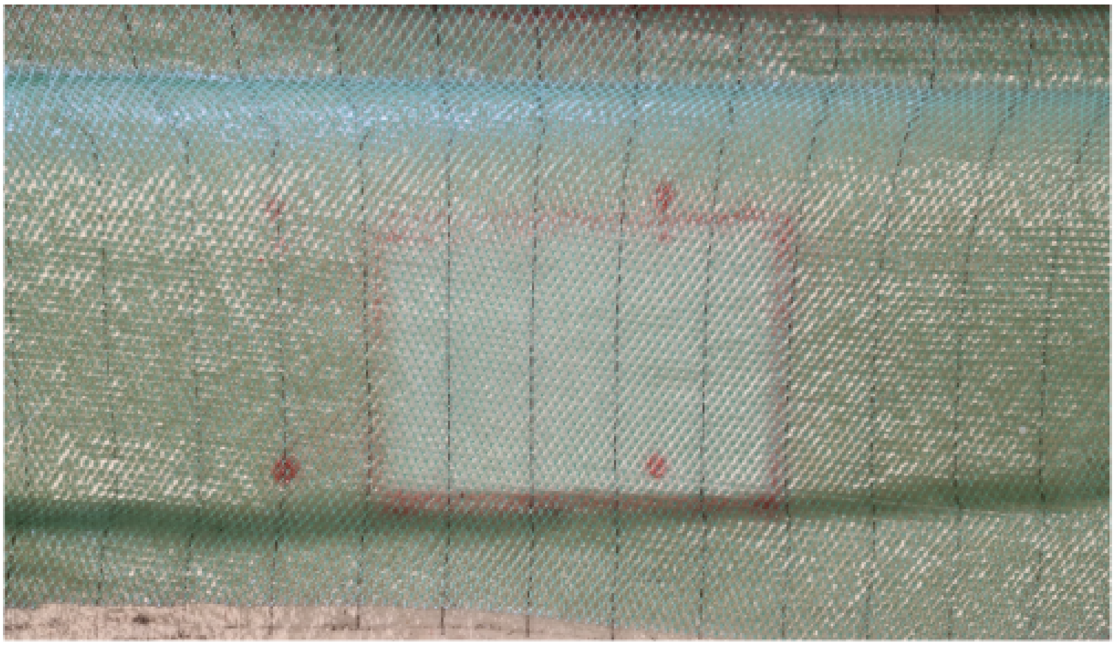

(a) inner surface

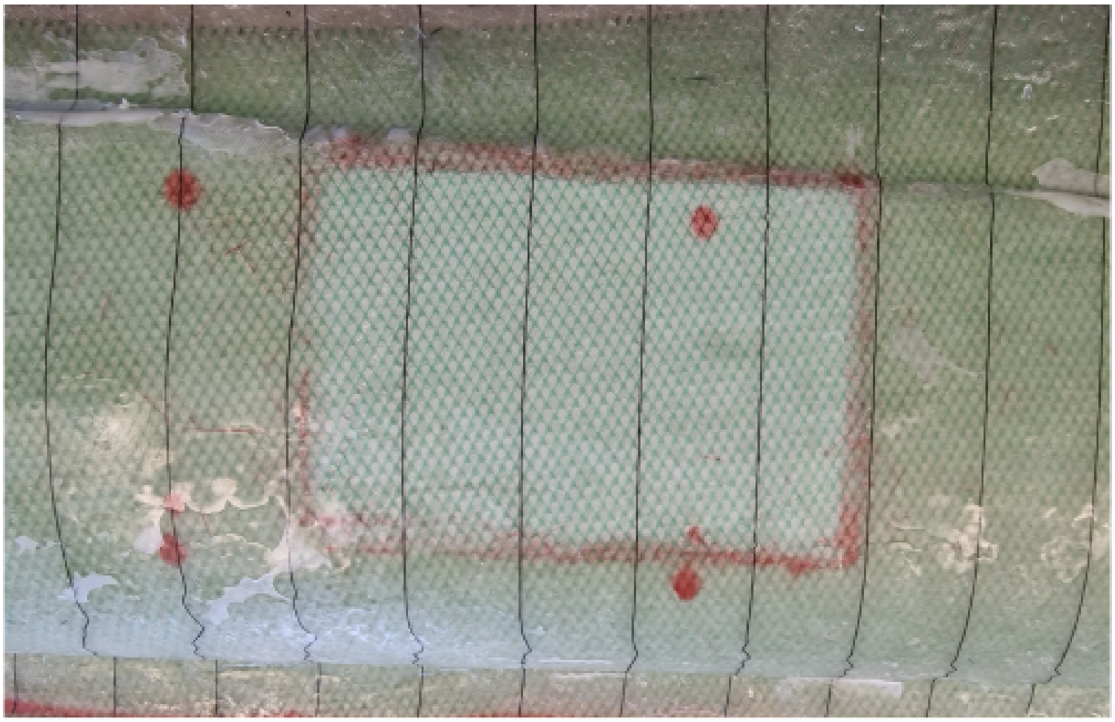

(b) outer surface

Figure. 5.22 Cured composite defect on (a) inner surface (b) outer surface

Figure 5.22 shows the composite defect on the inner and outer surface in the pressure side shell of the blade respectively. On the outer surface especially, it can be seen that the surface finish has some unevenness and some rough patches of dried resin layers. As these were insignificant rough patches which do not contribute to the overall strength or stiffness of the blade shell, they were removed easily by running a sand paper on top to make the surface smooth and even.

5.5 Design of Test Platform

Following the cantilever beam setup design described in the secondary sensor characterisation Chapter 3, the experiments and tests involving the "healthy" and "defective" blade consists of a L shaped test platform made from two modular pieces of high strength structural steel (refer Appendix D: technical CAD drawings). The vertical plate is 320 mm wide x 526 mm long x 40 mm thick. The base plate of this test stand has a thickness of 30 mm x 320 width x 400 mm length and has M-6 screw holes every 25 mm x 25 mm which were used to attach the base plate to the optical table as shown in Figure 5.23. The vertical part of the 90° test platform has a circular hole throughout for an adaptor plate to be fixed with eight M-8 screw holes to attach the adaptor plate of the blade root. The main features for this test platform design were adapted from Cairns et al., 2011, Valyou et al., 2015 and Desmond et al., 2015.

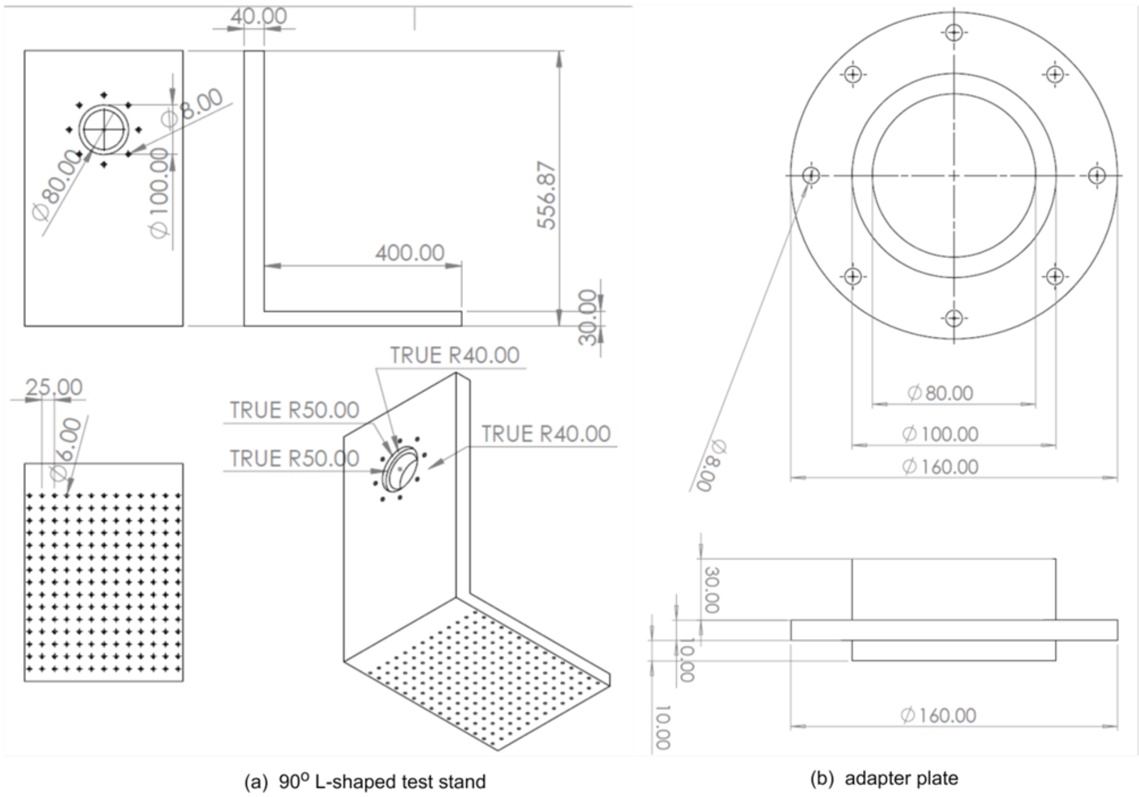

Figure. 5.23 Design of (a) 90° L-shaped test stand and (b) adapter plate for blade root

The blade adapter plate is specific to this blade root which potentially can be used in angular orientations of increments of 45 degrees (0°, 45°, 90°, 135°, 180°, 225°, 270°, 315°). It was made out of high-grade Aluminium and consists of a inner flange of 30 mm which was used to bond to the inside of the blade root and an outer flange of 10 mm which was used to insert and fix into the L shaped test platform. The adapter plate was then bolted in securely to the L shaped test platform as shown in Figure 5.24. In total, two adapter plates were made by the mechanical engineering workshop at the University of Hull to fit into the "healthy" and "defective" blade. By permanently bonding these plates to the blade, they were also useful in transferring and moving the blades within the laboratory spaces. The technical CAD drawing from the Solidworks design used for the machining at the workshop is attached in Appendix D. The blade orientation was changed several times to accommodate the different blade angles required for different loading scenarios and this was done by rotating and changing the position of the bolts at the root at the test platform. These orientation and angles are explained further in the next chapter. Figure 5.25 show the entire test stand assembly together with the 90 degree L shaped stand, adapter plate bonded with the blade root and the 1.8 m

Hull blade.

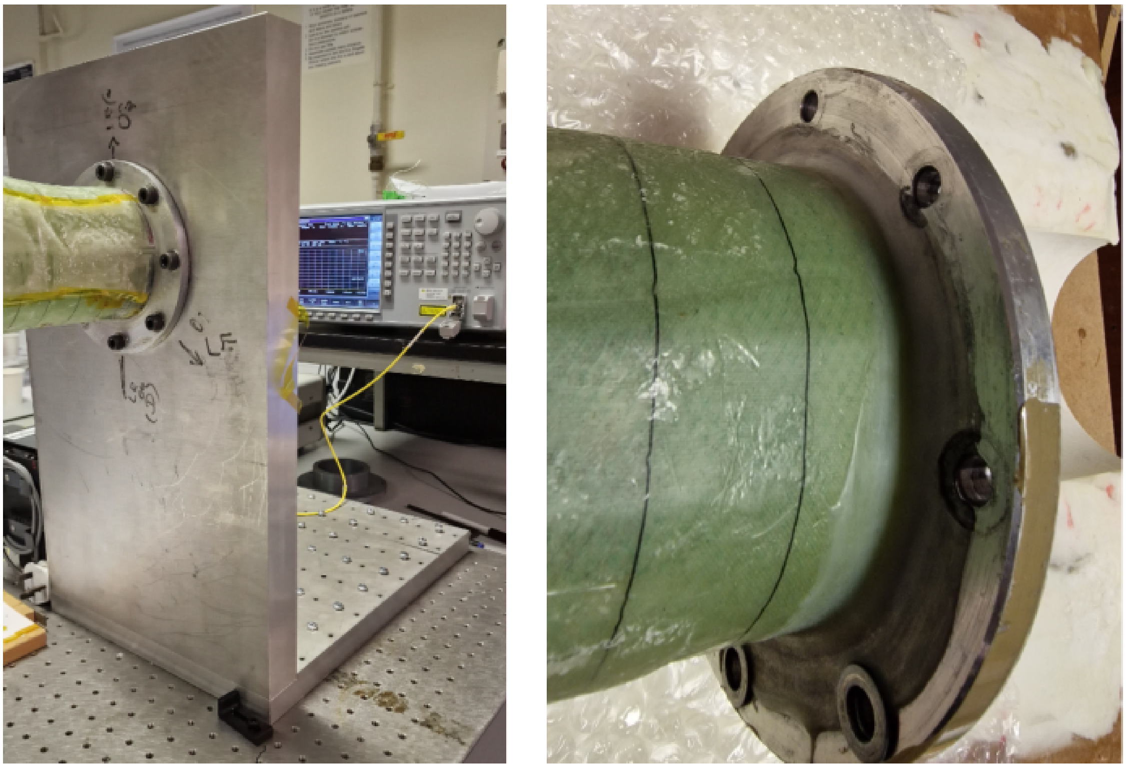

(a) 90° L-shaped test stand   (b) adapter plate attached with blade

Figure. 5.24 Photo (a) 90° L-shaped test stand attached with blade mounted on optical table and (b) adapter plate attached to blade root

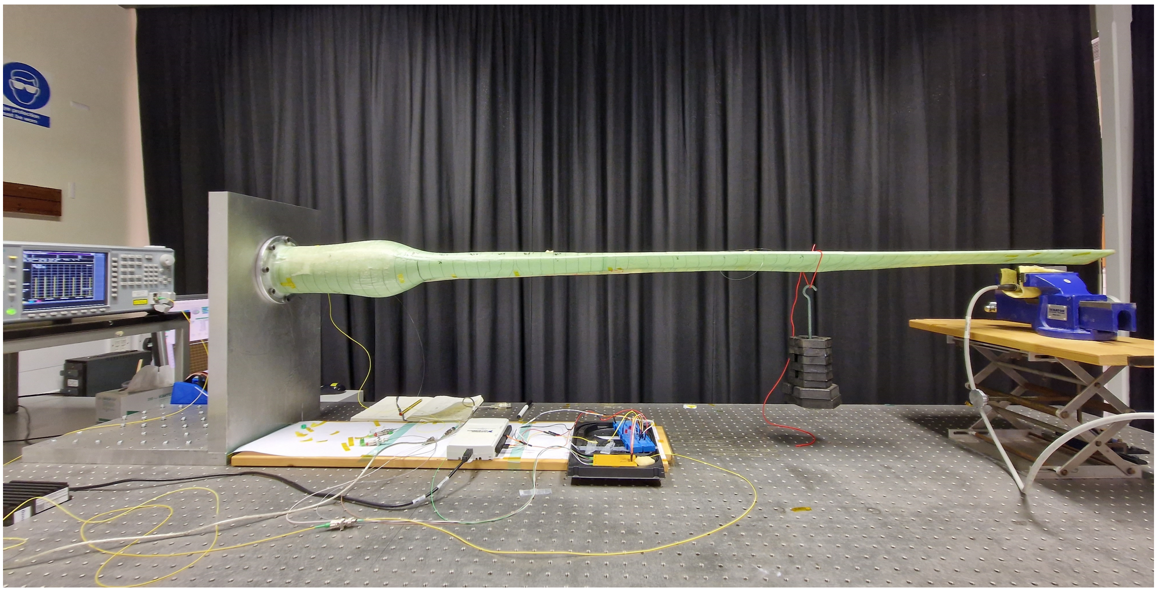

Figure. 5.25 Test Stand Assembly with Blade

5.6 Conclusion

In this chapter, the methodology for manufacturing the 1.8 m Hull Blade, a scaled composite wind turbine blade, was thoroughly outlined, detailing the processes from the creation of the female moulds to the final assembly of the blade. The design and construction of the composite structure, including both "healthy" and "defective" blades, were described in depth, focusing on the materials used, the step-by-step procedures, and the innovative techniques applied throughout. Notably, a relatively new approach to manufacturing composite structures with airfoil geometry was explored, using 3D printing for the female moulds, which proved to be a cost-effective and flexible method compared to traditional CNC machining.

A key aspect of this work was the introduction of the composite defect in the "defective" blade. This defect, created by intentionally removing glass fibre from a specific region (absence of reinforcement resulting in a resin-rich patch and reduced thickness), was designed to simulate and be representative of common manufacturing defects such as voids or delamination. The method for introducing this defect was carefully detailed in Section 5.4, providing a reproducible and controlled way to create the defect for testing purposes. The chapter also covered the design of a custom test platform, featuring a modular 90° L-shaped steel stand and an adapter plate for securely mounting the blade in various orientations, ensuring consistent testing under different loading scenarios. This setup facilitates precise evaluation of the blade's performance, particularly in relation to FBG sensors for strain measurement.

The methodologies described in this chapter, including the composite fabrication, defect introduction, and test platform design, lay the groundwork for the subsequent experiments and analyses detailed in the following chapter.

Chapter 6

Implementation & Testing: Static Loading Setup

6.1 Introduction

This chapter on the implementation and testing of the Hull blade is divided into several sections. The first section explains the necessary equations and assumptions used for the investigation of the estimated strain and the need for simplifying the cross sectional moment of inertia in both the X and Y directions. The distributed parameters consisting of structural properties such as blade length from root, thickness and width of blade are also given to support the calculations conducted. This is explained in detail for both the healthy and defective blade case. With this, the expected strain for a sample sensor array is discussed exploring the effect of defect on the expected strain. The subsequent sections of this chapter introduces and outlines the testing methodology undertaken by the author for wavelength division multiplexed (WDM) fibre Bragg grating (FBG) sensor characterisation for load monitoring and defect detection of the 1.8 m Hull blade. The experiment setup, static loading locations, sensor array mounting positions on the blade are provided in detail. Additional test setup for measuring blade tip displacement under varying loads and the detailed description of the testing procedure for all test cases/ scenarios undertaken and the specifications of all sensor arrays are also explained. Results obtained from both the healthy and defective blade test cases are provided in the next chapter along with the discussion.

6.2 Evaluation of cross sectional properties of blade

As the blade is a complex shape with non-linear geometrical properties, estimating the cross-sectional properties such as the second moments of area in the X and Y direction I_{xx} and I_{yy} require some key considerations. In the previous chapters, the preliminary sensor characterisation has been done on the basis of viewing the blade as a beam or a beam like structure. For the scaled blade experiments however, this theory is not accurate hence sensible assumptions should be made and valid numerical methods should be followed. For this, from a numerical calculations perspective, from the root up to the transition region, the blade has been approximated as a cylindrical shell and the from the transition region to the tip, the hollow blade shell has been approximated as an elliptical shell. Additionally, the scaled blade design and CAD model were used to verify and validate the cross-sectional properties of the manufactured blade. This is conducted mainly due to the fact that these cross sectional properties of the manufactured blade cannot be measured directly without physically altering (cutting-up) the blade structure.

From the design, the thickness and width from the blade root to the tip are taken as the thickness and the width of the inner surface of the blade shell (cavity). By including the thickness of the manufactured 1.8 m Hull Blade, 4.6 mm was added to both the thickness and width to represent the outer surface of the blade shell. As the thickness of the composite layer is uniform across all blade stations and cross-sections, ranging from root to tip for the healthy blade, the 4.6 mm thickness was consistently applied throughout the blade shell.

This difference in thickness compared to the composite beam used in the numerical modelling (3 mm) is due to variations in the manufacturing process. While the composite beam, being a straightforward rectangular slab, is relatively simple to cast, the blade shell (including the pressure and suction sides) is curved and requires multiple layers of glass fibre. After curing, the measured final thickness of the composite shell for the blade was 4.6 mm, reflecting the added complexity of its geometry and layering process. Due to the complex shape of the blade and the inability to access the inner cavity, the precise thickness of the shell could not be measured at all points. However, the thickness of the reinforcement layers was consistent across the structure, so the thickness was assumed to be uniform, except at the defect location.

From these structural parameters used in the model of the blade from Spaceclaim and Solidworks, the second moment of area in both X and Y axial directions as well as the X, Y, and Z coordinates of the centroid for each blade station (each airfoil section) has been obtained.

This is done by using the measure option and by extracting the mass properties of each planar face of each airfoil section at each blade station as shown in Figure 6.1 This also shows the distribution of airfoils from root to tip of the 1.8 m blade along with the outer shell surface modelled in Solidworks.

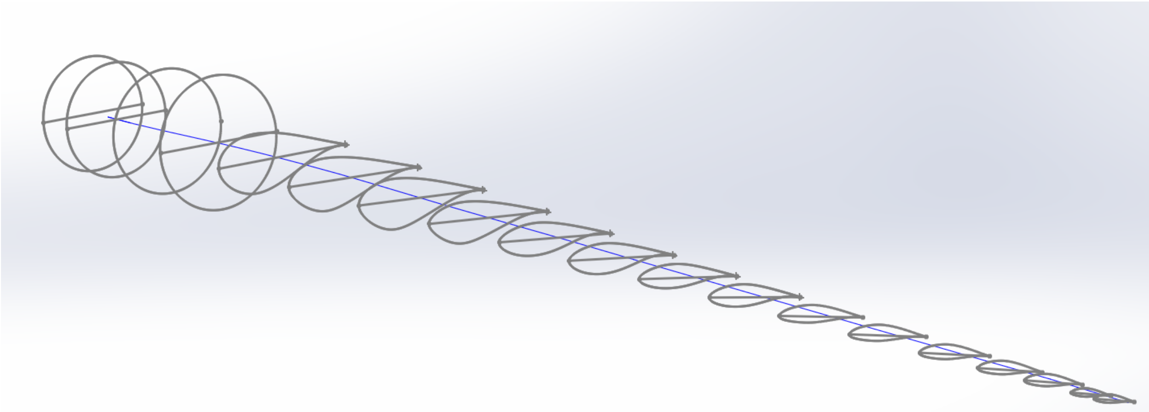

(a) Distribution of airfoils throughout the 1.8 m blade

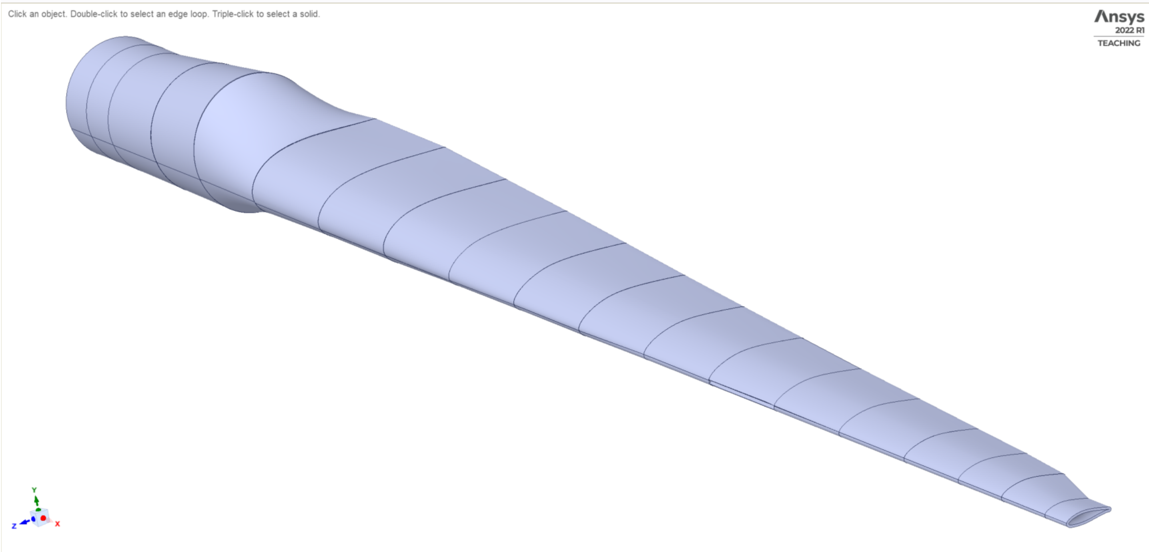

(b) Shell model of 1.8 m blade in Solidworks

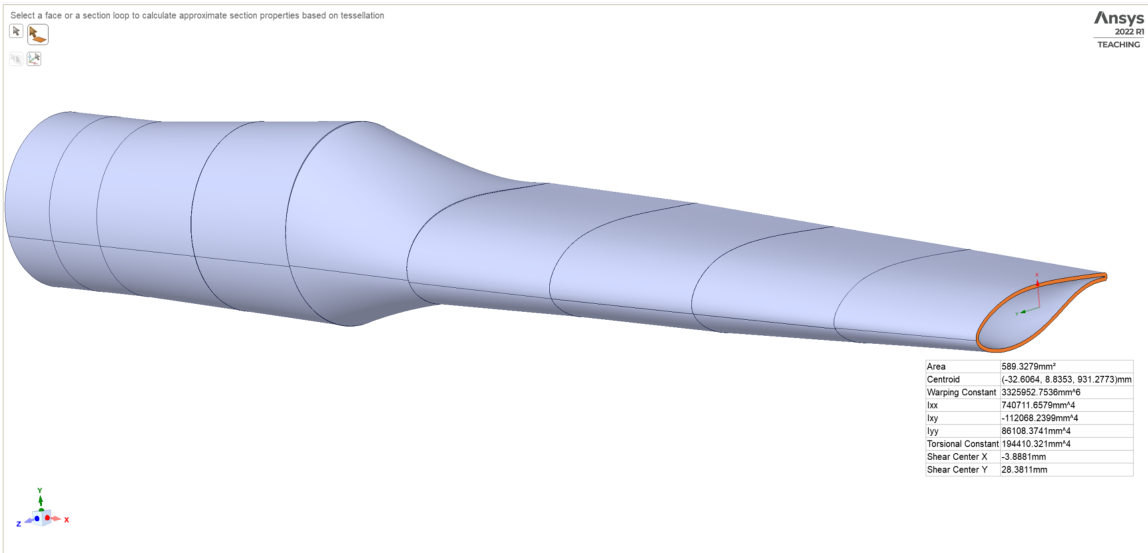

(c) Obtaining second moment of area and centroid values from blade model

Figure. 6.1 Modelling a 1.8 m blade in Solidworks from root to tip (a) Airfoils (b) Outer surface (c) Second moment of Area and Centroid for each section

Applying the modified equations for the second moment of area of elliptical structure for each blade station (airfoil section), it takes the form below; Equation 6.1 and Equation 6.2. The I_{xx} and I_{yy} from the Spaceclaim/ Solidworks design model, and the representative the second moment of area of the physically manufactured healthy blade obtained from the equations based on the parameters used for the manufacturing are compared in the upcoming sections.

$$I_{xx} = \frac{\pi\left(\mathrm{d_o t_o^3} - \mathrm{d_i t_i^3}\right)}{64} \tag{6.1}$$

$$I_{yy} = \frac{\pi\left(\mathrm{t_o d_o^3} - \mathrm{t_i d_i^3}\right)}{64} \tag{6.2}$$

where d represents the width, t the thickness, d_o and d_i the widths of the outer and inner shells, respectively, and t_o and t_i the thicknesses of the outer and inner shells, respectively. With these equations defined, the results for the healthy blade can be tabulated as follows.

Table 6.1 Second Moment of Area Ixx of Scaled 1.8 m Hull Blade

Blade Station	Distance from root (mm)	Outer Surface thickness (mm)	Outer Surface Width (mm)	Inner Cavity thickness (mm)	Inner Cavity Width (mm)	Ixx Outer Surface	Ixx Inner Cavity	Ixx Blade (mm^4)
1	0.0	108.3	108.3	103.7	103.7	6.75E+06	5.67E+06	1.08E+06
2	40.0	108.3	108.3	103.7	103.7	6.75E+06	5.67E+06	1.08E+06
3	120.0	117.4	117.4	112.8	112.8	9.33E+06	7.95E+06	1.38E+06
4	200.0	126.6	126.6	122.0	122.0	1.26E+07	1.09E+07	1.73E+06
5	300.1	58.6	138.0	54.0	133.4	1.37E+06	1.03E+06	3.32E+05
6	420.1	52.4	140.8	47.8	136.2	9.94E+05	7.30E+05	2.64E+05
7	540.1	50.4	135.1	45.8	130.5	8.49E+05	6.16E+05	2.34E+05
8	660.1	41.9	129.0	37.3	124.4	4.66E+05	3.17E+05	1.49E+05
9	780.2	33.9	121.9	29.3	117.3	2.34E+05	1.45E+05	8.84E+04
10	900.2	32.0	114.3	27.4	109.7	1.84E+05	1.11E+05	7.32E+04
11	1020.2	26.1	107.1	21.5	102.5	9.38E+04	5.02E+04	4.36E+04
12	1140.2	24.6	99.9	20.0	95.3	7.32E+04	3.75E+04	3.56E+04
13	1260.2	20.5	92.7	15.9	88.1	3.90E+04	1.73E+04	2.17E+04
14	1380.3	19.2	85.5	14.6	80.9	2.95E+04	1.23E+04	1.73E+04
15	1500.3	17.9	78.3	13.3	73.7	2.19E+04	8.45E+03	1.35E+04
16	1600.3	16.8	72.3	12.2	67.7	1.68E+04	6.02E+03	1.08E+04
17	1680.3	15.6	65.7	11.0	61.1	1.22E+04	3.98E+03	8.24E+03
18	1760.3	12.1	46.1	7.5	41.5	3.99E+03	8.52E+02	3.14E+03
19	1800.4	12.1	46.1	7.5	41.5	3.99E+03	8.52E+02	3.14E+03

Table 6.2 Second Moment of Area Iyy of Scaled 1.8 m Hull Blade

Blade Station	Distance from root (mm)	Outer Surface thickness (mm)	Outer Surface Width (mm)	Inner Cavity thickness (mm)	Inner Cavity Width (mm)	Iyy Outer Surface	Iyy Inner Cavity	Iyy Blade (mm^4)
1	0.0	108.3	108.3	103.7	103.7	6.75E+06	5.67E+06	1.08E+06
2	40.0	108.3	108.3	103.7	103.7	6.75E+06	5.67E+06	1.08E+06
3	120.0	117.4	117.4	112.8	112.8	9.33E+06	7.95E+06	1.38E+06
4	200.0	126.6	126.6	122.0	122.0	1.26E+07	1.09E+07	1.73E+06
5	300.1	58.6	138.0	54.0	133.4	7.56E+06	6.30E+06	1.27E+06
6	420.1	52.4	140.8	47.8	136.2	7.18E+06	5.93E+06	1.25E+06
7	540.1	50.4	135.1	45.8	130.5	6.10E+06	5.00E+06	1.10E+06
8	660.1	41.9	129.0	37.3	124.4	4.42E+06	3.53E+06	8.90E+05
9	780.2	33.9	121.9	29.3	117.3	3.02E+06	2.32E+06	6.93E+05
10	900.2	32.0	114.3	27.4	109.7	2.35E+06	1.78E+06	5.71E+05
11	1020.2	26.1	107.1	21.5	102.5	1.58E+06	1.14E+06	4.38E+05
12	1140.2	24.6	99.9	20.0	95.3	1.21E+06	8.51E+05	3.54E+05
13	1260.2	20.5	92.7	15.9	88.1	8.00E+05	5.33E+05	2.68E+05
14	1380.3	19.2	85.5	14.6	80.9	5.88E+05	3.79E+05	2.10E+05
15	1500.3	17.9	78.3	13.3	73.7	4.21E+05	2.61E+05	1.60E+05
16	1600.3	16.8	72.3	12.2	67.7	3.12E+05	1.86E+05	1.26E+05
17	1680.3	15.6	65.7	11.0	61.1	2.17E+05	1.23E+05	9.38E+04
18	1760.3	12.1	46.1	7.5	41.5	5.82E+04	2.63E+04	3.19E+04
19	1800.4	12.1	46.1	7.5	41.5	5.82E+04	2.63E+04	3.19E+04

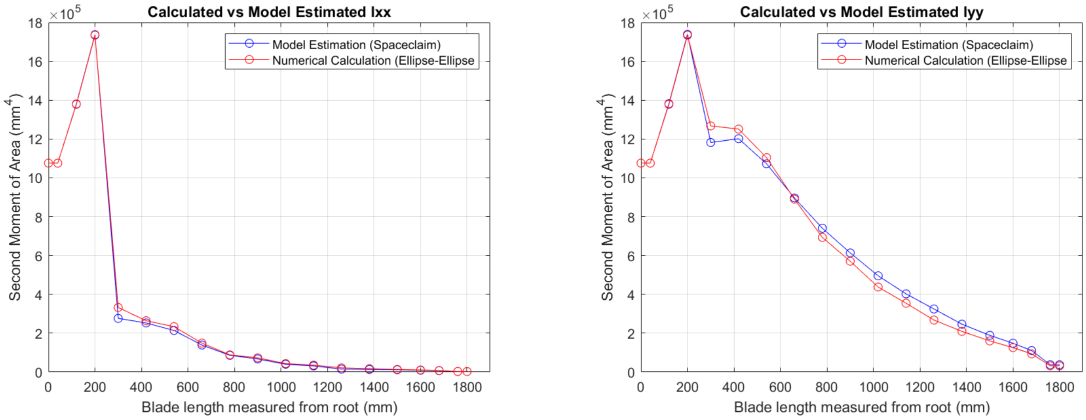

(a) Second moment of area Ixx

(b) Second moment of area Iyy

Figure. 6.2 Distribution of second moment of area (a) Ixx (b) Iyy

It can be seen that the first four points in both graphs shown in Figure 6.2 indicating the first 4 airfoil sections spanning a blade length of zero to 200 mm, both the I_{xx} and I_{yy} values of the estimated (from design) model as well as the measured model (from manufacturing) match near perfectly. One of the main reasons for this is the fact that those sections are cylindrical airfoils and for the estimation/ calculation based on the table, I_{xx} and I_{yy} equations use the formula of second moment of area of a cylindrical tube. Both the I_{xx} and I_{yy} values are exactly the same in Table 6.1 and Table 6.2 for the first four stations. A significantly large deviation can be seen at 300 mm (5th data point/ airfoil section/ blade station no: 5) for the estimated value vs measured I_{xx} and I_{yy}, where the transition region can be found, i.e. airfoils going from a cylindrical shape to a typical airfoil shape with a camber (DU 99-W-405 airfoil). The rest of the blade stations, the I_{xx} calculated from the design and the I_{xx} obtained from the composite match agree well with each other.

The comparison of the above two cases for I_{yy} however, deviate at several airfoil sections, particularly in two regions: around the transition region indicated by the blade length starting from 300 mm to 540 mm and secondly from about 800 mm upto about 1600 mm. This is mainly due to the gross approximation of the airfoil shape as an ellipse rather than an symmetrical or cambered airfoil, the calculation neglects the sharp trailing edge. The aerodynamic region, in particular blade length from 800 mm - 1600 mm take the shape of airfoil with a larger camber and chord length represented by airfoils DU 91-W-250 and DU 93-W-210 and then gradually take the shape of a thinner airfoil with much lower camber and chord lengths represented by NACA 64-618 airfoil, hence the calculated values are lower compared to the values obtained from the actual blade. The shapes and coordinates of all the airfoils used are given in Appendix A.

With the above assumptions, the cross sectional properties of the healthy blade were validate successfully, however for the defective blade, based on the parameters of the defect and its location, estimating the cross sectional properties I_{xx} and I_{yy} are slightly complicated. To evaluate these parameters numerically/ mathematically, with the same assumption that this cross section of the blade is assumed to be elliptical ring as shown in Figure 6.4c, the following derivation method was applied. The results obtained from this evaluation for the defective blade was then compared with the healthy blade's parameters for validation. The final results of the blade experiments incorporate these I_{xx}, I_{yy} and position of the neutral axis in the calculations, hence this validation is important for expected behaviour of the defect/ strain estimation later on. These final results will be explored in Chapter 7 of this thesis.

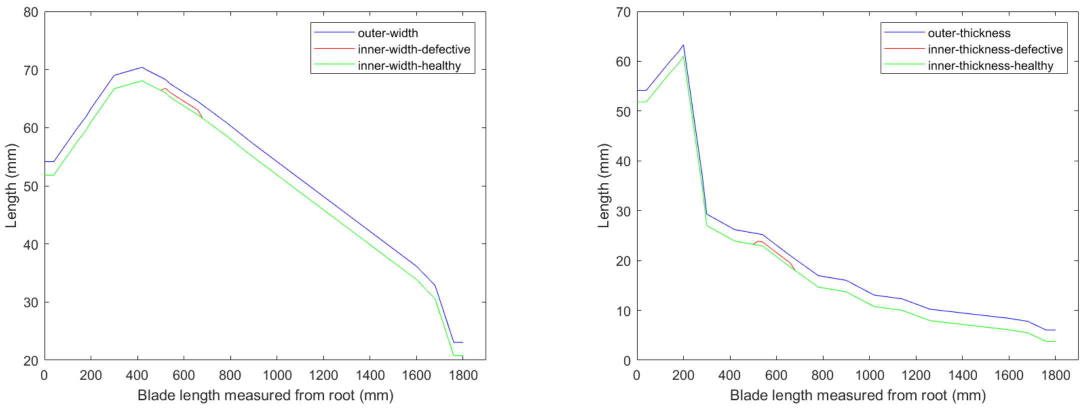

(a) Width of both blades

(b) Thickness of both blades

Figure. 6.3 Comparison between healthy and defective blade (a) width and (b) thickness

Figure 6.3 shows the width and thickness of both the outer ellipse and the inner ellipse for healthy as well as defective blade. It can be seen that the outer width and thickness for both blades are the same but the width and thickness of the defective blade is thinner at the location of the defect, compared to the healthy blade. This is representative of the change (reduction) in the stiffness of the composite material chosen for the defect, i.e. the thickness variation is also used to represent the change in Young's modulus in the above figure. The rest of the blade length is the same as the healthy blade where the width and the thickness do not have any variations.

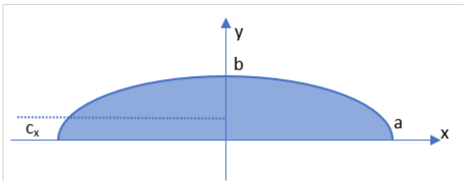

(a) Cross section showing solid half of healthy blade

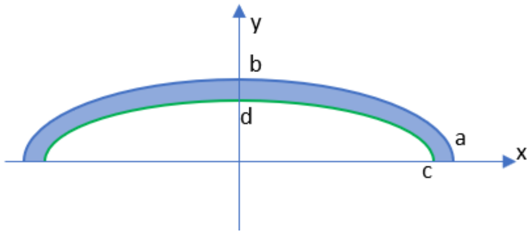

(b) Cross section showing hollow half of healthy blade

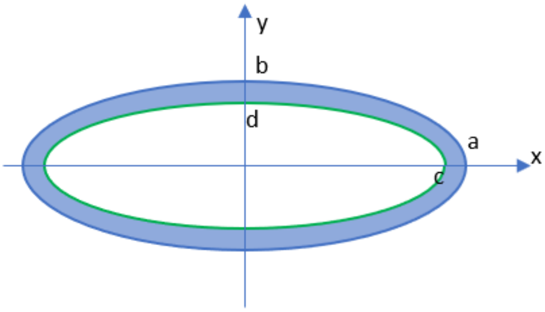

(c) Cross section showing the uniform top and bottom halves of healthy blade

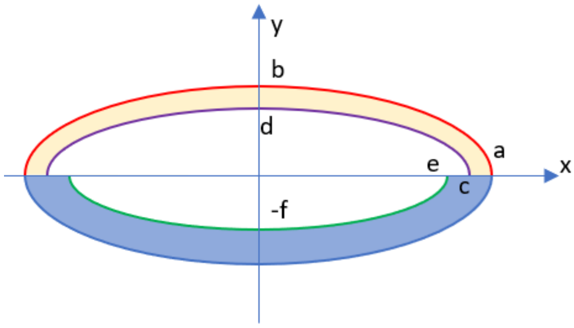

(d) Cross section showing the difference in thickness between top and bottom halves of defective blade

Figure. 6.4 Schematic diagram of cross sections of both blades (a) Solid half of healthy blade (b) Hollow half of healthy blade (c) Full cross section of healthy blade (d) Full cross section of defective blade

To derive the distributed I_{xx} of the healthy blade's cross section at different blade station, the cross section was first split in to three parts as shown in first three figures in Figure 6.4. The first shape/ part considered was the solid half ellipse. To make up the thickness of the blade, as mentioned previously, the cross-section of the blade shape was assumed to be elliptical. For this, the top half of the blade was then considered as a solid ellipse with a smaller hollow ellipse. This was repeated for both the top and bottom halves, which together make up the total cross-section of the blade: this is shown in the third figure in Figure 6.4 . Subsequently for the derivation of equations to estimate the I_{xx} and neutral axis of the healthy blade, the area was first determined for the different elliptical shapes considered and then the X-axis distance to the centroid was defined based on the notations shown in the figures. With these, the I_{xx} moment about the origin as well as the I_{xx} moment about the centroid were then derived for the outer, inner ellipse ring based on the solid half-ellipse. Table A.5 shows the equations obtained at each step for the different part of the ellipse and finally the upper and lower halves are added to obtain the total cross sectional Ixx moment of inertia. The final

X-component of the neutral axis is denoted as $x\bar{T}$ and this runs from the root to tip.

Similarly, to derive the I_{yy} of the total blade cross section at different blade station, the area was first calculated and then the Y-axis distance to the centroid was defined. With these, the I_{yy} moment about the origin as well as about the centroid were then derived for the outer, inner ellipse ring based on the solid half-ellipse. These equations for both area and centroid were first defined and then later the I_{xx} and I_{yy} were derived symbolically using MATLAB. Table A.6 in Appendix A shows the equations for each elliptical sections considered.

For the defective blade, the width and thickness was modified at the defect location based on the measured values from the actual defective blade manufactured. To allow a straightforward estimation of the I_{xx} and I_{yy} for the defective case, the top-half of the defective blade is assumed to have the defect entirely in its cross section with modified thickness, rather than a small section within the half elliptical cross-section. This feature spans only for the defective area lengthwise, covering from the blade length of 520 mm - 660 mm from root. This is illustrated in Figure 6.4d. For the rest of the location from root to tip, the width and thickness do not change and was the same as the healthy blade's geometrical properties. By substituting the appropriate values for a (outer thickness of the healthy blade), b (outer width of the healthy blade), c (inner width of the healthy blade), d (inner thickness of the healthy blade), e (modified/measured width at the defect), and f (modified/measured thickness at the defect) into the equations for both blade cases, Figure 6.5 was generated.

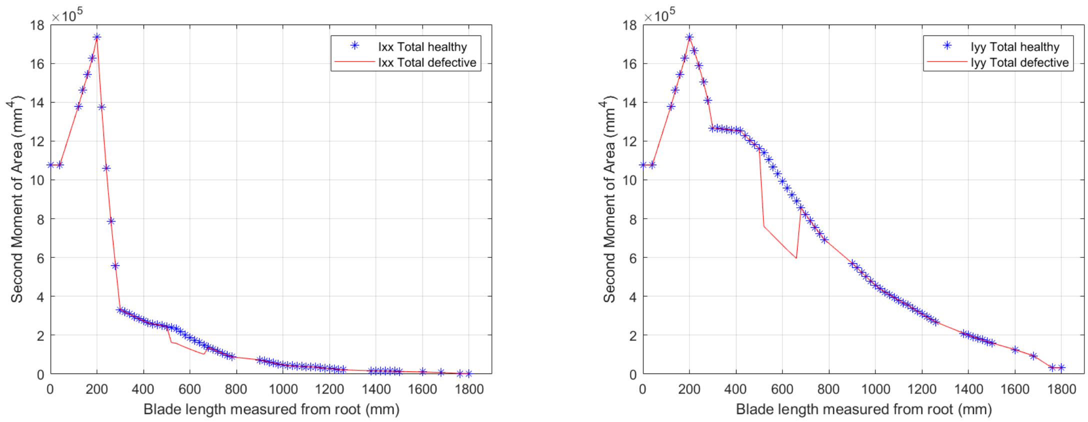

(a) Second moment of area Ixx

(b) Second moment of area Iyy

Figure. 6.5 Comparison of second moment of area calculated analytically for healthy and defective blades (a) Ixx and (b) Iyy

Looking at Figure 6.5, from 520 to 660 mm from the distance measured from the root, it can be seen that due to the presence of the defect/ composite material with the modified stiffness, the I_{xx} and I_{yy} for that range is lesser than the healthy blade case as expected.

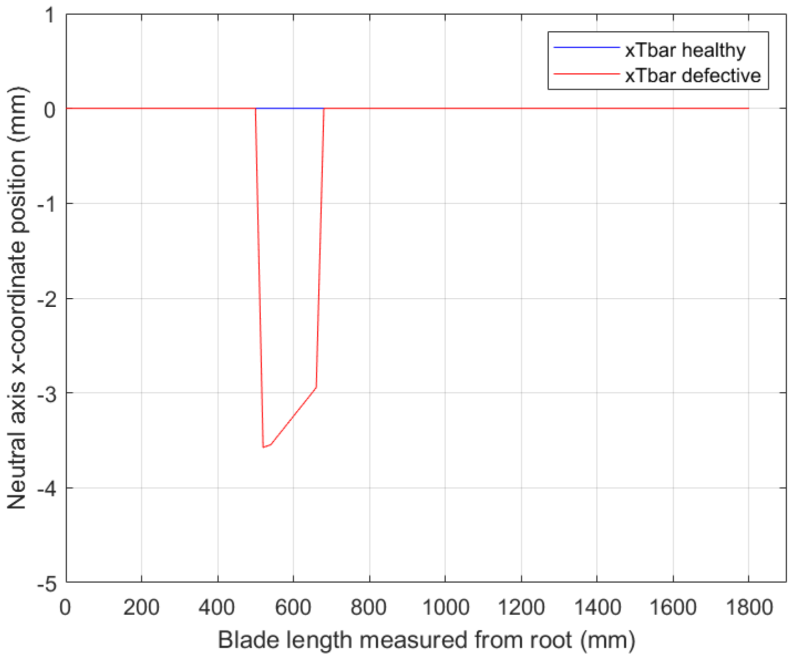

Figure. 6.6 X-coordinates of the neutral axis

Comparing the X-component of the neutral axes of both blades, it can be observed in Figure 6.6, the neutral axis of the defective blade moves away from the healthy case, again as expected. This is only at the defect location. As there was no effect of defect/ change in material composition in the Y-direction i.e. the changes are symmetric about the y axis of the defective blade, the Y axial component of the neutral axis remains unchanged from the healthy case. The distributed total value of the neutral axis's X-component was obtained by including the top and bottom half's respective X-component of the neutral axes. Compared to the healthy case, where both X and Y component of the neutral axis were zero, the defective case's top half neutral axis shifts as shown in Figure 6.7. Based on the manufactured blade, this shifting of the neutral axis is purely due to the shifting of the neutral axis in the top half, while the bottom half remains unchanged. Looking closely at the figure on the right, the shift can be seen clearly and was around 0.27 mm between the blade length 520 mm to 660 mm.

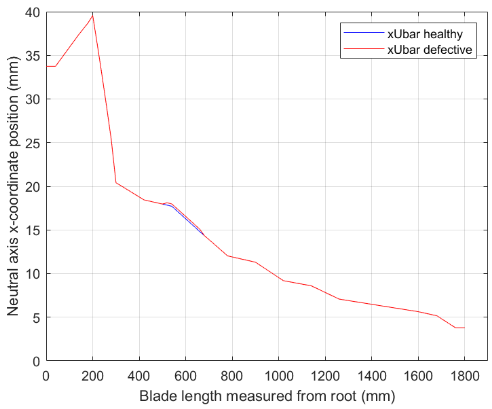

(a) Neutral axis of top half of blade

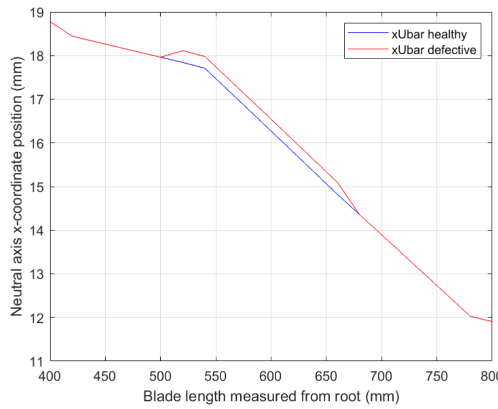

(b) Neutral axis of top half of blade spanning from 400 - 800 mm

Figure. 6.7 Location of neutral axis of top-half of blade (a) for entire blade span and (b) for blade span 400 - 800 = mm

With these I_{xx} and I_{yy} appropriately obtained for both the healthy and the defective blade, as well as the change in the position of neutral axis for the defective blade due to the presence of the defect, the expected strain was then estimated. This is further explained in Section 6.5 below. It should be noted that these are an approximation which allows an estimation of the I_{xx} and I_{yy} and hence the strain estimation also assumes that the defect covers half of the blade cross section, rather than a smaller patch.

6.3 Defining Loading Locations

The performance of the surface-bonded FBG for defect detection was assessed by applying the static loads in the form of laboratory weights at three different loading locations as shown in Figure 6.8. The first location denoted as L1 is approximately at 600 mm from root, coinciding with the centre point of the defective region. This location is found at 1/3 of blade length and also has clearance of both the root and transition region of the scaled wind turbine blade. The second loading point, denoted as L2 is at the aerodynamic region, at about 2/3 of the blade length measured at 1200 mm from root. The final loading point, denoted as L3 is at almost at the tip about 1800 mm from the root to investigate the tip loading conditions of the blade.

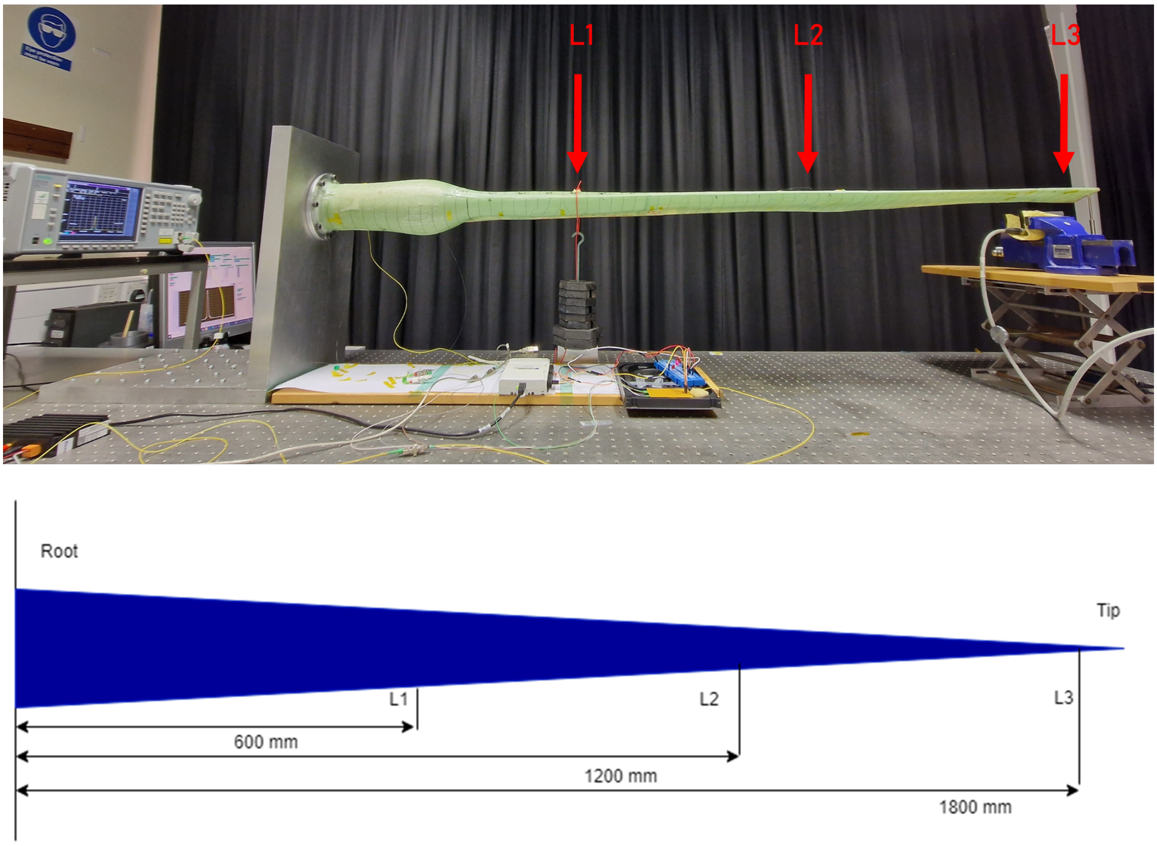

Figure. 6.8 Loading Locations

Table 6.3 Locations of load application on blade

Position	Distance from Root (mm)	Max Load (N)
L1	600 mm	51.01
L2	1200 mm	51.01
L3	1800 mm	26.49

Unlike the studies conducted by Lee and Park, 2016, Niezrecki et al., 2013, Chen, Semenov, et al., 2021 and Lee, Kang, et al., 2015, the blade does not go under static testing until complete collapse, as this particular set of tests are conducted to evaluate the response of the surface bonded FBGs under small load application to induce smaller variations in strain. Hence, the target maximum load for the first two loading locations are 51.01 N corresponding to a applied weight of 5.2 kg (5 kg in weights and 0.2 kg in the weight of the hook). A maximum load of 26.49 N (2.5 kg weights + 0.2 kg hook weight) was selected for the loading location L3, near the tip of the blade.

6.4 Orientations and Mounting setup for flapwise and edgewise loading

The scaled Hull blade was tested in both flapwise, edgewise loading conditions as well as at an angle. This was done by mounting the blade at different angular orientations with respect to the position of the leading edge position and testing platform/adaptor plate as shown in Figure 6.9.

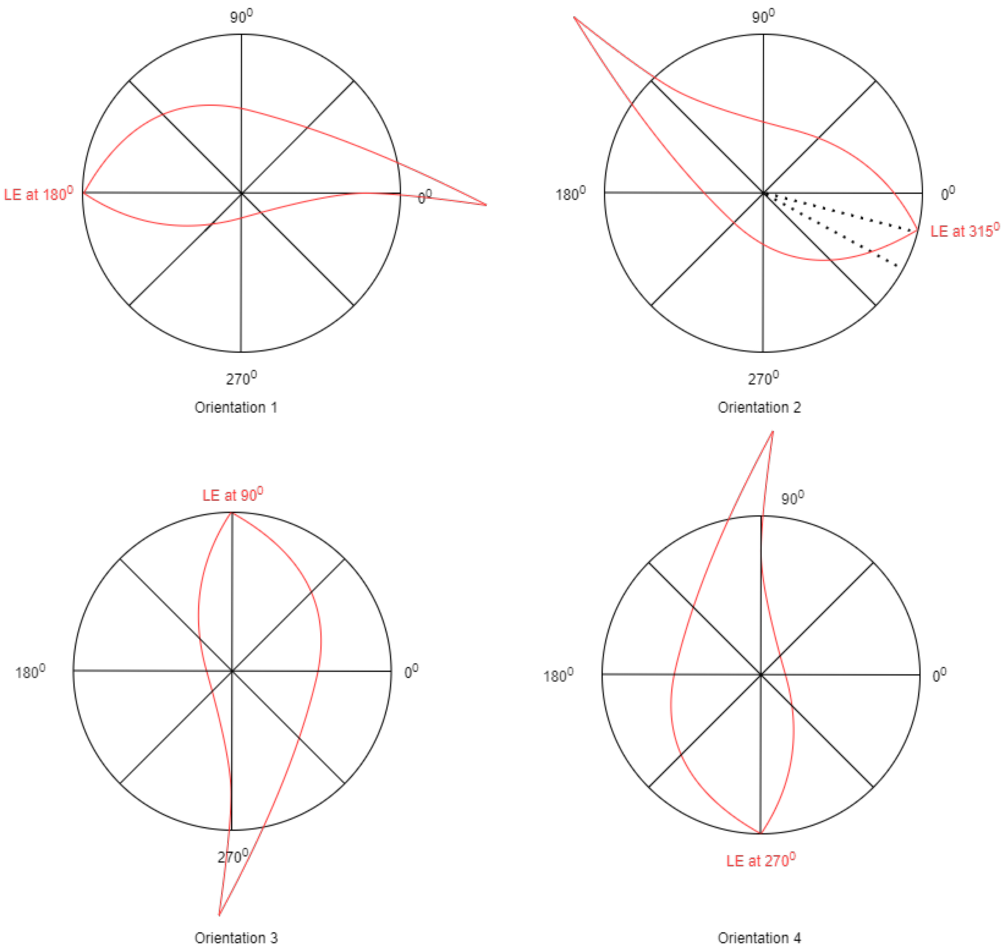

Figure. 6.9 Blade Mounting Orientations

The first orientation, O1 was mounted with the leading edge position at 180° to enable flapwise static testing where the pressure side of the blade is facing upwards. For this set of experiments, this is considered as the positive flapwise direction. Orientation 2, O2 depicts negative flapwise direction but with a slight angular disposition to enable a mixed-orientation static testing at 315°. Orientation 3 (O3) and Orientation 4 (O4) denotes positive edgewise and negative edgewise directions respectively. and are positioned at 90° and 270° according to the figure above. The blade has a length of 1800 mm and a maximum chord length of 140 mm at its widest point. For this structure, a vibration-isolating optical table was used to mount the test platform at one end with the root of the blade fixed to it and the tip of the blade extending upto the other end of the optical table. Generally, bending motion and torsional motion of a typical wind turbine blade can induce different damage mechanisms within the blade i.e. shear webs. The main failure mechanism is usually compressive buckling failure in the shear web as it is the main load bearing component of the blade Lee and Park, 2016.

Table 6.4 Orientations and bending type of the blade

Orientation	**Angular position of LE**	**Bending Type**
O1	180°	Flapwise - Positive
O2	315°	Flapwise - Negative
O3	90°	Edgewise - Positive
O4	270°	Edgewise - Negative

6.5 Expected Strain Profile/ Theoretical Effect of Defect

With 3 loading positions and 4 angular orientations of the blade, this gives 12 possible test cases. Within these test cases, more sub-cases are considered depending on the applied load. For any given loading location, six loading cases were recorded. Starting from zero load/weight/strain, the weights were added in sequence and in multiples of 1 kg for L2 and L1 until the maximum load of 49 N is reached. For L3, as it is the tip, to avoid loading it too aggressively, the weights were added in increments of 500 g, reaching a maximum load of 24.525 N. Altogether, 3 L x 4 O x 6 W = 72 load cases were considered each for healthy and defective blade individually.

$$\varepsilon_{\text{surface}} = \frac{Fl\bar{z}}{EI} \tag{6.3}$$

where F is the load applied, l is the distance between the point of interest and the point of load application and $\bar{z}$ is the distance between the point of interest and the neutral axis. E and I denote the Young's modulus of the material and the second moment of area relating to the point of interest respectively. It is important to estimate the strain at different paths along the blade to evaluate the theoretical effect of defect. This is useful in the validation of the results from the FBG arrays later for both the healthy and defective blade case. The surface strain can be calculated using this Equation 6.3. The neutral axis is constructed from the tri-axial centroid points (X,Y and Z) of each airfoil section taken from the Spaceclaim model of the 1.8 m Hull blade. Having this neutral axis, any point of interest for surface strain estimation can be considered. Both pressure side and suction side surfaces were used for bonding the FBG sensor arrays and using the above mentioned technique, the exact sensor point on the surface of the blade, the vertical and horizontal distance of the sensor location and the neutral axis and subsequently, the strain at the sensor location can be estimated. The force on the blade is further resolved into flapwise and edgewise components as illustrated in Figure 6.10. Depending on the weights applied, the angle at which it is applied (blade orientation or blade angle) as well as the internal twist angle distributed throughout the blade, the force at each point of the blade varies from root to tip.

Using these parameters, the expected strain profile on pressure side of the blade is calculated for both healthy and defective blade.

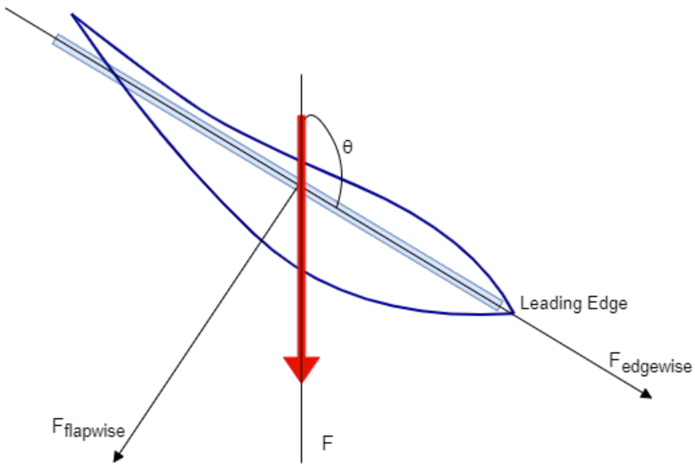

Figure. 6.10 Flapwise and Edgewise Strain for Blade

$$\text{Edgewise Force, } F_e = F\cos(\theta) \tag{6.4}$$

$$\text{Flapwise Force, } F_f = F\sin(\theta) \tag{6.5}$$

Here in Figure 6.10, the blade orientation or the blade angle Theta (°) is the angle between the force applied direction and the direction of the LE of the blade and is measured clockwise. the distributed blade twist from root to tip is denoted by Alpha (°) is the angle between the horizontal line (parallel to the ground) and the chord line of the airfoil measured anticlockwise. The twist distribution starts with 13.308° at the root as shown in Table 4.4 Chapter 4 and decreases to 0.106° going down towards the tip. It should be noted that the orientation angle shown in Figure 6.9 and the orientation angles mentioned in Table 6.5 are different because the figure is used just for illustration purposes hence the angles mentioned there denote the physical position of the leading edge with respect to the adapter plate. For the calculations however, the orientation angle is measured as the angles between the leading edge position and the force applied position. Hence an additional 90° is added to each orientation angle as shown in the Table 6.5. With these angles sorted, the forces can be represented as follows

Table 6.5 Flapwise and Edgewise forces resolved for different orientations

Theta $\theta(°)$	O1: 270°	O2: 115°	O3: 180°	O4: 0°
Flapwise Force	-Fsin θ	-Fsin θ	Fsin θ	Fsin θ
Edgewise Force	Fcos θ	Fcos θ	-Fcos θ	-Fcos θ
Flapwise force with twist Alpha $\alpha(°)$	-Fsin$(\theta-\alpha)$	-Fsin$(\theta-\alpha)$	Fsin $(\theta+\alpha)$	Fsin $(\theta+\alpha)$
Edgewise force with twist Alpha $\alpha(°)$	Fcos$(\theta-\alpha)$	Fcos$(\theta-\alpha)$	-Fcos $(\theta+\alpha)$	-Fcos $(\theta+\alpha)$

With these formulae for the forces resolved, the surface strain can be calculated at selected points on top of the blade. For example, Table 6.7 and Table 6.8 below show the flapwise and edgewise forces loaded at location L3 mounted at Orientation 1, for the sensing points in Array 1 bonded at a distance of 320 mm from root and ends at 720 mm in the pressure side surface of the blade. The next table, shows the distributed surface strain based on the Ixx and Iyy values already obtained for the manufactured Hull blade model (refer table X in chapter 5). This expected surface strain was calculated using the vertical and horizontal distance from sensor to the neutral axis. As mentioned previously in chapter 5, these distances as well as the location of the neutral axis was determined by using the mass properties function for the cross-sectional planer area for each station of the Spaceclaim model of the Hull blade.

Table 6.6 Loading conditions considered for strain estimation

Orientation Angle $\theta(^\circ)$ at O1	**Young's Modulus E [GPa]**	**Applied load Location L3 [mm]**
270	11.60	1800

Flapwise surface strain ε_f is calculated using the below Equation 6.6 where y is the vertical distance of sensor location to the location of the neutral axis. L is the sensor distance from the loading point. The edgewise surface strain ε_e is calculated using the Equation 6.7 where x is the horizontal distance of sensor location to the location of the neutral axis. Hence the strain measured by the FBG sensor at any point (resultant strain) will be a combination of both the flapwise and edgewise strain components as shown in Equation 6.8.

$$\varepsilon_f = \frac{F \sin\theta L y}{E I_{xx}} \tag{6.6}$$

$$\varepsilon_e = \frac{F \cos\theta L x}{E I_{yy}} \tag{6.7}$$

$$\varepsilon = \varepsilon_e + \varepsilon_f \tag{6.8}$$

Table 6.7 Flapwise force resolved for Array 1: O1-L3

Flapwise Force [N] for each sensor in Array 1 for applied loads								
FBG ID	**Sensor Wavelength [nm]**	**Position on Blade [mm]**	**Twist angle $\alpha(^\circ)$**	**Force Applied [N]**				
				26.49	**21.58**	**16.68**	**11.77**	**6.87**
A1-S7	1560	320	13.00	25.81	21.03	16.25	11.47	6.69
A1-S6	1555	390	11.94	25.91	21.12	16.32	11.52	6.72
A1-S5	1550	460	11.04	26.00	21.18	16.37	11.55	6.74
A1-S4	1545	520	10.38	26.05	21.23	16.40	11.58	6.75
A1-S3	1540	570	9.87	26.09	21.26	16.43	11.60	6.77
A1-S2	1535	640	9.20	26.15	21.30	16.46	11.62	6.78
A1-S1	1530	720	8.40	26.20	21.35	16.50	11.65	6.79

Table 6.8 Edgewise force resolved for Array 1: O1-L3

Edgewise Force [N] for each sensor in Array 1 for applied loads								
FBG ID	**Sensor Wavelength [nm]**	**Position on Blade [mm]**	**Twist angle $\alpha(^\circ)$**	**Force Applied [N]**				
				26.49	**21.58**	**16.68**	**11.77**	**6.87**
A1-S7	1560	320	13.00	5.96	4.86	3.75	2.65	1.55
A1-S6	1555	390	11.94	5.48	4.46	3.45	2.43	1.42
A1-S5	1550	460	11.04	5.07	4.13	3.19	2.25	1.32
A1-S4	1545	520	10.38	4.77	3.89	3.01	2.12	1.24
A1-S3	1540	570	9.87	4.54	3.70	2.86	2.02	1.18
A1-S2	1535	640	9.20	4.24	3.45	2.67	1.88	1.10
A1-S1	1530	720	8.40	3.87	3.15	2.44	1.72	1.00

Table 6.9 Flapwise strain component for each sensor in Array 1

Flapwise Strain for each sensor in Array 1 for applied loads									
FBG ID	**Sensor Wavelength [nm]**	**Position on Blade**	**Cross sectional Ixx [mm]**	***Vertical distance [mm]**	**Force Applied [N]**				
					26.49	**21.58**	**16.68**	**11.77**	**6.87**
A1-S7	1560	320	3.21E+05	36.94	360.20	288.16	216.12	144.08	72.04
A1-S6	1555	390	2.75E+05	26.29	286.16	228.93	171.70	114.47	57.23
A1-S5	1550	460	2.54E+05	24.74	278.37	222.70	167.02	111.35	55.67
A1-S4	1545	520	2.40E+05	24.48	279.93	223.95	167.96	111.97	55.99
A1-S3	1540	570	2.03E+05	23.98	311.99	249.59	187.19	124.80	62.40
A1-S2	1535	640	1.62E+05	22.30	344.86	275.89	206.92	137.95	68.97
A1-S1	1530	720	1.16E+05	19.96	400.89	320.71	240.53	160.36	80.18

Table 6.10 Edgewise strain component for each sensor in Array 1

Edgewise Strain for each sensor in Array 1 for applied loads									
FBG ID	**Sensor Wavelength [nm]**	**Position on Blade [mm]**	**Cross sectional Iyy [mm]**	***Horizontal distance [mm]**	**Force Applied [N]**				
					26.49	**21.58**	**16.68**	**11.77**	**6.87**
A1-S7	1560	320	1.27E+06	4.15	2.37	1.90	1.42	0.95	0.47
A1-S6	1555	390	1.25E+06	5.79	2.92	2.34	1.75	1.17	0.58
A1-S5	1550	460	1.20E+06	7.08	3.28	2.62	1.97	1.31	0.66
A1-S4	1545	520	1.14E+06	11.79	5.19	4.16	3.12	2.08	1.04
A1-S3	1540	570	1.03E+06	15.78	7.04	5.63	4.23	2.82	1.41
A1-S2	1535	640	9.24E+05	8.79	3.85	3.08	2.31	1.54	0.77
A1-S1	1530	720	7.88E+05	6.70	2.93	2.35	1.76	1.17	0.59

Table 6.11 Resultant Strain for Array 1: O1-L3

Resultant strain [uE] for each sensor in Array 1 for applied loads							
FBG ID	**Sensor Wavelength [nm]**	**Position on Blade [mm]**	**Force Applied [N]**				
			26.49	**21.58**	**16.68**	**11.77**	**6.87**
A1-S7	1560	320	362.57	290.06	217.54	145.03	72.51
A1-S6	1555	390	289.09	231.27	173.45	115.64	57.82
A1-S5	1550	460	281.65	225.32	168.99	112.66	56.33
A1-S4	1545	520	285.13	228.10	171.08	114.05	57.03
A1-S3	1540	570	319.03	255.23	191.42	127.61	63.81
A1-S2	1535	640	348.72	278.97	209.23	139.49	69.74
A1-S1	1530	720	403.82	323.06	242.29	161.53	80.76

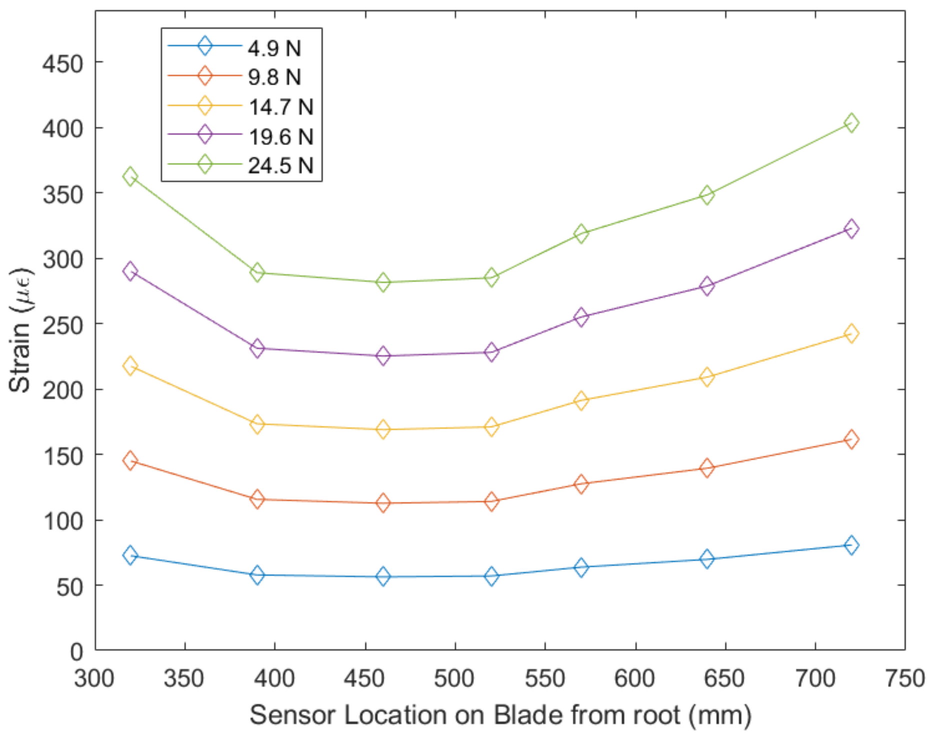

Figure. 6.11 Expected strain for Array 1 sensors at O1-L3

Figure 6.11 illustrates the expected strain distribution along Array 1 sensors located at O1-L3, plotted as sensor location versus strain. The data, derived from Table 6.11, demonstrates that as the applied load increases, the measured strain also increases, following a consistent trend. Notably, the FBG sensors mounted at positions 640 mm and 720 mm from the root measure higher strain values compared to those in the middle of the array. This variation can be attributed to the individual sensor's horizontal and vertical distances from the neutral axis of the blade and different second moment and different moment.

The observed strain pattern aligns with classical beam bending theory, specifically the Euler-Bernoulli beam theory, which states that bending strain is proportional to the distance from the neutral axis of a beam under load. Sensors located further from this axis experience greater tensile or compressive strains.

This expected strain distribution serves as a theoretical baseline for validating the experimental FBG measurements on the blade. By comparing the experimental data to these expected strain patterns, the accuracy of sensor placement and the effectiveness of the measurement system can be evaluated. In the following chapter, these comparisons are further analysed to confirm the validity of the measured strains against the theoretical predictions.

6.6 Defining Sensor Mounting Locations

The five wavelength division multiplexed (WDM) FBG sensor arrays were manufactured by FBGS FBGS, 2022 with the following specifications defined by the author. To differentiate each sensor in the arrays, the consequent FBGs within the array have 5 nm gradual difference in their Bragg wavelength, i.e. 1530 nm, 1535 nm, 1540 nm,....etc. The lead-in length for Arrays 1-4 was specified as 1000 mm so that this additional length can be used to manoeuvre the position of the arrays during sensor-bonding. The lead out was determined to be 500 mm at the end of the fibre. Each array was of different total length and had a single connector at the beginning of the fibre/ near lead-in and these arrays were designed to work only in reflection-mode.

The physical distance between each FBG sensor in the five sensor-arrays utilised are given in the following tables. These distances were defined specifically for each array, so that they could be used in specific sides of the blades/surfaces, for example, to cover the defect, to cover the entire length from root to tip and to cover interface between non-defect and defective region in pressure-side/ suction-side. Array 2 was the longest fibre of all the sensor-arrays used and has 18 FBGs starting with wavelength 1519 nm and ends with the final FBG at 1587 nm. The gratings/ FBG sensors are 10 mm each and they have 4 nm wavelength difference between each adjacent sensors. Array 3 has eight FBG sensors. It starts from 1527 nm and with 5 nm wavelength difference, increases gradually and stops with the last sensor at a reflecting wavelength of 1562 nm. Array 4 has seven FBGs starting with 1531 nm and ends with 1561 nm. Each FBG on arrays 1-4 were easily distinguishable as these sensors have unique reflecting Bragg wavelength defined. Wavelengths of FBGs in Array 5 were identical to FBG wavelengths of Array 1, however these arrays were used in the two different blades so that the results can be easily differentiated.

The physical spacing between the sensors for arrays 1-3 and array 5 were non-uniform. The only uniformly spaced array was A4 where each sensor was placed 260 mm from the adjacent sensor and this was used on the healthy blade to measure strain from root to tip covering the entire length of the blade on the suction side. Tables with the array specifications in Appendix C present the nominal wavelength, as defined by the author for DTG fibre manufacturing. These tables also include the measured central (or Bragg) wavelength on the fibre spool under slight tension. The small difference between the nominal and measured wavelengths does not impact the experiments, as calibration was performed beforehand (as detailed in the preliminary sensor characterization in Chapter 3). Additionally, the strain measured in the experiments was referenced to the initial wavelength at zero strain. The reflection or the reflectivity of these sensors were in the range of 20-35 %, which were typical of the manufacturing method used for draw tower gratings (DTG) - FBG.

Forty seven FBG sensors were attached to the outside the blade on the pressure and suction sides before testing. Table 6.12 and Table 6.13 show the position and distance of the FBGs from the blade root. These positions were selected based on the expected strain profile/ effect of defect estimated in section 6.5 as well as the spacing and specification of the FBGs' already defined for sensor array manufacture. Out of these, 46 FBG sensors belong to five different array of fibres and one T-FBG was a stand-alone strain-insensitive, temperature-only FBG mounted at the root. The strain measuring FBGs are bonded manually one-by-one, leaving enough time for the previous sensor to be bonded and cured completely. Each 10 mm FBG is bonded at two points of adhesion on 5 mm either sides of the grating length using cyanoacrylate. These adhesion points were marked first with a pen and secured temporarily using tapes while the adhesion points on the blades are prepared with the application of a primer purchased from RS Components. the first point of adhesion was glued using cyanoacrylate, and the second point was glued while the sensor/fibre between the two adhesion points were under tension. This was done by stretching the bit of the fibre in between and applying a pre-strain. This was to prevent any sagging during and after sensor bonding. The pre-strain applied was manually monitored on the optical spectrum analyser's interface and by looking at the FBG peak moving to the right. Based on the graph lines/ markers pre-set, the wavelength shift of about 0.3 nm was selected to be used for pre-strain contribution.

Table 6.12 Locations and position of FBGs on the healthy blade

Array ID	FBG ID	Sensor Wavelength (nm)	Distance from Root (mm)	PS or SS
	S1	1530	745	PS
	S2	1535	673	PS
	S3	1540	601	PS
A1	S4	1545	541	PS
	S5	1550	481	PS
	S6	1555	409	PS
	S7	1560	337	PS
	S1	1531	140	SS
	S2	1536	400	SS
	S3	1540	655	SS
A4	S4	1546	915	SS
	S5	1551	1175	SS
	S6	1556	1435	SS
	S7	1561	1690	SS

P = Pressure side, S = Suction side

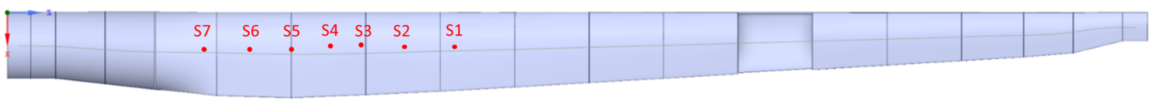

(a) Pressure side FBG sensors - Array 1

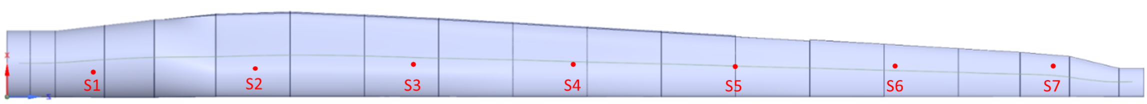

(b) Suction side FBG sensors - Array 4

Figure. 6.12 Schematic diagram of healthy blade with the locations of surface-bonded FBGs (a) Pressure side FBG sensors - Array 1 (b) Suction side FBG sensors - Array 4

Table 6.13 Locations and position of FBGs on the defective blade

Array ID	**FBG ID**	**Sensor Wavelength (nm)**	**Distance from Root (mm)**	**PS or SS**
A3	S1	1527	525	PS
	S2	1532	565	PS
	S3	1537	600	PS
	S4	1542	640	PS
	S5	1547	675	PS
	S6	1552	730	PS
	S7	1557	775	PS
	S8	1562	835	PS
A5	S1	1530	460	PS
	S2	1535	490	PS
	S3	1540	520	PS
	S4	1545	550	PS
	S5	1550	620	PS
	S6	1555	660	PS
	S7	1560	690	PS
	S8	1565	725	PS
A2	S1	1519	165	SS
	S2	1523	265	SS
	S3	1527	360	SS
	S4	1531	485	SS
	S5	1535	610	SS
	S6	1539	730	SS
	S7	1543	850	SS
	S8	1547	975	SS
	S9	1551	1095	SS
	S10	1555	1220	SS
	S11	1559	1340	SS
	S12	1563	1460	SS
	S13	1567	1580	SS
	S14	1571	1670	SS
	S15	1575	1745	SS
	S16	1579	1800	SS

P = Pressure side, S = Suction side

Array-3 (A3) is bonded right on the middle line of the defect and Array-5 (A5) was bonded on the defect-non defective surface interface line as shown in Figure 6.14 and the schematic diagram Figure 6.13.

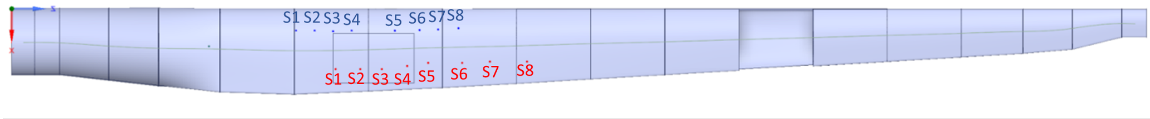

(a) Pressure side FBG sensors - Array 3 and 5

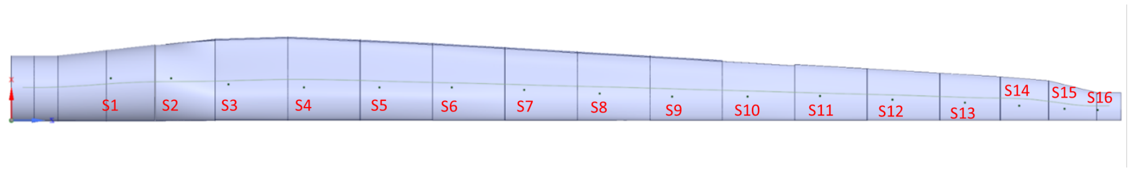

(b) Suction side FBG sensors - Array 2

Figure. 6.13 Schematic diagram of defective blade with the locations of surface-bonded FBGs (a) Pressure side FBG sensors - Arrays 3 (in blue) and 5 (in red) (b) Suction side FBG sensors - Array 2 (in red)

Although Array 2 was manufactured with 18 sensors, due to the drastic change in curvature/ shape of the blade, particularly near the transition region, the total bonded length of the fibre had to be reduced by leaving the last 2 sensors un-bonded and un-used for the blade loading experiments.

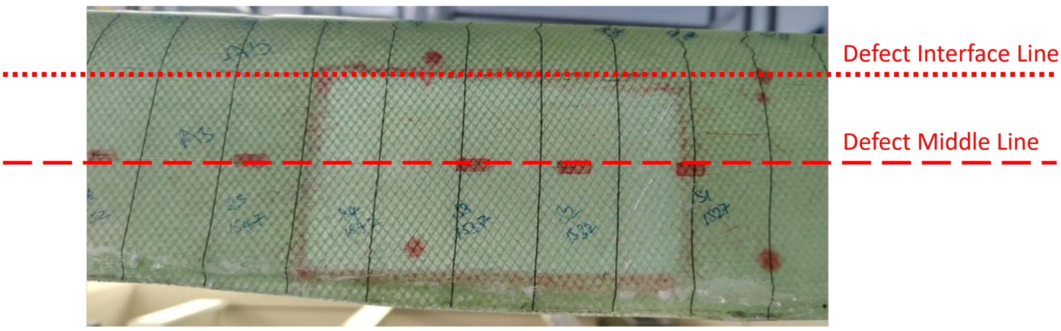

Figure. 6.14 FBG arrays bonded on the defective region

6.7 Temperature Measurement System

Unlike the strain measuring FBGs, the strain-insensitive temperature only FBG was manufactured at a grating length of 40 mm. The grating was housed by a steel tube as shown in Figure 6.15 and had a measurement range of -22.5°C to 110°C with a temperature accuracy of 1°C and a precision of 0.2°C. The total length of the fibre with this single FBG was 1 metre and this was connected to Channel 4 of the optical switch and was mounted near the root of the blade for all test cases for continuous temperature monitoring. The nominal wavelength of this temperature-FBG was measured at 1564.061 nm at 22.5°C as per the datasheet provided by the manufacturer. (Refer Appendix E: Technical Data sheets for full details). Calibration of this DTG-FBG has already been done and is covered under Chapter 3. The temperature sensitivity based on the calibration results were deemed as 10.51 pm/°C. The equations used to express the temperature monitored using this DTG is given below,

Figure. 6.15 Strain-insensitive Temperature only FBG

$$T = \mathrm{Tref} - \frac{S_1}{2S_2} + \sqrt{\left(\frac{S_1}{2S_2}\right)^2 + \frac{1}{S_2}\ln\left(\frac{\lambda}{\lambda_{\mathrm{Tref}}}\right)} \tag{6.9}$$

where, T: current temperature, expressed in [°C]

T_{ref}: 22.5°C, the reference temperature for which S_1 and S_2 are calculated

S_1 and S_2: temperature sensitivities of the FBG
λ: current DTG wavelength [nm]
λ_{Tref}: the reference wavelength i.e., the wavelength at the reference temperature T_{ref} [nm]

The parameters λ_{Tref}, S_1 and S_2 for the DTG are defined in the table below,

Table 6.14 Parameters for Temperature estimation using Temperature-FBG

DTG N°	λ_{Tref}**[nm]**	**Temperature factor S1** [$°C^{-2}$]	**Temperature factor S2** [$°C^{-2}$]	**Temperature error** [°C]
TP 01	1564.061	6.4019E-06	7.8390E-09	0.4

6.8 Deflection Measurement System

With the optical spectrum analyser monitoring and recording the spectra from the FBG sensor arrays, additional tools were deployed to measure the tip deflection of the blade similar to the preliminary and secondary experiments conducted (Refer Chapter 3). Here, a 50 mm dial gauge was mounted from beneath the blade to measure deflections as the blade undergoes static load application. For each load case considered, the dial gauge measurement was recorded; starting from zero load until maximum load was reached. In Figure 6.8, the deflection measurement system with the dial gauge fixed on a support stand can be seen clearly near the tip of the blade. The position at which the dial gauge moves along with the blade was marked clearly at 1810 mm and the same point was used for all test cases including positive, negative flapwise loading (O1 and O2) as well as both positive and negative edgewise bending or loading (O3 and O4). The equation used to calculate tip deflection of the 1.8 m Hull blade is given below, these were based on the deflection equations for a typical rectangular cantilever beam at different points conducted by Craig Jr and Taleff, 2020 but they have been modified to fit the Hull blade scenario.

Deflection of blade between root and load application point,

$$d = \frac{Fs^2}{6EI}(3L_n - s) \tag{6.10}$$

Deflection of blade beyond load application point in the length towards the tip,

$$d = \frac{F{L_n}^2}{6EI}\left(3L - L_n\right) \tag{6.11}$$

Deflection of blade at load application point,

$$d = \frac{F{L_n}^3}{3EI} \tag{6.12}$$

where: d: deflection of the beam [mm]
F: load applied [N]
s: distance as indicated/ distance between measurement point and [mm]
L: Length of blade [mm]
E: Young's modulus of the resultant composite material [N/mm^2]
I: Second moment of area [mm^4]
L_n: Load application point [mm]; where n=1,2,3

6.9 Testing Procedure

The scaled blade tests were performed starting from loading location L1, L2 and finally in location L3 in this sequence for each orientation. The static load was applied by hanging weights on a hook-stand on a cable attached around the loading location. As the weights were added incrementally, the blade was displaced downwards slightly. Readings from each FBG array along the blade were recorded one after the other using the optical switch to switch between the arrays at each load increment upto the maximum load. Figure 6.16 shows the schematic diagram of the configuration used for the defective blade experiments with the four arrays selected as previously mentioned in section 6.6. On the 1x4 optical switch, the first 3 channels were connected to each wavelength division multiplexed strain-measuring FBG array A3, A5 and A2 and the last channel was connected to the dedicated temperature-measuring FBG. Similarly, the healthy blade experiments were conducted with Array 1 and Array 4 connected to optical switch channels 1 and 2 respectively and with the temperature-FBG connected to channel 3.

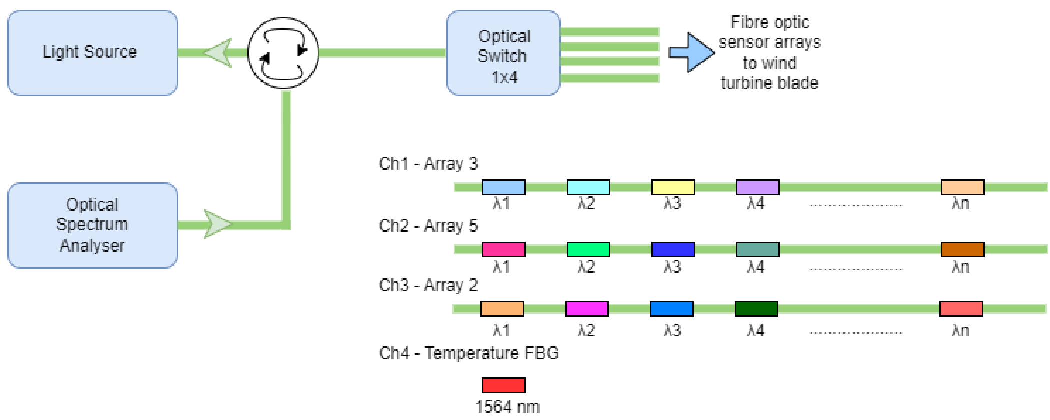

Figure. 6.16 Schematic diagram for defective blade's sensor system: configuration of FBGs arrays on different channels of the system

Starting from zero load application, between each loading case, a few minutes waiting time was spent for the weights to settle and any fluctuations and residual vibrations to die down. The data acquisition was conducted for approximately three minutes for each array used. This time was required for the entire spectrum of multiple FBGs peaks in a single array could be scanned and saved properly without data loss or improper data recording in the user PC. As the blade was loaded in both positive and negative bending case i.e. in both upward and downward directions, the blade remained in the linear elastic region. This technique was also followed in the full-scale blade tests described in Al-Khudairi et al., 2017. For each array, the wavelength range of the spectrum on the OSA and the automated data acquisition was selected to include all sensors and their peaks in one spectrum to monitor change in wavelength shift and peak wavelength changing in one-go for each case. Once this process was complete for the first orientation/ the blade was carefully de-mounted at the adapter plate-test stand interconnection point and rotated to the next desired orientation and blade angle and screwed on again to the test stand. This process was repeated until all tests for all the orientations, loading locations were performed and results recorded.

Starting from zero load application, a few minutes of waiting time was allowed between each loading case to let the weights settle and to minimise fluctuations or residual vibrations. Data acquisition was conducted for approximately three minutes for each array, ensuring that the full spectrum of multiple FBG peaks was scanned and saved without data loss or improper recording on the user computer.
The blade was loaded incrementally in both positive and negative bending cases (upward and downward directions), with strain measurements monitored throughout the process. To ensure the blade remained within the elastic region, the applied loads were conservatively

chosen based on prior experimental studies of composite beams (explored in Chapter 3). The strain data was continuously observed for any non-linear trends or unexpected behaviour. Additionally, after each unloading step, the strain values returned to their baseline without residual deformation, confirming that the blade remained in its elastic range throughout testing.

The load was defined as the applied weights, which were converted into equivalent forces using the acceleration due to gravity. These forces were further verified by calculating the expected bending moment and strain distribution using theoretical models, ensuring that they corresponded with the experimental setup. This technique was also followed in the full-scale blade tests described in Al-Khudairi et al., 2017. For each array, the wavelength range of the spectrum on the OSA/automated data acquisition was selected to include all sensors/all peaks in one spectrum to monitor the change in wavelength shift/peak wavelength changing in one go for each case.

6.10 Test Rig Limitations

The test was designed to host static loading experiments where the root of the blade is positioned horizontally with the root and the tip being horizontal. For dynamic excitation and modal analysis tests however, it would be ideal to have an angled adapter plate and a mounting frame.

6.11 Conclusions

In this chapter, the details of the implementation and testing of the static loading for the Hull Blade is explored. Section 6.2 of this chapter compares and validates the cross sectional properties of the physical blade vs the design based on the distributed structural and geometrical properties. Using lab-weights/ by hanging weights on the blade at different loading locations, the static loading tests were conducted while also mounting the blade at different angles to cover flapwise and edgewise bending/ loading conditions. The FBG sensor arrays were surface-bonded on both healthy and defective blade, while making sure enough sensors cover the defective region of interest. For the healthy blade, two arrays, each consisting of 7 wavelength division multiplexed (WDM) FBG sensors in a single fibre array was bonded at pressure and suction side, giving a total of 14 strain-measuring FBGs for this blade. For the defective blade, the suction side covers a single long fibre array of 16 FBG sensors surface bonded from root to tip with 2 arrays each consisting of 8 strain-measuring FBGs covering in and around the composite structural defective region. As the performance of FBGs for the defective blade was more of interest for this investigation, a total of 32 FBGs were deployed for this blade. An additional temperature-only (insensitive to strain) FBG was used in both blade cases at the root to measure the changes in ambient temperature constantly. With these sensors, the optical spectrum analyser, optical switch to switch between the different arrays and the LabVIEW based data acquisition system, resultant spectra and deflection measurement from 72 loading cases were recorded successfully spanning over a period of two weeks.

Although real-time data processing was not implemented to validate measured strain during the experiments, the expected strain profile was calculated using appropriate equations and reasonable assumptions before the testing procedure began. This also eliminates the uncertainty for results analysis described in the next chapter. Nevertheless, during the loading tests, the FBG-array spectrum monitored on the interface of the optical spectrum analyser showed changes in the peak wavelength and the wavelength shift were detectable and were characteristic of the weights applied (showing tensile and compressive and increasing and decreasing behaviour based on the direction of wavelength shift).

Chapter 7

Results, Evaluation and Discussion

7.1 Introduction

This chapter collates all the results taken from the static load tests for both healthy and defective blade and evaluates the performance of the bonded FBGs for load monitoring as well as defect detection. Firstly, a section on how the spectral data from the sensors were processed is given, and the subsequent sections can be grouped in two major parts: results from healthy blade and results from defective blade. These sections describe and discuss the recorded experimental results with the provision of FBG spectra and graphs for each orientation and loading cases considered. The effect of temperature, deflection of the blade during the experiments are also investigated. An additional section on the comparison of the healthy vs defective case, particularly the performance of the sensors at the defect location and the minimum strain detected is also provided. Finally, under the conclusion section, an overall summary of evaluation/ overview of discussion of all results is provided along with the discussion of the optimum number of sensors/ spacing required to detect defects of certain size considered in this experiments.

7.2 Post processing in MATLAB

The data collected from the LabVIEW Data acquisition system was labelled appropriately by orientation-location-load applied-array measured and were saved for further analysis. The raw spectra data recorded by the optical spectrum analyser (OSA) were first plotted in Matlab to verify the appropriate wavelength shift trend (left or right shift) according to the load applied and the direction of strain and the orientation of blade as well as to look for any abnormalities in FBG peak in reflection mode. Any distorted graphs resulting from incomplete data save were discarded. To this pre-processed and pre-sorted data, additional processing techniques were then applied as follows,

(a) The base of each spectrum was brought to zero for several reasons: This is an important pre-processing technique used to separate the spectroscopic signal from any interference and to remove background effects or noise. Only when the baseline is zero can the Gaussian fit be properly applied to find the correct wavelength of each FBG peak's centroid.

$$y = \sum_{i=1}^{n} a_i e^{\left[-\left(\frac{x-b_i}{c_i}\right)^2\right]} \tag{7.1}$$

(b) Using the Matlab curve-fitting tool, the numerical fitting was done according to the equation above, to first identify a: amplitude, b: centre wavelength and c: peak width. As a first-order Gaussian fit was considered for each individual FBG peak, the n=1.

(c) A first order Gaussian function was then fitted to whole peak of FBG graph and not just a selected section such as the Full Width Half Maximum (FWHM) so that the entire bandwidth and the amplitude can be included for the estimation of the centroid/ peak wavelength which results in more accuracy.

The output response from the Gaussian fitted function to each of the raw data of the FBG peak were both plotted as shown in figure below Figure 7.1. Once this was deemed correct, the same technique was applied to all the spectra under each test case considered, i.e. for all load cases one by one. Starting with the zero load case, for each sensing FBG-loading location, altogether 6 resulting graphs, one for each load applied were obtained. Having completed this step, the wavelength shift was then calculated taking the peak wavelength of the first zero load case as the starting reference wavelength Equation 7.2. The subsequent peak wavelengths were extracted from that reference wavelength. This wavelength was determined by estimating the centroid of each peak and then values were subtracted from the first peak wavelength determined.

$$\Delta\lambda_s = \Delta\lambda|_{\max_{\Delta\lambda}\left(S_{ref}(\lambda)S_m(\lambda-\Delta\lambda)\right)} \tag{7.2}$$

Where $\Delta\lambda_s$ is estimated as the maximum of the correlation between the reference spectrum and the shifted replica of the measured one, S_{ref} is the reference spectrum and $S_m(\lambda)$ is the measured spectrum at each instant.

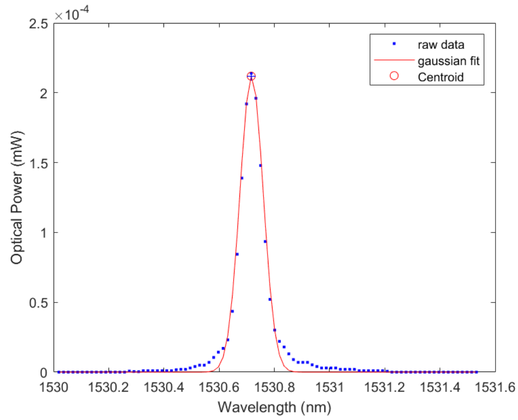

Figure. 7.1 Raw Data from Optical Spectrum Analyser vs Gaussian fitted data

The figure above shows both the raw data as well as the Gaussian fitted data for comparison. Using the Gaussian fit, centroid of the peak and its wavelength of the FBG spectrum has also been identified and is denoted in the same figure. It can be observed that the Gaussian fit covers the entire amplitude of the spectrum from bottom to the peak without changing the shape, the full width while omitting any distortive features of the FBG spectrum without changing the bandwidth of the signal, i.e. so that the main peak is unaffected by the side-lobes seen in the spectrum. The same technique was applied to each spectrum for all the FBGs utilised and the centroid of the peak and its wavelength was extracted accordingly for wavelength shift and strain estimation and further analysis.

7.3 Temperature Effects

The ambient temperature in the laboratory where the experiments were being conducted were measured similar to the strain measurements i.e. for each loading case in each loading location. Within the measurements taken for each loads, the temperature-FBG spectra were collated, plotted and then the 1st order Gaussian function was fit as shown above. For this, the centroid wavelengths for each spectrum were extracted. Finally, the wavelength-to-temperature conversion were done using the Equation 6.9 shown in Chapter 6. Some of the selected plots are given below.

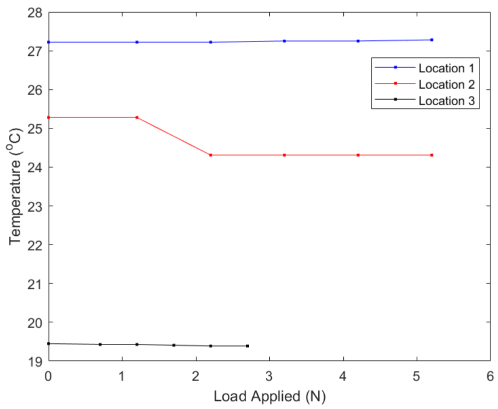

(a) Orientation 1 (O1)

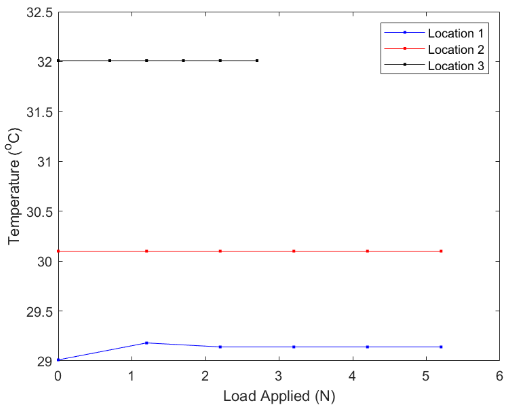

(b) Orientation 2 (O2)

Figure. 7.2 Temperature measurements throughout (a) Orientation 1 (B) Orientation 2 testing campaign

It can be seen that within each measurement campaign for each location, the temperature variation does not vary much and does not exceed the value of $\pm 1°$C. Comparing the trends altogether show that depending the time of day that the measurements/ static loading testing was conducted, the temperature range also varies. For example, the Orientation 1 tests were conducted starting with L1 at mid-day and ended with L3 which lasted till late evening. Going from the L1 to L3, the temperature range keeps dropping. This can be seen in Orientation 2 tests as well in Figure 7.2. However, as the difference between first temperature measurement, which was considered to be the reference temperature and the last measurement within the same measurement period is less than one degree, the influence of ambient temperature can be excluded from the estimation of the overall wavelength shift for that campaign. This was repeated for each case under each orientation for both blades. The temperature in the laboratory space was also kept constant throughout the day by the central heating system and there were no external influences affecting the temperature and the measurement systems.

7.4 Results analysis & discussion for healthy and defective blades

A total of 72 experimental test cases were conducted to evaluate the performance of the WDM-FBG sensor system under various loading conditions for both healthy and defective blades. Given the extensive nature of the dataset, a thorough analysis reveals a variety of insights that contribute to a deeper understanding of the sensor system's effectiveness in measuring strain and detecting defects. In order to conduct a structured discussion, the results have been categorised into the following key sections:

1. Spectral analysis of bonded FBGs, for both healthy and defective blades.
2. Sensor wavelength vs strain measured for each array.
3. Expected vs measured strain for each orientation.
4. Sensor Location vs strain at maximum applied load.

These sections focus on the critical aspects of sensor behaviour, strain measurements, and the detection capabilities for both healthy and defective blade scenarios.

7.4.1 Spectral analysis of bonded FBGs

From the raw data obtained using the optical spectrum analyser (OSA), the wavelength and corresponding optical power can be plotted to reproduce the spectra. However, this would generate hundreds of spectra, making detailed evaluation impractical. Therefore, only selected spectra are presented to describe key features and trends of FBGs bonded to both pressure-side and suction-side surfaces. This analysis is further explored in the following sections.

For the FBG arrays bonded to both the healthy, defective blade and on the defect, this approach was followed. The spectra obtained from static loading tests were re-plotted using MATLAB to verify the wavelength shift behaviour of the FBG sensors. In this subsection, selected figures illustrate the spectral characteristics of FBGs bonded to healthy and defective blades, including those bonded directly over the defect and at the interface of defective and non-defective material surfaces.

To further analyse the spectral shift of FBGs on the suction side, spectra from sensors in Array A2 have been included. Special attention has been given to FBG sensors covering the defective region of interest.

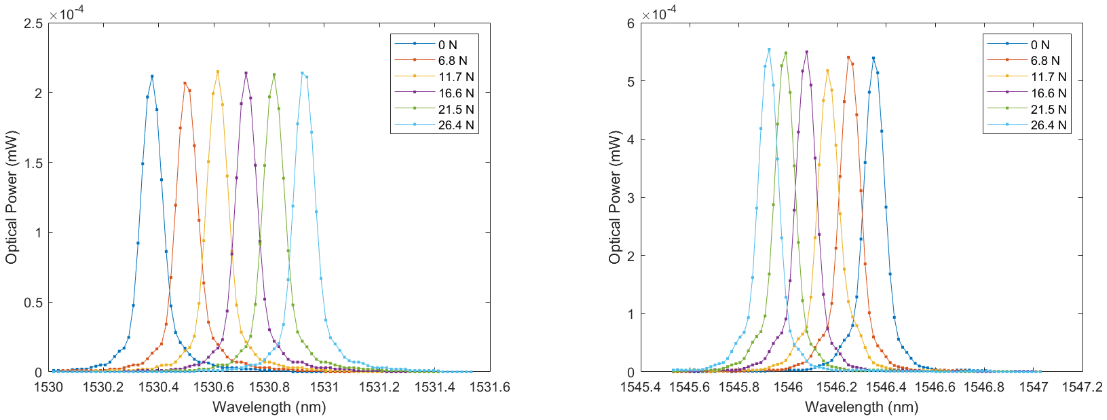

(a) Array 1: 1530 nm

(b) Array 4: 1546 nm

Figure. 7.3 Wavelength shift of FBGs showing right and left spectral shift (a) 1530 nm FBG in A1 at L3-O1 (b) 1546 nm FBG in A4 at L3-O1

The collection of spectra from each FBG bonded under increasing loads has resulted in hundreds of figures (47 sensors x 4 orientations x 3 loading locations). However, for analysing tensile and compressive trends, recorded spectra for the pressure-side bonded Array 1 and suction-side bonded Array 4 in Orientation O1, with loads applied at Location L3 (tip-loaded case), have been selected. This particular configuration was chosen as it represents a typical cantilever beam case for comparison.

Figure 7.3 shows the spectra for the FBG with Bragg wavelength 1530 nm found in Array 1 (A1) under increasing applied loads. Here, with the raw data plotted as a graph, it can be seen clearly that as the load increases, the peak wavelength moves to the right as expected for an FBG sensor array bonded on the pressure side, where the blade surface is facing upwards and the force is applied towards downwards. The sensor experiences tension; hence, the spectra shift to the right as the data acquisition system captures and records the relevant wavelength and optical power data. The same methodology was followed for an arbitrary FBG in Array 4 with a Bragg wavelength of 1546 nm as seen in Figure 7.3. Here, for the same applied (increasing) loads, the spectrum shifts to the left as the FBG is bonded on the suction side, where the blade surface is facing downwards in this Orientation O1. These two figures are selected and included here only for the purpose of illustrating and confirming the right-shift and left-shift trend of the FBG spectra depending on the blade orientation and which surface the sensor was bonded and to demonstrate that the spectral peak remains approximately Gaussian.

The defective region was covered by four FBGs from Array 3 and four FBGs from Array 5 as illustrated in the Figure 7.4 and Table 7.1 below.

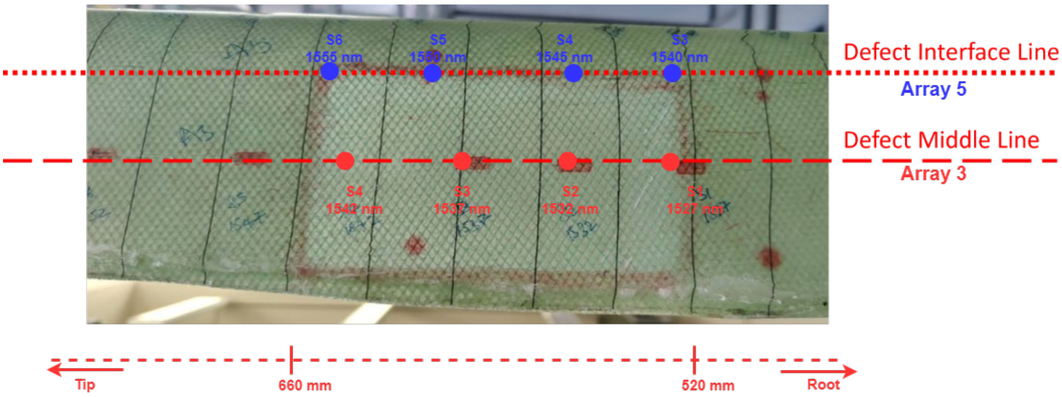

Figure. 7.4 Intentionally introduced defect on the pressure side of the blade

Table 7.1 FBGs covering the defective region

DTG N°	Array ID	FBG-ID	Sensor Wavelength (nm)	Location on Defect (mm)
1	Array 3	S1	1527	525
2		S2	1532	565
3		S3	1537	600
4		S4	1542	640
5	Array 5	S3	1540	520
6		S4	1545	550
7		S5	1550	620
8		S6	1555	660
Defect covers from 520 mm to 660 mm on the blade				

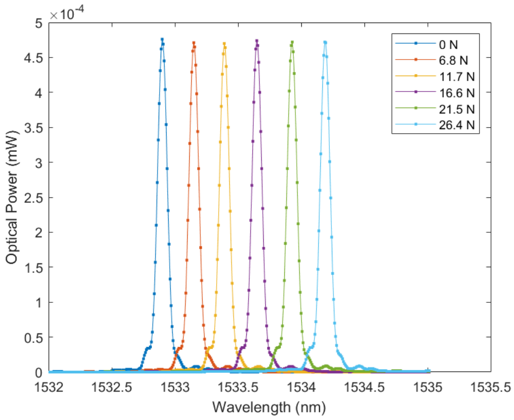

(a) Array 3: 1532 nm - right shift

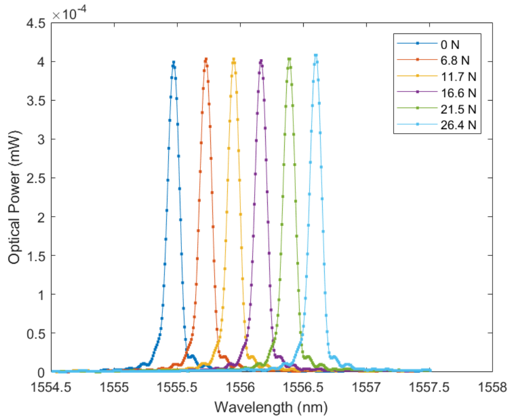

(b) Array 5: 1555 nm - right shift

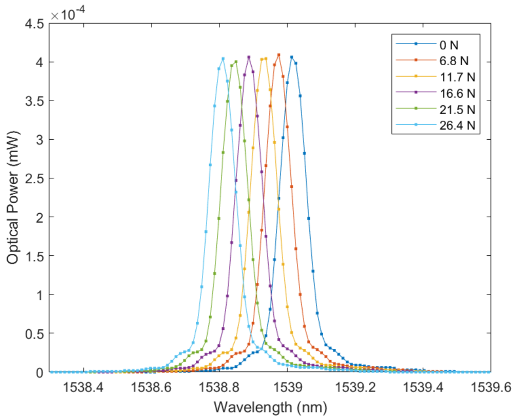

(c) Array 2: 1539 nm - left shift

Figure. 7.5 Wavelength shift of FBGs showing right and left spectral shift (a) Array 3: 1532 nm (b) Array 5: 1555 nm (c) Array 2: 1539 nm at L3-O1

Key observations from Figure 7.5 show that all FBGs in both Arrays 3 and 5 exhibit rightward spectral shifts under increasing loads, confirming tensile strain. The magnitude of wavelength shift is influenced by both sensor location and loading position. FBG-2 of Array 3 (Bragg wavelength 1532 nm) and FBG-6 of Array 5 (Bragg wavelength 1555 nm) cover the defect, leading to significantly higher wavelength shifts compared to FBGs outside the defect region. This suggests that the presence of a defect introduces localised strain concentrations, which amplify the sensor response. Furthermore, FBG-6 in Array 2, bonded on the non-defective suction-side surface, exhibits a leftward spectral shift in Orientation 2, confirming expected compression behaviour. This highlights the reliability of the sensor placement strategy in distinguishing tensile and compressive strains under different loading conditions.

7.4.2 Sensor Wavelength vs Strain Measured

This section examines the relationship between the sensor wavelength of each FBG and the corresponding strain measured for both the healthy and defective blades. Plotting the sensor wavelength against strain provides a straightforward method to evaluate strain distribution patterns across the array under increasing applied loads. More importantly, these plots help determine which sensors are functioning correctly i.e. showing a linear response and which may be malfunctioning due to improper bonding or other experimental inconsistencies.

To illustrate this, Figure 7.6 shows the results for Orientation 1, with loading applied at Location 3. This figure has been selected as a representative case, given that a total of 24 such figures exist for the healthy blade alone, covering both Arrays 1 and 4. Although only a sample is included here, similar figures have been plotted for all orientation-loading location-array combinations to assess the conformity of sensors to expected linear behaviour.

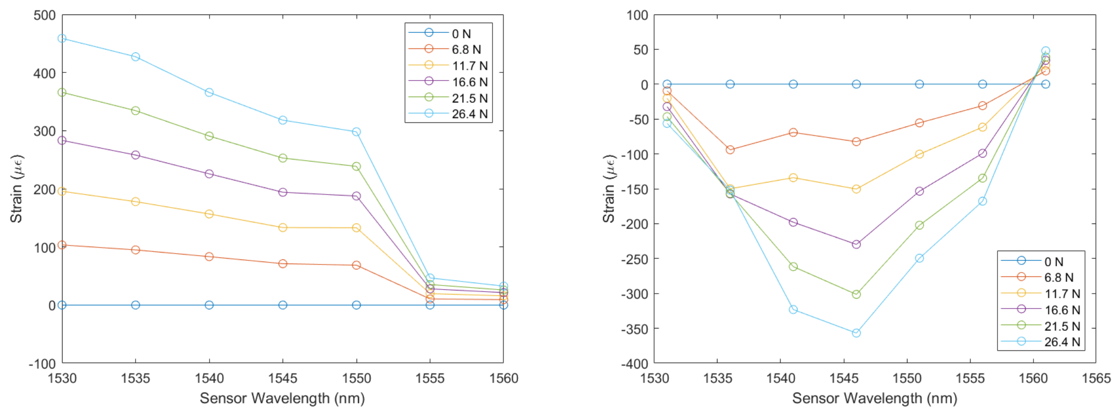

(a) Array 1 (b) Array 4

Figure. 7.6 Sensor Wavelength vs Strain Measured for (a) Array 1 in O1-L3 (b) Array 4 in O1-L3

Although not included or shown in this section, for each orientation-loading location-array these figures have been plotted to evaluate which sensors are not conforming to the expected linear behaviour.

In the first part of Figure 7.6, a deviation from the expected linear strain response is observed in the last two FBGs of Array 1, bonded on the healthy blade. These FBGs, with Bragg wavelengths of 1555 nm and 1560 nm, fail to show the anticipated linear increase in strain under applied loads. This deviation suggests possible issues such as localised bonding defects or misalignment during sensor attachment

A similar analysis was conducted for the defective blade to evaluate whether the sensors bonded over the defective region and adjacent areas maintained a linear strain response under increasing applied loads. As previously noted, the eight FBGs covering the defective region belong to two different arrays, making it crucial to assess their behaviour individually. Additionally, verification was performed to ensure that the suction-side array correctly measured either compression or tension based on the orientation and loading condition.

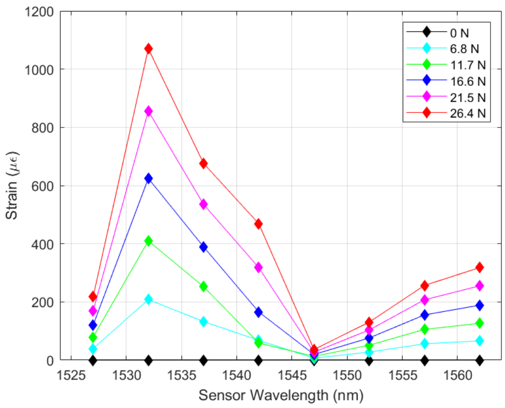

(a) Array 3

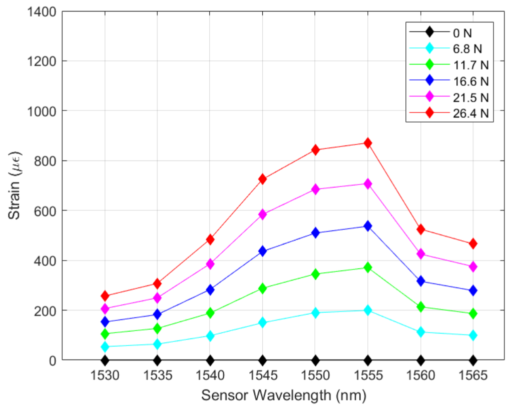

(b) Array 5

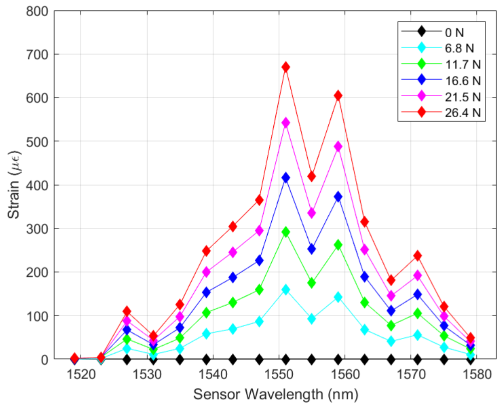

(c) Array 2

Figure. 7.7 Sensor Wavelength vs Strain Measured for (a) Array 3 (b) Array 5 (c) Array 2 all taken at Location 3

In the defective region, Array 3 was bonded directly over the defect and was covered by four FBGs: S1–S4, with Bragg wavelengths of 1527 nm, 1532 nm, 1537 nm, and 1542 nm. In contrast, Array 5 was positioned at the interface between the defective and non-defective regions. Within this array, S3–S6 specifically covered the defect interface, with Bragg wavelengths of 1540 nm, 1545 nm, 1550 nm, and 1555 nm. This positioning allowed for a comparative assessment of strain distribution both within the defect and at the transition zone, where strain concentration effects may be more pronounced. The first two figures in Figure 7.7 depict the behaviour of Arrays 3 and 5, both mounted on the pressure side of the defective blade. Within Array 3, the second FBG (Bragg wavelength: 1532 nm) exhibits a consistent linear increase in measured strain. This trend is similarly observed for the third and fourth FBGs, indicating reliable sensor performance. However, the first FBG, despite being located on the defective region, does not show the expected strain increase. A plausible explanation is poor bonding, which could have resulted in inadequate strain transfer from the blade surface to the sensor. The fifth FBG (Bragg wavelength: 1547 nm) also shows irregular measurements, with strain values clustered around zero. This anomaly further supports the hypothesis of improper bonding at the sensor site.

Array 5 was bonded along the defect interface, as shown in Figure 7.4. The middle four FBGs, which directly covered the defect, displayed excellent linear strain responses, confirming effective strain transfer and sensor reliability. The first and last two FBGs, though not covering the defect, also showed a linear increase in strain, reinforcing the idea that this array was properly bonded without significant issues.

The 16 FBGs in Array 2, which spanned from the root to the tip of the suction side, exhibited varying degrees of spectral shift under increasing loads. Multiple peaks were observed for some sensors, suggesting potential effects from uneven surface bonding or local bending effects. Despite these variations, the majority of FBGs in this array followed a linear trend in strain response, indicating no severe bonding defects throughout the blade.

The deviations observed in certain FBGs, particularly in Arrays 1 and 3, highlight the impact of bonding quality on sensor performance. Poorly bonded FBGs may lead to inaccurate strain readings, either due to mechanical detachment or stress concentrations that distort the strain distribution. The presence of multiple peaks in some suction-side sensors suggests possible micro-bending effects, which may result from slight misalignment of the FBGs during bonding.
Furthermore, the significant difference in spectral shifts between defective and non-defective regions emphasises the potential of FBG sensors for SHM. The heightened response of FBGs over the defect suggests that such sensors could be utilised for early defect detection,

allowing for preventative maintenance and improved reliability of composite structures.

In subsequent sections, a detailed comparison between measured and expected strain will be presented to further assess the accuracy and consistency of FBG sensor readings across different orientations and loading conditions.

7.4.3 Expected vs Measured Strain: Orientation 1

Comparing the results of the healthy and defective blades under each orientation provides crucial insights into the performance of the FBG sensor system and mechanical behaviour of the wind turbine blade. By examining strain distributions at different loading locations, it becomes possible to identify deviations caused by defects and understand their impact on the structural integrity of the blade. This analysis helps in assessing the sensitivity of FBG sensors in detecting structural inconsistencies, validating strain predictions, and determining the reliability of different sensor placements. Furthermore, understanding how defects influence strain patterns under different loading conditions enables better predictive maintenance strategies, reducing the risk of failure and improving the overall efficiency and lifespan of wind turbine blades.

To evaluate strain distribution along the blade length, strain (Y-axis) is plotted against sensor location (X-axis). This visualisation shows the mounting positions of sensors relative to the overall blade length. Both expected strain (ES) and measured strain (MS) are plotted, with circular markers indicating MS and asterisk markers representing ES.

Healthy blade results: Figure 7.9 and Figure 7.10 present the strain measurements from both the pressure-side FBG Array (A1) and suction-side FBG Array (A4) when the blade was mounted in Orientation 1 (O1). In this setup, the pressure side faced upwards while the suction side faced downwards, as illustrated in Figure 7.8. The red lines in these figures indicate the locations where loads were applied.

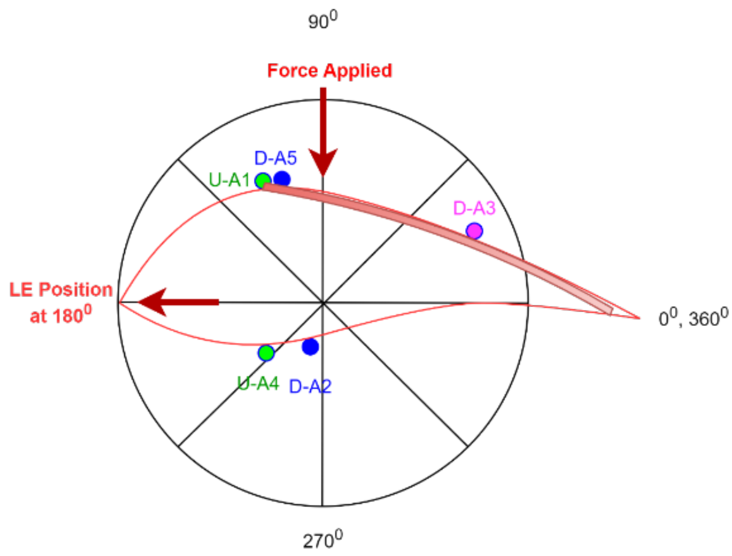

Figure. 7.8 Orientation 1 with all arrays

For the healthy blade, Array 1 (A1) had seven FBGs bonded to the pressure-side, positioned closely along the blade length. Figure 7.9 shows both the expected and measured strain values for each applied load at various sensor positions. In L1, the measured strains beyond the loading point (right of the red dashed line) show negative values, whereas the expected strains are zero. This discrepancy may stem from the increased significance of noise due to the low strain levels in this region. Additionally, the measured strains at 300 mm and 400 mm are notably lower than expected, potentially due to variations in sensor performance caused by bonding inconsistencies or misalignment.

At loading location L2, the expected and measured strains exhibit good agreement, except for the first two sensing points. While minor deviations exist, the general trend follows the predicted strain distribution. Some FBGs recorded slightly higher strains than expected, which may indicate localised stress concentrations In the tip-loaded case (L3), the expected and measured strains closely align, confirming the structural integrity of the healthy blade under this load configuration.

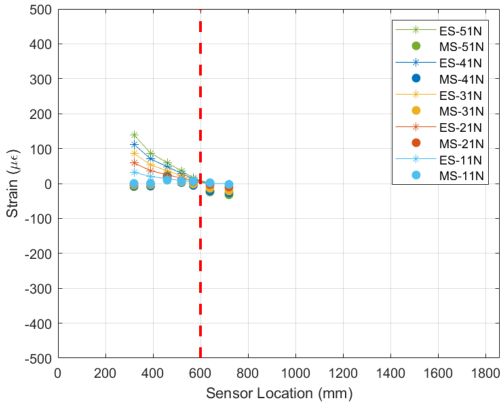

(a) Location 1

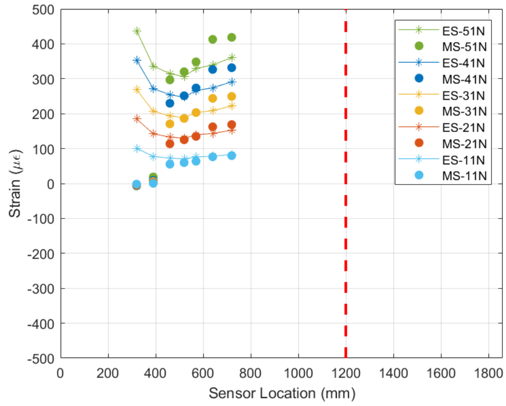

(b) Location 2

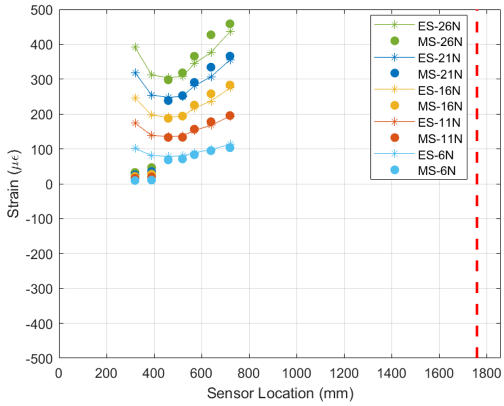

(c) Location 3

Figure. 7.9 Measured vs expected strain for healthy blade (a) L1 (b) L2 (c) L3 for A1 at O1

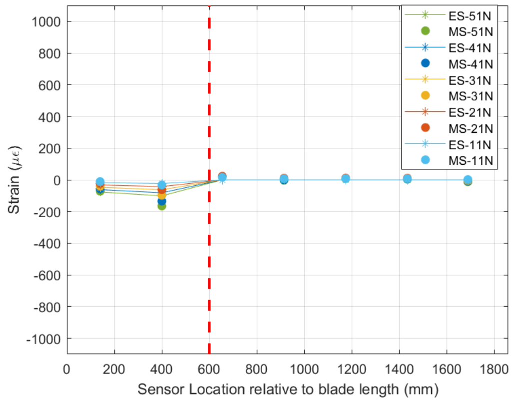

(a) Location 1

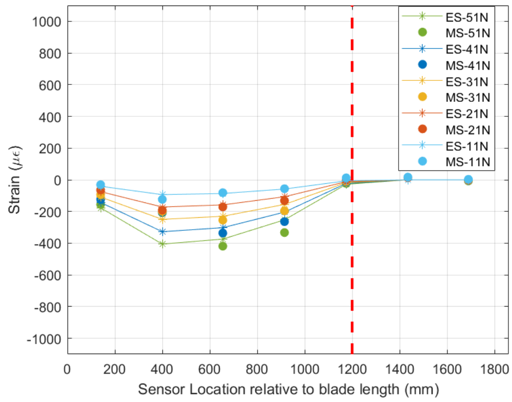

(b) Location 2

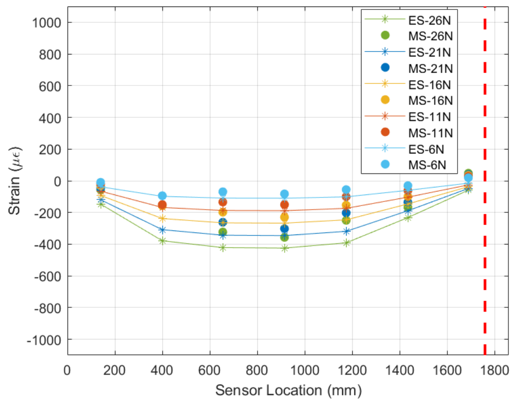

(c) Location 3

Figure. 7.10 Measured vs expected strain for healthy blade (a) L1 (b) L2 (c) L3 for A4 at O1

For Array 4 (A4), which covered nearly the entire length of the blade on the suction side, the sensors experienced compressive strain. At L1 and L2, compressive trends were recorded before the loading points, as anticipated. The strain magnitudes for L1 were lower than for L2, which aligns with expected load distribution principles. As seen in A1 results at L1, the strain after the loading points is zero. At L3, the agreement between expected and measured strains improves, further validating the strain modelling accuracy for a healthy blade.

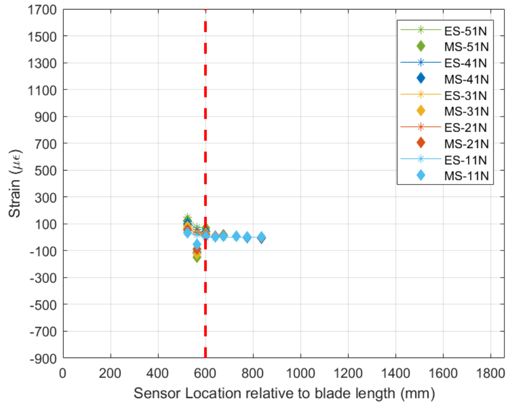

(a) Location 1

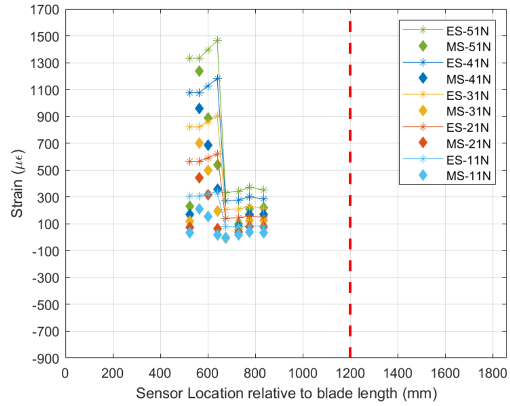

(b) Location 2

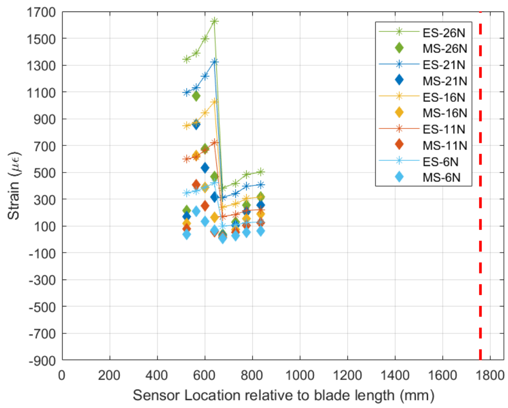

(c) Location 3

Figure. 7.11 Measured vs expected strain for defective blade (a) L1 (b) L2 (c) L3 for A3 at O1

Defective blade results: For the defective blade, FBG Array 3 (A3) was bonded in the middle of the defect region, spanning 520 mm to 660 mm lengthwise on the blade, passing over the L1 loading location which is at 600 mm lengthwise (Figure 7.4). Compared to the healthy blade, the defective region exhibits altered material properties, where the absence of fibre reinforcement and reduced thickness leads to a significantly diminished Young's modulus. This change, in turn, causes a shift in the neutral axis and a decrease in stiffness, reflected in the lower moment of inertia (lower I_{xx}, I_{yy}). Under the highest applied load (26 N) at L3, the first four FBGs in A3 shown in Figure 7.11 recorded strain values ranging from 1345 to 1630 $\mu\varepsilon$. However, an anomaly was observed at the FBG bonded at 565 mm (FBG-S2-1532 nm), where the measured strain (1070 $\mu\varepsilon$) was significantly lower than the expected 1390 $\mu\varepsilon$. This discrepancy suggests either minor delamination at the sensor bonding interface or variations in stress distribution due to the defect's influence. At L1, where the loading point coincided with the defect centreline, the strain results were heavily distorted by noise. The interference from the defect's altered stiffness led to inconsistent strain readings, making L1 an unreliable position for defect evaluation. Instead, the tip-loaded (L3) case provided the most reliable strain measurements for assessing defect-related deformations.

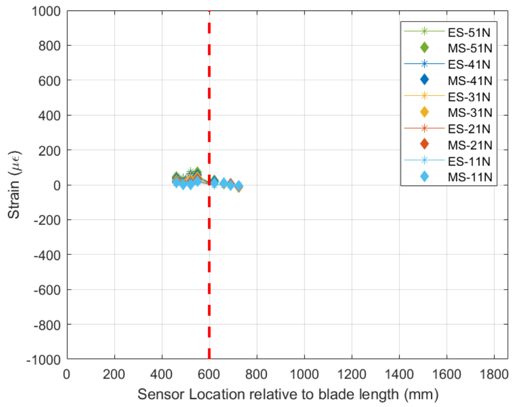

(a) Location 1

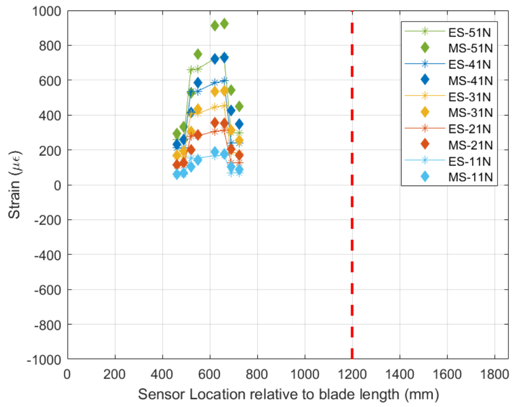

(b) Location 2

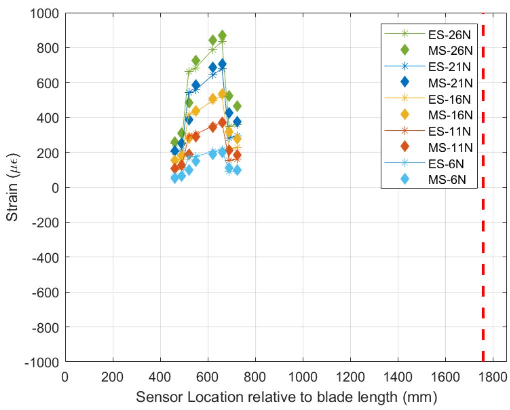

(c) Location 3

Figure. 7.12 Measured vs expected strain for defective blade (a) L1 (b) L2 (c) L3 for A5 at O1

FBG Array 5 (A5) was bonded along the interface between the defective and healthy composite materials. The expected strain estimations for A5 considered a combined Young's modulus to represent both materials, as shown in the equation:

$$E_{\text{Defect Interface}} = \frac{E_{\text{Healthy}} + E_{\text{Defective}}}{2} \tag{7.3}$$

For L3, the measured and expected strain values showed excellent agreement across all eight FBGs, with both magnitude and trend closely matching (Figure 7.12). However, at L2, the difference between expected and measured strain increased as the load was raised, indicating that the defect's influence on strain distribution became more pronounced at this location. At L1, where the defect centreline aligned with the loading position, measured strains showed significant distortion, except for FBG-1 and FBG-4, where minor deviations from expected values were recorded. Overall, the L1 strain readings were unreliable for defect characterisation due to excessive noise and interference from the coinciding load and defect positions.

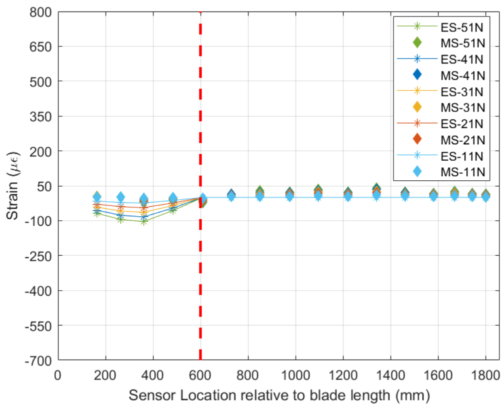

(a) Location 1

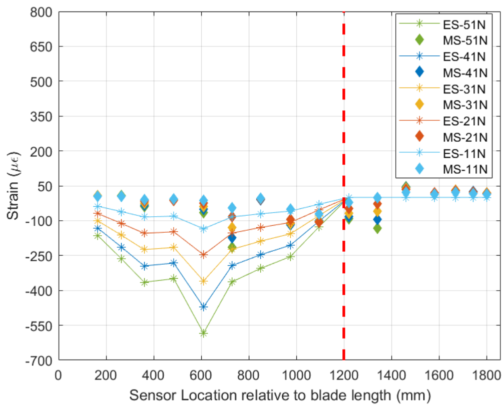

(b) Location 2

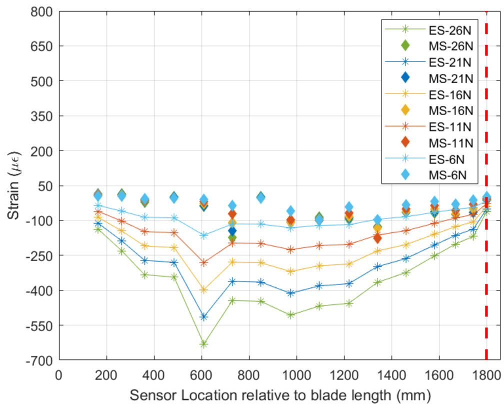

(c) Location 3

Figure. 7.13 Measured vs expected strain for defective blade (a) L1 (b) L2 (c) L3 for A2 at O1

FBG Array 2 (A2) was bonded along the entire length of the blade on the suction side. Across all test cases, the measured strain values were considerably lower than expected.

When loaded at L1 and L2, the blade behaved as a cantilever, with maximum expected strain occurring before the load point and being influenced by the pressure-side defect. At L1, the expected strain beyond the loading point was zero, but measured strains exceeded 50 $\mu\varepsilon$, indicating localised stress redistributions likely caused by defect-induced stiffness variations. This suggests that while A2 captured some strain deviations related to the defect, its effectiveness in detecting the defect was limited compared to arrays bonded closer to the defect region (A3, A5).

Critical analysis and key insights

- **Reliability of Different Loading Locations:** Among the three loading locations, L1 and L2 exhibited distortions and L3 (tip load) produced the most reliable strain data, especially for evaluating defect-induced strain variations. L1 results were highly distorted due to noise and direct loading point-defect interaction, making it the least effective for defect detection.

- **Effectiveness of FBG Arrays and sensor positioning:** The results highlight a critical finding; FBGs positioned directly over the defect (Array 3) struggle to capture the full strain response, whereas those mounted at the defect interface (Array 5) provide significantly higher detection accuracy. This suggests that strain concentration effects at the defect interface are more predictable rather than necessarily larger in magnitude. While absolute strain values may not always be higher at the interface, the strain distribution in this region follows a more consistent trend, making it easier to detect and characterise defects based on deviations from the expected strain profile.

- **Transition at Defect Interface:** The results confirm that an averaged Young's modulus represents the defective region accurately, as demonstrated by the improved agreement in A5's strain measurements.

Overall, while Orientation 1 provided critical insights into the defect's influence on strain distribution, the distortions observed reinforce the importance of choosing appropriate loading conditions (e.g., L3) for more accurate defect assessments.

7.4.4 Expected vs Measured Strain: Orientation 2

Healthy blade results: For the healthy blade, Orientation 2 was mounted in such a way that Array A1 faced downwards and Array A4 faced upwards, subjecting the blade to a negative flapwise motion at a slight angle (Figure 7.14). In both arrays (A1 and A4), the tip-loaded case (last figure of Figure 7.15 and Figure 7.16) shows excellent agreement between the expected and measured strain values. However, in the case of loading at L1, both A1 and A4 recorded significantly lower strains than expected, with the discrepancy increasing under higher loads. Beyond the loading point, the sensors of both A1 and A4 deviate from the expected strain trend, which suggests either a structural non-linearity or external influences affecting strain measurement.

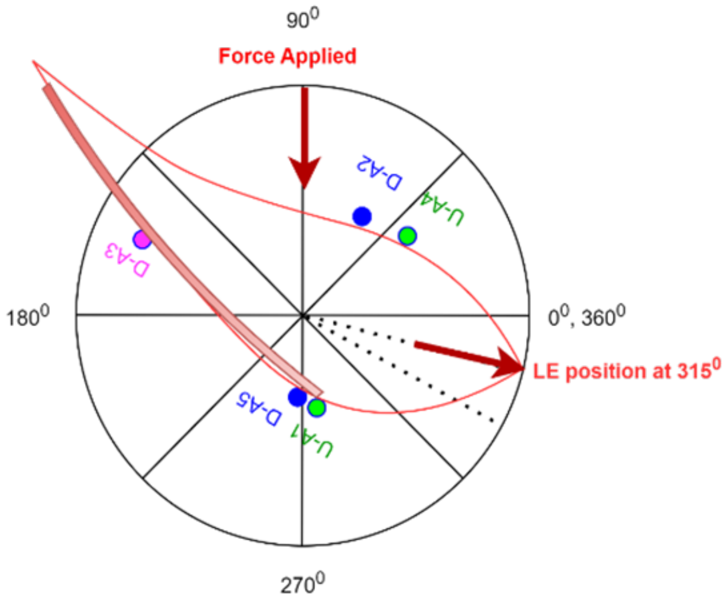

Figure. 7.14 Orientation 2 with all arrays

At L2, the expected vs. measured strain discrepancy was much lower. Only the first two sensors of A1 exhibited deviations, while the rest of the sensors followed the expected trend. Notably, at all loading points and orientations, the first two sensors of A1 consistently deviated from expected trends, indicating potential sensor misalignment, local defects, or inaccuracies in strain transfer to the sensor. Additionally, expected strains were calculated without considering variations in ambient temperature, whereas real measurements were influenced by temperature changes in the laboratory space.

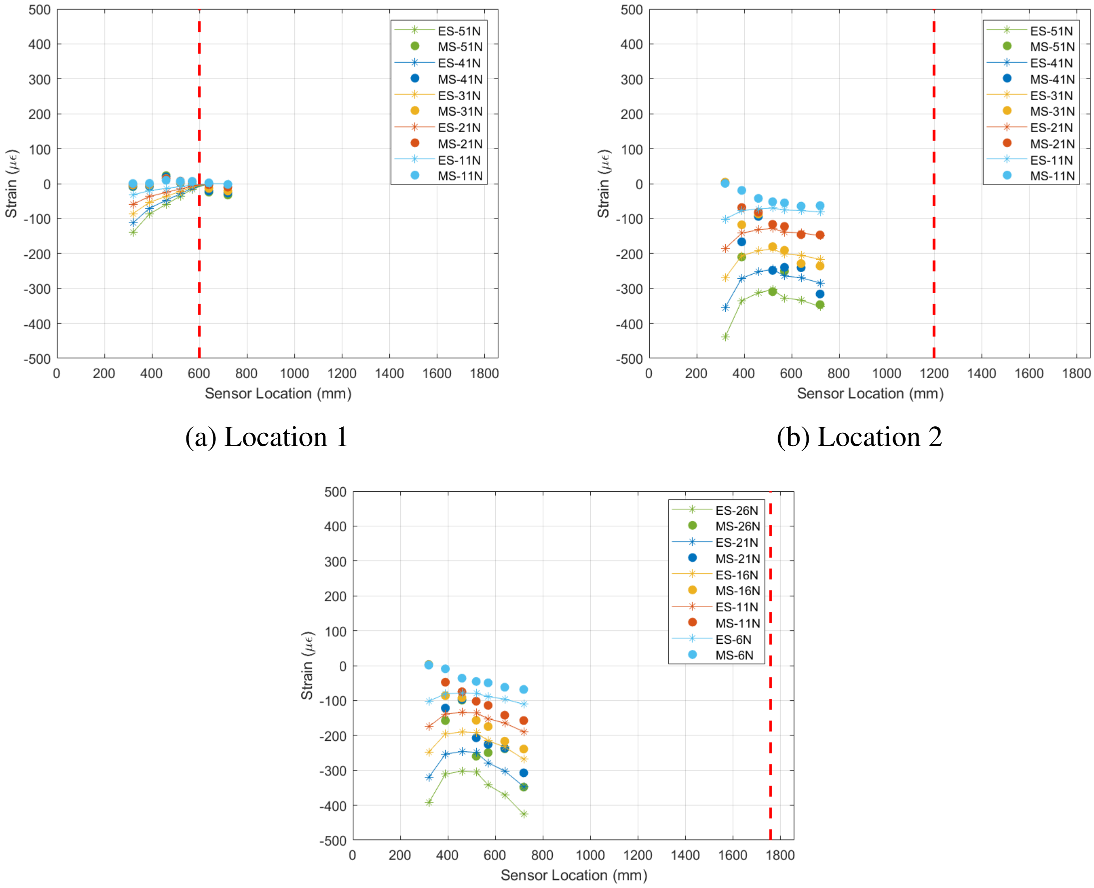

(a) Location 1

(b) Location 2

(c) Location 3

Figure. 7.15 Measured vs expected strain for healthy blade (a) L1 (b) L2 (c) L3 for A1 at O2

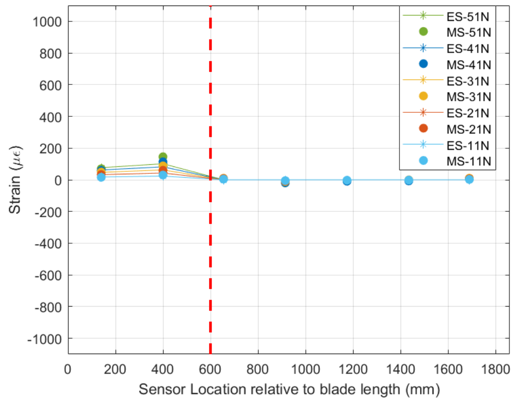

(a) Location 1

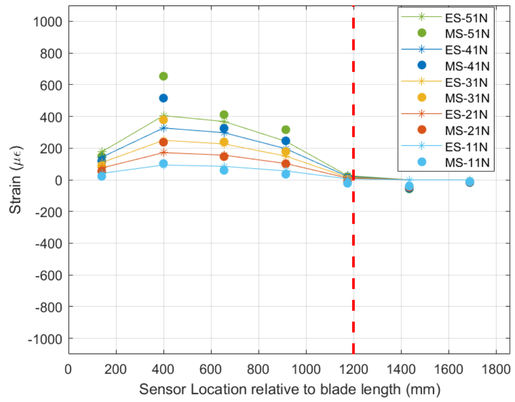

(b) Location 2

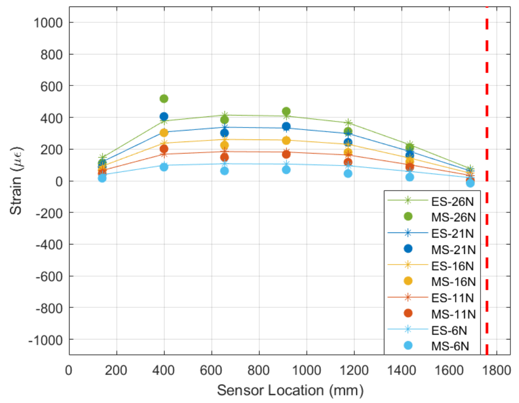

(c) Location 3

Figure. 7.16 Measured vs expected strain for healthy blade (a) L1 (b) L2 (c) L3 for A4 at O2

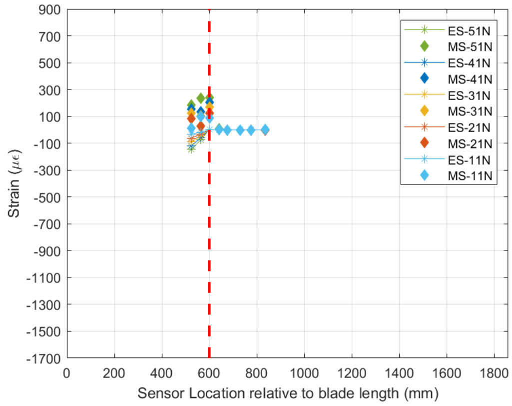

(a) Location 1

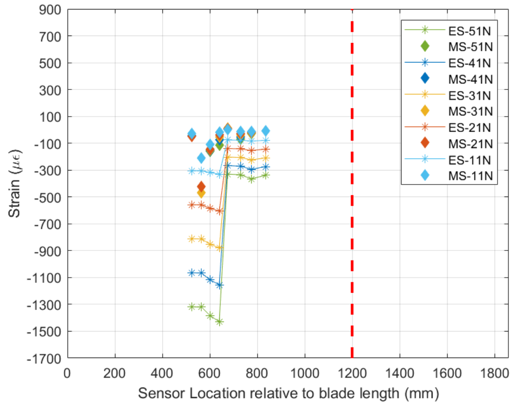

(b) Location 2

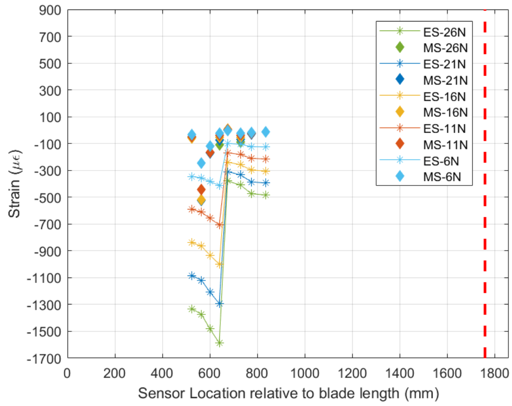

(c) Location 3

Figure. 7.17 Measured vs expected strain for defective blade (a) L1 (b) L2 (c) L3 for A3 at O2

Defective blade results: For the defective blade, Orientation 2 represents a negative flapwise bending moment as shown in Figure 7.14, which means that the strain is of almost the same magnitude as in positive flapwise bending but reverses sign (compressive instead of tensile strain). Looking at Figure 7.17, Array 3 results revealed significant discrepancies, with all sensors failing to align with expected strain values. The only instance of agreement occurred beyond L1, where measured strain values approached zero, likely due to reduced stiffness and redistribution of strain near the defect region.

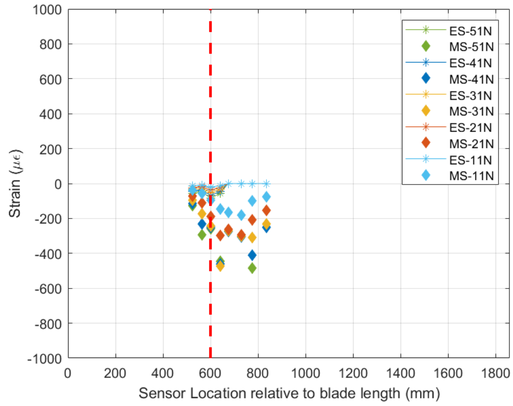

(a) Location 1

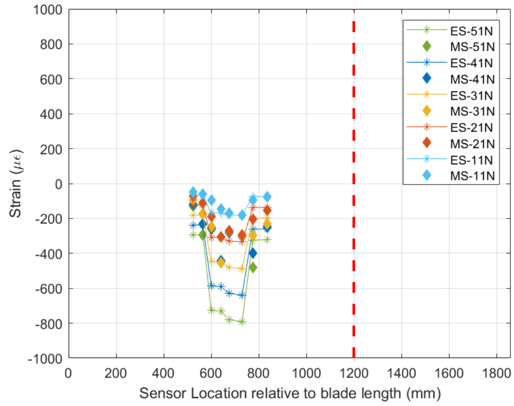

(b) Location 2

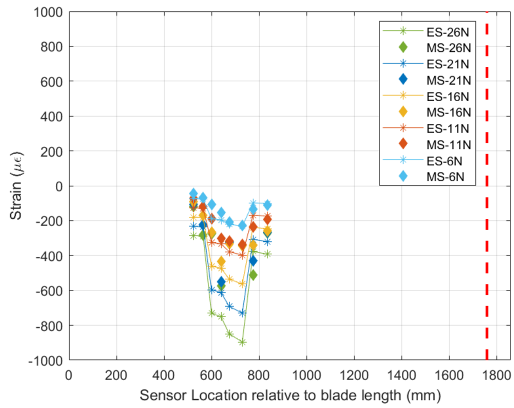

(c) Location 3

Figure. 7.18 Measured vs expected strain for defective blade (a) L1 (b) L2 (c) L3 for A5 at O2

Looking at Figure 7.18 results from Array 5, unlike the previous orientation, sensors recorded lower strain values than expected, particularly at higher loads in the L3 case. At lower loads (6 N and 11 N), agreement was better for both L3 and L2. However, for L1, the expected strain was around 70 $\mu\varepsilon$, yet all sensors recorded significantly higher and erratic strain values, showing no systematic behaviour. When a region of the blade has reduced stiffness; due to material discontinuities, fibre reinforcement loss, or thickness reduction, the structural integrity in that area can be compromised, making it more susceptible to instability under compressive loads. This suggests that at L1, the interaction of defect stiffness variation and load positioning severely affects measurement reliability.

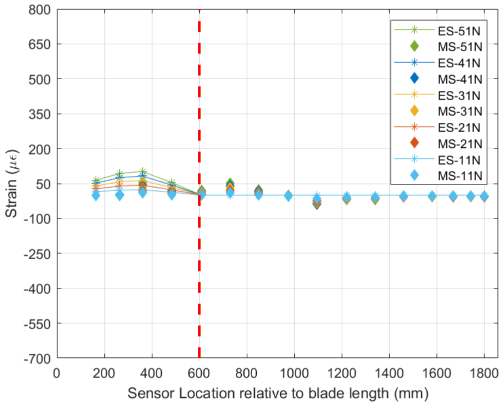

(a) Location 1

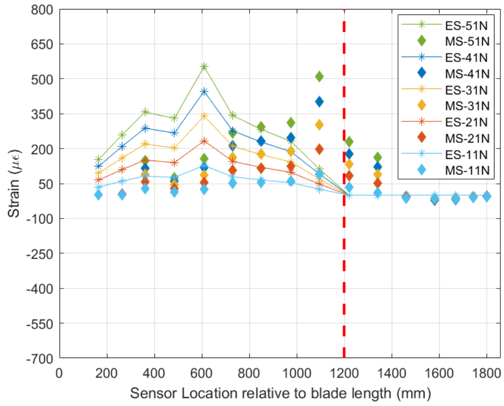

(b) Location 2

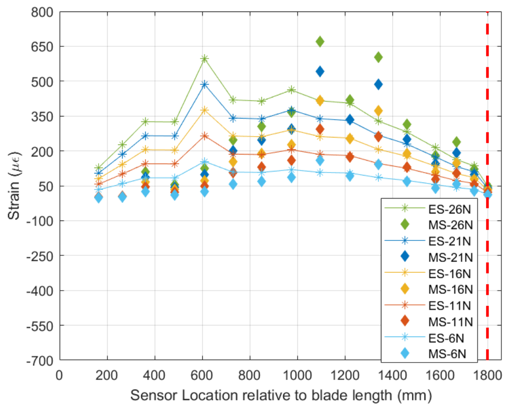

(c) Location 3

Figure. 7.19 Measured vs expected strain for defective blade (a) L1 (b) L2 (c) L3 for A2 at O2

In the defective blade, looking at Figure 7.19 Array 2 results, from L3 mostly aligned with expected values, with only minor deviations where FBGs recorded slightly higher strain than expected. For L2, agreement was observed between 800 mm and 1000 mm of blade length, but beyond this region, measured strain values remained higher than zero, contrary to expectations. At L1, almost all sensors, except S12-S16, were out of the expected range, further emphasising the difficulty of obtaining reliable data near the defect region at this loading position.

Critical analysis and key insights

- **Reliability of Different Loading Locations:** Tip-loaded cases (L3) provided the most reliable and consistent measurements across both healthy and defective blades, as observed in previous orientations. L2 showed moderate agreement, with slight deviations at higher loads, suggesting that strain distribution remains predictable until external effects, such as sensor positioning and defect interaction, dominate. L1 consistently resulted in the most unreliable strain readings, particularly in the defective blade, due to the coincidence of the defect mid-line with the loading position, leading to non-uniform stiffness distribution and erratic strain propagation.

- **Effectiveness of FBG Arrays and sensor positioning:** Array 5 showed better alignment with expected strain behaviour under positive flapwise loading, especially at higher loads. This suggests that Array 5 sensors may be more suited for detecting strain under specific loading conditions, especially tip-loading scenarios.

- **Transition at Defect Interface:** At the interface between defective and non-defective material (monitored by Array 5), expected strain trends were better captured in the positive flapwise bending orientation. In negative flapwise bending, agreement deteriorated, particularly at L1, where the measured strains were erratic and highly deviated. This suggests that load application near the defect can introduce noise and distortions.

7.4.5 Expected vs Measured Strain: Orientation 3

Orientation 3 represents the positive edgewise bending moment, where the applied force is directed downwards opposite to the leading-edge direction, as shown in Figure 7.20. This orientation primarily induces edgewise strain, which is generally lower than the flapwise strain observed in previous cases.

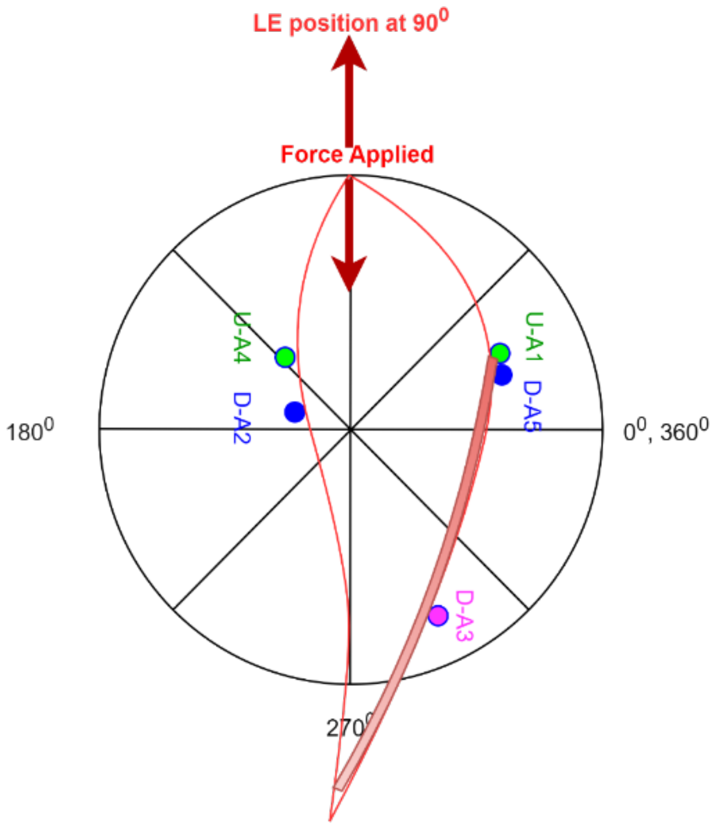

Figure. 7.20 Orientation 3 with all arrays

Healthy blade results: For the healthy blade, Figure 7.21 illustrates the strain response of Array A1 under different loading conditions. At L1, the measured and expected strains are mostly aligned, except for FBG-S7 (320 mm) and FBG-S6 (390 mm), which exhibit deviations. However, for L2 and L3, the measured strains are significantly higher across all sensors, suggesting the presence of an additional contributing factor influencing the tensile strain within Array A1. This could be attributed to local structural non-uniformities or minor variations in the bonding quality of the FBGs. A notable observation in the tip-loaded case shown in last figure of Figure 7.21, is the localised strain increment at FBG-S3 (570 mm, 1540 nm), while the other sensors maintain a consistent linear trend. This localised variation could indicate either an isolated stress concentration or minor imperfections in the blade surface at that location.

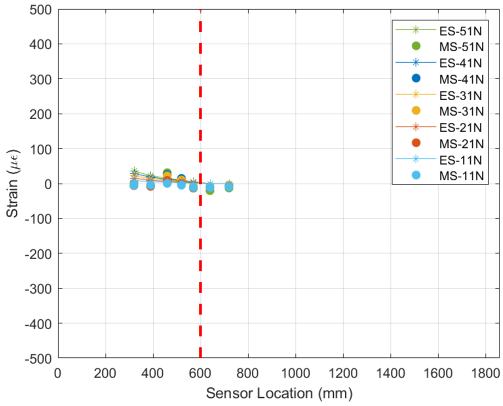

(a) Location 1

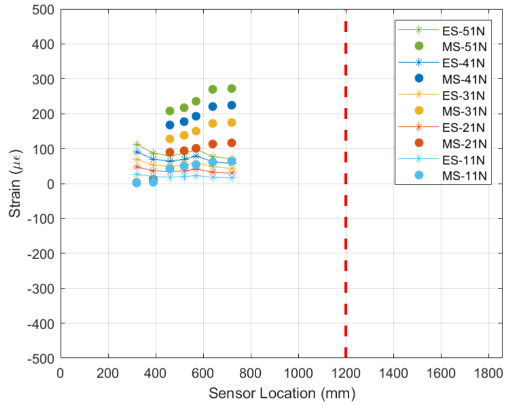

(b) Location 2

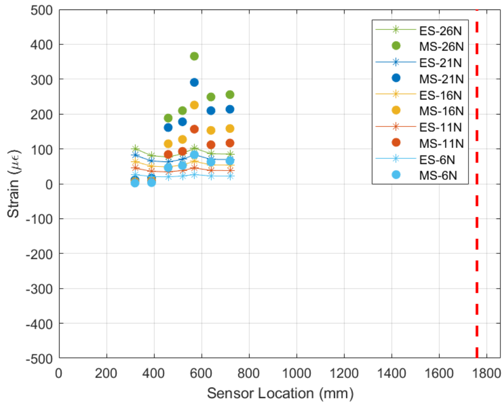

(c) Location 3

Figure. 7.21 Measured vs expected strain for healthy blade (a) L1 (b) L2 (c) L3 for A1 at O3

For Array A4, which was bonded to the suction side facing eastward (Figure 7.22), the maximum expected strain for L3 (tip loading) was -130 $\mu\varepsilon$ for a load of 26.48 N. The negative sign signifies compressive strain. However, results shown in Figure 7.22 reveals that the actual measured strain exceeded expectations, reaching -200 $\mu\varepsilon$, suggesting either minor variations in blade stiffness or sensor over-sensitivity to applied loads. For L1 and L2, the measured strains are largely in agreement with the expected trends, with L1 exhibiting a higher peak strain (790 $\mu\varepsilon$ at 51.01 N). This suggests that, while edgewise loading is generally lower in magnitude compared to flapwise loading, localised strain variations can still emerge depending on sensor positioning and blade material distribution.

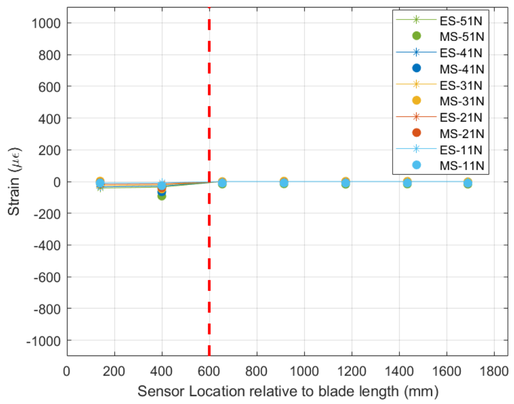

(a) Location 1

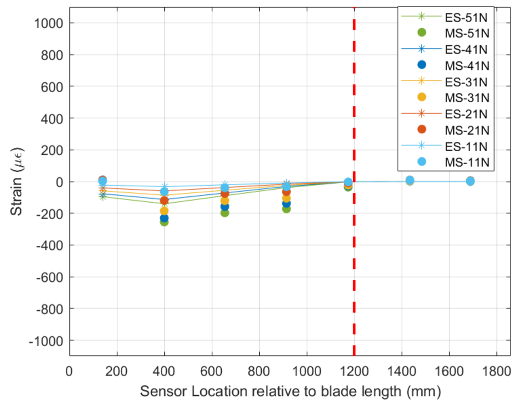

(b) Location 2

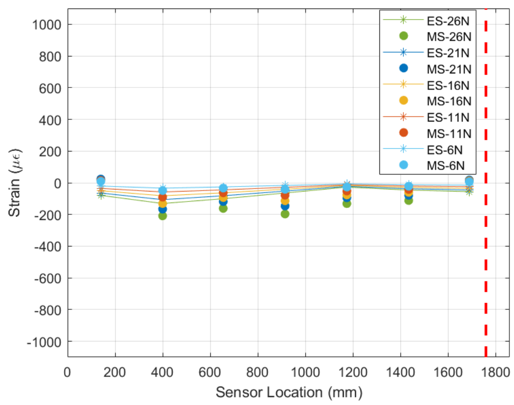

(c) Location 3

Figure. 7.22 Measured vs expected strain for healthy blade (a) L1 (b) L2 (c) L3 for A4 at O3

Defective blade results: For the defective blade, Orientation 3 predominantly induces edgewise strain, leading to lower overall strain values (Refer Figure 7.20). At L3 results shown in Figure 7.23 , except for FBG-S2 (1532 nm) and FBG-S3 (1537 nm), all other sensors exhibit reasonable agreement with expected strain values. The final two FBGs (FBG-S7 and FBG-S8) show the most accurate readings, aligning well with predictions. This suggests that, despite the presence of a defect, certain sensor locations remain relatively unaffected, maintaining good measurement reliability. At L2, both expected and measured strain values remain low (100 $\mu\varepsilon$), although one sensor measures an unexpectedly high strain. This deviation may stem from prior measurement errors, particularly spectral misalignment in scanning.

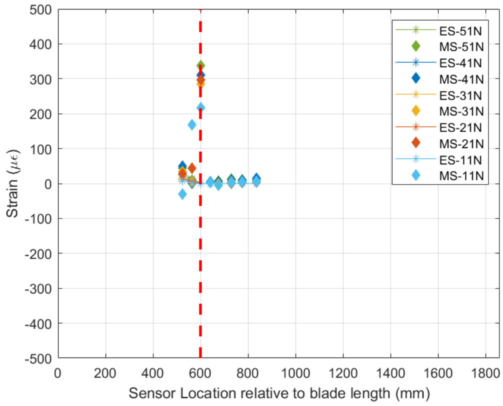

(a) Location 1

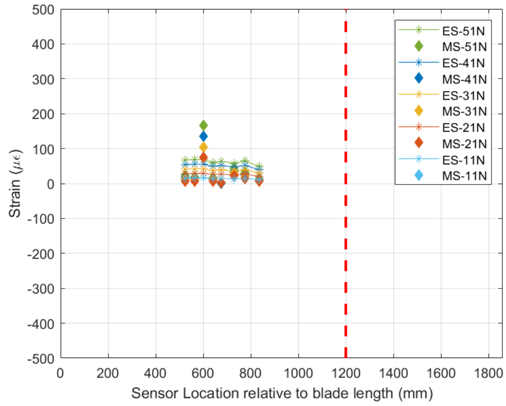

(b) Location 2

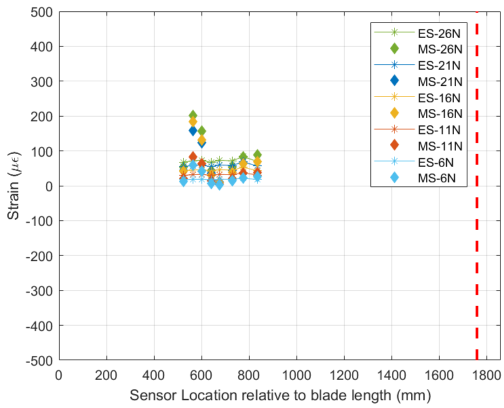

(c) Location 3

Figure. 7.23 Measured vs expected strain for defective blade (a) L1 (b) L2 (c) L3 for A3 at O3

At Location 1 (L1), a significant deviation is observed, particularly for FBG-S3 (600 mm, 1537 nm), which records an unusually high strain. Other sensors measure low strain values close to zero, aligning with expectations. The deviation in FBG-S3 suggests either an anomaly in local stiffness at that position or measurement noise caused by edgewise force redistribution at the defect site.

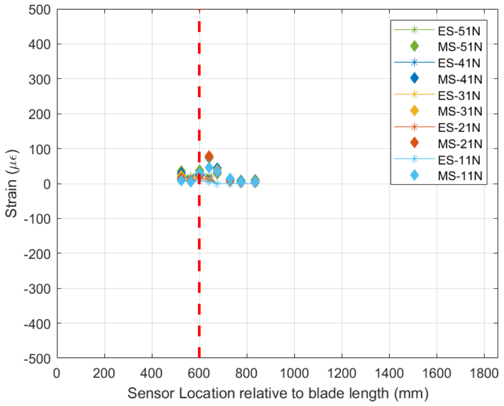

(a) Location 1

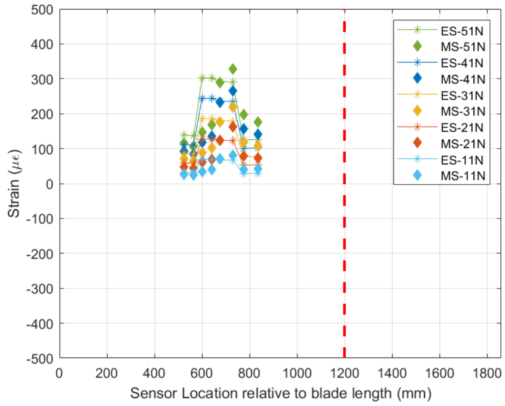

(b) Location 2

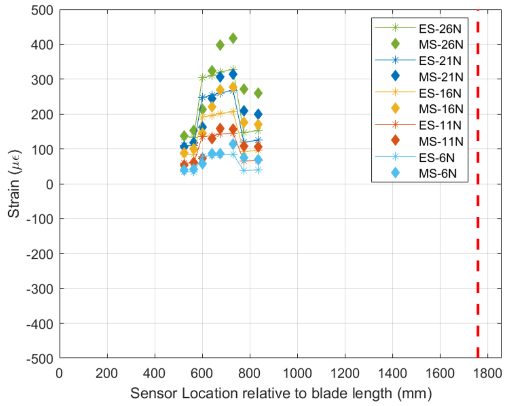

(c) Location 3

Figure. 7.24 Measured vs expected strain for defective blade (a) L1 (b) L2 (c) L3 for A5 at O3

For Array 5, most of the strain comes from the edgewise force component when resolved. For the L3 case, the maximum expected strain was around 315 $\mu\varepsilon$ on average for the sensors covering the defect interface line. The measured strain on average for those same sensors covering the defective was around 340 $\mu\varepsilon$, which was slightly higher than the expected values. However, looking at the results from location 3 in Figure 7.24, it can be seen that the measured strains for the 3rd FBG records significantly lower and the 5th FBG records significantly higher strain compared to their expected strain counterparts. Similarly, the same can be observed for the L2 case in Figure 7.24. Here, the average expected strain over the defective region was predicted to be 290 $\mu\varepsilon$ whereas the measured strains were at 230 $\mu\varepsilon$ which was slightly lower. Within the sensors bonded at the defective region, the same observation made for L3 case can be seen repeated here. Considering the L1 case, where both the loading location and the mid-point of the defective region coincide, the measured strains do not show any agreement apart from the first FBG sensor for all applied loads, while the rest of the sensors throughout the array were heavily noisy. The last two FBGs measure close to zero strain as expected as shown in the first figure of Figure 7.24.

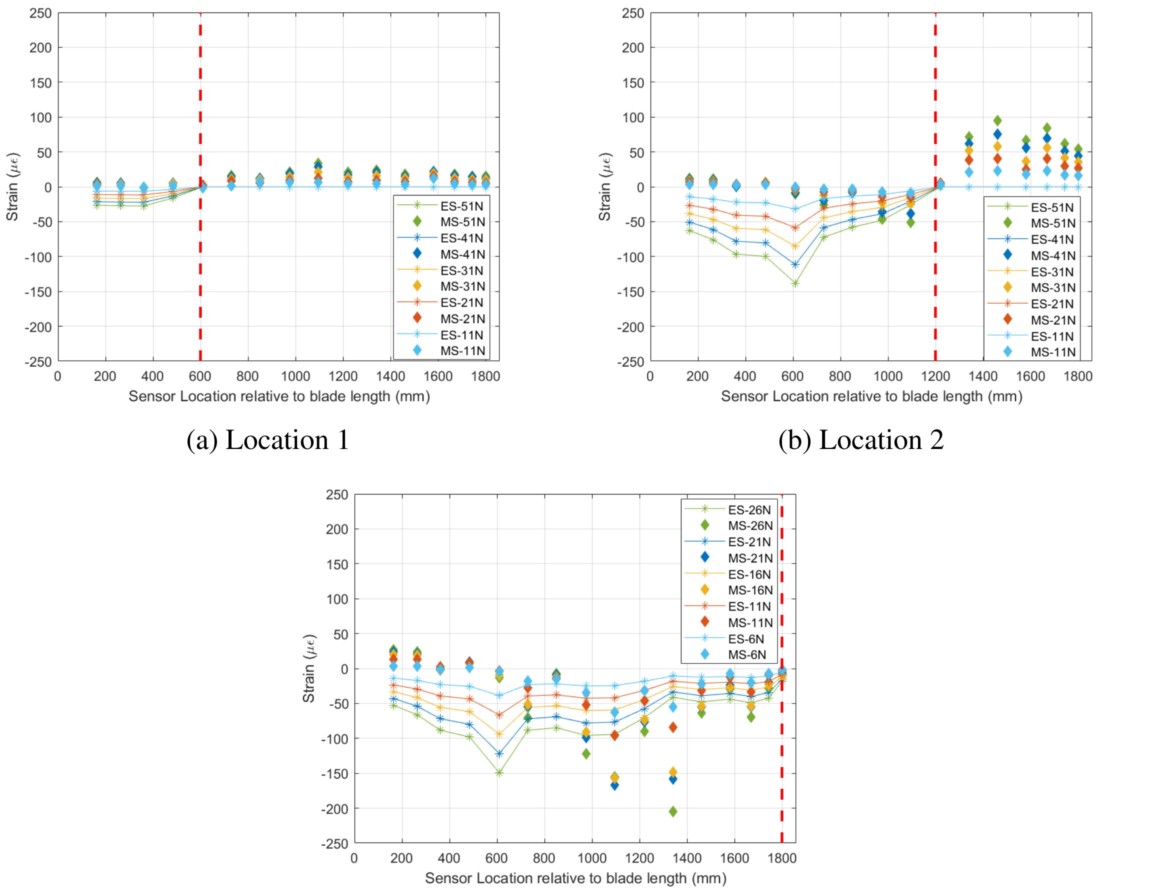

(a) Location 1

(b) Location 2

(c) Location 3

Figure. 7.25 Measured vs expected strain for defective blade (a) L1 (b) L2 (c) L3 for A2 at O3

Array 2 also measures very low strains compared to expected values (Refer Figure 7.25). Compared to the previous flapwise cases, for the same applied loads, the edgewise strain for the blades are generally lower with the maximum being -150 $\mu\varepsilon$. However, looking at L3 case, two FBGs in Array 2 measure beyond the expected strain but the rest of the readings for the same FBGs do not show any alignment to its expected counterparts. This random erogenous measurement gets discarded in the L2 case. Here, the maximum measure strains are well below the expected range. The strains beyond the loading point are significantly higher than the expected zero strain level. The same observation can be seen for L1 case, making the edgewise strain measurement altogether unreliable for Array 2.

Critical analysis and key insights

- **Reliability of Different Loading Locations:** In Edgewise loading, the reliability of strain measurements varies across different loading locations (L1, L2, and L3). L1 exhibits the most inconsistencies, particularly in defective blade scenarios, where strain redistribution across the defect interface leads to unpredictable results. L2 shows better agreement in healthy blades but struggles in defective blades, with measurement inconsistencies in A3 and A5. L3 provides the most consistent results across both blade conditions, though some FBGs in A5 still deviate significantly. Additionally, since the moment of inertia is much larger in O3, the expected strain values are smaller, making measurement noise appear more significant, further complicating the reliability of strain readings. The expected strains in this orientation are already low, making accurate detection more challenging.

- **Effectiveness of FBG Arrays and sensor positioning:** A1 and A4 (healthy blade) exhibit mostly expected trends, except for localised discrepancies due to possible bonding issues. A5 (defective blade, defect interface) provides valuable insight into strain redistribution across defects but shows significant variability in readings. A2 (edgewise strain in defective blade) fails to provide reliable strain measurements, indicating poor sensor placement for edgewise loading scenarios.

- **Edgewise vs. Flapwise Behaviour:** Unlike flapwise loading, edgewise loading exhibits more localised strain variations, particularly near defects. This suggests that different FBG layouts should be considered depending on the primary loading mode.

7.4.6 Expected vs Measured Strain: Orientation 4

Orientation O4 represents the negative edgewise moment of the blade, where the direction of force application, as well as the leading edge, face downward. This is the exact opposite of Orientation O3, and thus, the expected strain trend should be the inverse of the O3 results.

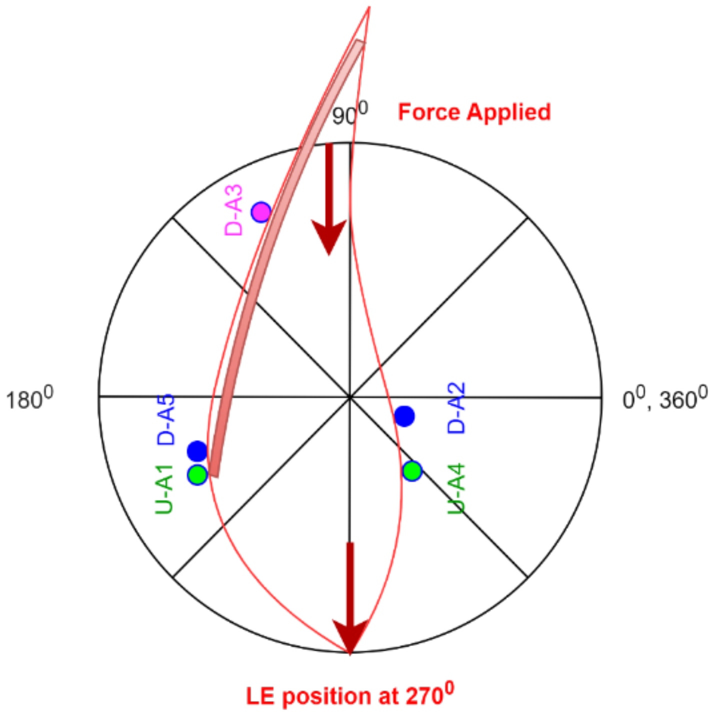

Figure. 7.26 Orientation 4 with all arrays

Healthy blade results: For the healthy blade, the tensile strain results for FBGs from Array A1 at loading locations L1 and L2 show inconsistencies. A random surge in measured strain at Location 1 for the FBG bonded at 570 mm (FBG-S3, 1540 nm) is observed in Figure 7.27. At Location 3, for load cases 26.49 N, 21.58 N, and 16.68 N (shown in the last figure of Figure 7.27), the experimental results deviate from the estimated strain profile, particularly for these load cases. However, for lower load cases, the measured tensile strains are at least within the expected range for the entire healthy blade case in this orientation.

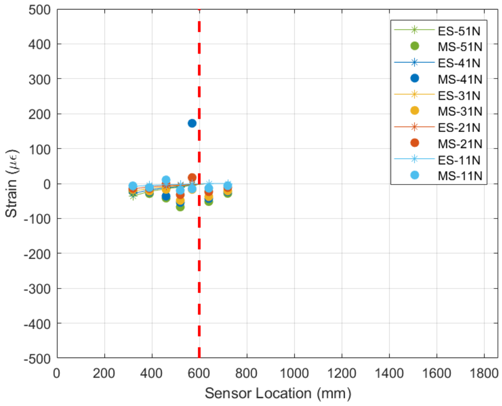

(a) Location 1

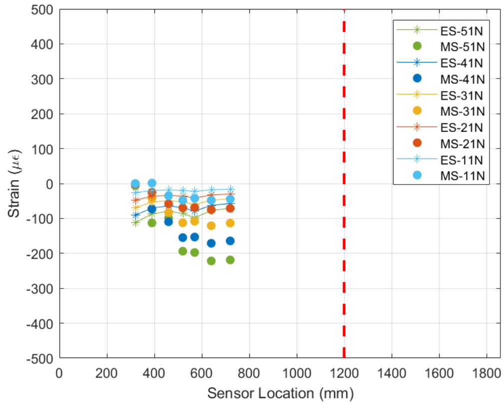

(b) Location 2

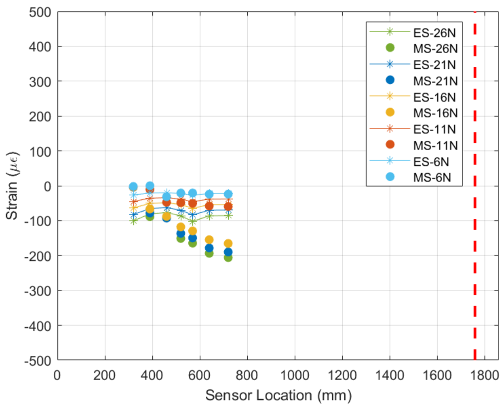

(c) Location 3

Figure. 7.27 Measured vs expected strain for healthy blade (a) L1 (b) L2 (c) L3 for A1 at O4

In contrast, for the L3 case in Array A4, a general agreement in trend is observed, although the sensors do not strictly follow the expected strain profile. At L2, the second FBG bonded at 400 mm records slightly higher strain across all load cases. However, apart from this, the rest of the sensors before the loading location generally align well with the expected values. At Location 1 (Figure 7.28), the measured strains are significantly lower for the last two FBGs, which were expected to show much higher strains. Multiple orientation measurements aid in verifying whether sensors are measuring within the expected range or if abnormalities arise due to sensor bonding issues or localised/random errors in measurement.

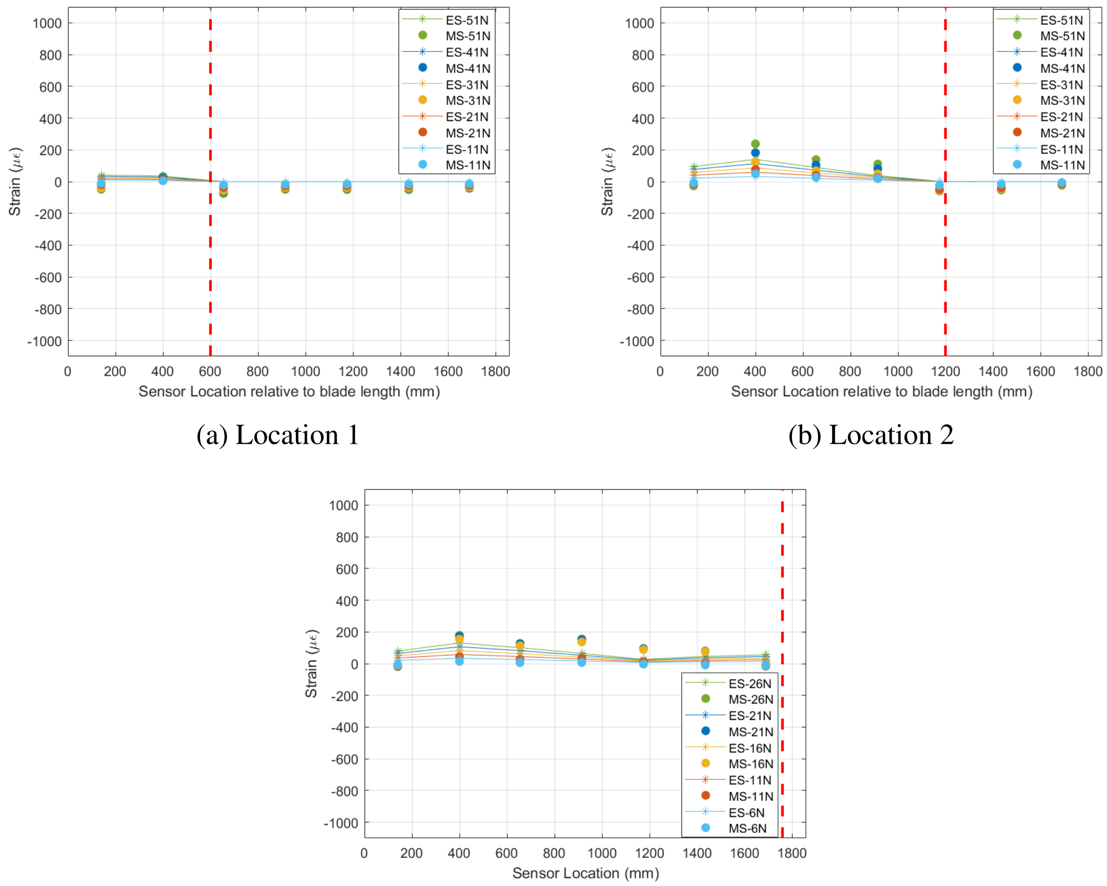

(a) Location 1

(b) Location 2

(c) Location 3

Figure. 7.28 Measured vs expected strain for healthy blade (a) L1 (b) L2 (c) L3 for A4 at O4

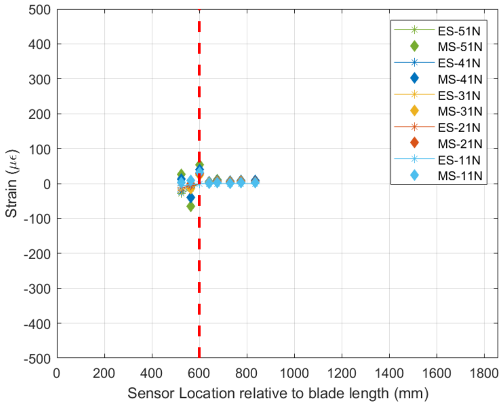

(a) Location 1

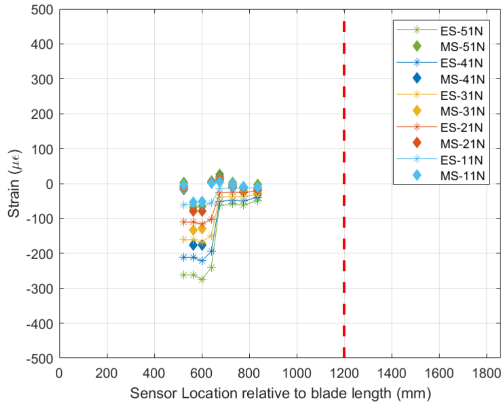

(b) Location 2

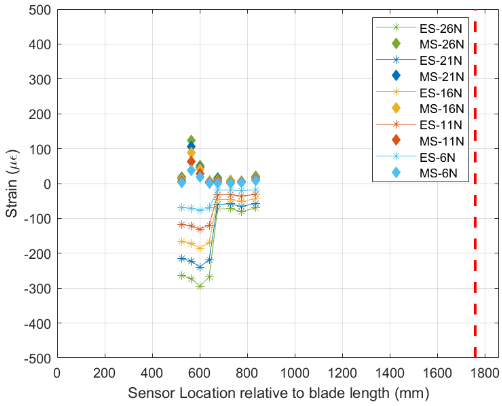

(c) Location 3

Figure. 7.29 Measured vs expected strain for defective blade (a) L1 (b) L2 (c) L3 for A3 at O4

Defective blade results: For the defective blade, Orientation O4 represents the negative edgewise moment, where the overall expected strain is lower compared to the flapwise mounting position. In location 3 results for Array 3 in Figure 7.29, the FBGs covering the defect show significantly lower strain. In the L2 results, the second and third FBGs demonstrate better alignment with the expected trend, albeit slightly lower than anticipated. However, in L1, both measured and expected strain values remain in the lower 0–20 $\mu\varepsilon$ range, making it inconclusive whether the sensors at L1 are accurately following the expected trend or if complications in the measurement process, as seen in L3 and L2, resulted in lower values.

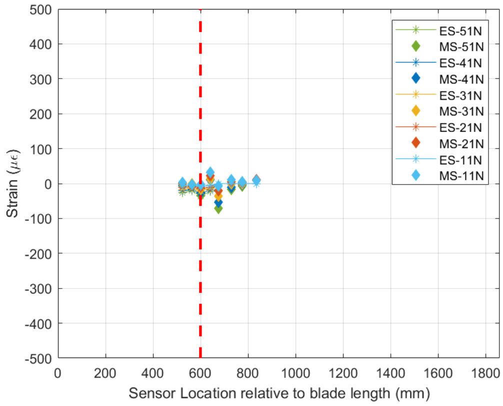

(a) Location 1

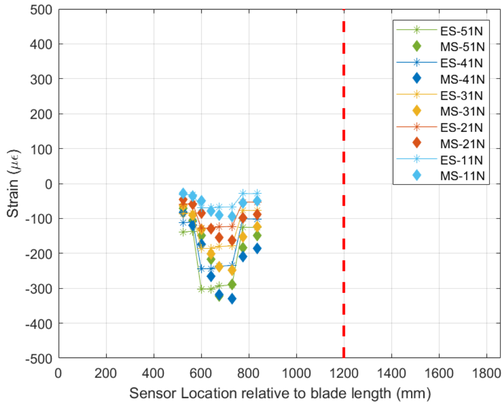

(b) Location 2

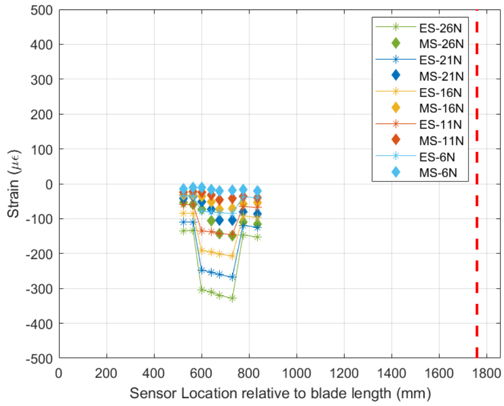

(c) Location 3

Figure. 7.30 Measured vs expected strain for defective blade (a) L1 (b) L2 (c) L3 for A5 at O4

Similar to the L3 and L2 case of Array 3, the FBGs of Array 5 in L3 and L2 case also show better alignment of the measured strains to the expected strain in L2 as seen in Figure 7.30. For L3, the sensors covering the defect do not show any agreement. L2 case shows better agreement across the Array and the overall average strain measured over the defective region also aligns well with the average of the expected strain trend. As both array's L3 case results show this effect, it can be concluded that the measurement process for L3 could have been erroneous. L1 again doesn't show good agreement and the results are heavily noisy due to the fact that both the defect and the loading position coincide.

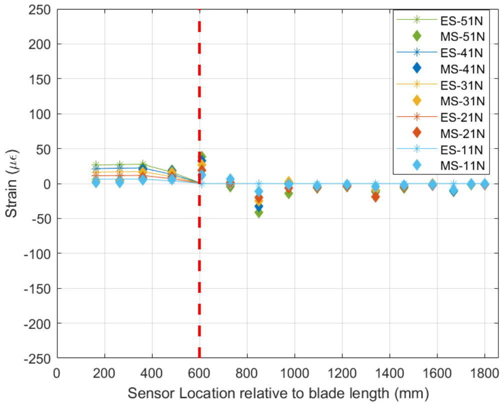

(a) Location 1

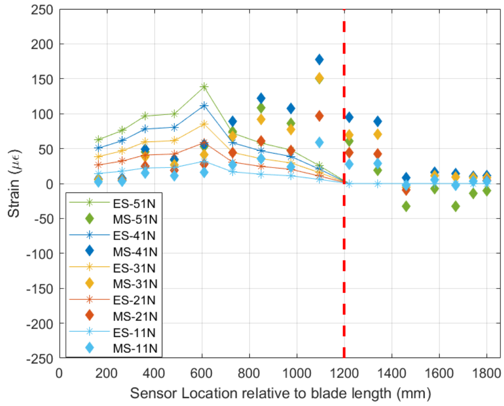

(b) Location 2

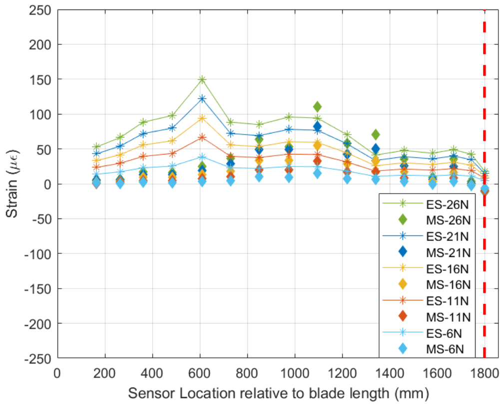

(c) Location 3

Figure. 7.31 Measured vs expected strain for defective blade (a) L1 (b) L2 (c) L3 for A2 at O4

For Array A2 in Orientation O4, some sensors exhibit good agreement with expected values in L3 and L2 as shown in Figure 7.31. However, no consistent relationship is observed among the sensors regarding strain trends for each given load. The L2 results show a discrepancy, where measured strains are significantly higher than expected, while L1 results fail to display a clear trend despite both measured and expected values remaining within the low 0–30 $\mu\varepsilon$ range. Collectively, the results indicate that testing in this edgewise orientation may not be ideal due to the inherently low expected strains.

Critical analysis and key insights

- **Sensor Performance in Edgewise Loading:** The results suggest that in edgewise orientation, especially O4, measured strain values are generally lower, with deviations in multiple cases. The expected strains in this orientation are already low, making accurate detection more challenging. Just like O3 the moment of inertia is much larger in O4, the expected strain values are smaller, making measurement noise appear more significant, further complicating the reliability of strain readings.

- **Effectiveness of FBG Arrays and sensor positioning:** considering the measurement reliability in Arrays A3 A5, the better agreement in L2 results for both arrays indicates that measurement reliability improves when the defect region is less influential or when loading conditions are more stable.
- **Relevance of Orientation Selection:** The results suggest that testing in the negative edgewise moment (Orientation 4) may not be ideal for detecting and analysing strain in both healthy and defective blades. Higher strain magnitudes, such as those seen in flapwise loading orientations, may provide more reliable data for sensor performance and defect analysis.

7.4.7 Sensor Location vs Strain at maximum load

Healthy blade results: The analysis compares the expected and measured strain along the healthy blade, with the load application marked by a dashed red line. The expected strain values from root to tip are represented by blue diamond points, while FBG sensor measurements are colour-coded for differentiation. Figure 7.32 presents data collected under maximum load conditions for the healthy blade.

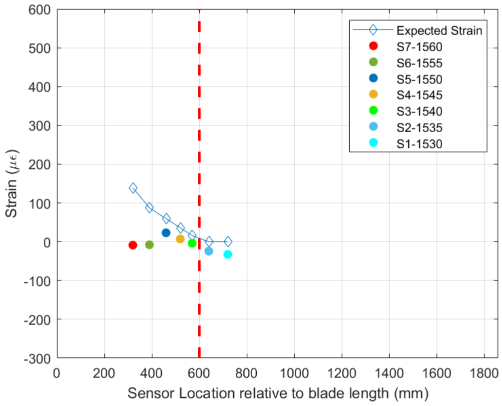

(a) Location 1

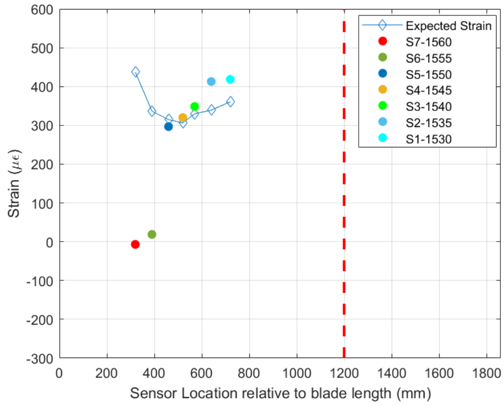

(b) Location 2

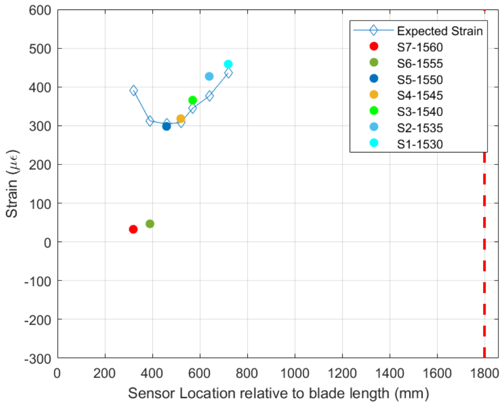

(c) Location 3

Figure. 7.32 Measured vs expected strain for healthy blade at maximum load for (a) L1 (b) L2 (c) L3 for A1 at O1

The results indicate that, for the most part, the measured strain values align well with the expected strain, except for a single sensing point at 400 mm. Between 330 mm and 750 mm, the strain trends follow a similar pattern, with the exception of the 400 mm mark, where the FBG array begins and ends. This can be observed across all loading cases (L1, L2, and L3), suggesting a possible boundary effect at this location. This anomaly may stem from slight inconsistencies in sensor bonding or local material properties that alter strain transmission to the sensor.

These experiments highlight the varying strain responses across different sections of the wind turbine blade when subjected to increasing point loads at the tip. The complexity of measuring the blade's structural elastic properties is evident, yet despite these challenges, the surface-mounted FBG sensor arrays effectively captured these variations. This demonstrates their potential for load monitoring and detecting small strain changes. Such changes can signal the onset of structural defects, making these sensors valuable for early-stage defect detection and SHM.

Defective blade results: For the location vs strain analysis of the defective blade at maximum load, the positive flapwise-tip loaded experiment (O1-L3) was selected for all arrays (3, 5, and 2), similar to the approach used for the healthy blade. The loading point is again indicated by the dashed red line, and both the expected and measured strain values (Y-axis) of each FBG are plotted against the sensors location relative to the blade length (X-axis).

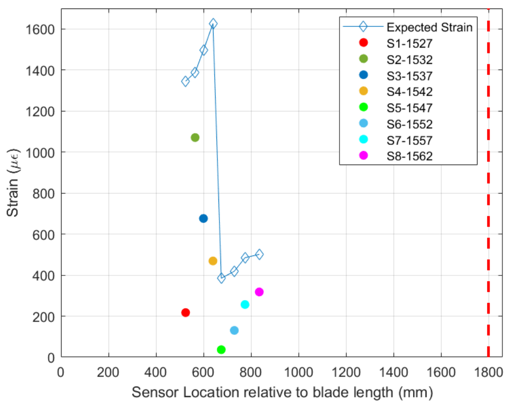

(a) Array 3

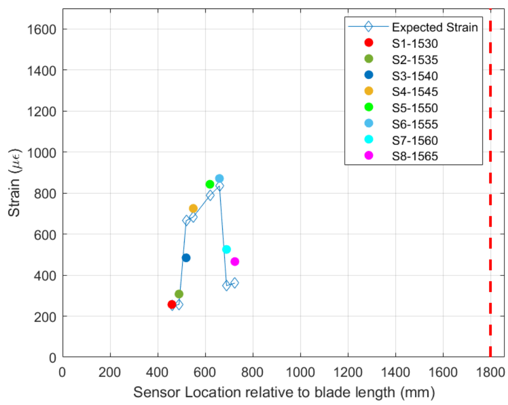

(b) Array 5

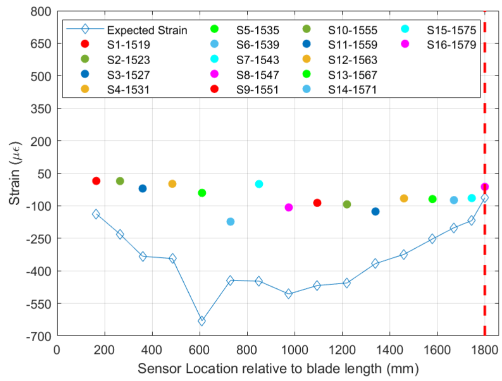

(c) Array 2

Figure. 7.33 Measured vs expected strain for defective blade at maximum load for (a) Array 3 (b) Array 5 (c) Array 2

At maximum load, the FBGs of interest for defect detection i.e. the first four sensors in Array 3 (1527 nm, 1532 nm, 1537 nm, and 1542 nm) do not comply with the expected trend. This inconsistency is observed across all experiment results, with these sensors measuring an average strain of approximately 600 $\mu\varepsilon$ compared to the expected 1400 $\mu\varepsilon$. This is less than half of the expected value, but it is still notably higher than the corresponding strain in the healthy blade, confirming a measurable influence of the defect.

Looking at other loading locations and orientations, these Array 3 FBGs record higher strain values but lack consistency across different experimental setups. The last four FBGs of Array 3 follow the expected trend but with a lower magnitude, possibly due to strain redistribution near the defect boundary.
The middle four FBGs of Array 5 (1540 nm, 1545 nm, 1550 nm, and 1555 nm), covering the defective/non-defective interface region, exhibit much better agreement with expected values. The last three of these four FBGs show minimal deviation, indicating that the transition region of the defect influences strain more predictably. In contrast, the first two FBGs show slight deviations, potentially due to localised stress variations at the defect boundary.

Array 2 results, as observed in previous experiments, are completely inconsistent with expected values across all orientations and loading positions. This confirms that surface-mounting sensors on the suction-side of the blade, where no defect is present, does not provide reliable defect-related strain data. Therefore, optimising sensor placement by prioritising defective-prone regions is essential for accurate structural monitoring.

7.5 Comparison of Healthy vs Defective blade - minimum detectable strain

For the investigation of how small a strain due to the presence of a defect that can be measured with this WDM-FBG array sensor system, the following investigation is considered. To support this, the expected strain over the defect (as sensed by the FBG in Array 3, indicated by ES in the figures) are compared with the expected strain if there's no defect (indicated as ESH in the figures). To explain further, the latter is calculated for the same array but when the neutral axis remains in position to represent the healthy blade case as do the cross-sectional properties I_{xx}, I_{yy} as well as the Young's modulus of the healthy (defect-free) composite material. This is indicated in Figure 7.34. This process is also applied to the defect interface line, where two distinct composite materials are present: the healthy material, which has nominal stiffness and fibre volume fraction, and the defective material, characterised by reduced stiffness due to a resin-rich region with a lack of fibre reinforcement.

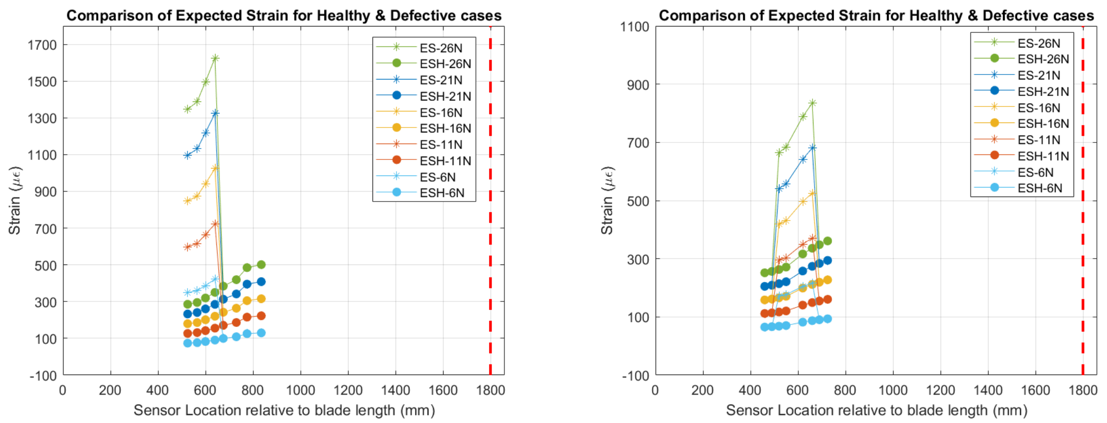

(a) Expected strain over the defect

(b) Expected strain on the defect interface

Figure. 7.34 Expected strain for healthy vs defective blade on (a) defect (b) defect interface

At the defect location, the defective blade shows a distinguishable higher strain response compared to the healthy blade as expected due to the presence of the defect. For Array 3 bonded in the middle line of the defect, looking at Figure 7.34, for the highest load, the difference between the average strain for the expected defective case (1400 $\mu\varepsilon$) and the expected strain healthy case (300 $\mu\varepsilon$) is around 1100 $\mu\varepsilon$. This difference goes down as the load decreases, i.e. for the 6 N case, the average expected strain of A3 over the defective region (due to the presence of defect) is estimated to be 380 $\mu\varepsilon$ and average expected strain of A3 over the same region (520 mm to 660 mm relative to the blade length) if there were no defect present is estimated to be 80$\mu\varepsilon$. Here, for this load case, the difference between the two cases become 300 $\mu\varepsilon$. This "difference" is denoted by x in the equations below. This can be compared with the difference of the actual average measured strain of A3 to its average expected strain of A3 when there's a defect present, denoted by y. The difference between the measured strain of the defective case and the expected strain of the healthy case is denoted by z.

$$D_{\text{Expected}} - H_{\text{Expected}} = x \tag{7.4}$$

$$D_{\text{Expected}} - D_{\text{Measured}} = y \tag{7.5}$$

$$D_{\text{Measured}} - H_{\text{Expected}} = z \tag{7.6}$$

By formulating these equations, it can be deduced that for an ideal scenario, y should be close to zero, with x and z equal. Alternatively, y/x should be as small as possible. By investigating the results from this analysis, the following observations can be made.

Highest Load 26.4 N,

$$D_{\text{expected}} - H_{\text{expected}} = 1400 - 300 = 1100\mu\varepsilon$$
$$D_{\text{Expected}} - D_{\text{Measured}} = 1400 - 600 = 800\mu\varepsilon$$
$$D_{\text{Measured}} - H_{\text{Expected}} = 600 - 300 = 300\mu\varepsilon$$

$(300/1100) * 100\% =$ only 27 % of strain due to presence of defect is detectable going from healthy blade to a blade with a defect.
$(600/1400) * 100\% =$ 43% of strain was measured experimentally from its expected strain value.

Lowest Load 6 N,

$$D_{\text{Expected}} - H_{\text{Expected}} = 380 - 80 = 300\mu\varepsilon$$
$$D_{\text{Expected}} - D_{\text{Measured}} = 380 - 110 = 270\mu\varepsilon$$
$$D_{\text{Measured}} - H_{\text{Expected}} = 110 - 80 = 30\mu\varepsilon$$

$(30/300) * 100\% =$ only 10 % of strain due to presence of defect is detectable going from a healthy blade to a blade with a defect.
$(110/380) * 100\% =$ 30% of strain was measured experimentally from its expected strain value.
Applying the same equations for the array bonded at the defect interface; Array 5, the following observations can be made.

Highest Load 26.4 N,

$$D_{\text{Expected}} - H_{\text{Expected}} = 740 - 300 = 440\mu\varepsilon$$
$$D_{\text{Expected}} - D_{\text{Measured}} = 740 - 730 = 10\mu\varepsilon$$
$$D_{\text{Measured}} - H_{\text{Expected}} = 730 - 300 = 430\mu\varepsilon$$

$(430/440) * 100\% =$ 97 % of strain due to presence of defect is detectable going from healthy/defect-free blade to a blade with a defect.
$(730/740) * 100\% =$ 98% of strain was measured experimentally from its expected strain value.

Lowest Load 6 N,

$$D_{\text{Expected}} - H_{\text{Expected}} = 190 - 80 = 110\mu\varepsilon$$
$$D_{\text{Expected}} - D_{\text{Measured}} = 190 - 160 = 30\mu\varepsilon$$
$$D_{\text{Measured}} - H_{\text{Expected}} = 160 - 80 = 80\mu\varepsilon$$

$(80/110) * 100\% =$ 73 % of strain due to presence of defect is detectable /defect-free blade to a blade with a defect.
$(160/190) * 100\% =$ 84% of strain was measured experimentally from its expected strain value.

From this, some key observations can be drawn out; as the load increases, the percentage of strain that can be measured due to the presence of a defect from a entirely defect-free case, also increases while the actual percentage of strain at the defect to its expected defective strain slightly increases. For lower loads applied, though the FBGs are able to detect/measure a slightly higher percentage of expected strain, these sensors based on these experiments alone will not be able to detect a significant percentage of strain due to the presence of defect compared to instance where there is no defect. It should be noted that the temperature effect should also be considered and assuming that all FBGs experience the same temperature, for a $\pm 1°$C change in ambient temperature, the wavelength shift would result in $\pm$10pm variation. This analysis is also influenced by the positioning of the sensors as seen in the comparison between Array 3 and 5, where the performance of the FBG sensors mounted right on the defect is somewhat poor compared to the FBGs mounted on the edge of the defect. This indicates that defect material has a more complex strain pattern than the surrounding blade. Building on these analysis conducted for the defective blade, early-stage defect detection could well be performed using FBGs on the defective interface as the smallest variation in strain coming from a defect by applying smaller variations in applied load were detectable.

Based on these 72 test cases alone, experimentally it can be said that to detect the presence of a defect, other non-defective locations could also be potentially explored. While this is true, mounting FBGs right at the defect has proven insightful yet opens up the need for further experimental investigations for better, accurate performance of the bonded FBGs. This could be done by increasing the number of times the experiment is repeated, by increasing the spatial resolution, i.e., have more FBGs close together covering the defect and around the defect and by trying different array-bonding/mounting configurations to suit the defect shape/ type. These could be potentially explored while maintaining a constant ambient temperature to remove any fluctuations during measurement process.

7.6 Blade Deflection

The deflection measurement system comprises of the dial gauge and is shown in Chapter 6. This dial gauge was capable of measuring upto 50 mm of deflection and was mounted at the tip for all experimental cases considered including edgewise loading. Here, the results from the measured deflection of both the healthy and defective blade are compared.

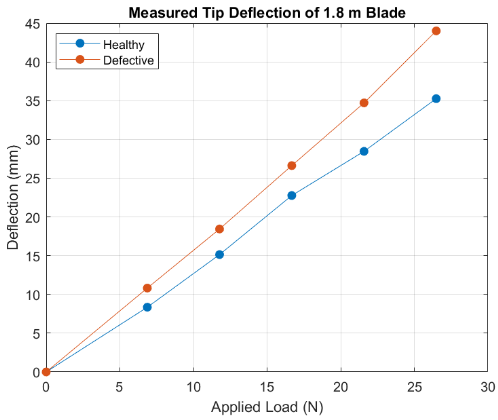

(a) Measured Tip Deflection

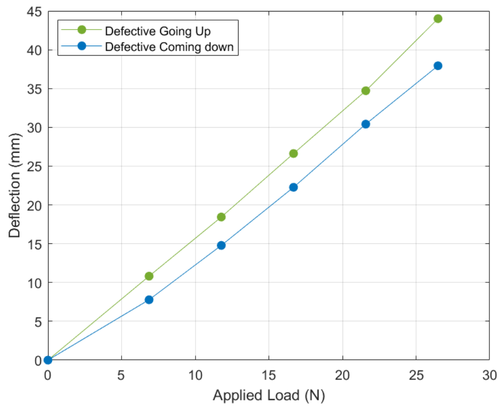

(b) Hysteresis Effect on measured deflection

Figure. 7.35 Measured tip deflection (a) Healthy vs defective (b) Hysteresis effect

Figure 7.35 shows the measured deflection for both the healthy and defective blades, mounted in Orientation 1 and loaded at the tip (L3 case). It is observed that the defective blade exhibits a higher tip deflection compared to the healthy blade. However, as seen in the second part Figure 7.35 the defective blade also displays a hysteresis effect, where the deflection values for the same loading condition are different during the loading and unloading phases; applying increasing loads at the tip vs taking off the weights decreasing the loads one by one. This observation was present in all the experiment cases for other orientations and loading location for both blades. However, only the O1-L3 results have been present here since the location represents flapwise-tip loaded-tip deflection case which is more reliable for this investigation. Overall, the tip deflection measurement using the dial gauge is not sufficiently accurate/free from hysteresis to be able to detect the defect.

An alternate method of measuring deflection is the laser displacement sensor. To evaluate the application of this device; Micro Epsilon's optoNCDT ILD 1302 intelligent laser optical displacement measurement system from MicroEpsilon, 2023 was used. This was mounted so that the tip deflection can be measured at the same position of that of the dial gauge measurement point. The measurement taken while the blade was loaded at L2 is given below.

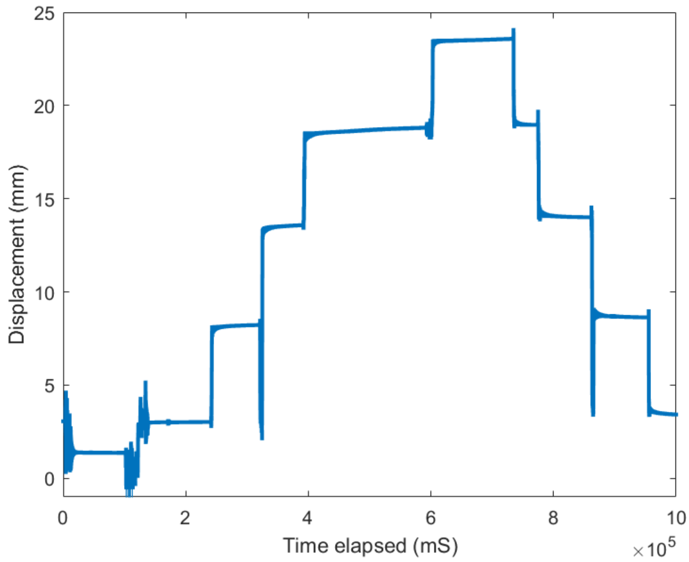

Figure. 7.36 Deflection measured using laser displacement sensor at L2

Looking at the results from the laser displacement sensor measuring at L2, it could be said that the hysteresis effect from this optical measurement device is less than hysteresis effect from the dial gauge, however - it should be noted that, after measuring the deflection with the dial gauge for all experiment cases, the placement of the dial gauge for the edgewise orientation was tricky and indicates that this was not a reliable method for measuring deflection. The laser displacement system could potentially be used but again, this could be applied only in selected orientations i.e. flapwise movement of the blade. when it comes to other laboratory scale systems for measuring deflections, especially for scaled blades/ parts of industrial sized blades, a more sophisticated non-destructive testing/measurement system is typically used. For example, thermography or digital image correlation using scanner systems used for the RELIABLADE project at Technical University of Denmark DTU, 2023.

7.7 Conclusions

This study successfully validated the use of a wavelength division multiplexing fibre Bragg grating (WDM-FBG) sensor system for monitoring strain and detecting defects in a 1.8 m wind turbine blade under various static load conditions. Across 72 experimental cases, spanning four distinct orientations, three loading positions, and six different static loads, the performance of the sensor arrays was rigorously evaluated through a series of post-processing techniques in MATLAB.

The key points observed from the results and discussion are explained below,

Loading Location: The experiments confirmed that the tip-loaded condition (L3) is the most reliable configuration for obtaining consistent strain measurements. While the L2 case also provided acceptable accuracy, the L1 configuration consistently exhibited significant distortions due to its direct coincidence with the load application point and clamp-induced interference. This highlights the importance of selecting appropriate loading positions to minimise noise and ensure effective strain capture.

Sensor Performance and Positioning: The analysis revealed that the location of FBG sensors relative to the defect plays a critical role in the sensor response. Sensors mounted directly over the defect (Array 3) often underperformed due to due to complex strain patterns within the defect area, compromised bonding and non-uniform strain transfer, whereas those positioned at the defect interface (Array 5) demonstrated much better alignment with the expected strain values. This observation underscores the need to optimise sensor placement for effective early-stage defect detection.

Orientation Effects and Loading: Flapwise loading generally produced higher strain magnitudes that aligned more closely with predictions, making it the preferred orientation for both healthy and defective blade assessments. In contrast, edgewise loading (Orientations O3 and O4) resulted in lower and more variable strain readings, particularly when defects were present. This suggests that flapwise configurations are better suited for the detection and characterisation of structural defects in wind turbine blades.

Temperature and Deflection Considerations: Although ambient temperature variations were minimal and controlled during the experiments, even small fluctuations could affect the wavelength shifts measured by the FBG sensors. Additionally, the blade deflection studies, conducted using both dial gauge and laser displacement sensors, revealed that while the laser system showed reduced hysteresis compared to the dial gauge, both methods have limitations. In practice, more advanced non-destructive testing techniques may be required for high-accuracy deflection measurements in larger or industrial-scale blades.

Defect Detectability: A comparative analysis between healthy and defective blade responses indicated that only a fraction of the strain due to the defect is detectable when sensors are mounted directly on the defect. However, when FBG sensors are positioned along the defect interface, the difference between the measured strain and the expected strain is markedly higher, demonstrating the sensor system's potential for early-stage defect detection. This finding highlights the promise of using strategically positioned FBG arrays for continuous SHM.

The comprehensive evaluation indicates that while the current WDM-FBG sensor system shows considerable promise as a SHM tool, its performance is highly dependent on sensor placement, loading configuration, and the inherent limitations of the measurement systems used. Future work could focus on enhancing sensor bonding techniques, increasing the spatial resolution of sensor arrays, and refining data processing methods. Moreover, integrating advanced temperature compensation and high-precision deflection measurement systems will further improve the reliability and sensitivity of defect detection in composite wind turbine blades. In summary, by addressing these aspects, the WDM-FBG sensor system can be further optimised to serve as an effective early warning mechanism for structural defects, ultimately contributing to the safety, maintenance efficiency, and operational longevity of wind turbine blades.

Chapter 8

Conclusions and Future Work

In this final conclusions chapter, the novelty of the research conducted, key findings and opportunity and potential for further development of the work are discussed. The significance and novelties of the work outlined in this thesis are,

1. A review of different types of defect present in wind turbine blades and the existing sensing, condition and SHM system used in the wind energy industry.

2. The application of surface-bonded wavelength division multiplexed FBGs for defect detection of wind turbine blades in laboratory experiments.

3. The validation of FBG results and investigation of average measured strain vs FBG sensing length to detect defects.

8.1 Key Results and Findings

In this section, key results and findings of each chapter are collated and re-emphasised. In this thesis, the performance of FBG for multi-point sensing and defect detection for laboratory scale wind turbine blade has been investigated. This has been accomplished and demonstrated through theoretical and mathematical methods as well as experimental measurements as described in detail in the previous chapters.

In Chapter 2, an overview of the different types of manufacturing-induced defects and operation-induced damages found in a wind turbine blade has been provided by reviewing existing published literature. The different condition monitoring, SHM systems and non-destructive testing techniques including the types of sensing systems have mapped against the different defect types to evaluate their suitability. This literature review has helped to identify that, out of the existing sensor systems which measure defects at a smaller level and at an early stage, quasi-distributed optical sensing has not been explored in depth for wind turbine blade-SHM applications. By comparing the different optical sensing methodologies and their principles, the commercially widely-available and more-reliable sensing technique i.e. classical Bragg grating based sensors were chosen as the most suitable to test and evaluate the primary aim of this thesis.

Chapter 3 starts off with how the FBGs used in this work have been produced using the draw tower method by the FBG supplier company FBGS (FBGS, 2022). Based on the working principle of FBGs, these gratings are sensitive to both strain and temperature hence this chapter provides detailed explanation on the preliminary characterisation of the FBG for strain and temperature. As explored in Chapter 3, one of the advantages of this type of sensor is that they can be produced in arrays where the different gratings each represent different Bragg wavelength; i.e. Wavelength Division Multiplexed. To simply and effectively test these sensors, a defect was defined as modified version the wind turbine blade's composite material. This was achieved by considering an area which has absence of fibre reinforcement/ area filled with purely resin which results in a reduced stiffness of the material as the defect.

A secondary characterisation experimentally demonstrated using these WDM-FBG arrays bonded on a simplified Aluminium cantilever beam; with and without defect (V shaped notch in the metal beam - to mimic the absence of material) show good agreement with the measured and the predicted strain values from finite element analysis. This characterisation when repeated for on a defect-free composite cantilever beam and a composite cantilever beam with a known defect present also show good agreement with the predicted FEA based strain results. Additionally, a novel investigation on the average measured strain over the defect by bonding a single grating at different sensing length has proved insightful in understanding strain pattern over the defect and has identified that to measure the smallest variations in strain accurately, the smaller the sensing length or bonded length is preferred. With this, the performance of these FBGs in a simplified rectangular testing coupon was easy to determine and served as a way of understanding the FBG sensing capabilities-defective composite material's behaviour. Although sophisticated commercial FBG-Strain measuring devices are available in the market, these are highly expensive and have limited functionalities. Therefore, to aid these tests a LabVIEW based data acquisition system was developed to interface the WDM-FBG sensor arrays, the optical spectrum analyser, the optical switch and the light source. For the data analysis of the FBG spectra obtained from these tests, a post-processing algorithm was drafted separately in MATLAB based on a Gaussian model for FBG peak fitting. To explain further, having shorter sensor lengths to measure a defect would result in having more sensors in and around the defect, improving spatial resolution. However, this leads to a trade-off between sensor length and the total number of sensors required. As demonstrated in Figure 3.69, increasing the sensor length from 10 mm to 20 mm allows for better defect detection with half the number of sensors, while extending it further to 30 mm results in only minor accuracy degradation but requires just one-third as many sensors. This trade-off highlights the importance of optimising sensor configurations for practical applications, ensuring a balance between accuracy and cost. Additionally, extracting more accurate strain estimates from the optical sensor's spectrum (for example, using Gaussian peak fitting) enhances measurement precision, providing more flexibility in selecting sensor length without compromising strain detection performance.

In Chapter 4, a series of simulations were conducted for the NREL 5MW baseline turbine using ASHES software to evaluate the blades' performance with and without defects. For this, the turbine blades have defects incorporated in their structural model in the form of stiffness reduction in the material at a certain point along the blade and were simultaneously tested under different wind field conditions. This analysis provides insight into how the different loads from oncoming wind influences the results if there is a defect present and also highlights the need for distributed sensing. Following this, the scaling laws used for the design and manufacture of the laboratory scaled Blade has been described in detail. This scaled-down model was based on the original NREL 5MW baseline reference turbine model. The 1:35 length-scale was chosen so that the scaled-down blade model can be reproduced for modelling as well as composite manufacturing. A smaller blade would be easier to manufacture but in reality cannot be labelled as a "laboratory scale blade". A bigger blade would require a bigger team working on the manufacturing process itself and also comes with higher costs.

The fifth chapter describes in detail about the standard manufacturing process followed in the wind energy industry as well as manufacturing process and steps taken to physically produce the two scaled blades. The design, development and manufacturing of the test stand and the adaptor plate is discussed. With these components ready, the different of experiments/ test cases completed are explored in Chapter 6. This also includes the explanation and justification for choosing the different orientations and loading locations and sensor bonding locations. The theoretical effect of the artificial defect was estimated with the help of mathematical calculations for the two blades in determining the cross sectional properties I_{xx} and I_{yy} for both the defective and the defect-free blade. To achieve this, assumptions have been made where the length-wise cross section of the blade is assumed as a thin elliptical shell made out of two a bigger ellipse (outer surface of blade) and the smaller ellipse (inner surface of the blade). Equations formulated and calculations made for the two blade models have been validated against each other as well as with the ANSYS-Spaceclaim design of the blade. During the course of these experiments, a separate deflection measurement system was also implemented using a dial gauge. Looking at the results, the tip deflection for the classical flapwise case using the dial ague has resulted in hysteresis rendering the deflection measurement via dial gauge un-reliable.

Throughout the elaborate discussion of the results in Chapter 7, the complex nature of the defect and the difficulty in measuring the defect became apparent. Unfortunately, the FBGs mounted right in the middle of the defect do not perform as effectively as expected, due to several reasons. One of the main factor is the absence of fibre reinforcement itself at the defective region as defined by the area with reduced stiffness. This type of defect resulted in that section and surface area being malleable and leads to the bonded fibre possibly getting slacked or getting loosened. This is evident in observing the sequence of the experiments conducted; where the first orientation/positive flapwise test show better agreement compared to the rest on the test cases i.e., negative flapwise, positive edgewise and negative edgewise case. Loading at location 1 has resulted in highly noisy measurements and generally shows poor agreement. As the expected strain for this loading location was also in the low range, any disturbances and noise would have a higher effect on the measured results. This is evident in almost all the orientations exhibiting the flapwise orientation and tip-loaded test cases are the most reliable cases. Another factor contributing to this poor performance of these FBGs is that the strain pattern over the defect itself is highly complex and non-linear. If each individual results for the measured vs the expected strain is studied, within the array, some FBGs do indeed measure in alignment to the expected values. However, while this is true, some other FBGs measure really low compared to their expected strain. Hence, judging the average strain over the defect is more realistic as opposed to sensor by sensor evaluation. However, it has been demonstrated that the series of FBGs mounted at the defect interface effectively measure the strain as expected and these could aid very well in differentiating when the blade is healthy and when there is a defect starting to occur.

Comparing both healthy blade and the defective blade, it should be noted that although both blade have the same model and design except the presence of the defect, manufacturing parameters i.e. thickness of blade shells and their uniformity all across the two blades may not be identical. A small variation in thickness or width of the blade may result in variations in the cross-sectional I_{xx} and I_{yy} properties estimated for the blade. These theoretical calculations would then deviate from the actual composite manufactured blade's cross-sectional properties. Remarkably, the ambient temperature measured by the strain insensitive, temperature-measurement-only FBG has recorded almost a constant temperature throughout the measurement campaign. However, if there were any huge temperature fluctuations of $\pm 1°C$ or over, this should be accounted for as this would result in a changes in measured strains since FBGs are sensitive to both strain and temperature.

8.2 Future Work

Building upon the experiments conducted for this thesis a few suggestions for further work are explored in this section. As blades have complex shape and structural properties from root to tip, the surface-bonded optical sensors will be influenced by these factors as well as the bonding/ structural imperfections found in the blade. To investigate this further, some of the short term future work include further validation of FBGs on the blades including repetitive testing of defective blade in the flapwise direction when tip loaded. This could be achieved by re-arranging the FBGs measuring the middle of the defect. Having another series of FBGs crossing the defect from leading edge to training edge would also be an insightful study. Bonding a second set of FBG on the other side of the defect-interface line would be useful in re-assuring the validation obtained from this thesis. As mentioned in the previous section, the measurements recorded for the experiments conducted for this thesis were done under controlled laboratory environment where the temperature was monitored constantly. To incorporate a real-operational environment and further validation of these FBG measuring strain, the laboratory space could be introduced with fluctuations in ambient temperature to analyse its effect on these test cases as well as use the measured temperature to compensate for the strain measurements of the FBGs in an operational wind farm setting.

The further development of the data acquisition system using LabVIEW could also be explored where the strains can be estimated real-time during the measurement campaign itself without additional post-processing. The Gaussian peak fitting algorithm developed in MATLAB could potentially be plugged in to the existing data acquisition system or could also be replicated in LabVIEW to expand its capabilities.

A few suggestions for long-term future work could also be conceptualised, provided that the above mentioned short term research and development based on the static loading tests are constructive. Following standard industry composites/component testing practices, the dynamic tests could be done to evaluate the performance of these FBGs when the blades are excited using a shaker or an actuator. Modal analysis and other continuous measurements could be taken to study the effectiveness of the surface bonding of the fibre arrays to the blade and defect region. Provided that these steps are done correctly and useful information has been extracted, multi-axial fatigue test could also be performed. These could also be validated against numerical models and simulations conducted for this blade and also be validated against other widely-used sensing technologies such as accelerometers and strain gauges.

Bibliography

Abushagur, A. A., Arsad, N., and Bakar, A. A. A. (2021). "Cantilever beam with a single fiber Bragg grating to measure temperature and transversal force simultaneously". In: *Sensors* 21.6, p. 2002.

Ahmed, F. and Jun, M. B. (2014). "Filament-based fabrication and performance analysis of fiber Bragg grating sensors using ultrashort pulse laser". In: *Journal of Micro-and Nano-Manufacturing* 2.2, p. 021007.

Amanzadeh, M., Aminossadati, S. M., Kizil, M. S., and Rakić, A. D. (2018). "Recent developments in fibre optic shape sensing". In: *Measurement* 128, pp. 119–137.

Bak, C., Zahle, F., Bitsche, R., Kim, T., Yde, A., Henriksen, L. C., Hansen, M. H., Blasques, J. P. A. A., Gaunaa, M., and Natarajan, A. (2013). "The DTU 10 MW reference wind turbine". In: *Danish wind power research 2013*.

Bang, H.-J., Kim, H.-I., and Lee, K.-S. (2012). "Measurement of strain and bending deflection of a wind turbine tower using arrayed FBG sensors". In: *International journal of precision engineering and manufacturing* 13.12, pp. 2121–2126.

Batay, S., Baidullayeva, A., Zhao, Y., Wei, D., Baigarina, A., Sarsenov, E., and Shabdan, Y. (2023). "Aerostructural design optimization of wind turbine blades". In: *Processes* 12.1, p. 22.

Berger, F., Kröger, L., Onnen, D., Petrović, V., and Kühn, M. (2018). "Scaled wind turbine setup in a turbulent wind tunnel". In: *Journal of Physics: Conference Series*. Vol. 1104. 1. IOP Publishing, p. 012026.

Bladena (2021). "The Blade Handbook". In: URL: https://www.bladena.com/uploads/8/7/3/7/87379536/blade_handbook_2021_v20.pdf.

Boresi, A. P. and Schmidt, R. J. (2002). *Advanced mechanics of materials*. John Wiley & Sons.

Cairns, D. S., Riddle, T., and Nelson, J. (2011). "Wind turbine composite blade manufacturing: The need for understanding defect origins, prevalence, implications and reliability". In: *Sandia National Laboratories, Albuquerque, New Mexico* 87185.

Canet, H., Bortolotti, P., and Bottasso, C. L. (2021). "On the scaling of wind turbine rotors". In: *Wind Energy Science* 6.3, pp. 601–626.

Carden, E. P. and Fanning, P. (2004). "Vibration based condition monitoring: a review". In: *Structural health monitoring* 3.4, pp. 355–377.

Cazzulani, G., Cinquemani, S., Marabelli, S., Bayati, I., and Belloli, M. (2018). "Vibration monitoring of wind-turbine blades through optical fiber sensors". In: *Smart Materials and Nondestructive Evaluation for Energy Systems IV*. Vol. 10601. International Society for Optics and Photonics, 106010O.

Chandrasekhar, K., Stevanovic, N., Corbetta, M., Dervilis, N., and Worden, K. (2017). "On the structural health monitoring of operational wind turbine blades". In: *11th Int. Workshop on Structural Health Monitoring*. Vol. 2017, pp. 2522–2529.

Chaviaropoulos, P. (2007). "Similarity rules for W/T up-scaling. UpWind Report, WP 1B4, 2007." In: URL: https://www.studeersnel.nl/nl/document/technische-universiteit-delft/wind-turbine-design/similarity-rules-for-wt-upscaling-2007/13331510.

Chen, R., Wang, H., Liu, L., Lin, B., Xie, S., and Cheng, M. (2005). “Ameliorated spatial division multiplexing system of FBG sensors based on novel wavelength detection and demodulation technique”. In: *Advanced Sensor Systems and Applications II*. Vol. 5634. SPIE, pp. 520–523.

Chen, T., Xu, X., Lalam, N., Ng, W., and Harrington, P. (2018). “Multi point strain and temperature sensing based on Brillouin optical time domain reflectometry”. In: *2018 11th International Symposium on Communication Systems, Networks & Digital Signal Processing (CSNDSP)*. IEEE, pp. 1–4.

Chen, X., Semenov, S., McGugan, M., Madsen, S. H., Yeniceli, S. C., Berring, P., and Branner, K. (2021). “Fatigue testing of a 14.3 m composite blade embedded with artificial defects–damage growth and structural health monitoring”. In: *Composites Part A: Applied Science and Manufacturing* 140, p. 106189.

Cheng, L. (2013). “Eddy current pulsed thermography for non-destructive evaluation of carbon fibre reinforced plastic for wind turbine blades”. PhD thesis. Newcastle University.

Chou, J.-S., Chiu, C.-K., Huang, I.-K., and Chi, K.-N. (2013). “Failure analysis of wind turbine blade under critical wind loads”. In: *Engineering Failure Analysis* 27, pp. 99–118.

Ciang, C. C., Lee, J.-R., and Bang, H.-J. (2008). “Structural health monitoring for a wind turbine system: a review of damage detection methods”. In: *Measurement science and technology* 19.12, p. 122001.

Clyne, T. W. and Hull, D. (2019). *An introduction to composite materials*. Cambridge university press.

Composite, E. (2022). *Easy Composite*. URL: https://www.easycomposites.co.uk/.

Coscetta, A., Minardo, A., Olivares, L., Mirabile, M., Longo, M., Damiano, M., and Zeni, L. (2017). “Wind turbine blade monitoring with Brillouin-based fiber-optic sensors”. In: *Journal of Sensors* 2017.

Craig Jr, R. R. and Taleff, E. M. (2020). *Mechanics of materials*. John Wiley & Sons.

Damiano, M. and D’Ettore, A. (2018). “Structural design of a multi-megawatt wind turbine blade with ONE SHOT BLADE Technology”. In: *Journal of Physics: Conference Series*. Vol. 1037. 4. IOP Publishing, p. 042002.

DenseLightSemiconductors (2022). *SLED with Drivers*. DenseLightSemiconductors. URL: https://www.denselight.com/products/sled-with-drivers/.

Desmond, M., Hughes, S., and Paquette, J. (2015). *Structural testing of the Blade Reliability Collaborative effect of defect wind turbine blades*. Tech. rep. National Renewable Energy Lab.(NREL), Golden, CO (United States).

Di Sante, R. (2015). “Fibre optic sensors for structural health monitoring of aircraft composite structures: Recent advances and applications”. In: *Sensors* 15.8, pp. 18666–18713.

Di Sante, R., Donati, L., Troiani, E., and Proli, P. (2014). “Evaluation of bending strain measurements in a composite sailboat bowsprit with embedded fibre Bragg gratings”. In: *Measurement* 54, pp. 106–117.

Doebling, S. W., Farrar, C. R., Prime, M. B., and Shevitz, D. W. (1996). “Damage identification and health monitoring of structural and mechanical systems from changes in their vibration characteristics: a literature review”. In.

Doliński, Ł., Krawczuk, M., and Żak, A. (2018). “Detection of delamination in laminate wind turbine blades using one-dimensional wavelet analysis of modal responses”. In: *Shock and vibration* 2018.

Douglas Cairns, L. A. W. (2016). “Wind Turbine Blade Reliability, Effectsof Manufacturing Defects andComposite Repairs”. In: URL: https://www.slideshare.net/sandiaecis/wind-turbine-blade-reliability-effects-of-manufacturing-defects-and-composite-repairs.

DTU (2023). *RELIABLADE Full scale blade testing*. Tech. rep. Technical University of Denmark. URL: https://www.reliablade.com/work-packages/work-package-7.

Dupuis, R. (2010). “Application of oil debris monitoring for wind turbine gearbox prognostics and health management”. In: *Annual Conference of the PHM Society*. Vol. 2. 1.

Dutton, A. (2004). “Thermoelastic stress measurement and acoustic emission monitoring in wind turbine blade testing”. In: *European Wind Energy Conference London*, pp. 22–25.

Esu, O. O. (2016). “Vibration-based condition monitoring of wind turbine blades”. PhD thesis. Loughborough University.

Eum, S., Kageyama, K., Murayama, H., Uzawa, K., Ohsawa, I., Kanai, M., Kobayashi, S., Igawa, H., and Shirai, T. (2007). “Structural health monitoring using fiber optic distributed sensors for vacuum-assisted resin transfer molding”. In: *Smart materials and structures* 16.6, p. 2627.

Eum, S., Kageyama, K., Murayama, H., Ohsawa, I., Uzawa, K., Kanai, M., and Igawa, H. (2006). “Process and Health Monitoring Using Fiber Optic Distributed Sensors for Wind Turbine Blades”. In.

FBGS, F. T. G. (2022). “DTG FSG Technology”. In: URL: https://fbgs.com/technology/dtg-fsg-technology.

FBGS-Technologies (2022). “FemtoSecond Gratings (FSG)”. In: URL: https://fbgs.com/components/femtosecond-gratings-fsg/.

Feng, K., Cui, J., Jiang, X., Li, J., and Tan, J. (2016). “Analysis and simulation method of the cantilever FBG sensors”. In: *Seventh International Symposium on Precision Mechanical Measurements*. Vol. 9903. SPIE, pp. 370–375.

Gaertner, E., Rinker, J., Sethuraman, L., Zahle, F., Anderson, B., Barter, G. E., Abbas, N. J., Meng, F., Bortolotti, P., Skrzypinski, W., et al. (2020). *IEA wind TCP task 37: definition of the IEA 15-megawatt offshore reference wind turbine*. Tech. rep. National Renewable Energy Lab.(NREL), Golden, CO (United States).

García, D. and Tcherniak, D. (2019). “An experimental study on the data-driven structural health monitoring of large wind turbine blades using a single accelerometer and actuator”. In: *Mechanical Systems and Signal Processing* 127, pp. 102–119.

Gikunoo, E. (2019). “Composite Materials”. In: URL: https://egikunoo.files.wordpress.com/2019/11/mse-451-composite-materials-slides-a.pdf.

Glavind, L., Olesen, I. S., Skipper, B. F., and Kristensen, M. V. (2013). “Fiber-optical grating sensors for wind turbine blades: a review”. In: *Optical Engineering* 52.3, p. 030901.

GlobalWindEnergyCouncil (2023). “Global Wind Report 2023”. In: URL: https://gwec.net/globalwindreport2023/.

Gu, H., Liu, W., Gao, Q., and Zhang, Y. (2021). “A review on wind turbines gearbox fault diagnosis methods”. In: *Journal of Vibroengineering* 23.1, pp. 26–43.

Güemes, A., Fernández-López, A., Díaz-Maroto, P. F., Lozano, A., and Sierra-Perez, J. (2018). “Structural health monitoring in composite structures by fiber-optic sensors”. In: *Sensors* 18.4, p. 1094.

Hahn, F., Kensche, C., Paynter, R., Dutton, A., Kildegaard, C., and Kosgaard, J. (2002). “Design, fatigue test and NDE of a sectional wind turbine rotor blade”. In: *Journal of Thermoplastic Composite Materials* 15.3, pp. 267–277.

Hansen, M. (2015). *Aerodynamics of wind turbines*. Routledge.

Heaney, P. S., Ivanco, T. G., and Bilgen, O. (2018). “Distributed sensing of a cantilever beam and plate using a fiber optic sensing system”. In: *2018 Applied Aerodynamics Conference*, p. 3482.

Heinecke, F. and Willberg, C. (2019). “Manufacturing-induced imperfections in composite parts manufactured via automated fiber placement”. In: *Journal of Composites Science* 3.2, p. 56.

Hua, Y., Kasavajhala, A. R. M., and Gu, L. (2013). “Elastic–plastic analysis and strength evaluation of adhesive joints in wind turbine blades”. In: *Composites Part B: Engineering* 44.1, pp. 650–656.

Hwang, G.-S., Ma, C.-C., and Huang, D.-W. (2011). “Dynamic strain measurements of a cantilever using the improved bonding fiber Bragg grating”. In: *Journal of Vibration and Control* 17.14, pp. 2199–2212.

Jasiūnienė, E., Raišutis, R., Šliteris, R., Voleišis, A., and Jakas, M. (2008). “Ultrasonic NDT of wind turbine blades using contact pulse-echo immersion testing with moving water container”. In: *Ultragarsas* 63.3, pp. 28–32.

Jensen, F., Arconada, J., Werk, M., Berggreen, C., Sørensen, J., Zhong, G., and Haans, W. (2023). "Torsional Effects on Wind Turbine Blades and Impact on Field Damages". In: *IOP Conference Series: Materials Science and Engineering*. Vol. 1293. 1. IOP Publishing, p. 012005.

Jones, R. M. (2018). *Mechanics of composite materials*. CRC press.

Jonkman, J., Butterfield, S., Musial, W., and Scott, G. (2009). *Definition of a 5-MW reference wind turbine for offshore system development*. Tech. rep. National Renewable Energy Lab.(NREL), Golden, CO (United States).

Jüngert, A. (2008). "Damage Detection in wind turbine blades using two different acoustic techniques". In: *The NDT Database & Journal (NDT)*.

Kashyap, R. (2009). *Fiber bragg gratings*. Academic press. URL: https://www.sciencedirect.com/book/9780123725790/fiber-bragg-gratings.

Katnam, K., Comer, A., Roy, D., Da Silva, L., and Young, T. (2015). "Composite repair in wind turbine blades: an overview". In: *The Journal of Adhesion* 91.1-2, pp. 113–139.

Katsaprakakis, D. A., Papadakis, N., and Ntintakis, I. (2021). "A comprehensive analysis of wind turbine blade damage". In: *Energies* 14.18, p. 5974.

Kensche, C. W. (2006). "Fatigue of composites for wind turbines". In: *International journal of fatigue* 28.10, pp. 1363–1374.

Kersey, A. D., Davis, M. A., Patrick, H. J., LeBlanc, M., Koo, K., Askins, C., Putnam, M., and Friebele, E. J. (1997). "Fiber grating sensors". In: *Journal of lightwave technology* 15.8, pp. 1442–1463.

Al-Khudairi, O., Hadavinia, H., Little, C., Gillmore, G., Greaves, P., and Dyer, K. (2017). "Full-scale fatigue testing of a wind turbine blade in flapwise direction and examining the effect of crack propagation on the blade performance". In: *Materials* 10.10, p. 1152.

Kliewer, K. S. (2018). "Fiber Optic Methods for Structural Health Monitoring based on Dynamic Curvature and Displacement". PhD thesis. Princeton University.

Krause, T., Preihs, S., and Ostermann, J. (2015). "Acoustic emission damage detection for wind turbine rotor blades using airborne sound". In: *Proceedings of the 10th International Workshop on Structural Health Monitoring (IWSHM2015)*.

Kreuzer, M. (2006). "Strain measurement with fiber Bragg grating sensors". In: *HBM, Darmstadt, S2338-1.0 e*, pp. 1–9.

Leal-Junior, A. G., Theodosiou, A., Diaz, C. R., Marques, C., Pontes, M. J., Kalli, K., and Frizera, A. (2019). "Simultaneous measurement of axial strain, bending and torsion with a single fiber Bragg grating in CYTOP fiber". In: *Journal of Lightwave Technology* 37.3, pp. 971–980.

Leapfrog (2020). *Leapfrog Xcel 3D Printer*. URL: https://www.lpfrg.com/products/leapfrog-xcel/.

Lee, H. G., Kang, M. G., and Park, J. (2015). "Fatigue failure of a composite wind turbine blade at its root end". In: *Composite Structures* 133, pp. 878–885.

Lee, H. G. and Park, J. (2016). "Static test until structural collapse after fatigue testing of a full-scale wind turbine blade". In: *Composite structures* 136, pp. 251–257.

Lee, H.-W., Park, H.-J., Lee, J.-H., and Song, M. (2007). "Accuracy improvement in peak positioning of spectrally distorted fiber Bragg grating sensors by Gaussian curve fitting". In: *Applied optics* 46.12, pp. 2205–2208.

Li, D., Ho, S.-C. M., Song, G., Ren, L., and Li, H. (2015). "A review of damage detection methods for wind turbine blades". In: *Smart Materials and Structures* 24.3, p. 033001.

Li, L., He, H., and Lin, Y. (2009). "Study on the spatial division multiplexing technique of fiber Bragg grating sensors". In: *2009 Symposium on Photonics and Optoelectronics*. IEEE, pp. 1–3.

Li, R., Tan, Y., Chen, Y., Hong, L., and Zhou, Z. (2019). "Investigation of sensitivity enhancing and temperature compensation for fiber Bragg grating (FBG)-based strain sensor". In: *Optical Fiber Technology* 48, pp. 199–206.

Liang, X., Geng, Z., Li, J., Zhang, P., and Liu, W. (2020). "Axial Micro-Strain Sensor Based on FM-FBG via Dual-Mode ML-FMF in Sensor Networks". In: *Journal of Computer and Communications* 8.10, pp. 1–6.

Liu, Y., Zhang, J.-M., Min, Y.-T., Yu, Y., Lin, C., and Hu, Z.-Z. (2023). “A digital twin-based framework for simulation and monitoring analysis of floating wind turbine structures”. In: *Ocean Engineering* 283, p. 115009.

López-Higuera, J. M., Cobo, L. R., Incera, A. Q., and Cobo, A. (2011). “Fiber optic sensors in structural health monitoring”. In: *Journal of lightwave technology* 29.4, pp. 587–608.

Lorenzo, E. D., Petrone, G., Manzato, S., Peeters, B., Desmet, W., and Marulo, F. (2016). “Damage detection in wind turbine blades by using operational modal analysis”. In: *Structural Health Monitoring* 15.3, pp. 289–301.

Lun, T. L. T., Wang, K., Ho, J. D., Lee, K.-H., Sze, K. Y., and Kwok, K.-W. (2019). “Real-time surface shape sensing for soft and flexible structures using fiber Bragg gratings”. In: *IEEE Robotics and Automation Letters* 4.2, pp. 1454–1461.

Ma, Z. and Chen, X. (2018). “Fiber Bragg gratings sensors for aircraft wing shape measurement: Recent applications and technical analysis”. In: *Sensors* 19.1, p. 55.

Márquez, F. P. G., Tobias, A. M., Pérez, J. M. P., and Papaelias, M. (2012). “Condition monitoring of wind turbines: Techniques and methods”. In: *Renewable energy* 46, pp. 169–178.

Martin, R. W., Sabato, A., Schoenberg, A., Giles, R. H., and Niezrecki, C. (2018). “Comparison of nondestructive testing techniques for the inspection of wind turbine blades’ spar caps”. In: *Wind Energy* 21.11, pp. 980–996.

Martinez-Luengo, M., Kolios, A., and Wang, L. (2016). “Structural health monitoring of offshore wind turbines: A review through the Statistical Pattern Recognition Paradigm”. In: *Renewable and Sustainable Energy Reviews* 64, pp. 91–105.

Marulo, F., Petrone, G., D’Alessandro, V., and Di Lorenzo, E. (2014). “Operational modal analysis on a wind turbine blade”. In: *Proceedings Of International Conference On Noise And Vibration Engineering (ISMA2014) And International Conference On Uncertainty In Structural Dynamics (USD2014)*, pp. 783–798.

Measures, R. M. (1993). “Fiber optic sensing for composite smart structures”. In: *Composites Engineering* 3.7-8, pp. 715–750.

Mehdikhani, M., Gorbatikh, L., Verpoest, I., and Lomov, S. V. (2019). “Voids in fiber-reinforced polymer composites: A review on their formation, characteristics, and effects on mechanical performance”. In: *Journal of Composite Materials* 53.12, pp. 1579–1669.

MicroEpsilon (2023). *Intelligent laser optical displacement measurement optoNCDT 1302 Datasheet*. URL: http://www.micro-epsilon.pl/download/man--optoncdt-1302--en.pdf.

Mikkelsen, L. P. and Mishnaevsky Jr, L. (2017). “Computational modelling of materials for wind turbine blades: Selected DTU wind energy activities”. In: *Materials* 10.11, p. 1278.

Miller, E. J., Pena, F., Jordan, A., Hudson, L., and Lokos, W. (2019). “Evaluation of wing load calibration and sensing methods using conventional strain gages and a fiber optic sensing system installed on a straight tapered wing”. In: *AIAA Scitech 2019 Forum*, p. 0227.

Mishnaevsky, L., Branner, K., Petersen, H. N., Beauson, J., McGugan, M., and Sørensen, B. F. (2017). “Materials for wind turbine blades: an overview”. In: *Materials* 10.11, p. 1285.

Moll, J., Arnold, P., Mälzer, M., Krozer, V., Pozdniakov, D., Salman, R., Rediske, S., Scholz, M., Friedmann, H., and Nuber, A. (2018). “Radar-based structural health monitoring of wind turbine blades: The case of damage detection”. In: *Structural Health Monitoring* 17.4, pp. 815–822.

Myrent, N., Adams, D. E., and Griffith, D. T. (2015). “Wind turbine blade shear web disbond detection using rotor blade operational sensing and data analysis”. In: *Philosophical Transactions of the Royal Society A: Mathematical, Physical and Engineering Sciences* 373.2035, p. 20140345.

NationalAerospaceLaboratoriesIndia, C. (2020). *Vacuum Enhanced Resin Infusion Technology*. Tech. rep. URL: https://nal.res.in/en/techniques/vacuum-enhanced-resin-infusion-technology.

Nicolas, M. J., Sullivan, R. W., and Richards, W. L. (2016). “Large scale applications using FBG sensors: determination of in-flight loads and shape of a composite aircraft wing”. In: *Aerospace* 3.3, p. 18.

Niezrecki, C., Avitabile, P., Chen, J., Sherwood, J., Lundstrom, T., LeBlanc, B. P., Hughes, S., Desmond, M., Beattie, A. G., Klute, S. M., et al. (2013). *Inspection and Monitoring of Wind Turbine Blade Embedded Defects During Fatigue Testing.* Tech. rep. Sandia National Lab.(SNL-NM), Albuquerque, NM (United States).

Okabe, Y., Yashiro, S., Tsuji, R., Mizutani, T., and Takeda, N. (2002). "Effect of thermal residual stress on the reflection spectrum from fiber Bragg grating sensors embedded in CFRP laminates". In: *Composites Part A: Applied Science and Manufacturing* 33.7, pp. 991–999.

Owen, R. B., Inman, D. J., and Ha, D. S. (2010). "A multi-mode structural health monitoring system for wind turbine blades and components". In: *Annual Conference of the PHM Society*. Vol. 2. 1.

Park, S., Park, T., and Han, K. (2011). "Real-time monitoring of composite wind turbine blades using fiber Bragg grating sensors". In: *Advanced Composite Materials* 20.1, pp. 39–51.

Phelps, C. and Singleton, J. (2011). "Wind turbine blade design". In: *Cornell University, M. Eng. Report*.

Price, S. J. and Figueira, R. B. (2017). "Corrosion protection systems and fatigue corrosion in offshore wind structures: current status and future perspectives". In: *Coatings* 7.2, p. 25.

Raghavan, L. (2015). "Industrial looks at ways of manufacturing defects of fiber reinforced polymer composites." PhD thesis.

Raišutis, R., Jasiūnienė, E., and Žukauskas, E. (2008). "Ultrasonic NDT of wind turbine blades using guided waves". In: *Ultragarsas/Ultrasound* 63.1, pp. 7–11.

Rumsey, M., Paquette, J., White, J., Werlink, R., Beattie, A., Pitchford, C., and Dam, J. van (2008). "Experimental results of structural health monitoring of wind turbine blades". In: *46th AIAA aerospace sciences meeting and exhibit*, p. 1348.

Rumsey, M. A. (2011). "An evaluation of sensing technologies in a wind turbine blade: some issues, challenges and lessons learned". In: *Industrial and Commercial Applications of Smart Structures Technologies 2011*. Vol. 7979. International Society for Optics and Photonics, 79790G.

Salameh, J. P., Cauet, S., Etien, E., Sakout, A., and Rambault, L. (2018). "Gearbox condition monitoring in wind turbines: A review". In: *Mechanical Systems and Signal Processing* 111, pp. 251–264.

Sanati, H., Wood, D., and Sun, Q. (2018). "Condition monitoring of wind turbine blades using active and passive thermography". In: *Applied Sciences* 8.10, p. 2004.

Schenato, L. (2017). "A review of distributed fibre optic sensors for geo-hydrological applications". In: *Applied Sciences* 7.9, p. 896.

Schroeder, K., Ecke, W., Apitz, J., Lembke, E., and Lenschow, G. (2006). "A fibre Bragg grating sensor system monitors operational load in a wind turbine rotor blade". In: *Measurement science and technology* 17.5, p. 1167.

Schubel, P. J. and Crossley, R. J. (2012). "Wind turbine blade design". In: *Energies* 5.9, pp. 3425–3449.

Schubel, P., Crossley, R., Boateng, E., and Hutchinson, J. (2013). "Review of structural health and cure monitoring techniques for large wind turbine blades". In: *Renewable energy* 51, pp. 113–123.

SercaloMicrotechnologyLtd (2022). *Fast Fiber Optic Switch SW 1x4*. Sercalo Microtechnology Ltd. URL: https://www.sercalo.com/products/mems-switches-products/sw.

Sheibani, M. and Akbar Akbari, A. (2013). "Investigation of damage detection in blade root joints of a 100 kW wind turbine using frequency tracking". In: *Journal of Vibroengineering* 15.1, pp. 364–373.

Sheng, S., Fields, J., Cooperman, A., and Shields, M. (2023). *Wind Plant Operations and Maintenance Challenges and Research Opportunities*. Tech. rep. National Renewable Energy Lab.(NREL), Golden, CO (United States).

Sieros, G., Chaviaropoulos, P., Sørensen, J. D., Bulder, B. H., and Jamieson, P. (2012). "Upscaling wind turbines: theoretical and practical aspects and their impact on the cost of energy". In: *Wind energy* 15.1, pp. 3–17.

Sierra-Pérez, J., Torres-Arredondo, M. A., and Güemes, A. (2016). "Damage and nonlinearities detection in wind turbine blades based on strain field pattern recognition. FBGs, OBR and strain gauges comparison". In: *Composite Structures* 135, pp. 156–166.

Simis (2022). *ASHES: wind turbine simulation*. URL: https://www.simis.io/pages/features/.

Solrun Traustadottir, A. O. (2017). "Method of producing aerofoils". In: URL: https://patents.google.com/patent/US10391722B1/en.

Sørensen, B. F., Joergensen, E., Debel, C. P., Jensen, F., Jensen, H., Jacobsen, T., and Halling, K. (2004). "Improved design of large wind turbine blade of fibre composites based on studies of scale effects - Phase 2". In: *Risø National Laboratory Summary Report*.

Sørensen, B. F., Lading, L., and Sendrup, P. (2002). "Fundamentals for remote structural health monitoring of wind turbine blades". In: *Risø National Laboratory: A Pre-Project Report*.

Sotoudeh, V., Black, R. J., Moslehi, B., and Plavsic, A. (2010). *Fiber-optic defect and damage locator system for wind turbine blades*. Tech. rep. Intelligent Fiber Optic Systems Corp.(IFOS).

Technica (2021). "Customized FBG Sensor Datasheet". In: URL: https://technicasa.com/wp-content/uploads/2017/01/T10-Customized-FBG-Sensor-1.pdf.

Tosi, D. (2017). "Review and analysis of peak tracking techniques for fiber Bragg grating sensors". In: *Sensors* 17.10, p. 2368.

Tosi, D., Olivero, M., and Perrone, G. (2012). "Performance analysis of peak tracking techniques for fiber Bragg grating interrogation systems". In: *Journal of Microwaves, Optoelectronics and Electromagnetic Applications* 11, pp. 252–262.

Valyou, D. N., Arsenault, T. J., Janoyan, K., Marzocca, P., Post, N., Grappasonni, C., Arras, M., Coppotelli, G., Cardenas, D., Elizalde, H., et al. (2015). "Development and Commissioning of a Small/Mid-Size Wind Turbine Test Facility". In: *33rd Wind Energy Symposium*, p. 1000.

Vassilopoulos, A. P. (2023). "Fatigue behavior and life prediction of wind turbine blade composite materials". In: *Advances in Wind Turbine Blade Design and Materials*. Elsevier, pp. 287–340.

Veers, P., Bottasso, C. L., Manuel, L., Naughton, J., Pao, L., Paquette, J., Robertson, A., Robinson, M., Ananthan, S., Barlas, T., et al. (2023). "Grand challenges in the design, manufacture, and operation of future wind turbine systems". In: *Wind Energy Science* 8.7, pp. 1071–1131.

Wang, R., Fang, Y., Gao, Q., Li, Y., Yang, X., and Chen, Z. (2023). "Quantitative Visualization of Buried Defects in GFRP via Microwave Reflectometry". In: *Sensors* 23.14, p. 6629.

Wen, B., Tian, X., Jiang, Z., Li, Z., Dong, X., and Peng, Z. (2020). "Monitoring blade loads for a floating wind turbine in wave basin model tests using Fiber Bragg Grating sensors: A feasibility study". In: *Marine Structures* 71, p. 102729.

Westergaard, C. H. (2013). "Bladena's new simple retrofit for increased reliability and repair of the trailing edge bonds". In: *Sandia National Laboratories Wind Reliability workshop*. URL: https://www.slideshare.net/sandiaecis/westergaard-sandia-2013-wind-plant-reliability-workshop.

WindEurope (2023). *Wind energy in Europe 2023 Statistics and the outlook for 2024 2030*. Tech. rep. URL: https://windeurope.org/intelligence-platform/product/wind-energy-in-europe-2023-statistics-and-the-outlook-for-2024-2030/.

Wolfgang, E. (2008). "Applications of Fibre Bragg Grating Sensors". In: URL: https://pdfs.semanticscholar.org/71ba/795d660ca2f98b115ea929e88643a4cf4e47.pdf.

Yang, R., He, Y., and Zhang, H. (2016). "Progress and trends in nondestructive testing and evaluation for wind turbine composite blade". In: *Renewable and Sustainable Energy Reviews* 60, pp. 1225–1250.

Appendix A

Airfoil Data and Distributed Structural Properties of Blade

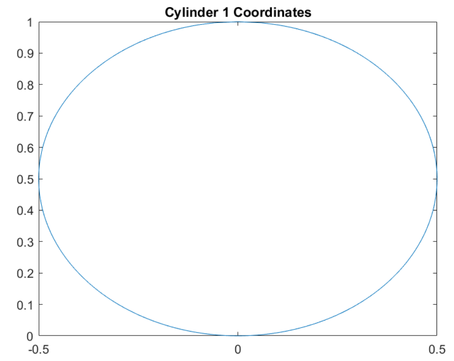

Figure. A.1 Cylinder 1 Coordinates

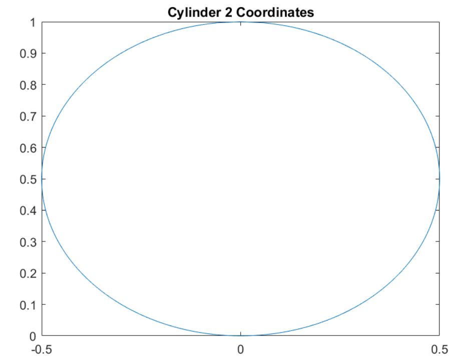

Figure. A.2 Cylinder 2 Coordinates

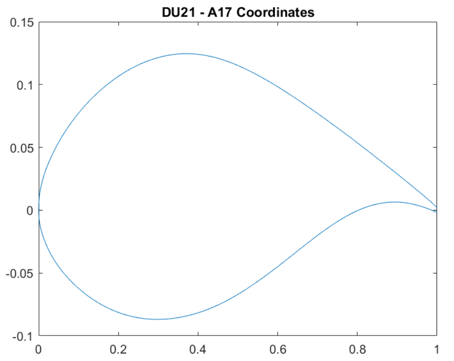

Figure. A.3 DU21-A17 Coordinates

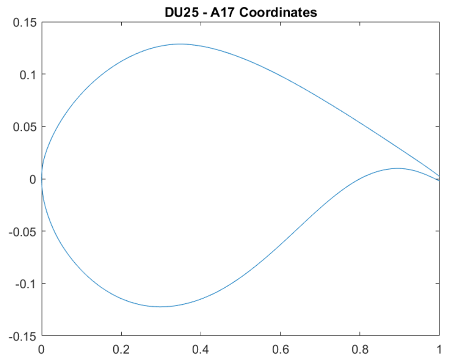

Figure. A.4 DU25-A17 Coordinates

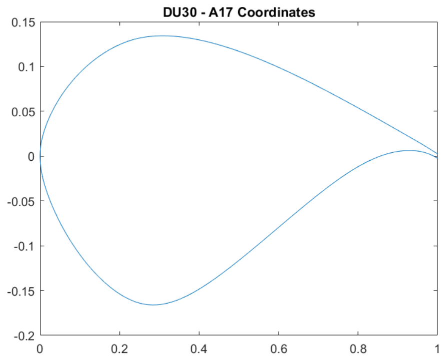

Figure. A.5 DU30-A17 Coordinates

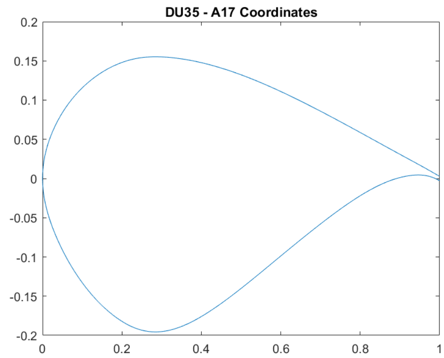

Figure. A.6 DU35-A17 Coordinates

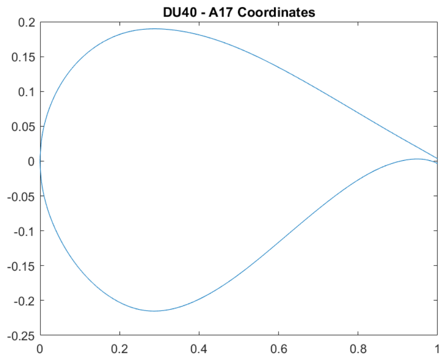

Figure. A.7 DU40-A17 Coordinates

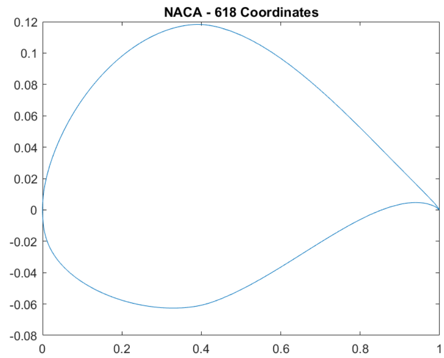

Figure. A.8 NACA-618 Coordinates

Table A.1 Distributed Structural Properties of NREL 5MW Blade

Node (-)	Blade Fraction (-)	Span (m)	Blade Mass Density (kg/m)	Flapwise Stiffness (Nm^2)	Edgewise Stiffness (Nm^2)	Torsional Stiffness (Nm^2)	Extensional Stiffness (N)	Aerodynamic Centre (-)
1	0.000	0.0	715.02	1.81E+10	1.81E+10	5.56E+09	9.73E+09	0.250
2	0.003	0.2	715.02	1.81E+10	1.81E+10	5.56E+09	9.73E+09	0.250
3	0.020	1.2	814.47	1.94E+10	1.96E+10	5.43E+09	1.08E+10	0.249
4	0.036	2.2	779.91	1.75E+10	1.95E+10	4.99E+09	1.01E+10	0.245
5	0.052	3.2	779.37	1.53E+10	1.98E+10	4.67E+09	9.87E+09	0.232
6	0.068	4.2	623.99	1.08E+10	1.49E+10	3.47E+09	7.61E+09	0.220
7	0.085	5.2	474.21	7.23E+09	1.02E+10	2.32E+09	5.49E+09	0.208
8	0.101	6.2	446.59	6.31E+09	9.14E+09	1.91E+09	4.97E+09	0.196
9	0.117	7.2	421.93	5.53E+09	8.06E+09	1.57E+09	4.49E+09	0.183
10	0.133	8.2	402.37	4.98E+09	6.88E+09	1.16E+09	4.03E+09	0.171
11	0.150	9.2	420.90	4.94E+09	7.01E+09	1.00E+09	4.04E+09	0.159
12	0.166	10.2	448.98	4.69E+09	7.17E+09	8.56E+08	4.17E+09	0.147
13	0.182	11.2	438.97	3.95E+09	7.27E+09	6.72E+08	4.08E+09	0.134
14	0.198	12.2	427.77	3.39E+09	7.08E+09	5.47E+08	4.09E+09	0.125
15	0.215	13.2	401.69	2.93E+09	6.24E+09	4.49E+08	3.67E+09	0.125
16	0.231	14.2	371.57	2.57E+09	5.05E+09	3.36E+08	3.15E+09	0.125
17	0.247	15.2	368.05	2.39E+09	4.95E+09	3.11E+08	3.01E+09	0.125
18	0.263	16.2	364.96	2.27E+09	4.81E+09	2.92E+08	2.88E+09	0.125
19	0.296	18.2	357.37	2.05E+09	4.50E+09	2.61E+08	2.61E+09	0.125
20	0.328	20.2	347.54	1.83E+09	4.24E+09	2.29E+08	2.36E+09	0.125
21	0.361	22.2	339.10	1.59E+09	4.00E+09	2.01E+08	2.15E+09	0.125
22	0.394	24.2	330.50	1.36E+09	3.75E+09	1.74E+08	1.94E+09	0.125
23	0.426	26.2	310.40	1.10E+09	3.45E+09	1.44E+08	1.63E+09	0.125
24	0.459	28.2	302.88	8.76E+08	3.14E+09	1.20E+08	1.43E+09	0.125
25	0.491	30.2	277.34	6.81E+08	2.73E+09	8.12E+07	1.17E+09	0.125

Table A.2 Distributed Structural Properties of NREL 5MW Blade contd.

Node	Blade Fraction	Span	Blade Mass Density	Flapwise Stiffness	Edgewise Stiffness	Torsional Stiffness	Extensional Stiffness	Aerodynamic Centre
(-)	(-)	(m)	(kg/m)	(Nm^2)	(Nm^2)	(Nm^2)	(N)	(-)
26	0.524	32.2	266.66	5.35E+08	2.55E+09	6.91E+07	1.05E+09	0.125
27	0.556	34.2	254.51	4.09E+08	2.33E+09	5.75E+07	9.23E+08	0.125
28	0.589	36.2	232.36	3.15E+08	1.83E+09	4.59E+07	7.61E+08	0.125
29	0.621	38.2	210.94	2.39E+08	1.58E+09	3.60E+07	6.48E+08	0.125
30	0.654	40.2	188.94	1.76E+08	1.32E+09	2.74E+07	5.40E+08	0.125
31	0.686	42.20	173.87	1.26E+08	1.18E+09	2.09E+07	5.31E+08	0.125
32	0.719	44.20	162.62	1.07E+08	1.02E+09	1.85E+07	4.60E+08	0.125
33	0.751	46.20	146.32	9.09E+07	7.98E+08	1.63E+07	3.76E+08	0.125
34	0.784	48.20	136.44	7.63E+07	7.10E+08	1.45E+07	3.29E+08	0.125
35	0.816	50.20	112.97	6.11E+07	5.18E+08	9.07E+06	2.44E+08	0.125
36	0.849	52.20	104.03	4.95E+07	4.55E+08	8.06E+06	2.12E+08	0.125
37	0.881	54.20	95.04	3.94E+07	3.95E+08	7.08E+06	1.82E+08	0.125
38	0.898	55.20	87.41	3.47E+07	3.54E+08	6.09E+06	1.60E+08	0.125
39	0.914	56.20	76.78	3.04E+07	3.05E+08	5.75E+06	1.09E+08	0.125
40	0.930	57.20	72.43	2.65E+07	2.81E+08	5.33E+06	1.00E+08	0.125
41	0.938	57.70	69.79	2.38E+07	2.62E+08	4.94E+06	9.22E+07	0.125
42	0.946	58.20	62.49	1.96E+07	1.59E+08	4.24E+06	6.32E+07	0.125
43	0.954	58.70	58.89	1.60E+07	1.38E+08	3.66E+06	5.33E+07	0.125
44	0.963	59.20	55.27	1.28E+07	1.19E+08	3.13E+06	4.45E+07	0.125
45	0.971	59.70	51.72	1.01E+07	1.02E+08	2.64E+06	3.69E+07	0.125
46	0.979	60.20	48.25	7.55E+06	8.51E+07	2.17E+06	2.99E+07	0.125
47	0.987	60.70	43.88	4.60E+06	6.43E+07	1.58E+06	2.13E+07	0.125
48	0.995	61.20	12.06	2.50E+05	6.61E+06	2.50E+05	4.85E+06	0.125
49	1.000	61.50	10.87	1.70E+05	5.01E+06	1.90E+05	3.53E+06	0.125

Table A.3 Distributed Structural Properties of Hull Blade 1.8m Blade

Node (-)	Blade Fraction (-)	Span (m)	Blade Mass Density (kg/m)	Flapwise Stiffness (Nm^2)	Edgewise Stiffness (Nm^2)	Torsional Stiffness (Nm^2)	Extensional Stiffness (N)	Aerodynamic Centre (-)
1	0.000	0.000	6.13E-01	1.33E+04	1.33E+04	4.09E+03	7.15E+03	0.250
2	0.003	0.006	6.13E-01	1.33E+04	1.33E+04	4.09E+03	7.15E+03	0.250
3	0.020	0.035	6.98E-01	1.43E+04	1.44E+04	3.99E+03	7.92E+03	0.249
4	0.036	0.064	6.68E-01	1.28E+04	1.43E+04	3.67E+03	7.39E+03	0.245
5	0.052	0.094	6.68E-01	1.12E+04	1.45E+04	3.43E+03	7.25E+03	0.232
6	0.068	0.123	5.35E-01	7.92E+03	1.09E+04	2.55E+03	5.59E+03	0.220
7	0.085	0.152	4.06E-01	5.31E+03	7.51E+03	1.71E+03	4.03E+03	0.208
8	0.101	0.181	3.83E-01	4.63E+03	6.72E+03	1.40E+03	3.65E+03	0.196
9	0.117	0.211	3.62E-01	4.06E+03	5.92E+03	1.15E+03	3.30E+03	0.183
10	0.133	0.240	3.45E-01	3.66E+03	5.06E+03	8.51E+02	2.96E+03	0.171
11	0.150	0.269	3.61E-01	3.63E+03	5.15E+03	7.36E+02	2.96E+03	0.159
12	0.166	0.299	3.85E-01	3.45E+03	5.26E+03	6.29E+02	3.06E+03	0.147
13	0.182	0.328	3.76E-01	2.90E+03	5.34E+03	4.94E+02	3.00E+03	0.134
14	0.198	0.357	3.67E-01	2.49E+03	5.20E+03	4.02E+02	3.00E+03	0.125
15	0.215	0.386	3.44E-01	2.15E+03	4.59E+03	3.30E+02	2.69E+03	0.125
16	0.231	0.416	3.18E-01	1.89E+03	3.71E+03	2.47E+02	2.31E+03	0.125
17	0.247	0.445	3.15E-01	1.75E+03	3.63E+03	2.29E+02	2.21E+03	0.125
18	0.263	0.474	3.13E-01	1.67E+03	3.53E+03	2.14E+02	2.12E+03	0.125
19	0.296	0.533	3.06E-01	1.51E+03	3.31E+03	1.92E+02	1.92E+03	0.125
20	0.328	0.591	2.98E-01	1.34E+03	3.12E+03	1.68E+02	1.73E+03	0.125
21	0.361	0.650	2.91E-01	1.17E+03	2.93E+03	1.47E+02	1.58E+03	0.125
22	0.394	0.708	2.83E-01	1.00E+03	2.75E+03	1.28E+02	1.43E+03	0.125
23	0.426	0.767	2.66E-01	8.10E+02	2.53E+03	1.06E+02	1.20E+03	0.125
24	0.459	0.826	2.59E-01	6.43E+02	2.31E+03	8.81E+01	1.05E+03	0.125
25	0.491	0.884	2.38E-01	5.00E+02	2.01E+03	5.96E+01	8.58E+02	0.125

Table A.4 Distributed Structural Properties of Hull Blade 1.8m Blade contd.

Node (-)	Blade Fraction (-)	Span (m)	Blade Mass Density (kg/m)	Flapwise Stiffness (Nm^2)	Edgewise Stiffness (Nm^2)	Torsional Stiffness (Nm^2)	Extensional Stiffness (N)	Aerodynamic Centre (-)
26	0.524	0.943	2.29E-01	3.93E+02	1.88E+03	5.07E+01	7.69E+02	0.125
27	0.556	1.001	2.18E-01	3.00E+02	1.71E+03	4.22E+01	6.78E+02	0.125
28	0.589	1.060	1.99E-01	2.31E+02	1.34E+03	3.37E+01	5.59E+02	0.125
29	0.621	1.118	1.81E-01	1.75E+02	1.16E+03	2.64E+01	4.76E+02	0.125
30	0.654	1.177	1.62E-01	1.29E+02	9.72E+02	2.02E+01	3.96E+02	0.125
31	0.686	1.235	1.49E-01	9.25E+01	8.69E+02	1.53E+01	3.90E+02	0.125
32	0.719	1.294	1.39E-01	7.88E+01	7.49E+02	1.36E+01	3.38E+02	0.125
33	0.751	1.352	1.25E-01	6.67E+01	5.86E+02	1.20E+01	2.76E+02	0.125
34	0.784	1.411	1.17E-01	5.60E+01	5.21E+02	1.07E+01	2.42E+02	0.125
35	0.816	1.470	9.68E-02	4.48E+01	3.81E+02	6.66E+00	1.79E+02	0.125
36	0.849	1.528	8.91E-02	3.63E+01	3.34E+02	5.92E+00	1.55E+02	0.125
37	0.881	1.587	8.14E-02	2.89E+01	2.90E+02	5.20E+00	1.33E+02	0.125
38	0.898	1.616	7.49E-02	2.55E+01	2.60E+02	4.47E+00	1.18E+02	0.125
39	0.914	1.645	6.58E-02	2.23E+01	2.24E+02	4.22E+00	8.02E+01	0.125
40	0.930	1.674	6.21E-02	1.95E+01	2.07E+02	3.91E+00	7.35E+01	0.125
41	0.938	1.689	5.98E-02	1.75E+01	1.92E+02	3.63E+00	6.77E+01	0.125
42	0.946	1.704	5.36E-02	1.44E+01	1.17E+02	3.11E+00	4.64E+01	0.125
43	0.954	1.718	5.05E-02	1.18E+01	1.01E+02	2.69E+00	3.92E+01	0.125
44	0.963	1.733	4.74E-02	9.42E+00	8.72E+01	2.30E+00	3.27E+01	0.125
45	0.971	1.748	4.43E-02	7.40E+00	7.46E+01	1.94E+00	2.71E+01	0.125
46	0.979	1.762	4.14E-02	5.54E+00	6.25E+01	1.59E+00	2.20E+01	0.125
47	0.987	1.777	3.76E-02	3.38E+00	4.72E+01	1.16E+00	1.56E+01	0.125
48	0.995	1.792	1.03E-02	1.84E-01	4.85E+00	1.84E-01	3.56E+00	0.125
49	1.000	1.800	9.31E-03	1.25E-01	3.68E+00	1.40E-01	2.59E+00	0.125

Table A.5 Ixx and Neutral Axis x-component Derivation

Part	Area	Distance to centroid	Moment about origin	Moment about centroid
Outer Ellipse 1	$\mathrm{AA} = \frac{\pi ab}{2}$	$x\bar{A} = \frac{4b}{3\pi}$	$\mathrm{IxA} = \frac{\pi ab^3}{8}$	$\mathrm{IxxA} = \frac{\pi ab^3}{8} - \frac{8ab^3}{9\pi}$
Inner Ellipse 1	$\mathrm{AB} = \frac{\pi cd}{2}$	$x\bar{B} = \frac{4d}{3\pi}$	$\mathrm{IxB} = \frac{\pi cd^3}{8}$	$\mathrm{IxxB} = \frac{\pi ab^3}{8} - \frac{8ab^3}{9\pi}$
Upper Ellipse	$\mathrm{AU} = \frac{\pi ab}{2} - \frac{\pi cd}{2}$	$x\bar{U} = \frac{\frac{2ab^2}{3} - \frac{2cd^2}{3}}{\frac{\pi ab}{2} - \frac{\pi cd}{2}}$	$\mathrm{IxU} = \frac{\pi ab^3}{8} - \frac{\pi cd^3}{8}$	$\mathrm{IxxU} = \frac{\left(\frac{2ab^2}{3} - \frac{2cd^2}{3}\right)^2}{\frac{\pi ab}{2} - \frac{\pi cd}{2}} + \frac{\pi ab^3}{8} - \frac{\pi cd^3}{8}$
		$\mathrm{ans} = \frac{4ab^2 - 4cd^2}{3\pi(ab-cd)}$		$\mathrm{ans} = \frac{\pi ab^3}{8} - \frac{\pi cd^3}{8} + \frac{8\left(ab^2 - cd^2\right)^2}{9\pi(ab-cd)}$
Outer Ellipse 2	$\mathrm{AC} = \frac{\pi ab}{2}$	$x\bar{C} = \frac{4b}{3\pi}$	$\mathrm{IxC} = \frac{\pi ab^3}{8}$	$\mathrm{IxxC} = \frac{\pi ab^3}{8} - \frac{8ab^3}{9\pi}$
Inner Ellipse 2	$\mathrm{AD} = \frac{\pi ef}{2}$	$x\bar{D} = \frac{4f}{3\pi}$	$\mathrm{IxD} = \frac{\pi ef^3}{8}$	$\mathrm{IxxD} = \frac{\pi ef^3}{8} - \frac{8ef^3}{9\pi}$
Lower Ellipse	$\mathrm{AL} = \frac{\pi ab}{2} - \frac{\pi ef}{2}$	$x\bar{L} = \frac{\frac{2ab^2}{3} - \frac{2ef^2}{3}}{\frac{\pi ab}{2} - \frac{\pi ef}{2}}$	$\mathrm{IxL} = \frac{\pi ab^3}{8} - \frac{\pi ef^3}{8}$	$\mathrm{IxxL} = \frac{\left(\frac{2ab^2}{3} - \frac{2ef^2}{3}\right)^2}{\frac{\pi ab}{2} - \frac{\pi ef}{2}} + \frac{\pi ab^3}{8} - \frac{\pi ef^3}{8}$
		$\mathrm{ans} = \frac{4ab^2 - 4ef^2}{3\pi(ab-ef)}$		$\mathrm{ans} = \frac{\pi ab^3}{8} - \frac{\pi ef^3}{8} + \frac{8\left(ab^2 - ef^2\right)^2}{9\pi(ab-ef)}$
Total Blade	$\mathrm{AT} = \pi ab - \frac{\pi cd}{2} - \frac{\pi ef}{2}$	$x\bar{T} == \frac{\frac{2cd^2}{3} - \frac{2ef^2}{3}}{\frac{\pi cd}{2} - \pi ab + \frac{\pi ef}{2}}$	$\mathrm{IxT} = \frac{a\pi b^3}{4} - \frac{c\pi d^3}{8} - \frac{e\pi f^3}{8}$	$\mathrm{IxxT} = \frac{\pi ab^3}{4} - \frac{\left(\frac{2cd^2}{3} - \frac{2ef^2}{3}\right)^2}{\frac{\pi cd}{2} - \pi ab + \frac{\pi ef}{2}} - \frac{\pi cd^3}{8} - \frac{\pi ef^3}{8}$
(U + L)		$\mathrm{ans} = \frac{4cd^2 - 4ef^2}{3\pi(cd-2ab+ef)}$		$\mathrm{ans} = \frac{\pi ab^3}{4} - \frac{8\left(cd^2 - ef^2\right)^2}{9\pi(cd-2ab+ef)} - \frac{\pi cd^3}{8} - \frac{\pi ef^3}{8}$

Table A.6 Iyy and Neutral Axis y-component Derivation

Part	Area	Distance to centroid	Moment about origin	Moment about centroid
Outer Ellipse 1	$\mathrm{AA} = \frac{\pi ab}{2}$	$y\bar{A} = \frac{4a}{3\pi}$	$\mathrm{IyA} = \frac{\pi a^3 b}{8}$	$\mathrm{IyyA} = \frac{\pi a^3 b}{8} - \frac{8a^3 b}{9\pi}$
Inner Ellipse 1	$\mathrm{AB} = \frac{\pi cd}{2}$	$y\bar{B} = \frac{4c}{3\pi}$	$\mathrm{IyB} = \frac{\pi c^3 d}{8}$	$\mathrm{IyyB} = \frac{\pi a^3 b}{8} - \frac{8a^3 b}{9\pi}$
Upper Ellipse	$\mathrm{AU} = \frac{\pi ab}{2} - \frac{\pi cd}{2}$	$y\bar{U} = \frac{\frac{2a^2b}{3} - \frac{2c^2d}{3}}{\frac{\pi ab}{2} - \frac{\pi cd}{2}}$	$\mathrm{IyU} = \frac{\pi a^3 b}{8} - \frac{\pi c^3 d}{8}$	$\mathrm{IyyU} = \frac{\left(\frac{2a^2b}{3} - \frac{2c^2d}{3}\right)^2}{\frac{\pi ab}{2} - \frac{\pi cd}{2}} + \frac{\pi a^3 b}{8} - \frac{\pi c^3 d}{8}$
		$\mathrm{ans} = \frac{4a^2b - 4c^2d}{3\pi(ab-cd)}$		$\mathrm{ans} = \frac{\pi a^3 b}{8} - \frac{\pi c^3 d}{8} + \frac{8\left(a^2b - c^2d\right)^2}{9\pi(ab-cd)}$
Outer Ellipse 2	$\mathrm{AC} = \frac{\pi ab}{2}$	$y\bar{C} = \frac{4a}{3\pi}$	$\mathrm{IyC} = \frac{\pi a^3 b}{8}$	$\mathrm{IyyC} = \frac{\pi a^3 b}{8} - \frac{8a^3 b}{9\pi}$
Inner Ellipse 2	$\mathrm{AD} = \frac{\pi ef}{2}$	$y\bar{D} = \frac{4e}{3\pi}$	$\mathrm{IyD} = \frac{\pi e^3 f}{8}$	$\mathrm{IyyD} = \frac{\pi e^3 f}{8} - \frac{8e^3 f}{9\pi}$
Lower Ellipse	$\mathrm{AL} = \frac{\pi ab}{2} - \frac{\pi ef}{2}$	$y\bar{L} = \frac{\frac{2a^2b}{3} - \frac{2e^2f}{3}}{\frac{\pi ab}{2} - \frac{\pi ef}{2}}$	$\mathrm{IyL} = \frac{\pi a^3 b}{8} - \frac{\pi e^3 f}{8}$	$\mathrm{IyyL} = \frac{\left(\frac{2a^2b}{3} - \frac{2e^2f}{3}\right)^2}{\frac{\pi ab}{2} - \frac{\pi ef}{2}} + \frac{\pi a^3 b}{8} - \frac{\pi e^3 f}{8}$
		$\mathrm{ans} = \frac{4a^2b - 4e^2f}{3\pi(ab-ef)}$		$\mathrm{ans} = \frac{\pi a^3 b}{8} - \frac{\pi e^3 f}{8} + \frac{8\left(a^2b - e^2f\right)^2}{9\pi(ab-ef)}$
Total Blade	$\mathrm{AT} = \pi ab - \frac{\pi cd}{2}$	$y\bar{T} = \frac{\frac{2c^2d}{3} - \frac{2e^2f}{3}}{\frac{\pi cd}{2} - \pi ab + \frac{\pi ef}{2}}$	$\mathrm{IyT} = \frac{b\pi a^3}{4} - \frac{d\pi c^3}{8} - \frac{f\pi e^3}{8}$	$\mathrm{IyyT} = \frac{\pi a^3 b}{4} - \frac{\left(\frac{2c^2d}{3} - \frac{2e^2f}{3}\right)^2}{\frac{\pi cd}{2} - \pi ab + \frac{\pi ef}{2}} - \frac{\pi c^3 d}{8} - \frac{\pi e^3 f}{8}$
(U + L)	$-\frac{\pi ef}{2}$	$\mathrm{ans} = \frac{4c^2d - 4e^2f}{3\pi(cd - 2ab + ef)}$		$\mathrm{ans} = \frac{\pi a^3 b}{4} - \frac{8\left(c^2d - e^2f\right)^2}{9\pi(cd - 2ab + ef)} - \frac{\pi c^3 d}{8} - \frac{\pi e^3 f}{8}$

Appendix B

MATLAB Code for Automated Gaussian Fit & FBG Peak Detection

The following piece of MATLAB code has been used to implement the 1st order Gaussian peak fitting for the FBG spectra. Appropriate annotations are included, the specific values can be change according to the suitable FBG specifications.

% Reading the raw data from FBG spectra

```
fname='Ch 1 - Array 3-001.xlsx'; % File Name of the first spectra saved
DataX = xlsread(fname,'B2:B2002'); % Wavelength Range Data Column
DataY = xlsread(fname,'C2:C2002'); % Optical Power Data Column
SW = xlsread(fname,'D2:D2'); % Starting Wavelength
SP = xlsread(fname,'E2:E2') - 1; % Sampling Points
Span = xlsread(fname,'F2:F2'); % Span

str1='Ch 1 - Array 3'_0;
str3 =' .xlsx';
DataNew = [];

for i=1:1:99

if (i >=1)  (i<=9)
str1='Ch 1 - Array 3_0 0';
```

$elseif(i >= 10)(i <= 99)$
$str1 =' Ch1 - Array3_0 0';$
end

str2=string(i); filename=strcat(str1,str2,str3); Data(:,:) = xlsread(filename,'B2:C2002');
DataNew = [DataNew,Data]; DataA = cell2mat(DataNew);
end

save DataArray3-O1-L3.mat % save the data from multiple spectra to a .mat file for additional data processing

----

% Reading the raw data from FBG spectra

load DataArray3-O1-L3.mat

% Plotting the raw data from FBG spectra

wstart = 1559.5 ; % starting wavelength range for analysis
ws = 394;
wend = 1561; % ending wavelength range for analysis
we = 1227;

NPWA1 = [];
PWWA1 = [];
MGA1 = [];

for j1 = 1:1:6

w1 = Data(:,1);
p1 = Data(:,j1+1)-min(Data(:,j1+1)); % bringing the baseline of the spectrum to zero

```
GFA1 = [w1 p1];

figure (1)
plot(w1,p1,'b.'); hold on;
xlabel ('Wavelength (nm)'); ylabel('Optical Power (mW)');
legend ('raw 0 N','raw 6.8 N','raw 11.7 N','raw 16.6 N','raw 21.5 N','raw 26.4 N');
title('Raw Data spectra under incraesing loads')

end
```

———————————————————-

Appendix C

FBG Array Specification

Table C.1 Array 1 Specifications

Specification	DTG N°	Nominal Position (mm)		Wavelength (nm)		Reflection (%)
		Absolute	Relative	Nominal	Measured**	
Array 1	Lead In	0	0	N/A	N/A	N/A
	1	1700	1700	1530	1529.88	25.3
	2	1772	72	1535	1534.88	24.2
	3	1844	72	1540	1539.92	34.1
	4	1904	60	1545	1544.94	24.2
	5	1964	60	1550	1549.93	29.6
	6	2036	72	1555	1554.90	23.9
	7	2108	72	1560	1559.90	30.6
	Lead Out	2608	500	N/A	N/A	N/A

**wavelength measured on spool under slight tension

Table C.2 Array 2 Specifications

Specification	**DTG N°**	**Nominal Position (mm)**		**Wavelength (nm)**		**Reflection (%)**
		Absolute	**Relative**	**Nominal**	**Measured****	
Array 2	Lead In	0	0	N/A	N/A	N/A
	1	1070	1070	1519	1518.93	33.4
	2	1131	61	1523	1522.96	33.2
	3	1207	76	1527	1526.95	27
	4	1299	92	1531	1530.93	31.6
	5	1406	107	1535	1534.91	34.6
	6	1528	122	1539	1538.95	32
	7	1650	122	1543	1542.95	30.8
	8	1772	122	1547	1546.95	28.6
	9	1894	122	1551	1550.92	32.1
	10	2016	122	1555	1554.94	31.2
	11	2138	122	1559	1558.93	29
	12	2260	122	1563	1562.93	31.6
	13	2382	122	1567	1566.93	26.5
	14	2504	122	1571	1570.93	31.8
	15	2611	107	1575	1574.99	28.9
	16	2703	92	1579	1578.97	26.6
	17	2779	76	1583	1582.95	27.2
	18	2840	61	1587	1586.94	27.8
	Lead Out	3340	500	N/A	N/A	N/A

**wavelength measured on spool under slight tension

Table C.3 Array 3 Specifications

Specification	**DTG N°**	**Nominal Position (mm)**		**Wavelength (nm)**		**Reflection (%)**
		Absolute	**Relative**	**Nominal**	**Measured****	
Array 3	Lead In	0	0	N/A	N/A	N/A
	1	1070	1070	1527	1526.89	30.5
	2	1108	38	1532	1531.92	30.2
	3	1146	38	1537	1536.92	31.9
	4	1184	38	1542	1541.92	30.7
	5	1222	38	1547	1546.94	30.5
	6	1273	51	1552	1551.95	30.8
	7	1324	51	1557	1556.96	33.1
	8	1388	64	1562	1561.94	30.8
	Lead Out	1888	500	N/A	N/A	N/A

**wavelength measured on spool under slight tension

Table C.4 Array 4 Specifications

Specification	**DTG N°**	**Nominal Position (mm)**		**Wavelength (nm)**		**Reflection (%)**
		Absolute	**Relative**	**Nominal**	**Measured****	
Array 4	Lead In	0	0	N/A	N/A	N/A
	1	1070	1070	1531	1530.92	34.3
	2	1330	260	1536	1535.89	29.1
	3	1590	260	1541	1540.91	30.3
	4	1850	260	1546	1545.89	29.9
	5	2110	260	1551	1550.92	28.3
	6	2370	260	1556	1555.91	28.2
	7	2630	260	1561	1560.92	26.3
	Lead Out	3130	500	N/A	N/A	N/A

**wavelength measured on spool under slight tension

Table C.5 Array 5 Specifications

Specification	DTG N°	Nominal Position (mm)		Wavelength (nm)		Reflection (%)
		Absolute	Relative	Nominal	Measured**	
Array 5	Lead In	0	0	N/A	N/A	N/A
	1	2800	2800	1530	1529.93	27.2
	2	2835	35	1535	1534.88	27.3
	3	2870	35	1540	1539.93	30.9
	4	2905	35	1545	1544.96	31.3
	5	2975	70	1550	1549.93	26.4
	6	3010	35	1555	1554.89	25.1
	7	3045	35	1560	1559.88	25.9
	8	3080	35	1565	1564.92	27.3
	Lead Out	3580	500	N/A	N/A	N/A

**wavelength measured on spool under slight tension

Appendix D

Technical/ CAD Drawings

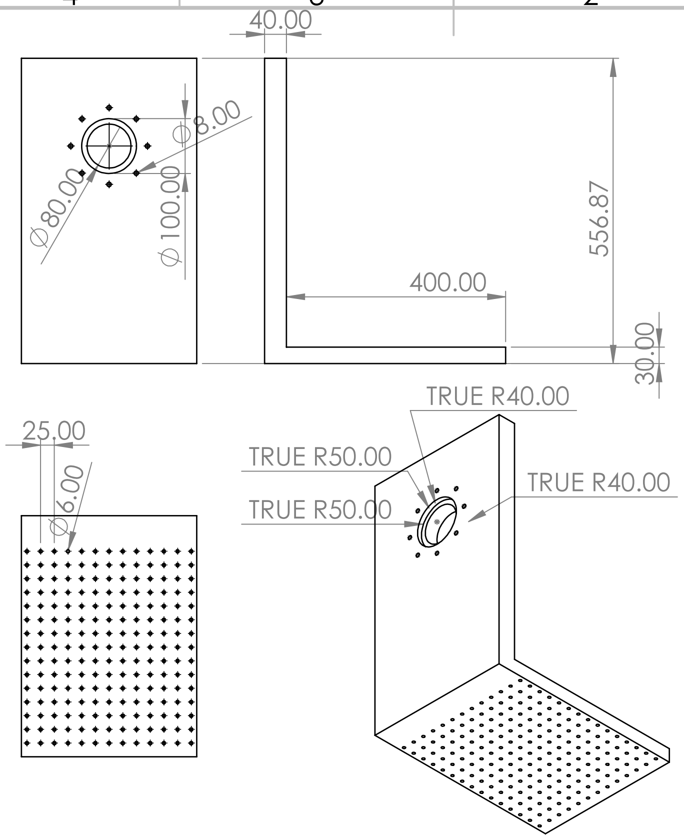

UNLESS OTHERWISE SPECIFIED:
DIMENSIONS ARE IN MILLIMETERS
SURFACE FINISH:
TOLERANCES:
LINEAR:
ANGULAR:

FINISH:

DEBURR AND BREAK SHARP EDGES

DO NOT SCALE DRAWING

REVISION

	NAME	SIGNATURE	DATE
DRAWN			
CHK'D			
APPV'D			
MFG			
Q.A			

TITLE:

MATERIAL:

WEIGHT:

DWG NO.

90deg teststand

A4

SCALE:1:10

SHEET 1 OF 1

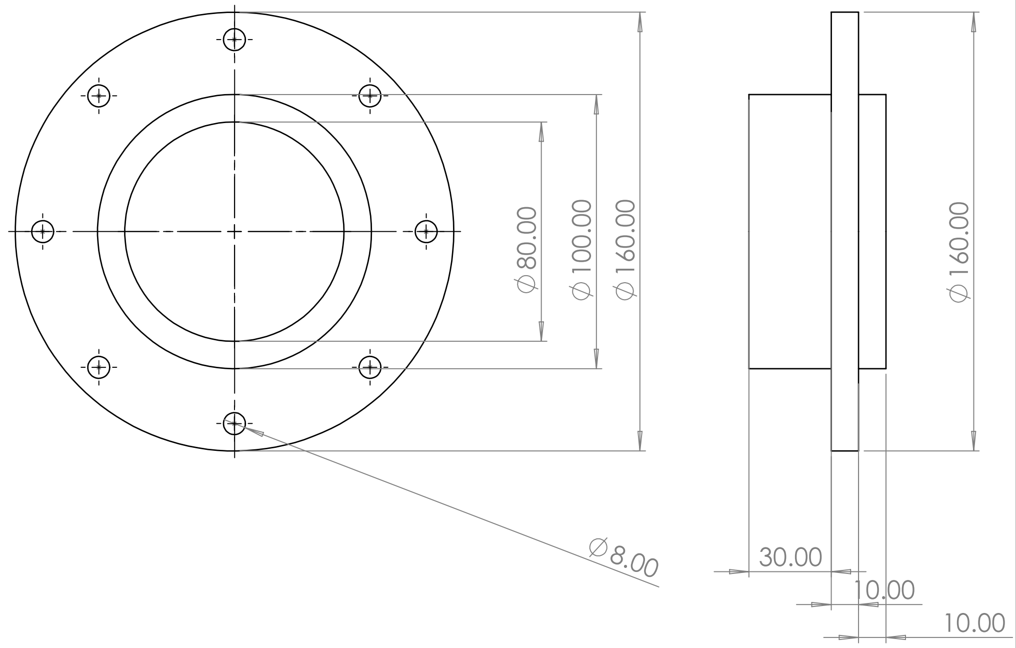

UNLESS OTHERWISE SPECIFIED:
DIMENSIONS ARE IN MILLIMETERS
SURFACE FINISH:
TOLERANCES:
LINEAR:
ANGULAR:

FINISH:

DEBURR AND BREAK SHARP EDGES

DO NOT SCALE DRAWING

REVISION

	NAME	SIGNATURE	DATE
DRAWN			
CHK'D			
APPV'D			
MFG			
Q.A			

TITLE:

MATERIAL:

DWG NO.

Adapter Block Plate_V2

A4

WEIGHT:

SCALE:1:2

SHEET 1 OF 1

Appendix E

Technical Data sheets

1 PRODUCT IDENTIFICATION

Product type	**TP-01**
Series number	F17918-0019-020
Reference work Instruction	WPM-15014-03

2 PRODUCT CONFIGURATION

	Value
Total sensor length	**40mm**
Pigtail length	**1mtr**
Pigtail material	**PVDF**
Connector type	**FC/APC**
Number of sensors	**1**
Housing material	**SS316**
Typical temperature precision	**0.2°C**
Temperature accuracy	**1°C**
Temperature range	**-22.5°C to 110°C**
Nominal wavelength at 22.5°C	**1564,061**

3 PRODUCT CHARACTERISATION

3.1 Wavelength spectrum

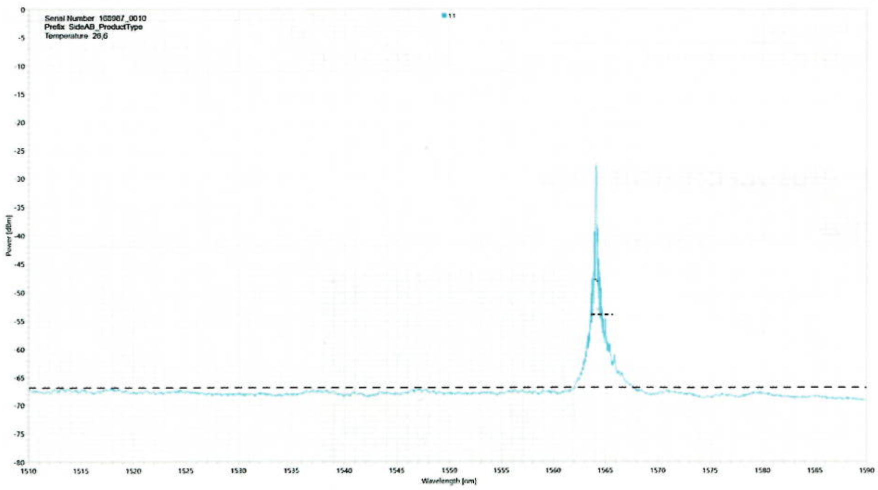

3.2 Calibration parameters

3.2.1 In case S2 is positive the temperature (T) can be expressed as:

$$T = Tref - \frac{S_1}{2S_2} + \sqrt{\left(\frac{S_1}{2S_2}\right)^2 + \frac{1}{S_2}\ln\left(\frac{\lambda}{\lambda_{Tref}}\right)}$$

3.2.2 In case S2 is negative the temperature (T) can be expressed as:

$$T = Tref - \frac{S_1}{2S_2} - \sqrt{\left(\frac{S_1}{2S_2}\right)^2 + \frac{1}{S_2}\ln\left(\frac{\lambda}{\lambda_{Tref}}\right)}$$

Where:

- T the current temperature (expressed in °C)
- T_{ref} = 22.5°C, the reference temperature for which S1 and S2 are calculated.

- S_1 and S_2 the temperature sensitivities of the FBG.
- λ is the current DTG wavelength;
- λ_{Tref} the reference wavelength i.e. the wavelength at the reference temperature T_{ref}

The parameters λ_{Tref}, S1, S2 for the DTG are defined in the table below:

DTG number	λ_{Tref} [nm]	Temperature factor S1 [°C^{-1}]	Temperature factor S2 [°C^{-2}]	Temp. error [°C]
DTG 1	**1564,061**	**6,4019E-06**	**7,8390E-09**	**0,4**

4 PRODUCT CONFORMITY

Product acceptance	Approved	
Comment		
For approval	**Name**	Michal Plevka
	Function	QC
	Date	4.1.2019
	Signature	

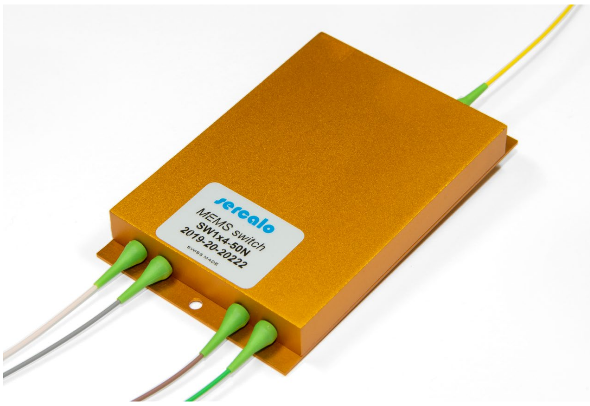

FAST FIBER OPTIC SW 1x4 SWITCH

OVERVIEW

The sercalo SW 1x4 switch is a very fast opto-mechanical switch working over both telecom wavelength windows from 1240 nm to 1600 nm. The highly reliable switching mechanism is based on micromechanical mirrors and features below 1 ms switching time and only 1.0 dB insertion loss.

The miniature package withstands rugged environments and is well suited for direct mounting on printed circuit boards.

FEATURES

- reliable
- 1.0 dB insertion loss
- 1 ms response time
- 60 dB crosstalk
- non-latching

APPLICATIONS

- Source Selection
- Protection Switching
- Monitoring
- Wavelength provisioning

ORDERING INFORMATION
SW1x4-9N

CONTACT
Sercalo Microtechnology Ltd.
Landstrasse 151, 9494 Schaan
Principality of Liechtenstein
Tel. +423 237 57 97 Fax. +423 237 57 48
www.sercalo.com Email: info@sercalo.com

Superluminescent LED Source

DL-BP1 1501A

Quick Guide

1 Documentation Package Download

1. Go to https://ibsen.com/about/customers/customer-download/dl-bp1-1501a-sled-light-source/
2. Type the password DLBPI15
3. Click the link to start downloading the .zip file
4. Extract the files from the compressed folder by right clicking on the .zip file and choosing "Extract All"
5. For Windows 32 bit:
    a. Copy the files from the "BP1 Win 32 bit version" directory to your Program Directory (created by yourself on your hard drive)
    b. Turn on the device power
    c. Connect the USB cable
    d. Run the 'BP1Interface.exe' file
6. For Windows 64 bit:
    a. Copy the files from the "BP1 Win 64 bit version" directory to your Program Directory (created by yourself on your hard drive)
    b. Install the 64 bit USB driver in accordance with the manual 'Bp1 driver update and installation manual.pdf'.
    c. Run the 'BP1 Interface v2.1.exe' file
7. The light source can also be operated via sample code supplied in the "Software Examples" folder.
   Note that the BP1 Superluminescent LED can be operated either via generic USD HID drivers or Cypress drivers.
   The BP1 executables will **ONLY** be able to communicate with the device once Cypress drivers has been correctly installed to your PC. If the Cypress drivers have been installed, only sample code relying on the Cypress drivers will work with the device.
   Should you wish to use generic Windows HID drivers instead, the Cypress drivers **MUST** be uninstalled for the BP1 SLED in order for it to be registered as a HID device.
   Check the Device Manager to confirm that the light source is correctly registered by the operating system as either a DenseLight BP1 source or a generic USB Input Device.

Cypress 3.4.7 drivers installed
The device is listed as DenseLight BP1 under Universal Serial Bus controllers

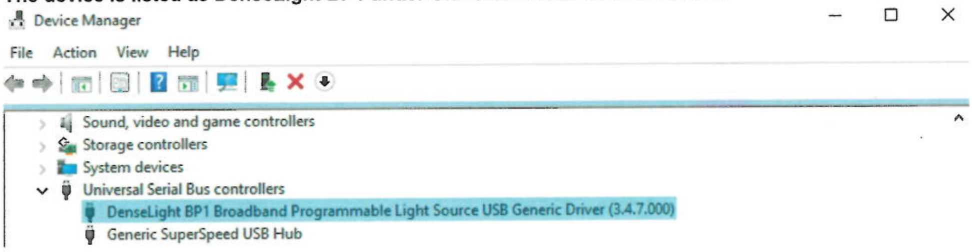

HID Device - Cypress 3.4.7 drivers has NOT been installed
The device is listed as USB Input Device under Human Interface Devices

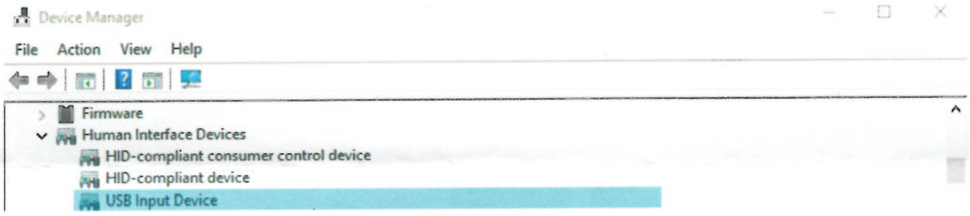

2 Revisions

Revision	Changed by	Short description of change
1	NHR	First version
2	NHR	CyUSB.dll file added to list of files to be copied
3	NHR	Web link corrected
4	NHR	Installation procedure for 32 bit and 64 bit corrected.
5	BR	Adding information about LabVIEW source code – point 7.
6	RBS	Added software sample code for Cypress drivers and HID interface.